

 Open access • Journal Article • DOI:10.1017/S0022112092002544

Receptivity of a laminar boundary layer to the interaction of a three-dimensional roughness element with time-harmonic free-stream disturbances — [Source link](#)

Mehran Tadjfar, R. J. Bodonyi

Institutions: Ames Research Center, Ohio State University

Published on: 01 Sep 1992 - Journal of Fluid Mechanics (Cambridge University Press)

Topics: Boundary layer, Stokes flow, Laminar flow, Reynolds number and External flow

Related papers:

- [Scattering of acoustic waves into Tollmien-Schlichting waves by small streamwise variations in surface geometry](#)
- [Boundary-Layer Receptivity to Long-Wave Free-Stream Disturbances](#)
- [Boundary layer receptivity](#)
- [The evolution of Tollmien-Schlichting waves near a leading edge](#)
- [A finite Reynolds number approach for the prediction of boundary layer receptivity in localized regions](#)

Share this paper:    

View more about this paper here: <https://typeset.io/papers/receptivity-of-a-laminar-boundary-layer-to-the-interaction-44e1639qwx>

INFORMATION TO USERS

The most advanced technology has been used to photograph and reproduce this manuscript from the microfilm master. UMI films the text directly from the original or copy submitted. Thus, some thesis and dissertation copies are in typewriter face, while others may be from any type of computer printer.

The quality of this reproduction is dependent upon the quality of the copy submitted. Broken or indistinct print, colored or poor quality illustrations and photographs, print bleedthrough, substandard margins, and improper alignment can adversely affect reproduction.

In the unlikely event that the author did not send UMI a complete manuscript and there are missing pages, these will be noted. Also, if unauthorized copyright material had to be removed, a note will indicate the deletion.

Oversize materials (e.g., maps, drawings, charts) are reproduced by sectioning the original, beginning at the upper left-hand corner and continuing from left to right in equal sections with small overlaps. Each original is also photographed in one exposure and is included in reduced form at the back of the book.

Photographs included in the original manuscript have been reproduced xerographically in this copy. Higher quality 6" x 9" black and white photographic prints are available for any photographs or illustrations appearing in this copy for an additional charge. Contact UMI directly to order.

U·M·I

University Microfilms International
A Bell & Howell Information Company
300 North Zeeb Road, Ann Arbor, MI 48106-1346 USA
313/761-4700 800/521-0600

Order Number 9111804

**Receptivity of a laminar boundary layer to the interaction of
a three-dimensional roughness element with time-harmonic
free-stream disturbances**

Tadjfar, Mehran, Ph.D.

The Ohio State University, 1990

Copyright ©1991 by Tadjfar, Mehran. All rights reserved.

U·M·I
300 N. Zeeb Rd.
Ann Arbor, MI 48106

NOTE TO USERS

**THE ORIGINAL DOCUMENT RECEIVED BY U.M.I. CONTAINED PAGES WITH
PHOTOGRAPHS WHICH MAY NOT REPRODUCE PROPERLY.**

THIS REPRODUCTION IS THE BEST AVAILABLE COPY.

**RECEPTIVITY OF A LAMINAR BOUNDARY LAYER TO THE
INTERACTION OF A THREE-DIMENSIONAL ROUGHNESS ELE-
MENT WITH TIME-HARMONIC FREE-STREAM DISTURBANCES**

DISSERTATION

**Presented in Partial Fulfillment of the Requirements for
the Degree Doctor of Philosophy in the Graduate
School of the Ohio State University**

By

Mehran Tadjfar, B.S., M.S.

*** * * * ***

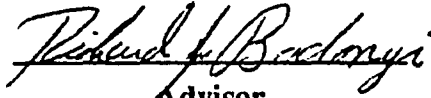
The Ohio State University

1990

Dissertation Committee

**R.J. Bodonyi
O.R. Burggraf
A.T. Conlisk
J.N. Scott**

Approved by


**Advisor
Department of Aeronautical
and
Astronautical Engineering**

To My Parents

ACKNOWLEDGMENTS

I wish to express my appreciation for the guidance and assistance of my advisor, Professor Richard J. Bodonyi.

Thanks go to Professor Odus R. Burggraf and Professor Frank T. Smith for many enlightening discussions. I am also grateful to Professor Thorwald Herbert for encouragement and recommending some of the references in this work. Dr. J. Kendall is acknowledged for providing results of his work.

I shall be forever indebted to my parents for teaching me respect for sciences and the value of higher education. I am also indebted to my sister for years of encouragement and belief in me.

The computer time on the CRAY Y-MP provided by the Ohio Supercomputer Center is greatly appreciated.

VITA

July 16, 1962	Born - Tehran, Iran
1982	B.S., Department of Mechanical Engineering, Northeastern University, Boston, Massachusetts
1985	M.S., Department of Mechanical and Aerospace Engineering, Case Western Reserve University, Cleveland, Ohio
1986-1990	Graduate Research and Teaching Associate, Department of Aeronautical and Astronautical Engineering, The Ohio State University Columbus, Ohio

PUBLICATIONS

- 1- Bodonyi, R.J., Welch, W.J.C., Duck, P.W., and Tadjfar, M.
"A Numerical Study of the Interaction Between Unsteady Free-stream Disturbances and Localized Variations in Surface Geometry" Journal of Fluid Mechanics, Vol. 209, Dec. 1989.
- 2- Tadjfar, M., Reshotko, E., Dybbs, A., and Edwards, R.V.
"Velocity Measurements Within Boundary Layer Roughness Using Index Matching" International Symposium on Laser Anemometry, ASME Tech. Conf., Miami, FL., Nov. 1985.
- 3- Tadjfar, M., Reshotko, E., Dybbs, A., and Edwards, R.V.
"Velocity Measurements In and About Roughness Array Using Matched-Index, Two-component Laser Anemometry" National Academy of Sciences, Washington, D.C., Oct. 1985.

Fields of Study

Major Field: Aeronautical and Astronautical Engineering

Studied Instability of Viscous Flows with: Professors R.J. Bodonyi, O.R. Burggraf, Th. Herbert, E. Reshotko, and F.T. Smith

TABLE OF CONTENTS

DEDICATION	ii
ACKNOWLEDGMENTS	iii
VITA	iv
LIST OF FIGURES	vii
INTRODUCTION	1
CHAPTER	PAGE
I. PROBLEM FORMULATION	6
I.1 Problem Statement	6
I.2 Steady-State Flow	13
I.3 Receptivity Problem	17
I.3.1 The Main Deck	18
I.3.2 The Upper Deck	23
I.3.3 The Lower Deck	26
I.3.4 Grid Transformation	30
II. NUMERICAL METHOD	35
II.1 Steady Flow	35
II.1.1 The Lower Deck	38
II.1.1a Modified Keller Box Method	38
II.1.1b Central Difference Method	43
II.1.2 The Upper Deck and Matching Conditions	45
II.2 Receptivity Problem	48
II.2.1 Finite Differences	51
III. STEADY-STATE RESULTS	62
III.1 Comparison with Prior Works	62
III.2 Flow Structure Over the Hump	66
III.3 Steady Flow Conclusions	88

IV.	DISTURBANCE FLOW RESULTS	101
IV.1	Receptivity of the Laminar Flow	101
IV.2	Detailed Flow Structure of an Amplifying Wave	130
IV.3	Disturbance Flow Due to a Hump with Local Separation	164
IV.4	Discussion and Conclusions	173
IV.4.1	Further Research	181
APPENDICES		
A	Upstream Boundary Conditions	182
A-1	Asymptotic Solutions	185
A-1.1	Outer Expansion	188
A-1.2	Inner Expansion	189
A-1.3	Results	190
B	λ Scalings	196
C	Flow Variables and Properties	203
D	T-S Wave Profiles in The Lower Deck	207
	LIST OF REFERENCES	211

LIST OF FIGURES

FIGURES		PAGE
1	The triple-deck flow structure.	7
2	Computational cell in the modified Keller-Box method.	39
3	Computational cell in the central-differences method.	51
4	The system of governing equations along the line at (i, j) .	56
5	Hump shape given by $F(x, y) = \exp[-x^2 - y^2]$.	63
6	Comparison of streamwise wall shear on the centerline, $Y=0$, with reference [24] (the dashed line).	64
7		68
a	Flow streamlines at the plane of symmetry for $h=1.0$.	68
b	Flow streamlines at the plane of symmetry for $h=2.8$.	68
c	Flow streamlines at the plane of symmetry for $h=4.5$.	69
8		69
a	Surface streamlines for the hump with $h=1.0$.	69
b	Surface streamlines for the hump with $h=2.8$.	70
c	Surface streamlines for the hump with $h=4.5$.	70
d	Surface streamlines for the hump with $h=4.5$ (enlarged).	71
9		73
a	Contour plot of steady pressure for the hump with $h=1.0$.	73

b	Contour plot of steady pressure for the hump with $h=2.8$.	74
c	Contour plot of steady pressure for the hump with $h=4.5$.	75
10		76
a	Contour plot of streamwise wall shear for the hump with $h=1.0$.	76
b	Contour plot of streamwise wall shear for the hump with $h=2.8$.	77
c	Contour plot of streamwise wall shear for the hump with $h=4.5$.	78
11		79
a	Contour plot of $A(X, Y)$ for the hump with $h=1.0$.	79
b	Contour plot of $A(X, Y)$ for the hump with $h=2.8$.	80
c	Contour plot of $A(X, Y)$ for the hump with $h=4.5$.	81
12		83
a	V-velocity contours at $X=-4.0$ for the hump with $h=4.5$.	83
b	W-velocity contours at $X=-4.0$ for the hump with $h=4.5$.	83
13		84
a	V-velocity contours at $X=-0.5$ for the hump with $h=4.5$.	84
b	W-velocity contours at $X=-0.5$ for the hump with $h=4.5$.	84
14		85
a	V-velocity contours at $X=0$ for the hump with $h=4.5$.	85
b	W-velocity contours at $X=0$ for the hump with $h=4.5$.	85
15	V-velocity contours at $X=0$ for the hump with $h=1.0$.	86
16	V-velocity contours at $X=0$ for the hump with $h=2.8$.	86

17		87
a	V-velocity contours at $X=0.5$ for the hump with $h=4.5$.	87
b	W-velocity contours at $X=0.5$ for the hump with $h=4.5$.	87
18		89
a	V-velocity contours at $X=5.0$ for the hump with $h=4.5$.	89
b	W-velocity contours at $X=5.0$ for the hump with $h=4.5$.	89
19	V-velocity contours at $X=5.0$ for the hump with $h=1.0$.	90
20	V-velocity contours at $X=5.0$ for the hump with $h=2.8$.	90
21	Streamwise wall shear along the line of symmetry, $Y=0$, for the steady flow over the humps with $h=1.0, 2.8$,& 4.5 .	91
22		93
a	Cross-flow streamlines pattern at $X=2.5$ ($h=4.5$) .	93
b	Cross-flow streamlines pattern at $X=3.0$ ($h=4.5$) .	94
c	Cross-flow streamlines pattern at $X=3.5$ ($h=4.5$) .	95
d	Cross-flow streamlines pattern at $X=4.0$ ($h=4.5$) .	96
e	Cross-flow streamlines pattern at $X=5.0$ ($h=4.5$) .	97
f	Cross-flow streamlines pattern at $X=10.0$ ($h=4.5$)	98
g	Evolution of the cross-flow vortex pair as it moves downstream by looking at figures 22a - 22f (reduced into one page, start from the figure in the lower left)	99
h	(Top) Representation of flow past a cylindrical roughness element on a flat plate (taken from AGARD-R-709 Fig. 47, Chap. I). (Bottom) Horseshoe vortices made visible by a sheet of smoke (taken from Van Dyke, M. "An Album of Fluid Motion", Fig. 93)	100
23		105

a	Contour plot of disturbance pressure for $h=1.0$, $S_0 = 1.0$, and $t = 0$.	105
b	Contour plot of disturbance pressure for $h=1.0$, $S_0 = 1.0$, and $t = \frac{\pi}{4}$.	106
c	Contour plot of disturbance pressure for $h=1.0$, $S_0 = 1.0$, and $t = \frac{\pi}{2}$.	107
d	Contour map of disturbance-pressure amplitude, $ p $, for $h=1.0$ and $S_0 = 1.0$.	108
24		109
a	Contour plot of $a(X,Y)$ for $h=1.0$, $S_0 = 1.0$, and $t = 0$.	109
b	Contour map of $ a(X,Y) $ for $h=1.0$ and $S_0 = 1.0$.	110
25	Contour plots of disturbance velocities, u and w , for $h=1.0$, $Y=0$, $S_0 = 1.0$ and $t = 0$.	112
26	Contour plots of disturbance velocities, u and w , for $h=1.0$, $Y=0$, $S_0 = 1.0$, and $t = \frac{\pi}{2}$.	113
27		114
a	Contour plot of disturbance pressure for $h=1.0$, $S_0 = 2.0$, and $t = 0$.	114
b	Contour plot of disturbance pressure for $h=1.0$, $S_0 = 2.0$, and $t = \frac{\pi}{2}$.	115
c	Contour map of disturbance-pressure amplitude, $ p $, for $h=1.0$ and $S_0 = 2.0$.	116
28		117

a	Contour plot of $a(X,Y)$ for $h=1.0$, $S_0 = 2.0$, and $t = 0$.	117
b	Contour map of $ a(X,Y) $ for $h=1.0$ and $S_0 = 2.0$.	118
29	Contour plots of disturbance u-velocity at $t = 0$, $t = \frac{\pi}{2}$ and its modulus for $h=1.0$, $Y=0$, and $S_0 = 2.0$.	119
30		121
a	Contour plot of $a(X,Y)$ for $h=1.0$, $S_0 = 3.0$, and $t = 0$.	121
b	Contour plot of $a(X,Y)$ for $h=1.0$, $S_0 = 3.0$, and $t = \frac{\pi}{2}$.	122
c	Contour map of $a(X,Y)$ amplitude, $ a $, for $h=1.0$ and $S_0 = 3.0$.	123
31		124
a	Contour plot of disturbance pressure for $h=1.0$, $S_0 = 3.0$, and $t = 0$.	124
b	Contour plot of disturbance pressure for $h=1.0$, $S_0 = 3.0$, and $t = \frac{\pi}{2}$.	125
32		126
a	Contour plot of du/dZ for $h=1.0$, $S_0 = 3.0$, and $t = 0$.	126
b	Contour plot of du/dZ for $h=1.0$, $S_0 = 3.0$, and $t = \frac{\pi}{2}$.	127
33		128
a	Contour plot of dv/dZ for $h=1.0$, $S_0 = 3.0$, and $t = 0$.	128
b	Contour plot of dv/dZ for $h=1.0$, $S_0 = 3.0$, and $t = \frac{\pi}{2}$.	129
34		131

a	Contour plots of disturbance u-velocity at $t = 0, \frac{\pi}{4},$ and $\frac{\pi}{2}$ for $h=1.0, Y=0,$ and $S_0 = 3.0.$	131
b	Contour plots of disturbance u-velocity at $t = \frac{3\pi}{4}, \pi,$ and $\frac{5\pi}{4}$ for $h=1.0, Y=0,$ and $S_0 = 3.0.$	132
c	Contour plots of disturbance u-velocity at $t = \frac{3\pi}{2}, \frac{7\pi}{4},$ and 2π for $h=1.0, Y=0,$ and $S_0 = 3.0.$	133
35	Contour plots of disturbance w-velocity at $t = 0$ and $t = \frac{\pi}{2}$ for $h=1.0, Y=0,$ and $S_0 = 3.0.$	134
36	Contour plots of disturbance velocities, u, v, and w at $t = 0$ for $h=1.0, Y=2.0,$ and $S_0 = 3.0.$	136
37	Contour plots of disturbance velocities, u, v, and w at $t = 0$ for $h=1.0, Y=4.0,$ and $S_0 = 3.0.$	137
38	Disturbance-flow streamlines in the X-Z plane at $Y=0$ for $h=1.0, t = 0$ and $S_0 = 3.0.$	138
39	Projection of disturbance-flow streamlines onto the X-Z plane at $Y=2.0$ for $h=1.0, t = 0$ and $S_0 = 3.0.$	139
40	Projection of disturbance-flow streamlines onto the X-Z plane at $Y=4.0$ for $h=1.0, t = 0$ and $S_0 = 3.0.$	140
41	Contour plot of w-velocity in the X-Y plane at $Z=3.9$ for $h=1.0, t = 0$ and $S_0 = 3.0.$	142
42	Projection of disturbance-flow streamlines onto the X-Y plane at $Z=3.9$ for $h=1.0, t = 0$ and $S_0 = 3.0.$	143
43	Projection of disturbance-flow velocity vector onto the X-Y plane at $Z=3.9$ for $h=1.0, t = 0$ and $S_0 = 3.0.$	144

44	Disturbance surface-streamlines for $h=1.0$, $t = 0$ and $S_0 = 3.0$	145
45	Contour plots of u -, v -, and w -velocity in the Y - Z plane at $X=-1.5$ for $h=1.0$, $t = 0$ and $S_0 = 3.0$.	147
46		148
a	Contour plots of u -, v -, and w -velocity in the Y - Z plane at $X=3.0$ for $h=1.0$, $t = 0$ and $S_0 = 3.0$.	148
b	Contour plot of u -velocity in the Y - Z plane at $X=3.0$ for $h=1.0$, $t = 0$ and $S_0 = 3.0$.	149
c	Projection of disturbance-flow streamlines onto the Y - Z plane at $X=3.0$ for $h=1.0$, $t = 0$ and $S_0 = 3.0$.	150
47		151
a	Contour plots of u -, v -, and w -velocity in the Y - Z plane at $X=4.2$ for $h=1.0$, $t = 0$ and $S_0 = 3.0$.	151
b	Contour plot of u -velocity in the Y - Z plane at $X=4.2$ for $h=1.0$, $t = 0$ and $S_0 = 3.0$.	152
c	Projection of disturbance-flow streamlines onto the Y - Z plane at $X=4.2$ for $h=1.0$, $t = 0$ and $S_0 = 3.0$	153
48		154
a	Contour plots of u -, v -, and w -velocity in the Y - Z plane at $X=6.0$ for $h=1.0$, $t = 0$ and $S_0 = 3.0$	154
b	Contour plot of u -velocity in the Y - Z plane at $X=6.0$ for $h=1.0$, $t = 0$ and $S_0 = 3.0$	155
c	Projection of disturbance-flow streamlines onto the Y - Z plane at $X=6.0$ for $h=1.0$, $t = 0$ and $S_0 = 3.0$	156
49		157

a	Contour plots of u-, v-, and w-velocity in the Y-Z plane at X=7.2 for h=1.0, $t = 0$ and $S_0 = 3.0$	157
b	Contour plot of u-velocity in the Y-Z plane at X=7.2 for h=1.0, $t = 0$ and $S_0 = 3.0$	158
c	Projection of disturbance-flow streamlines onto the Y-Z plane at X=7.2 for h=1.0, $t = 0$ and $S_0 = 3.0$.	159
50		160
a	Contour plots of u-, v-, and w-velocity in the Y-Z plane at X=8.7 for h=1.0, $t = 0$ and $S_0 = 3.0$.	160
b	Contour plot of u-velocity in the Y-Z plane at X=8.7 for h=1.0, $t = 0$ and $S_0 = 3.0$.	161
c	Projection of disturbance-flow streamlines onto the Y-Z plane at X=8.7 for h=1.0, $t = 0$ and $S_0 = 3.0$.	162
51	Projection of disturbance-flow streamlines onto the Y-Z plane at X=3.0, 4.2, 6.0, 7.2, and 8.7 for h=1.0, $t = 0$ and $S_0 = 3.0$ (start with the lower left figure).	163
52	Plot of disturbance pressure at Y=0 for h=4.5, $S_0 = 1.0$, and $t = 0$.	165
53		167
a	Contour plot of disturbance pressure for h=4.5, $t = 0$ and $S_0 = 1.0$.	167
b	Contour plot of disturbance pressure for h=4.5, $t = \frac{\pi}{2}$ and $S_0 = 1.0$.	168
54		169

a	Contour plots of u- and w-velocity in the X-Z plane at Y=0 for h=4.5, $t = 0$ and $S_0 = 1.0$ (the middle figure is a magnification of the u contours near the hump).	169
b	Contour plots of u- and w-velocity in the X-Z plane at Y=0 for h=4.5, $t = \frac{\pi}{4}$ and $S_0 = 1.0$ (the middle figure is a magnification of the u contours near the hump).	170
c	Contour plots of u- and w-velocity in the X-Z plane at Y=0 for h=4.5, $t = \frac{\pi}{2}$ and $S_0 = 1.0$ (the middle figure is a magnification of the u contours near the hump).	171
d	Contour plots of u- and w-velocity in the X-Z plane at Y=0 for h=4.5, $t = \frac{3\pi}{4}$ and $S_0 = 1.0$ (the middle figure is a magnification of the u contours near the hump).	172
55	Plot of disturbance pressure for h=1.0, at Y=0, $t = 0$ and $S_0 = 1.0$.	175
56	Plot of disturbance pressure for h=1.0, at Y=0, $t = 0$ and $S_0 = 2.5$.	176
57	Plot of disturbance pressure for h=1.0, at Y=0, $t = 0$ and $S_0 = 4.0$.	177
58	Contours of signal amplitude and their evolution in time for a wave packet observed experimentally (taken from reference [4]).	178
59	Profiles of u_{rms} (defined by equation (D-1)) in the lower deck for an amplifying wave, $S_0 = 3.0$, $Re = 1000000$, and $\delta = .01$, for two different Y-locations, Y=0 and Y=1.0, downstream of the hump, h=1, at: X = 1.5, 3.0, 4.2, 6.0, 7.2, 8.7, and 10.2.	210

Introduction

Boundary-layer transition has been one of the most active areas of research in fluid mechanics. Two types of transition are generally considered. The first type, bypass transition, is the process in which the external disturbances: sound, free-stream turbulence etc. or the internal disturbances: vibrations, roughness etc. are strong enough that vortex stretching and other nonlinear mechanisms directly lead to turbulence without going through the known instability mechanisms. The second type is the so called "quiet" environment transition in which transition evolves gradually, as has been experimentally documented, and can be followed by theory or numerical computations. [1,2,3]

The latter type is broken into four stages of development [3]:

- (1) Receptivity
- (2) Primary Instability
- (3) Secondary Instability
- (4) Breakdown

Most of the work in boundary-layer stability theory has been on the behavior of the individual normal-mode solutions of the linearized, parallel stability equations. Numer-

ous methods have been suggested to calculate the neutral stability curves and growth rates of these normal modes. Even the widely used e^N method is based on the amplitude ratio of the most unstable mode of the linear theory. However, in natural transition a spectrum of instability waves are present and the boundary layers found in practice are not parallel. The local Reynolds number is constantly changing and the energy is being redistributed by the interaction of all the modes. This has brought attention of experimental investigations to the evolution of wave packets in the boundary layer (see Gaster [4,5,6], Gilev et al. [7] , Kachenov [8] and Mack & Kendall [9]). In fact, Gaster [6] found that even very weak wave packets, with velocity fluctuations of the order of 5×10^{-4} when normalized by the free-stream velocity, are influenced by the nonparallel and nonlinear effects. Theoretical study of the wave packets has been slow due to the complexity of the numerical computations (see Gaster [5] , Mack and Kendall [9]).

Receptivity is the means by which a particular forced disturbance enters the boundary layer and initiates the transition process. If the initial disturbances are sufficiently large, they can grow by forcing mechanisms to nonlinear levels and eventually lead to turbulence (transition of the first type) and therefore, bypass the well known mechanisms of the second type. If they are small, they will tend to excite free disturbances in the boundary layer which are better known as Tollmien-Schlichting waves. These T-S waves will go through other stages of transition depending on the nature of the problem. It is this first stage in the transition process, which is the subject of this study.

Receptivity is fundamentally different from the classical eigenvalue stability problem. It is a boundary-value problem, since it involves the response of the boundary layer to an externally imposed disturbance. However, naturally occurring free-stream disturbances travel at much higher speeds than instability waves. Therefore, characteristic wavelengths of the free-stream disturbances at a given frequency are much longer than the T-S waves. Hence, a wavelength conversion is required to transfer energy from these long waves to the much shorter T-S waves. This wavelength conversion is the core of receptivity problem (see Reshotko [10]). Goldstein [11,12,13,14] using an asymptotic method showed that the wavelength conversion takes place at locations where the mean flow exhibits rapid changes and nonparallel effects are important. Examples are near the leading edge or any regions downstream where locally the boundary layer has to adjust rapidly to local pressure gradients (roughness, blowing, etc.).

Here we are interested in the interaction of small protuberances (on the scale of T-S wavelengths) in the surface geometry and unsteady free-stream disturbances. Using the triple-deck scalings of Stewartson [15], Goldstein [12] showed that small surface variations can produce a large coupling between T-S waves and the imposed disturbance, when these variations are sufficiently rapid (order of T-S wavelength). However, Goldstein's analysis is limited in that he took the linearized solution of Stewartson for the steady flow and his entire analysis is limited to the linearized case of a very small hump.

Recently, Bodonyi, Welch, Duck and Tadjfar [16] have considered a numerical

study of the interaction of free-stream disturbances and a small two-dimensional roughness element placed on a flat plate. In that study the two-dimensional nonlinear viscous-inviscid triple-deck equations were solved numerically to provide the basic steady motion. It was shown that the unsteady motion is governed by the unsteady linearized triple-deck equations, in suitably scaled variables. The solution was assumed to be harmonic in time. Numerical solutions were found for a range of values of frequency of the imposed free-stream disturbances and the hump height. It was found that the amplitude of all disturbance quantities grow without bound, downstream of the hump, if $S_0 > 2.29\dots$, where S_0 is the scaled Strouhal number based on the frequency of the free-stream disturbances. For values of $S_0 < 2.29\dots$, the disturbances eventually decay to zero amplitude and the flow remains stable. Thus the numerical solutions illustrate the growth or decay of the T-S waves generated by the interaction between the free-stream disturbance and the two-dimensional roughness element, depending on the value of the scaled Strouhal number.

In this study, analysis of Bodonyi et al. is extended to the interaction of a three-dimensional protuberance and the time harmonic disturbances in the free-stream. The three-dimensional nonlinear triple-deck equations are solved numerically to provide the basic steady-state motion. It is shown that the governing equations for the unsteady motion are the unsteady linearized three-dimensional triple-deck equations. These equations can only be solved numerically. The interaction of free-stream disturbances with the local pressure gradients induced by the hump's presence introduces a spectrum of all

spatial disturbances in the boundary layer. These disturbances travel downstream in the growing boundary layer and amplify or decay while interacting with each other. Again it was found that the growth or decay of T-S waves are dependant on the scaled Strouhal number. However, the three dimensionality manifests itself in spanwise wavelength selection and modulation. It is also found that the growth of T-S waves is confined to a wedge shape region downstream of the roughness element.

CHAPTER I

PROBLEM FORMULATION

I.1 Problem Statement

We shall consider the receptivity of a laminar boundary layer on a flat plate to the interaction of a small three-dimensional wall roughness element with free-stream time-harmonic disturbances. A small three-dimensional protuberance, of the order of the triple-deck structure (explained below), is placed at a distance L^* from the leading edge on an otherwise flat plate. The flow is assumed to be incompressible with a uniform free-stream velocity plus a small time harmonic oscillation of frequency ω imposed at infinity: $u^* = U_\infty^* [1 + \delta e^{-i\omega t}]$; where $\delta \ll 1$. Consider a cartesian coordinate system (x, y, z) , nondimensionalized by length L^* , with x in the streamwise direction, y in the spanwise direction, and z in the vertical direction with the origin taken at the leading edge. Also, time t is nondimensionalized by frequency ω .

The triple-deck structure is the asymptotic distinguished limit of the Navier-Stokes

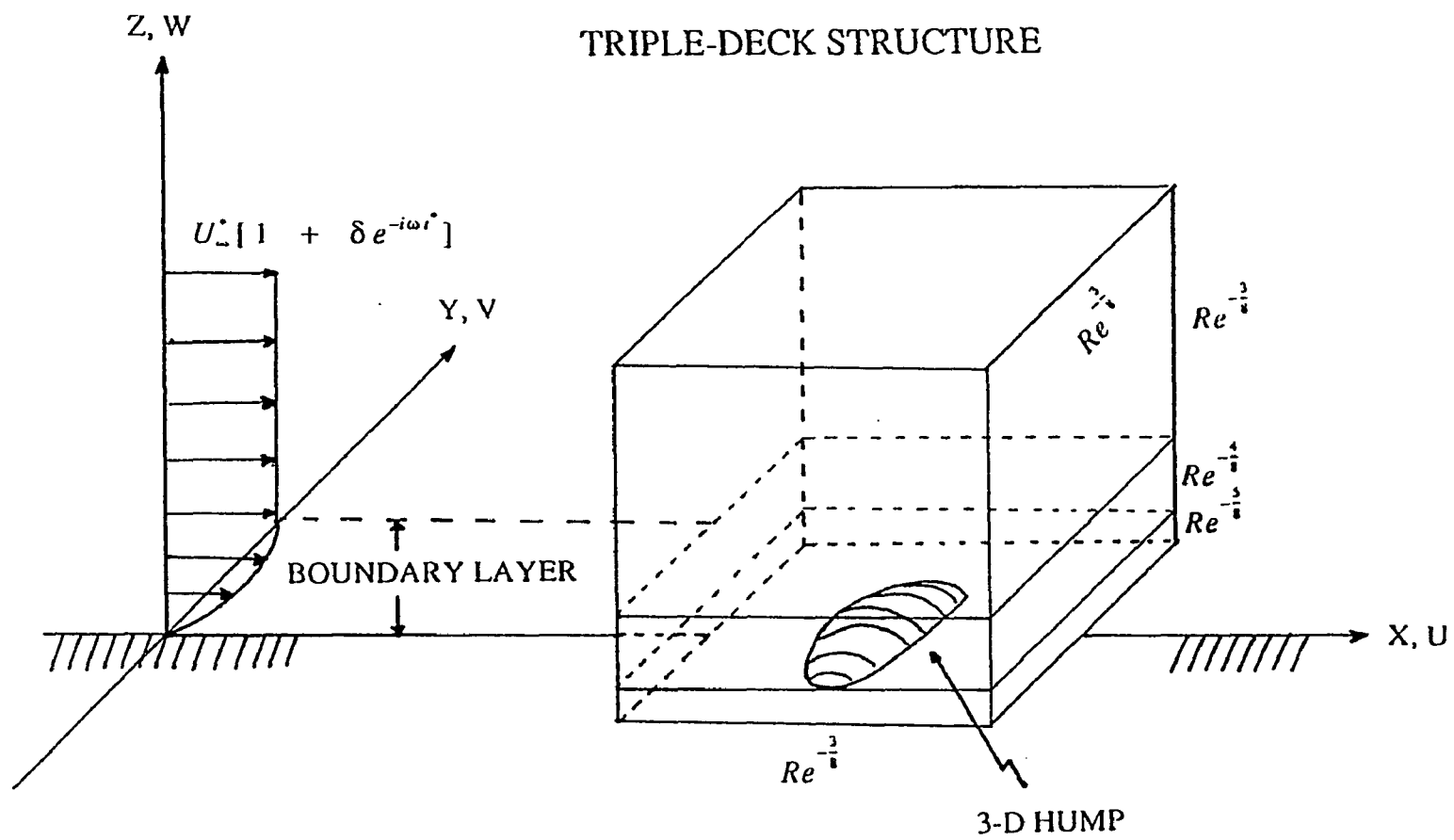


Figure 1. The triple-deck flow structure.

equations describing a small local flow structure, smaller than order one, in the boundary layer of an external flow at high Reynolds number (see figure 1). This flow structure could be caused by suction, slot-injection, wall turning, etc. or in our problem by a small 3-D wall roughness. The Reynolds number is defined as:

$$Re = \frac{U_*^* L^*}{\nu} , \quad (1-1)$$

where ν is the kinematic viscosity of the fluid. This structure was discovered by Stewartson [17] and also, independently, by Messiter [18] and by Neiland [19]. Over the past twenty years it has found many applications in steady and unsteady flows [15,20,21].

Suppose we have a flow structure in the boundary layer of length $\lambda \ll 1$, but $\lambda \gg Re_*^{-\frac{1}{2}}$ (order of boundary-layer thickness) in the x and y directions. The velocities (u, v, w) and pressure p are nondimensionalized by U_*^* and ρU_*^{*2} , respectively. The boundary-layer thickness is of the order $Re_*^{-\frac{1}{2}}$ and in most of the boundary layer the streamwise velocity, u , is of order one. Conservation of momentum in the x-direction requires that:

$$S \partial_t u + [u \partial_x + v \partial_y + w \partial_z] u = -\partial_x p + Re_*^{-1} [\partial_{xx} + \partial_{yy} + \partial_{zz}] u \quad (1-2)$$

Where S is the Strouhal number defined by:

$$S = \frac{\omega L^*}{U_*^*} . \quad (1-3)$$

Over most of the boundary layer, the main deck where $z \sim O\left(Re^{-\frac{1}{2}}\right)$, the changes occurring to the incoming boundary layer (within the flow structure considered) are inviscid since convective terms (i.e. $u \partial_x u$) are of order $1/\lambda$ while viscous terms (i.e. $Re^{-1} \partial_{xx} u$) are of order one or smaller. However, in a small viscous sublayer near the wall, the lower deck where $z \sim O\left(\epsilon Re^{-\frac{1}{2}}\right)$ with $\epsilon \ll 1$, viscous terms should be as important as the convective terms, in order to satisfy the no slip condition. This viscous sublayer is located in the linear velocity profile region of the boundary layer. Hence, here the streamwise velocity $u \sim O(\epsilon)$. Therefore, the convective terms are of the order ϵ^2/λ and the viscous terms are of order $1/\epsilon$. Balancing the two terms would require that $\lambda = \epsilon^3$.

Equating the pressure term ($\partial_x p$) to the convective and viscous terms would require the viscous pressure in the lower deck to be of the order ϵ^2 . There is no pressure gradient normal to the wall in the boundary layer. Hence, another potential flow region, the upper deck where z is of the order λ , is required to relate the induced pressure to the displacement of the boundary layer. The majority of the boundary-layer flow, i.e. that in the main deck, is displaced by the viscous lower deck. Therefore, the induced inviscid pressure in the upper deck is of the order $\epsilon Re^{-\frac{1}{2}}/\lambda$ (slope of the displaced boundary layer). To have viscous-inviscid interaction the two pressures should be equal, $\epsilon^2 = \epsilon Re^{-\frac{1}{2}}/\lambda$, which necessitate that $\lambda = Re^{-\frac{3}{8}}$ and $\epsilon = Re^{-1/8}$.

Now let's consider how the unsteadiness can be established in the boundary layer. The smallest magnitude of the unsteady term that can become important would first show up in the lower deck, which demands $S \partial_t \mu$ to be of order ϵ^{-1} to match with viscous terms. Therefore, only high frequency, $S \sim O(\epsilon^{-2})$, disturbances would penetrate into the boundary layer¹. Frequencies lower than $O(\epsilon^{-2})$ would be of higher-order terms. In fact the triple-deck scalings are exactly the same as those given by the classical stability theory of C.C. Lin [22]. Lin showed the asymptotic behavior of the lower branch of the neutral stability curve at high Reynolds number is given by:

$$\alpha^* L^* \propto Re^{\frac{3}{4}} \quad \text{or} \quad F \propto Re^{\frac{6}{4}}, \quad (1-4)$$

where α^* is the dimensional wavenumber and F is the nondimensional frequency defined as:

$$F = \frac{\omega v}{U_\infty^2} = S Re^{-1}. \quad (1-5)$$

This implies that the T-S waves would have the same wavelength as the dimensions of our triple-deck structure and the same frequency. In addition, it should be mentioned that the lower deck has the same thickness, $O(\epsilon^5 L^*)$, as the classical Stokes layer that forms upstream of the triple-deck structure due to the free-stream oscillation, and we are only

¹ Applicability of the triple-deck theory to the boundary-layer transition was first shown by F.T. Smith, "On the non-parallel flow stability of the Blasius boundary layer", Proc. of Roy. Soc. A366, p. 573 1979.

considering roughness elements whose height is of the scale of the lower-deck thickness.

Guided by the above discussion, we can formulate our problem as follows. We wish to consider small humps of size $O(\epsilon^3 L^*)$ in the streamwise and spanwise directions (order of T-S wavelength) and height $O(\epsilon^5 L^*)$. Thus, we define the rescaled independent variables (superscript "*" indicates dimensional variables) :

$$(x, y) = \epsilon^{-3} \frac{(x^* - L^*, y^*)}{L^*} \quad \text{and} \quad t = \omega t^* , \quad (1-6)$$

$$z_l = \epsilon^{-5} \frac{z^*}{L^*} \quad \text{in the lower deck} , \quad (1-7a)$$

$$z_m = \epsilon^{-4} \frac{z^*}{L^*} \quad \text{in the main deck} , \quad (1-7b)$$

$$z_u = \epsilon^{-3} \frac{z^*}{L^*} \quad \text{in the upper deck} . \quad (1-7c)$$

The total flow parameters can be written as a steady flow part plus a small unsteady perturbation of $O(\delta)$:

$$\vec{V}_F(\vec{x}, t) = \vec{V}(\vec{x}) + \delta \vec{v}(\vec{x}, t) , \quad (1-8)$$

$$P_F(\vec{x}, t) = P(\vec{x}) + \delta p(\vec{x}, t) . \quad (1-9)$$

Furthermore, the Navier-Stokes equations for an incompressible flow are written as:

$$\nabla \cdot \vec{V}_F = 0 , \quad (1-10)$$

$$S \partial_t \vec{V}_F + \vec{V}_F \cdot \nabla \vec{V}_F = -\nabla P_F + Re^{-1} \nabla^2 \vec{V}_F . \quad (1-11)$$

Thus substituting equations (1-8) and (1-9) into the Navier-Stokes equations we have:

$$\nabla \cdot \vec{V} + \delta \nabla \cdot \vec{v} = 0 , \quad (1-12)$$

and,

$$\begin{aligned} & \vec{V} \cdot \nabla \vec{V} + \nabla P - Re^{-1} \nabla^2 \vec{V} \\ & + \delta \{ S \partial_t \vec{v} + \vec{v} \cdot \nabla \vec{V} + \vec{V} \cdot \nabla \vec{v} + \nabla p - Re^{-1} \nabla^2 \vec{v} \} \\ & + \delta^2 \{ \vec{v} \cdot \nabla \vec{v} \} = 0 . \end{aligned} \quad (1-13)$$

The steady-state motion satisfies the Navier Stokes equations to the "zeroth" order :

$$\nabla \cdot \vec{V} = 0 , \quad (1-14a)$$

$$\vec{V} \cdot \nabla \vec{V} = -\nabla P + Re^{-1} \nabla^2 \vec{V} . \quad (1-14b)$$

Subtracting equations (1-14) from equations (1-12) and (1-13) and neglecting the second order terms in δ , we obtain the linearized Navier-Stokes equations governing the unsteady motion of the perturbed flow:

$$\nabla \cdot \vec{v} = 0 , \quad (1-15a)$$

$$S \partial_t \vec{v} + \vec{v} \cdot \nabla \vec{V} + \vec{V} \cdot \nabla \vec{v} = -\nabla p + Re^{-1} \nabla^2 \vec{v} . \quad (1-15b)$$

I.2 Steady-State Flow

As shown in previous steady triple-deck analyses² the fundamental problem reduces to a consideration of the lower and upper-deck equations. We shall solve the governing equations in both upper and lower decks simultaneously, subject to appropriate boundary and matching conditions. The flow in the lower deck is governed by the three-dimensional boundary-layer equations. The appropriately scaled variables in the lower deck for the steady flow are:

$$U(x, y, z_l) = \varepsilon U_1(x, y, z_l) + O(\varepsilon^2) , \quad (1-16a)$$

$$V(x, y, z_l) = \varepsilon V_1(x, y, z_l) + O(\varepsilon^2) , \quad (1-16b)$$

$$W(x, y, z_l) = \varepsilon^3 W_1(x, y, z_l) + O(\varepsilon^4) , \quad (1-16c)$$

$$P(x, y, z_l) = \varepsilon^2 P_1(x, y, z_l) + O(\varepsilon^3) , \quad (1-16d)$$

and the governing equations in the lower deck are:

² The final form of equations resulting from this analysis are presented here for the steady state problem. However, for the receptivity problem this procedure is outlined in its entirety. (See section 1.3)

$$\partial_x U_1 + \partial_y V_1 + \partial_{z_1} W_1 = 0 , \quad (1-17a)$$

$$U_1 \partial_x U_1 + V_1 \partial_y U_1 + W_1 \partial_{z_1} U_1 = -\partial_x P_1 + \partial_{z_1 z_1} U_1 , \quad (1-17b)$$

$$U_1 \partial_x V_1 + V_1 \partial_y V_1 + W_1 \partial_{z_1} V_1 = -\partial_y P_1 + \partial_{z_1 z_1} V_1 , \quad (1-17c)$$

$$P_1 = P_1(x, y) \text{ only} , \quad (1-17d)$$

subject to the boundary conditions:

$$U_1 = V_1 = W_1 = 0 \quad \text{on} \quad z_1 = hF(x, y) , \quad (1-18b)$$

$$U_1 \rightarrow \lambda z_1 , \quad V_1, W_1, P_1 \rightarrow 0 \quad \text{as} \quad x \rightarrow -\infty \text{ and/or } y \rightarrow \pm \infty , \quad (1-18b)$$

$$U_1 \rightarrow \lambda (z_1 + A(x, y)) \quad \text{as} \quad z_1 \rightarrow \infty , \quad (1-18c)$$

$$\partial_x V_1 \rightarrow -\frac{\partial_y P_1(x, y)}{\lambda z_1} \quad \text{as} \quad z_1 \rightarrow \infty , \quad (1-18d)$$

where $\lambda \equiv U'_B(0)$ is the slope of the incoming velocity profile at the wall, $F(x, y)$ is the scaled order one hump shape, and h is an order one scaling parameter (with respect to the lower deck). $A(x, y)$ is the negative of the boundary-layer displacement thickness, and it is defined by asymptotic matching of all three decks.

The main deck (or middle layer) is simply a streamwise continuation of the upstream boundary layer. To first order, viscous forces are insignificant, and the governing equations can be solved analytically. This solution can be expressed physically as a simple transverse shift of the undisturbed boundary-layer flow. From the steady-state solution in the main deck we have :

$$U(\vec{x}_m) = U_B(z_m) + \varepsilon A(x, y) U_B' + O(\varepsilon^2) , \quad (1-19a)$$

$$V(\vec{x}_m) = \varepsilon^2 \frac{D(x, y)}{U_B} + O(\varepsilon^3) , \quad (1-19b)$$

$$W(\vec{x}_m) = -\varepsilon^2 \partial_x A(x, y) U_B + O(\varepsilon^3) , \quad (1-19c)$$

$$P(\vec{x}_m) = \varepsilon^2 P_1(x, y) + O(\varepsilon^3) , \quad (1-19d)$$

where $U_B(z_m)$ is the velocity profile of the incoming Blasius boundary layer and $D(x, y)$ is given by:

$$D(x, y) = - \int_{-\infty}^x \partial_y P_1(\xi, y) d\xi . \quad (1-19d)$$

Equations (1-17) are coupled to the governing equations in the upper deck . The flow variables are appropriately scaled in the upper deck as:

$$U(x, y, z_u) = 1 + \varepsilon^2 \hat{U}_1(x, y, z_u) + O(\varepsilon^3) , \quad (1-20a)$$

$$V(x, y, z_u) = \varepsilon^2 \hat{V}_1(x, y, z_u) + O(\varepsilon^3) , \quad (1-20b)$$

$$W(x, y, z_u) = \varepsilon^2 \hat{W}_1(x, y, z_u) + O(\varepsilon^3) , \quad (1-20c)$$

$$P(x, y, z_u) = \varepsilon^2 \hat{P}_1(x, y, z_u) + O(\varepsilon^3) . \quad (1-20d)$$

It can be shown that the upper-deck problem reduces to a consideration of Laplace's equation for the steady pressure:

$$\nabla^2 \hat{P}_1(x, y, z_u) = 0 , \quad (1-21)$$

subject to the following boundary conditions:

$$\hat{P}_1 \rightarrow 0 \quad \text{as} \quad x \rightarrow -\infty , \quad (1-22a)$$

$$\hat{P}_1 \rightarrow 0 \quad \text{as} \quad y \rightarrow \pm\infty , \quad (1-22b)$$

$$\hat{P}_1 \rightarrow 0 \quad \text{as} \quad z_u \rightarrow \infty , \quad (1-22c)$$

$$\partial_x \hat{P}_1 \rightarrow 0 \quad \text{as} \quad x \rightarrow \infty . \quad (1-22d)$$

Also, matching between the upper and main decks requires that:

$$\hat{P}_1(x, y, z_u \rightarrow 0) = P_1(x, y) , \quad (1-23a)$$

and
$$\partial_{z_u} \hat{P}_1(x, y, z_u \rightarrow 0) = \partial_{zz} A(x, y) . \quad (1-23b)$$

The above coupled equations with the given boundary and matching conditions present a well-posed problem. The nonlinear three-dimensional viscous-inviscid interaction problem given above can only be solved numerically for finite values of h . Therefore, we look for a numerical solution of the above equations. To avoid numerical instabilities, Smith [23] proposed a unique finite-difference technique to solve the above equations, which was later extended by Bodonyi and Duck [24]. Using the same approach as taken by them, a finite-difference program based on the modified Keller box method [25] has been developed to solve for the steady flow. Details of the above numerical method and its differences with their scheme will be discussed in Chapter 2. In addition a few improvements over the scheme of reference [24] and the effect of these improvements on the numerical results will be discussed in Chapter 3.

I.3 Receptivity Problem

The receptivity problem of the interaction between free-stream time harmonic disturbances and a three-dimensional hump has the triple-deck structure as long as the hump height is of the order of the lower deck $O(\epsilon^5)$. Furthermore, we are only interested in relatively high frequency free-stream disturbances, therefore, we choose $S = O(\epsilon^{-2})$. This is of the same order as the Tollmien-Schlichting wave frequency at and upstream of the lower branch of the neutral stability curve. Thus we define a scaled Strouhal number S_0 such that:

$$S_0 = \epsilon^2 S . \quad (1-24)$$

As noted above, we are looking for solutions that are harmonic in time, since the problem is linear and our forcing free-stream disturbances are given as such. Therefore, we may write for our perturbation properties:

$$\vec{v}(\vec{x}, t) = \text{Real} \{ e^{-it} \vec{v}_c(\vec{x}) \} , \quad (1-25a)$$

$$p(\vec{x}, t) = \text{Real} \{ e^{-it} p_c(\vec{x}) \} . \quad (1-25b)$$

For convenience, the subscript "c" is dropped and all the perturbation-flow properties are assumed to be complex. As stated in section 1.1 , we are going to apply the triple-deck analysis to this problem in order to obtain the governing equations pertinent to this problem.

I.3.1 The Main Deck

In the main deck, the continuation of the incoming boundary layer where $z \propto \varepsilon^4$, the expansions for flow properties may be written as³:

$$u(x, y, z_m) = u_0(x, y, z_m) + \varepsilon u_1(x, y, z_m) + \varepsilon^2 u_2(x, y, z_m) + \dots, \quad (1-26a)$$

$$v(x, y, z_m) = v_0(x, y, z_m) + \varepsilon v_1(x, y, z_m) + \varepsilon^2 v_2(x, y, z_m) + \dots, \quad (1-26b)$$

$$w(x, y, z_m) = \varepsilon w_0(x, y, z_m) + \varepsilon^2 w_1(x, y, z_m) + \varepsilon^3 w_2(x, y, z_m) + \dots, \quad (1-26c)$$

$$p(x, y, z_m) = \varepsilon p_0(x, y, z_m) + \varepsilon^2 p_1(x, y, z_m) + \varepsilon^3 p_2(x, y, z_m) + \dots. \quad (1-26d)$$

The continuity equation (1-15a), after canceling " e^{-u} " and using the stretched coordinates, becomes:

$$\partial_x u + \partial_y v + \varepsilon^{-1} \partial_{z_m} w = 0. \quad (1-27)$$

Substituting the velocity expansions into the above equation gives the continuity equation for all orders of ε :

$$O(\varepsilon^i): \quad \partial_x u_i + \partial_y v_i + \partial_{z_m} w_i = 0 \quad \text{where } i=0,1,2,\dots. \quad (1-28)$$

³ The justification of this expansion may seem awkward at first, but it is soon realized that this is the only logical form it can take (see Stewartson [15]). The w expansion starts with order ε to satisfy the continuity equation. Also it is shown by Stewartson that the only consistent expansion for the pressure, p , should start with order ε .

Furthermore, from the x-component of the momentum equation (1-15b), in the main deck we have:

$$\begin{aligned}
 e^{-i\omega t} & \left(-i\varepsilon^{-2} S_0 \mu + \varepsilon^{-3} (u \partial_x + v \partial_y + \varepsilon^{-1} w \partial_{z_m}) U \right. \\
 & \left. + \varepsilon^{-3} (U \partial_x + V \partial_y + \varepsilon^{-1} W \partial_{z_m}) u \right) \quad (1-29) \\
 & = -\varepsilon^{-3} \partial_x p + \left(\varepsilon^2 \partial_{xx} + \varepsilon^2 \partial_{yy} + \partial_{z_m z_m} \right) u \quad .
 \end{aligned}$$

By canceling " $e^{-i\omega t}$ " factor and substituting the expansions for velocity and pressure, we have:

$$\begin{aligned}
 & -i\varepsilon^{-2} S_0 (u_0 + \varepsilon u_1 + \varepsilon^2 u_2 + \dots) \\
 & + \varepsilon^{-3} \partial_x U (u_0 + \varepsilon u_1 + \varepsilon^2 u_2 + \dots) \\
 & + \varepsilon^{-3} \partial_y U (v_0 + \varepsilon v_1 + \varepsilon^2 v_2 + \dots) \\
 & + \varepsilon^{-4} \partial_{z_m} U (\varepsilon w_0 + \varepsilon^2 w_1 + \varepsilon^3 w_2 + \dots) \\
 & + \varepsilon^{-3} U \partial_x (u_0 + \varepsilon u_1 + \varepsilon^2 u_2 + \dots) \\
 & + \varepsilon^{-3} V \partial_y (u_0 + \varepsilon u_1 + \varepsilon^2 u_2 + \dots) \\
 & + \varepsilon^{-4} W \partial_{z_m} (u_0 + \varepsilon u_1 + \varepsilon^2 u_2 + \dots)
 \end{aligned}$$

$$\begin{aligned}
&= \tag{1-30} \\
&- \varepsilon^{-3} \partial_x (\varepsilon p_0 + \varepsilon^2 p_1 + \varepsilon^3 p_2 + \dots) \\
&+ \varepsilon^2 \partial_{xx} (u_0 + \varepsilon u_1 + \varepsilon^2 u_2 + \dots) \\
&+ \varepsilon^2 \partial_{yy} (u_0 + \varepsilon u_1 + \varepsilon^2 u_2 + \dots) \\
&+ \partial_{z_m z_m} (u_0 + \varepsilon u_1 + \varepsilon^2 u_2 + \dots) .
\end{aligned}$$

Using the steady-state solution and substituting equations (1-19) into equation (1-30), we obtain from the largest terms :

$$O(\varepsilon^{-3}): \quad U_B'(z_m) w_0 + U_B(z_m) \partial_x u_0 = 0 , \tag{1-31}$$

where $U_B(z_m)$ is the velocity profile of the incoming Blasius boundary layer and for the next largest terms we have:

$$\begin{aligned}
O(\varepsilon^{-2}): \quad &-iS_0 u_0 + U_B' \partial_x A u_0 + U_B' w_1 + A U_B'' w_0 \tag{1-32} \\
&+ U_B \partial_x u_1 + U_B' A \partial_x u_0 - U_B \partial_x A \partial_{z_m} u_0 = -\partial_x p_0 .
\end{aligned}$$

Similarly the y-momentum equation in the main-deck can be written as:

$$\begin{aligned}
e^{-i} (&-i\varepsilon^{-2} S_0 v + \varepsilon^{-3} (u \partial_x + v \partial_y + \varepsilon^{-1} w \partial_{z_m}) v \\
&+ \varepsilon^{-3} (U \partial_x + V \partial_y + \varepsilon^{-1} W \partial_{z_m}) v \tag{1-33} \\
&= -\varepsilon^{-3} \partial_y p + (\varepsilon^2 \partial_{xx} + \varepsilon^2 \partial_{yy} + \partial_{z_m z_m}) v) .
\end{aligned}$$

Again by cancelling " e^{-iu} " factor and substituting all the expansions into the above equation, from the largest terms we obtain:

$$\begin{aligned} O(\varepsilon^{-3}): \quad U_B(z_m) \partial_x v_0 &= 0 \quad \text{or} \quad \partial_x v_0 = 0 \\ &\Rightarrow v_0 = v_0(y, z_m) \quad \text{only,} \end{aligned} \quad (1-34)$$

and for the next largest terms we have:

$$O(\varepsilon^{-2}): \quad -iS_0 v_0 + U_B \partial_x v_1 - U_B \partial_x A \partial_{z_m} v_0 = -\partial_y p_0 . \quad (1-35)$$

However, upstream as $x \rightarrow -\infty$, we must approach the solution to the unsteady boundary-layer equations (see Appendix A); there we must require that

$$v \rightarrow 0 \quad \Rightarrow \quad v_0(y, z_m) \equiv 0 . \quad (1-36)$$

Similarly the z-momentum equation in the main deck can be written as:

$$\begin{aligned} e^{-iu} \left(-i\varepsilon^{-2} S_0 w + \varepsilon^{-3} \left(u \partial_x + v \partial_y + \varepsilon^{-1} w \partial_{z_m} \right) W \right. \\ \left. + \varepsilon^{-3} \left(U \partial_x + V \partial_y + \varepsilon^{-1} W \partial_{z_m} \right) w \right. \\ \left. = -\varepsilon^{-4} \partial_{z_m} p + \left(\varepsilon^2 \partial_{xx} + \varepsilon^2 \partial_{yy} + \partial_{z_m z_m} \right) w \right) . \end{aligned} \quad (1-37)$$

After canceling the " e^{-iu} " factor and substituting all the expansions into equation (1-37),

we have:

$$O(\varepsilon^{-3}): \quad \partial_{z_m} p_0 = 0 \quad \Rightarrow \quad p_0 = p_0(x, y) , \quad (1-38)$$

and for the next largest terms we have:

$$O(\epsilon^{-2}): \quad U_B \partial_x w_0 = -\partial_{z_m} p_1 . \quad (1-39)$$

Equations (1-28) and (1-31) imply:

$$w_0(x, y, z_m) = c(x, y) U_B(z_m) , \quad (1-40)$$

where $c(x, y)$ is some arbitrary function to be determined, and since as $x \rightarrow -\infty$ from equations (A-57) we know,

$$w_0 \rightarrow 0 \text{ and } u_0 \rightarrow 1 .$$

Integrating equation (1-31) gives:

$$u_0(x, y, z_m) - u_0(-\infty, y, z_m) = -U_B'(z_m) \int_{-\infty}^x c(\xi, y) d\xi . \quad (1-41)$$

After redefining $c(x, y)$ in terms of a new arbitrary function $a(x, y)$ we obtain:

$$u_0(x, y, z_m) = 1 + a(x, y) U_B'(z_m) , \quad (1-42a)$$

$$w_0(x, y, z_m) = -\partial_x a(x, y) U_B(z_m) . \quad (1-42b)$$

Also, by integrating equation (1-35) we obtain:

$$v_1(x, y, z_m) = \frac{d(x, y)}{U_B(z_m)} , \quad (1-43)$$

where $d(x, y)$ is yet another undetermined arbitrary function.

Summarizing our results in the main deck we have:

$$u(x, y, z_m) = 1 + a(x, y) U_B'(z_m) + O(\epsilon) , \quad (1-44a)$$

$$v(x, y, z_m) = \epsilon \frac{d(x, y)}{U_B(z_m)} + O(\epsilon^2) , \quad (1-44b)$$

$$w(x, y, z_m) = -\epsilon \partial_x a(x, y) U_B(z_m) + O(\epsilon^2) , \quad (1-44c)$$

$$p(x, y, z_m) = \epsilon p_0(x, y) + O(\epsilon^2) . \quad (1-44d)$$

I.3.2 The Upper Deck

Taking the limit of equations (1-44) as $z_m \rightarrow \infty$ in the main deck , we obtain:

$$u \rightarrow 1 + O(\epsilon) , \quad (1-45a)$$

$$v \rightarrow \epsilon d(x, y) + O(\epsilon^2) , \quad (1-45b)$$

$$w \rightarrow -\epsilon \partial_x a(x, y) + O(\epsilon^2) , \quad (1-45c)$$

$$p \rightarrow \epsilon p_0(x, y) + O(\epsilon^2) . \quad (1-45d)$$

Therefore, in the upper deck, where $z \propto \epsilon^3$, the expansions for flow properties may be written as:

$$u(x, y, z_u) = 1 + \varepsilon \hat{u}_1(x, y, z_u) + \varepsilon^2 \hat{u}_2(x, y, z_u) + \dots, \quad (1-46a)$$

$$v(x, y, z_u) = \varepsilon \hat{v}_1(x, y, z_u) + \varepsilon^2 \hat{v}_2(x, y, z_u) + \dots, \quad (1-46b)$$

$$w(x, y, z_u) = \varepsilon \hat{w}_1(x, y, z_u) + \varepsilon^2 \hat{w}_2(x, y, z_u) + \dots, \quad (1-46c)$$

$$p(x, y, z_u) = \varepsilon \hat{p}_1(x, y, z_u) + \varepsilon^2 \hat{p}_2(x, y, z_u) + \dots. \quad (1-46d)$$

Substituting the above expansions into the governing equations (1-15), and using the steady-state solution given by equations (1-20), the highest order terms of $O(\varepsilon^{-2})$ give :

$$\text{Cont. :} \quad \partial_x \hat{u}_1 + \partial_y \hat{v}_1 + \partial_z \hat{w}_1 = 0, \quad (1-47a)$$

$$\text{x-mom. :} \quad -i S_0 + \partial_x \hat{u}_1 = -\partial_x \hat{p}_1, \quad (1-47b)$$

$$\text{y-mom. :} \quad \partial_x \hat{v}_1 = -\partial_y \hat{p}_1, \quad (1-47c)$$

$$\text{z-mom. :} \quad \partial_x \hat{w}_1 = -\partial_z \hat{p}_1. \quad (1-47d)$$

It can be shown by differentiating equations (1-47) with respect to x, y and z, respectively, and after using equation (1-47a), that the unsteady pressure in the upper deck satisfies Laplace's equation:

$$\nabla^2 \hat{p}_1(x, y, z_u) = 0. \quad (1-48)$$

Additionally, the boundary condition as $x \rightarrow -\infty$ and/or $z_u \rightarrow \infty$ is given by:

$$\hat{p}_1 \rightarrow i S_0 x. \quad (1-49)$$

Furthermore, the matching between upper and main deck requires:

$$\hat{p}_1(x, y, z_u \rightarrow 0) = p_0(x, y) , \quad (1-50)$$

and,

$$\hat{v}_1(x, y, z_u \rightarrow 0) = d(x, y) , \quad (1-51)$$

$$\hat{w}_1(x, y, z_u \rightarrow 0) = -\partial_x a(x, y) . \quad (1-52)$$

Using equation (1-47d) and the above matching condition, we can write:

$$\partial_{z_u} \hat{p}_1(x, y, z_u \rightarrow 0) = \partial_{xx} a(x, y) . \quad (1-53)$$

The governing equation for the pressure in the upper deck is elliptic and in order to have a well-posed problem, we also need boundary conditions for the unsteady pressure for $x \rightarrow \infty$ and $y \rightarrow \pm\infty$. However, this is not a trivial task. Since the governing equations in the lower deck are parabolic, boundary conditions are not needed for them as $x \rightarrow \infty$. Bodonyi et al. [16] imposed a radiation condition on the outgoing pressure disturbances in the upper deck for their two-dimensional problem. Following their approach we can impose a similar condition:

$$\partial_x \hat{p}_1 - i K_x \hat{p}_1(x, y, z_u) \rightarrow 0, \quad \text{as } x \rightarrow \infty , \quad (1-54)$$

$$\partial_y \hat{p}_1 - i K_y \hat{p}_1(x, y, z_u) \rightarrow 0, \quad \text{as } y \rightarrow \pm\infty . \quad (1-55)$$

They used two different methods to evaluate the wavenumbers , K_x and K_y , which depend on S_0 . First they used the solution of the classical Orr-Sommerfeld eigenvalue problem for the Stokes' layer flow . Alternatively, it was computed iteratively from the numerical computations. Its value was estimated from the relation ;

$$\frac{(\partial_x p_1)}{i p_1}$$

at some location $x_{downstream}$, reasonably far downstream, and then it was fed back into the numerical computations. Numerically, the results indicated slight differences between the two methods. This is not too surprising since the viscous-inviscid interaction is a local phenomenon and far downstream the behavior should approach that of the classical stability theory. Here we calculate both K_x and K_y iteratively during the numerical calculations.

I.3.3 The Lower Deck

The flow structure is completed by determining the flow structure in the lower deck. Taking the limit as $z_m \rightarrow 0$ on the main-deck flow properties, equations (1-44), we obtain:

$$u \rightarrow O(1) , \quad (1-56a)$$

$$v \rightarrow O(1) , \quad (1-56b)$$

$$w \rightarrow O(\epsilon^2) , \quad (1-56c)$$

$$p \rightarrow O(\epsilon) . \quad (1-56d)$$

Therefore, in the lower deck, where $Z \propto \epsilon^5$, the expansions for flow properties may be written as:

$$u(x, y, z_l) = \bar{u}_0(x, y, z_l) + O(\epsilon) , \quad (1-57a)$$

$$v(x, y, z_l) = \bar{v}_0(x, y, z_l) + O(\epsilon) , \quad (1-57b)$$

$$w(x, y, z_l) = \epsilon^2 \bar{w}_0(x, y, z_l) + O(\epsilon^3) , \quad (1-57c)$$

$$p(x, y, z_l) = \epsilon \bar{p}_0(x, y, z_l) + O(\epsilon^2) . \quad (1-57d)$$

Also, the steady-state solutions in the lower deck are given by equations (1-16). Substituting the above expansions into the governing equations, the highest order terms of $O(\epsilon^{-2})$ give :

$$\partial_x \bar{u}_0 + \partial_y \bar{v}_0 + \partial_{z_l} \bar{w}_0 = 0 , \quad (1-58a)$$

$$\begin{aligned} & -i S_0 \bar{u}_0 + \partial_x U_1 \bar{u}_0 + \partial_y U_1 \bar{v}_0 + \partial_{z_l} U_1 \bar{w}_0 \\ & + U_1 \partial_x \bar{u}_0 + V_1 \partial_y \bar{u}_0 + W_1 \partial_{z_l} \bar{u}_0 \\ & = -\partial_x \bar{p}_0 + \partial_{x, z_l} \bar{u}_0 , \end{aligned} \quad (1-58b)$$

$$\begin{aligned}
& -i S_0 \bar{v}_0 + \partial_x V_1 \bar{u}_0 + \partial_y V_1 \bar{v}_0 + \partial_{z_1} V_1 \bar{w}_0 \\
& + U_1 \partial_x \bar{v}_0 + V_1 \partial_y \bar{v}_0 + W_1 \partial_{z_1} \bar{v}_0 \\
& = -\partial_y \bar{p}_0 + \partial_{z_1} \bar{v}_0 ,
\end{aligned} \tag{1-58c}$$

$$\bar{p}_0 = \bar{p}_0(x, y) . \tag{1-58d}$$

The above equations are subject to the following boundary conditions:

$$\bar{u}_0 = \bar{v}_0 = \bar{w}_0 = 0 \text{ on } z_1 = h F(x, y) . \tag{1-59}$$

Furthermore, as $x \rightarrow -\infty$ we have (see appendix A) :

$$\bar{u}_0 \rightarrow 1 - e^{i^{3/2} S_0^{1/2} z_1} , \tag{1-60a}$$

$$\bar{v}_0, \bar{w}_0 \rightarrow 0 , \tag{1-60b}$$

$$\bar{p}_0 \rightarrow i S_0 x , \tag{1-60c}$$

in order to match with the upstream flow properties.

In addition, by matching to the main-deck flow properties as $z_1 \rightarrow \infty$, for the velocities

in the lower deck, we have:

$$\bar{u}_0 \rightarrow 1 + \lambda a(x, y) , \quad (1-61a)$$

$$\bar{v}_0 \rightarrow \frac{d(x, y)}{\lambda z_l} , \quad (1-61b)$$

$$\bar{w}_0 \rightarrow -\lambda z_l \partial_x a(x, y) . \quad (1-61c)$$

In equations (1-61) we have used the fact that:

$$\text{as } z_m \rightarrow 0 \quad U_B \rightarrow \lambda z_m \quad \text{where } \lambda \equiv U_B'(0) . \quad (1-62)$$

Also, from matching the x-derivative of the v-velocity between the lower and the main decks and using the y-momentum equation in the main deck, equation (1-35), we can write,

$$\text{as } z_l \rightarrow \infty \quad \partial_x \bar{v}_0 \rightarrow -\frac{\partial_y \bar{p}_0(x, y)}{\lambda z_l} . \quad (1-63)$$

It should be noted that $a(x, y)$ is the negative of the unsteady displacement thickness and it is related to the upper-deck pressure through equation (1-53). Therefore, by matching pressure in the boundary layer to the upper-deck pressure, we have:

$$\hat{p}_1(x, y, z_u \rightarrow 0) = p_0(x, y) . \quad (1-64)$$

I.3.4 Grid Transformation

Before we apply the Prandtl transposition theorem⁴ we define a set of new rescaled variables to scale out the constant λ . The effect of this transformation is the same as setting $\lambda = 1$ in all the governing equations (see Appendix B). Now we are going to apply Prandtl's theorem to transform our computational domain in the lower deck into a cubical box⁵, that is to turn the bottom wall with the roughness into a flat plate in the transformed coordinates.

Let,

$$x \rightarrow \xi \quad \partial_x () = \partial_\xi () - h \partial_\xi F \partial_z () , \quad (1-65a)$$

$$y \rightarrow \eta \quad \partial_y () = \partial_\eta () - h \partial_\eta F \partial_z () , \quad (1-65b)$$

$$z - hF(x, y) \rightarrow z \quad \partial_z () = \partial_z . \quad (1-65c)$$

Using the above transformation and defining,

$$w^T \equiv w - h \partial_\xi F u - h \partial_\eta F v , \quad (1-66a)$$

$$W^T \equiv W - h \partial_\xi F U - h \partial_\eta F V . \quad (1-66b)$$

⁴ See Rosenhead, L. "Laminar Boundary Layers", chap. 5 part 2 section 8

⁵ The upper deck domain is already a cube

The governing equations in the lower deck become:

$$\partial_{\xi} u + \partial_{\eta} v + \partial_z w^T = 0 , \quad (1-67a)$$

$$\begin{aligned} -i S_0 u + \partial_{\xi} U u + \partial_{\eta} U v + \partial_z U w^T \\ + U \partial_{\xi} u + V \partial_{\eta} u + W^T \partial_z u \\ = -\partial_{\xi} p + \partial_{zz} u , \end{aligned} \quad (1-67b)$$

$$\begin{aligned} -i S_0 v + \partial_{\xi} V u + \partial_{\eta} V v + \partial_z V w^T \\ + U \partial_{\xi} v + V \partial_{\eta} v + W^T \partial_z v \\ = -\partial_{\eta} p + \partial_{zz} v , \end{aligned} \quad (1-67c)$$

$$p = p(\xi, \eta) , \quad (1-67d)$$

subject to the following boundary conditions :

$$u = v = w^T = 0 \quad \text{on} \quad z=0 . \quad (1-68)$$

Also, as $\xi \rightarrow -\infty$,

$$u \rightarrow 1 - \exp(i^{3/2} S_0^{1/2} z) , \quad (1-69a)$$

$$v, w^T \rightarrow 0 , \quad (1-69b)$$

$$p \rightarrow i S_0 \xi , \quad (1-69c)$$

and as $z \rightarrow \infty$, we have (after dropping terms of $O\left(\frac{1}{z^2}\right)$):

$$u \rightarrow 1 + a(\xi, \eta), \quad (1-70a)$$

$$\partial_\xi v \rightarrow -\frac{\partial_\eta p(\xi, \eta)}{(z + hF)}. \quad (1-70b)$$

Finally, consider the following transformation. Subtract out the upstream Stokes-flow solutions so that the upstream boundary conditions become homogeneous. Therefore, we define the transformation:

$$u^T = u - (1 - \exp(i^{3/2} S_0^{1/2} z)), \quad (1-71a)$$

$$p^T = p - i S_0 \xi. \quad (1-71b)$$

Again, after substituting all the transformations into the equations (1-67), in the lower deck we have (here for simplicity, we drop the superscript "T"):

$$\partial_\xi u + \partial_\eta v + \partial_z w = 0, \quad (1-72a)$$

$$\begin{aligned} & (\partial_\xi U - i S_0) u + \partial_\eta U v + \partial_z U w \\ & + U \partial_\xi u + V \partial_\eta u + W \partial_z u \\ & + \partial_\xi p - \partial_{zz} u \end{aligned} \quad (1-72b)$$

$$= -\partial_\xi U + \left(\partial_\xi U + i^{3/2} S_0^{1/2} W \right) \exp\left(i^{3/2} S_0^{1/2} z \right),$$

$$\begin{aligned}
& (\partial_\eta V - i S_0) v + \partial_\xi V u + \partial_x V w \\
& + U \partial_\xi v + V \partial_\eta v + W \partial_x v \\
& + \partial_\eta p - \partial_{xx} v
\end{aligned} \tag{1-72c}$$

$$= -\partial_\eta V \left(1 - \exp\left(i^{\frac{3}{2}} S_0^{\frac{1}{2}} z \right) \right),$$

$$p = p(\xi, \eta). \tag{1-72d}$$

The boundary conditions after the transformation are:

$$u = v = w = 0 \quad \text{on } z = 0, \text{ for all } \xi \text{ \& } \eta, \tag{1-73}$$

$$u, v, w \rightarrow 0 \quad \text{and/or} \quad \begin{array}{l} \text{as } \xi \rightarrow -\infty, \text{ for all } \eta \text{ \& } z \\ \text{as } |\eta| \rightarrow \infty, \text{ for all } \xi \text{ \& } z \end{array} \tag{1-74}$$

also, as $z \rightarrow \infty$ (for all ξ \& η), the matching conditions to the main deck become,

$$u \rightarrow a(\xi, \eta) + \exp\left(i^{\frac{3}{2}} S_0^{\frac{1}{2}} z \right), \tag{1-75a}$$

$$\partial_\xi v \rightarrow \frac{\partial_\eta p(\xi, \eta)}{(z + hF)}. \tag{1-75b}$$

In the upper deck, for the sake of having a uniform notation, we rewrite

$(x, y, z_u) \rightarrow (\xi, \eta, z_u)$ and also define:

$$\hat{p} = \hat{p} - i S_0 \xi. \tag{1-76}$$

The governing equation with appropriate boundary conditions on the pressure change to,

$$\partial_{\xi\xi} \hat{P} + \partial_{\eta\eta} \hat{P} + \partial_{z_\mu z_\mu} \hat{P} = 0 , \quad (1-77)$$

$$\hat{p}(\xi, \eta, z_\mu) \rightarrow 0 \text{ as } \begin{array}{l} \xi \rightarrow -\infty \text{ for all } \eta \text{ \& } z_\mu \\ z_\mu \rightarrow \infty \text{ for all } \xi \text{ \& } \eta \end{array} , (1-78a)$$

$$\partial_\xi \hat{p} - i K_\xi \hat{p} \rightarrow 0 , \text{ as } \xi \rightarrow \infty \text{ for all } \eta \text{ \& } z_\mu , \quad (2-78b)$$

$$\partial_\eta \hat{p} - i K_\eta \hat{p} \rightarrow 0 , \text{ as } \eta \rightarrow \pm\infty \text{ for all } \xi \text{ \& } z_\mu . \quad (2-78c)$$

Also, the matching conditions with the lower deck are :

$$\hat{p}(\xi, \eta, z_\mu \rightarrow 0) = p(\xi, \eta) , \quad (1-79a)$$

$$\partial_{z_\mu} \hat{p}(\xi, \eta, z_\mu \rightarrow 0) = \partial_{\xi\xi} a(\xi, \eta) . \quad (1-79b)$$

The relationships between all the above transformed variables and flow properties with their physical counterparts are summarized in Appendix C.

CHAPTER II

NUMERICAL METHOD

II.1 Steady Flow

Following the approach of Smith [23], to avoid exponential growth of "departure eigensolutions", we define the skewed shear parameters:

$$\bar{U} = \partial_{\xi} U + \partial_{\eta} V \quad , \quad \bar{W} = \partial_{\xi} W \quad \text{and} \quad \bar{E} = [\partial_{\xi\xi} + \partial_{\eta\eta}] P(\xi, \eta) \quad . \quad (2-1)$$

Using the above definitions and differentiating the governing equations in the lower deck given by (1-17) (note: λ is scaled out of the problem. See Appendix B), we can write :

$$\partial_{\xi} \bar{U} + \partial_x \bar{W} = 0 \quad , \quad (2-2)$$

$$U \partial_{\xi} \bar{U} + \partial_x U \bar{W} + \bar{E} - \partial_{xx} \bar{U} = -RH \quad , \quad (2-3)$$

where RH is given by

$$\begin{aligned}
RH &= (\partial_\xi U)^2 + (\partial_\eta V)^2 + 2 \partial_\eta U \partial_\xi V + \partial_\eta W \partial_z V \\
&+ V (\partial_{\xi\eta} U + \partial_{\eta\eta} V) - W \partial_x W .
\end{aligned} \tag{2-4}$$

Using the fact that as $\xi \rightarrow -\infty$, $\partial_\xi A \rightarrow 0$, for later convenience, we can define a new function,

$$\int_{-\infty}^{\xi} B(x, \eta) dx = \partial_\xi A . \tag{2-5}$$

Therefore, boundary conditions (1-18) transform to:

$$\bar{U} = \bar{W} = 0 \quad \text{on} \quad z=0 , \tag{2-6}$$

$$\bar{U}, \bar{W}, \bar{E} \rightarrow 0 \quad \text{as} \quad \xi \rightarrow -\infty . \tag{2-7}$$

Also, as $z \rightarrow \infty$, it can be shown that

$$\bar{U} \rightarrow \int_{-\infty}^{\xi} B(x, \eta) dx + h \partial_\xi F(\xi, \eta) , \tag{2-8}$$

$$\bar{W} \rightarrow -z [B(\xi, \eta) + h \partial_{\xi\xi} F(\xi, \eta)] . \tag{2-9}$$

As an alternative boundary condition we could approximate the momentum equation

(2-3) as $z \rightarrow \infty$,

$$\bar{W} + \bar{E} \rightarrow -U [B + h \partial_{\xi\xi} F] - (\partial_\xi U)^2 . \tag{2-10}$$

Similarly for the upper-deck pressure, we define

$$\hat{E}(\xi, \eta, z_u) = \partial_{\xi\xi} \hat{P}(\xi, \eta, z_u) + \partial_{\eta\eta} \hat{P}(\xi, \eta, z_u) . \tag{2-11}$$

Hence the governing equation in the upper deck, equation (1-21), can be written as,

$$\partial_{\xi\xi} \hat{E} + \partial_{\eta\eta} \hat{E} + \partial_{z_u z_u} \hat{E} = 0 , \quad (2-12)$$

and the boundary conditions (1-22) and the matching conditions (1-23) become:

$$\hat{E} \rightarrow 0 \quad \text{as} \quad \begin{array}{l} \xi \rightarrow -\infty \\ \eta \rightarrow \pm\infty , \\ z_u \rightarrow \infty \end{array} , \quad (2-13a)$$

$$\partial_{\xi} \hat{E} \rightarrow 0 \quad \text{as} \quad \xi \rightarrow \infty , \quad (2-13b)$$

$$\hat{E} (\xi, \eta, z_u \rightarrow 0) = \bar{E} (\xi, \eta) , \quad (2-14a)$$

$$\partial_{z_u} \hat{E} (\xi, \eta, z_u \rightarrow 0) = \partial_{\xi\xi} B (\xi, \eta) + \partial_{\eta\eta} B (\xi, \eta) . \quad (2-14b)$$

Following Bodonyi and Duck [24] an iterative multi-sweep technique, using forward marching in a quasi 2-D manner is used to solve the above equations. Assuming an initial guess for the flow field, U, V, W and therefore RH , the governing equations in lower- and upper-decks are solved simultaneously for $\bar{U}, \bar{W}, \bar{E}, B$ and \hat{E} . Having found \bar{E} , the Poisson's equation (2-11) in the upper deck is solved to evaluate the pressure. Next the η -momentum equation, equation (1-17c), is marched forward in ξ to update the values of V . Finally, the remaining velocity components are determined by integrating the skewed shears to get back the primitive variables. All the above steps constitute one global iteration. The solution obtained after one iteration, is used as an initial guess for the next iterative step. Global iteration is continued until convergence is attained on the streamwise velocity U .

It should also be noted that for regions of reversed flow the parabolic direction of the flow changes locally so that the forward-marching scheme used here becomes unstable. To overcome this difficulty the approximation suggested by Reyhner and Flugge-Lotz [27] is implemented in the back flow regions. As shown by Williams [33], this approximation is only valid and have little effect on the solution, if the reversed flow velocities are small in magnitude.

Two separate finite-difference schemes are developed to solve the above numerical problem. The reason for this is explained in Chapter 3 when discussing the steady flow results. The two different schemes mentioned above are described next.

II.1.1 The Lower Deck

II.1.1a Modified Keller Box Method

The ξ , η , and z axes are discretized using the indices $i = 0, 1, 2, \dots, nx - 1, nx$, $j = 0, 1, 2, \dots, ny - 1, ny$, and $k = 1, 2, 3, \dots, n - 1, n$ respectively. The grid spacings are given by $\Delta\xi$, $\Delta\eta$, and Δz_k , which would allow variable grid spacing in the normal direction to the wall. The governing equations in the lower deck are approximated employing the modified Keller box method [25]. The differencing is implicit and second order in accuracy. At any η location, flow variables and their first derivatives are written using central differences making use of the four points at the corners of a "box" about

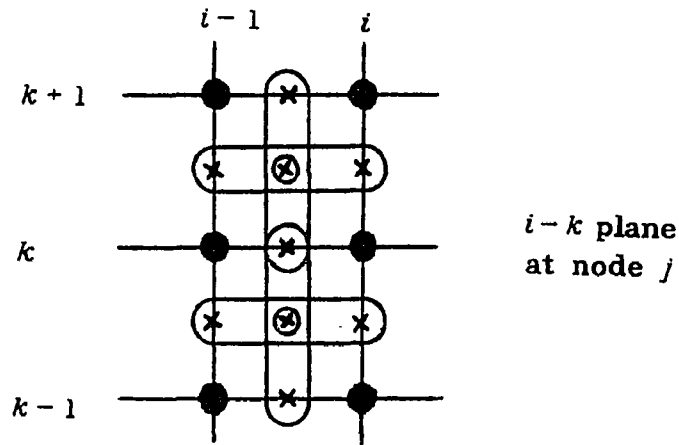


Figure 2. Computational cell in the modified Keller-Box method.

the node at $(i - \frac{1}{2}, j$ and $k - \frac{1}{2})$ (see Figure 2). The continuity equation becomes:

$$\left[\frac{U_i^j - U_{i-1}^j}{\Delta \xi} \right]^{k-\frac{1}{2}} + \left[\frac{W_i^k - W_{i-\frac{1}{2}}^k}{\Delta z_k} \right] = 0 \quad (2-15)$$

It may be written in the following form:

$$B1^k \frac{U_i^{k-1}}{W_i} + B2^k \frac{U_i^{k-1}}{U_i} + B3^k \frac{U_i^k}{W_i} + B4^k \frac{U_i^k}{U_i} = RC^k \quad (2-16)$$

where

$$\begin{aligned}
B2^k &= B4^k = 1 , \\
B1^k &= -\kappa_k = -B3^k , \\
\kappa_k &= \frac{\Delta \xi_k}{\Delta z_k} ,
\end{aligned} \tag{2-17}$$

$$\text{and, } RC^k = -B1^k \frac{j^{k-1}}{W_{i-1}} + \frac{j^{k-1}}{U_{i-1}} - B3^k \frac{j^k}{W_{i-1}} + \frac{j^k}{U_{i-1}} . \tag{2-18}$$

In this method the second derivatives are replaced with first derivatives through introduction of additional variables and equations. Then these new equations are differenced in adjacent boxes and after some algebraic manipulations the new variables are eliminated to get the working form of the governing equations. Following the above procedure the momentum equation may be written as:

$$\begin{aligned}
A1^k \frac{j^{k-1}}{W_i} + A2^k \frac{j^{k-1}}{U_i} + A3^k \frac{j^k}{W_i} + A4^k \frac{j^k}{U_i} \\
+ A5^k \frac{j^{k+1}}{U_i} + A6^k \frac{j^{k+1}}{W_i} + A7^k \frac{j}{E_i} = RM^k ,
\end{aligned} \tag{2-19}$$

and the coefficients are given by,

$$A1^k = \frac{\Delta z_k}{4} [\partial_x^j U]_{i-\frac{1}{2}}^{k-\frac{1}{2}} , \tag{2-20a}$$

$$A2^k = \frac{K_F}{2 \kappa_k} \frac{j^{k-\frac{1}{2}}}{U_{i-\frac{1}{2}}} - \frac{1}{\Delta z_k} , \tag{2-20b}$$

$$A3^k = \frac{\Delta z_k}{4} [\partial_x^j U]_{i-\frac{1}{2}}^{k-\frac{1}{2}} + \frac{\Delta z_{k+1}}{4} [\partial_x^j U]_{i-\frac{1}{2}}^{k+\frac{1}{2}}, \quad (2-20c)$$

$$A4^k = \frac{K_F}{2 \aleph_k} U_{i-\frac{1}{2}}^{k-\frac{1}{2}} + \frac{K_F}{2 \aleph_{k+1}} U_{i-\frac{1}{2}}^{k+\frac{1}{2}} + \frac{1}{\Delta z_k} + \frac{1}{\Delta z_{k+1}}, \quad (2-20d)$$

$$A5^k = \frac{\Delta z_{k+1}}{4} [\partial_x^j U]_{i-\frac{1}{2}}^{k+\frac{1}{2}}, \quad (2-20e)$$

$$A6^k = \frac{K_F}{2 \aleph_{k+1}} U_{i-\frac{1}{2}}^{k+\frac{1}{2}} - \frac{1}{\Delta z_{k+1}}, \quad (2-20f)$$

$$A7^k = \frac{\Delta z_k + \Delta z_{k+1}}{2}, \quad (2-20g)$$

where K_F is the FLARE parameter, and

$$\begin{aligned} RM^k &= - \Delta z_k RH_{i-\frac{1}{2}}^{k-\frac{1}{2}} - \Delta z_{k+1} RH_{i-\frac{1}{2}}^{k+\frac{1}{2}} - \frac{1}{2} (\Delta z_k + \Delta z_{k+1}) \frac{j}{E_{i-1}} \\ &+ \frac{K_F}{2 \aleph_k} U_{i-\frac{1}{2}}^{k-\frac{1}{2}} \left[\frac{j^k}{U_{i-1}} + \frac{j^{k-1}}{U_{i-1}} \right] + \frac{K_F}{2 \aleph_{k+1}} U_{i-\frac{1}{2}}^{k+\frac{1}{2}} \left[\frac{j^{k+1}}{U_{i-1}} + \frac{j^k}{U_{i-1}} \right] \\ &\quad - \frac{\Delta z_k}{4} [\partial_x^j U]_{i-\frac{1}{2}}^{k-\frac{1}{2}} \left[\frac{j^k}{W_{i-1}} + \frac{j^{k-1}}{W_{i-1}} \right] \\ &\quad - \frac{\Delta z_{k+1}}{4} [\partial_x^j U]_{i-\frac{1}{2}}^{k+\frac{1}{2}} \left[\frac{j^{k+1}}{W_{i-1}} + \frac{j^k}{W_{i-1}} \right] \end{aligned} \quad (2-21)$$

$$- \frac{1}{\Delta z_k} \left[\overset{j}{U}_{i-1}^k - \overset{j}{U}_{i-1}^{k-1} \right] + \frac{1}{\Delta z_{k+1}} \left[\overset{j}{U}_{i-1}^{k+1} - \overset{j}{U}_{i-1}^k \right].$$

Also, $RH_{i-\frac{1}{2}}^{j, k-\frac{1}{2}}$ is given below, and $RH_{i-\frac{1}{2}}^{j, k+\frac{1}{2}}$ is simply an index shift,

$$\begin{aligned} RH_{i-\frac{1}{2}}^{j, k-\frac{1}{2}} &= \left([\partial_{\xi}^j U]_{i-\frac{1}{2}}^{k-\frac{1}{2}} \right)^2 + \left([\partial_{\eta}^j V]_{i-\frac{1}{2}}^{k-\frac{1}{2}} \right)^2 \\ &+ W_{i-\frac{1}{2}}^{j, k-\frac{1}{2}} \left([\partial_{\eta x}^j V]_{i-\frac{1}{2}}^{k-\frac{1}{2}} + [\partial_{\xi x}^j U]_{i-\frac{1}{2}}^{k-\frac{1}{2}} \right) \\ &+ 2 [\partial_{\eta}^j U]_{i-\frac{1}{2}}^{k-\frac{1}{2}} [\partial_{\xi}^j V]_{i-\frac{1}{2}}^{k-\frac{1}{2}} + [\partial_{\eta}^j W]_{i-\frac{1}{2}}^{k-\frac{1}{2}} [\partial_x^j V]_{i-\frac{1}{2}}^{k-\frac{1}{2}} \\ &+ V_{i-\frac{1}{2}}^{j, k-\frac{1}{2}} \left([\partial_{\eta}^j U]_{i-\frac{1}{2}}^{k-\frac{1}{2}} + [\partial_{\eta}^j V]_{i-\frac{1}{2}}^{k-\frac{1}{2}} \right). \end{aligned} \quad (2-22)$$

Here each term is defined as:

$$\begin{aligned} [\partial_{\xi}^j U]_{i-\frac{1}{2}}^{k-\frac{1}{2}} &= \left[\frac{1}{\Delta \xi} \left(\overset{j}{U}_i - \overset{j}{U}_{i-1} \right) \right]^{k-\frac{1}{2}} \\ &= \frac{1}{2} \left[\frac{1}{\Delta \xi} \left(\overset{j}{U}_i - \overset{j}{U}_{i-1} \right) + \frac{1}{\Delta \xi} \left(\overset{j}{U}_i^{k-1} - \overset{j}{U}_{i-1}^{k-1} \right) \right], \end{aligned} \quad (2-23)$$

and,

$$\begin{aligned}
[\partial_{\eta z}^j V]_{i-\frac{1}{2}}^{k-\frac{1}{2}} &= \left[\partial_{\eta} \left(\frac{V^k - V^{k-1}}{\Delta z} \right) \right]_{i-\frac{1}{2}} \quad (2-24) \\
&= \frac{1}{2 \Delta \eta \Delta z} \left[\left(\frac{V^{j+1k} - V^{j+1k-1}}{V} \right) - \left(\frac{V^{j-1k} - V^{j-1k-1}}{V} \right) \right]_{i-\frac{1}{2}} \\
&= \frac{1}{4 \Delta \eta \Delta z} \left[\left(\frac{V_i^{j+1k} - V_i^{j+1k-1} - V_i^{j-1k} + V_i^{j-1k-1}}{V} \right) \right. \\
&\quad \left. + \left(\frac{V_{i-1}^{j+1k} - V_{i-1}^{j+1k-1} - V_{i-1}^{j-1k} + V_{i-1}^{j-1k-1}}{V} \right) \right].
\end{aligned}$$

The remaining terms are similarly defined.

II.1.1b Central Difference Method

The lower-deck equations are also centrally differenced in a second, "duplicate", scheme. The grid spacings are given by $\Delta \xi$, $\Delta \eta$, and Δz , which do not allow for a variable grid spacing in the direction normal to the wall in contrast to the previous scheme. The continuity equation is differenced as before and its coefficients are the same as given before when Δz_k is replaced by Δz . However, in the momentum equation all the derivatives and flow parameters are written about the node at $(i - \frac{1}{2}, j \text{ and } k)$. Therefore, the coefficients of the momentum equation are changed and are given below:

$$A1^k = A5^k = 0 , \quad (2-25a)$$

$$A2^k = A6^k = -\frac{1}{2(\Delta z)^2} , \quad (2-25b)$$

$$A3^k = \frac{1}{2} [\partial_x^j U]_{i-\frac{1}{2}}^k , \quad (2-25c)$$

$$A4^k = \frac{K_F}{\Delta \xi} \bar{U}_{i-\frac{1}{2}}^k + \frac{1}{(\Delta z)^2} , \quad (2-25d)$$

$$A7^k = \frac{1}{2} , \quad (2-25e)$$

and,

$$\begin{aligned} RM^k = & - RH_{i-\frac{1}{2}}^k + \frac{K_F}{\Delta \xi} \bar{U}_{i-\frac{1}{2}}^k \bar{U}_{i-1}^k \quad (2-26) \\ & - \frac{1}{2} [\partial_x^j U]_{i-\frac{1}{2}}^k \bar{W}_{i-1}^k - \frac{1}{2} \bar{E}_{i-1}^k \\ & + \frac{1}{2(\Delta z)^2} \left[\bar{U}_{i-1}^{k+1} - 2\bar{U}_{i-1}^k + \bar{U}_{i-1}^{k-1} \right] , \end{aligned}$$

where,

$$\begin{aligned}
RH_{i-\frac{1}{2}}^{j,k} &= \left([\partial_{\xi}^j U]_{i-\frac{1}{2}}^k \right)^2 + \left([\partial_{\eta}^j V]_{i-\frac{1}{2}}^k \right)^2 \\
&+ W_{i-\frac{1}{2}}^{j,k} \left([\partial_{\eta x}^j V]_{i-\frac{1}{2}}^k + [\partial_{\xi x}^j U]_{i-\frac{1}{2}}^k \right) \\
&+ 2 [\partial_{\eta}^j U]_{i-\frac{1}{2}}^k [\partial_{\xi}^j V]_{i-\frac{1}{2}}^k + [\partial_{\eta}^j W]_{i-\frac{1}{2}}^k [\partial_x^j V]_{i-\frac{1}{2}}^k \\
&+ V_{i-\frac{1}{2}}^{j,k} \left([\partial_{\xi \eta}^j U]_{i-\frac{1}{2}}^k + [\partial_{\eta \eta}^j V]_{i-\frac{1}{2}}^k \right). \tag{2-27}
\end{aligned}$$

II.1.2 The Upper Deck and Matching Conditions

The Laplacian of $\hat{E}(\xi, \eta, z_u)$ in the upper deck is centrally differenced about the node (i, j, q) , where the upper deck is discretized using index $q = 1, 2, 3, \dots, m-1, m$, and the mesh spacing, Δz_u . Therefore, we can write:

$$Q_1 \hat{E}_i^{j,q-1} + Q_2 \hat{E}_i^{j,q} + Q_3 \hat{E}_i^{j,q+1} = RUE^q, \tag{2-28}$$

where
$$Q_1 = -\frac{1}{(\Delta z_u)^2}, \quad Q_3 = Q_1, \tag{2-29a}$$

$$Q_2 = \frac{2}{(\Delta \xi)^2} + \frac{2}{(\Delta \eta)^2} + \frac{2}{(\Delta z_u)^2}, \tag{2-29b}$$

and,

$$RUE^q = \frac{1}{(\Delta\xi)^2} \left[\hat{E}_{i-1}^{jq} + \hat{E}_{i+1}^{jq} \right] + \frac{1}{(\Delta\eta)^2} \left[\hat{E}_i^{j-1q} + \hat{E}_i^{j+1q} \right]. \quad (2-30)$$

The extra equations to close the problem along the direction normal to the wall are provided by the matching conditions. From equation (2-10) at the edge of the lower deck we have,

$$\frac{j^n}{W_i} + \frac{j}{E_i} = -\dot{U}_i \left(\frac{j}{B_i} + [\partial_{\xi\xi}^j F]_i \right) - \left([\partial_\xi^j U]_i^n \right)^2, \quad (2-31)$$

or

$$K_1 \frac{j^n}{W_i} + K_2 \frac{j}{B_i} + K_3 \frac{j}{E_i} = RU, \quad (2-32)$$

where
$$K_1 = K_3 = 1, \quad K_2 = \dot{U}_i^n, \quad (2-33a)$$

and,
$$RU = -\dot{U}_i^n [\partial_{\xi\xi}^j F]_i - \left([\partial_\xi^j U]_i^n \right)^2. \quad (2-33b)$$

Also, at the outer edge of the lower deck, from equation (2-8), U approaches,

$$\frac{j^n}{U_i} \rightarrow \int_0^i \frac{j}{B_\alpha} d\alpha + h [\partial_\xi^j F]_i. \quad (2-34)$$

Integrating by trapezoidal rule we can write,

$$K_4 \overset{j}{U}_i + K_5 \overset{j}{B}_i = RB , \quad (2-35)$$

where
$$K_4 = 1 , K_5 = -\frac{\Delta\xi}{2} , \quad (2-36a)$$

and,
$$RB = [\partial_{\xi}^j F]_i + \sum_{m=1}^{i-1} \Delta\xi \overset{j}{B}_m . \quad (2-36b)$$

Finally, using the matching condition (2-14b) we can write ,

$$[\partial_{\xi}^j \hat{E}]_i = [\partial_{\xi\xi}^j B]_i + [\partial_{\eta\eta}^j B]_i , \quad (2-37)$$

or using a second-order differenced first derivative,

$$K_6 \overset{j}{B}_i + K_7 \overset{j}{E}_i^1 + K_8 \overset{j}{E}_i^2 + K_9 \overset{j}{E}_i^3 = RE , \quad (2-38)$$

where
$$K_6 = \frac{4 \Delta z_u}{(\Delta\xi)^2} + \frac{4 \Delta z_u}{(\Delta\eta)^2} , K_7 = -3 , K_8 = 4 , K_9 = -1 , \quad (2-39a)$$

and
$$RE = \frac{2 \Delta z_u}{(\Delta\xi)^2} \left(\overset{j}{B}_{i+1} + \overset{j}{B}_{i-1} \right) + \frac{2 \Delta z_u}{(\Delta\eta)^2} \left(\overset{j+1}{B}_i + \overset{j-1}{B}_i \right) . \quad (2-39b)$$

Using the above procedure at any node (i, j) we can solve the system of equations shown in matrix form in figure 4 to obtain $\bar{U}, \bar{W}, \bar{E}, B$ and \hat{E} for all k and q .

II.2 Receptivity Problem

For the unsteady problem the governing equations in the lower deck with the appropriate boundary conditions are given by equations (1-72) - (1-75) in Chapter 1. Similarly, in the upper deck, the governing equations are given by equations (1-76) - (1-79). Again in a similar fashion to the steady problem, we define the disturbance skewed shear parameters:

$$\bar{u} = \partial_{\xi} u + \partial_{\eta} v \quad , \quad \bar{w} = \partial_{\xi} w \quad \text{and} \quad \bar{e} = [\partial_{\xi\xi} + \partial_{\eta\eta}] p(\xi, \eta) \quad . \quad (2-40)$$

Furthermore, define a new function,

$$\int_{-\infty}^{\xi} b(x, \eta) \, dx = \partial_{\xi} a(\xi, \eta) \quad . \quad (2-41)$$

Using the above definitions and differentiating the governing equations (1-72), it can be shown that:

$$\partial_{\xi} \bar{u} + \partial_z \bar{w} = 0 \quad , \quad (2-42)$$

$$\begin{aligned} -i S_0 \bar{u} + U \partial_{\xi} \bar{u} + W \partial_z \bar{u} + \partial_z U \bar{w} \\ + \bar{e} - \partial_{xx} \bar{u} = rh \quad , \end{aligned} \quad (2-43)$$

where, rh is given by,

$$\begin{aligned}
rh &= -(1+u)(\partial_{\xi\xi} U + \partial_{\eta\eta} V) \\
&+ \left(\partial_{\xi\xi} U + \partial_{\eta\eta} V + i^{\frac{3}{2}} S_0^{\frac{1}{2}} \partial_{\xi} W \right) \exp\left(i^{\frac{3}{2}} S_0^{\frac{1}{2}} z \right) \\
&- w \left(\partial_{x\xi} U + \partial_{x\eta} V \right) \\
&- \partial_{\xi} W \partial_x u - 2 \partial_{\xi} U \partial_{\xi} u - 2 \partial_{\eta} V \partial_{\eta} v \\
&- 2 \partial_{\xi} V \partial_{\eta} u - 2 \partial_{\eta} U \partial_{\xi} v \\
&- \partial_{\eta} W \partial_x v - \partial_x V \partial_{\eta} w \\
&- v \left(\partial_{\eta\xi} U + \partial_{\eta\eta} V \right) \\
&- V \left(\partial_{\eta\xi} u + \partial_{\eta\eta} v \right), \tag{2-44}
\end{aligned}$$

and the boundary conditions, equations (1-73) and (1-74) transform to:

$$\bar{u} = \bar{w} = 0 \quad \text{on} \quad z = 0, \tag{2-45a}$$

$$\bar{u}, \bar{w}, \bar{e} \rightarrow 0 \quad \text{as} \quad \xi \rightarrow -\infty. \tag{2-45b}$$

Also, as $z \rightarrow \infty$, it can be shown that:

$$\bar{u} \rightarrow \int_{-\infty}^{\xi} b(x, \eta) dx. \tag{2-46}$$

As an alternative boundary condition we could approximate the momentum equation

(2-43) as $z \rightarrow \infty$,

$$\begin{aligned} \bar{w} + \bar{e} &\rightarrow i S_0 \int_{-\infty}^{\xi} b(x, \eta) dx - U(z \rightarrow \infty) b(\xi, \eta) \\ &- 2 \partial_{\xi} U(z \rightarrow \infty) \partial_{\xi} u - \partial_{\xi \xi} U(z \rightarrow \infty) (1 + u) . \end{aligned} \quad (2-47)$$

Similarly for the upper-deck pressure, we define

$$\hat{e}(\xi, \eta, z_u) = \partial_{\xi \xi} \hat{p}(\xi, \eta, z_u) + \partial_{\eta \eta} \hat{p}(\xi, \eta, z_u) . \quad (2-48)$$

Therefore, the governing equation (1-77) in the upper deck becomes,

$$\partial_{\xi \xi} \hat{e} + \partial_{\eta \eta} \hat{e} + \partial_{z_u z_u} \hat{e} = 0 , \quad (2-49)$$

and the boundary conditions (1-78a) and the matching conditions (1-79) become:

$$\hat{e}(\xi, \eta, z_u) \rightarrow 0 \quad \text{as} \quad \begin{array}{l} \xi \rightarrow -\infty \\ z_u \rightarrow \infty \end{array} , \quad (2-50)$$

$$\hat{e}(\xi, \eta, z_u \rightarrow 0) = \bar{e}(\xi, \eta) , \quad (2-51a)$$

$$\partial_{z_u} \hat{e}(\xi, \eta, z_u \rightarrow 0) = \partial_{\xi \xi} b(\xi, \eta) + \partial_{\eta \eta} b(\xi, \eta) . \quad (2-51b)$$

We also need boundary conditions as $\xi \rightarrow \infty$ and $\eta \rightarrow \pm\infty$. The radiation conditions (1-78b) and (1-78c) are imposed at these boundaries. Here we calculate both K_{ξ} and K_{η} iteratively during the numerical computations at a location near the appropriate boundaries. Therefore, at these boundaries we can write:

$$\partial_{\xi} \hat{e} \rightarrow i K_{\xi} \hat{e}(\xi, \eta, z_u), \quad \text{as } \xi \rightarrow \infty , \quad (2-52a)$$

$$\partial_{\eta} \hat{e} \rightarrow i K_{\eta} \hat{e}(\xi, \eta, z_u), \quad \text{as } \eta \rightarrow \pm\infty . \quad (2-52b)$$

The receptivity problem is solved by the same iterative multi-sweep technique described before for the steady problem.

II.2.1 Finite Differences

The governing equations for the receptivity problem are differenced using a second order accurate scheme. The mesh is the same as the one used for the steady-state problem and the results of the steady-state solution are stored for all mesh points, since they are needed to evaluate the coefficients in the unsteady problem. Flow properties and their derivatives are centrally differenced about the node at $(i - \frac{1}{2}, j \text{ and } k)$ (figure 3).

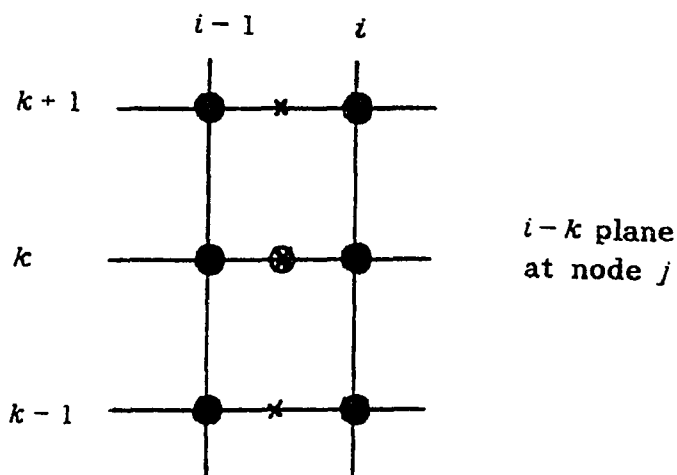


Figure 3. Computational cell in the central-differences method.

The continuity equation (2-42) in the lower deck can be written as :

$$b1^k \frac{j^{k-1}}{w_i} + b2^k \frac{j^{k-1}}{u_i} + b3^k \frac{j^k}{w_i} + b4^k \frac{j^k}{u_i} = rc^k , \quad (2-53)$$

where,

$$\begin{aligned} b2^k &= b4^k = 1 , \\ b1^k &= -\kappa = -b3^k , \\ \kappa &= \frac{\Delta \xi}{\Delta z} , \end{aligned} \quad (2-54)$$

$$\text{and, } rc^k = -b1^k \frac{j^{k-1}}{w_{i-1}} + \frac{j^{k-1}}{u_{i-1}} - b3^k \frac{j^k}{w_{i-1}} + \frac{j^k}{u_{i-1}} . \quad (2-55)$$

The momentum equation (2-43) in the lower deck is given by:

$$\begin{aligned} a1^k \frac{j^{k-1}}{w_i} + a2^k \frac{j^{k-1}}{u_i} + a3^k \frac{j^k}{w_i} + a4^k \frac{j^k}{u_i} \\ + a5^k \frac{j^{k+1}}{u_i} + a6^k \frac{j^{k+1}}{w_i} + a7^k \frac{j}{e_i} = rm^k , \end{aligned} \quad (2-56)$$

where,

$$a1^k = a5^k = 0 , \quad (2-57a)$$

$$a2^k = -\frac{1}{4(\Delta z)} \frac{j^k}{W_{i-\frac{1}{2}}} - \frac{1}{2(\Delta z)^2} , \quad (2-57b)$$

$$a3^k = \frac{1}{2} [\partial_z^j U]_{i-\frac{1}{2}}^k , \quad (2-57c)$$

$$a4^k = -\frac{i}{2}S_0 + \frac{K_F}{\Delta\xi} U_{i-\frac{1}{2}}^{jk} + \frac{1}{(\Delta z)^2}, \quad (2-57d)$$

$$a6^k = \frac{1}{4(\Delta z)} W_{i-\frac{1}{2}}^{jk} - \frac{1}{2(\Delta z)^2}, \quad (2-57e)$$

$$a7^k = \frac{1}{2}, \quad (2-57f)$$

and

$$\begin{aligned} rm^k &= rh_{i-\frac{1}{2}}^{jk} + \frac{i}{2}S_0 \frac{j^k}{u_{i-1}} + \frac{K_F}{\Delta\xi} U_{i-\frac{1}{2}}^{jk} \frac{j^k}{u_{i-1}} \\ &\quad - \frac{1}{4(\Delta z)} W_{i-\frac{1}{2}}^{jk} \left[\frac{j^{k+1}}{u_{i-1}} - \frac{j^{k-1}}{u_{i-1}} \right] \\ &\quad - \frac{1}{2} [\partial_z^j U]_{i-\frac{1}{2}}^k \frac{j^k}{w_{i-1}} - \frac{1}{2} \frac{j}{e_{i-1}} \\ &\quad + \frac{1}{2(\Delta z)^2} \left[\frac{j^{k+1}}{u_{i-1}} - 2\frac{j^k}{u_{i-1}} + \frac{j^{k-1}}{u_{i-1}} \right]. \end{aligned} \quad (2-58)$$

The matching conditions (2-47) and (2-46) are given by:

$$K_1 \frac{j^n}{w_i} + K_{10} \frac{j^n}{u_i} + K_2 \frac{j}{b_i} + K_3 \frac{j}{e_i} = ru, \quad (2-59)$$

$$\text{where } K_1 = K_3 = 1, \quad K_2 = U_i^{jn}, \quad K_{10} = -iS_0, \quad (2-60)$$

$$\text{and } ru = -[\partial_\xi^j U]_i^n \frac{1}{\Delta\xi} \left(\frac{j^n}{u_{i+1}} - \frac{j^n}{u_{i-1}} \right) - [\partial_{\xi\xi}^j U]_i^n \left(1 + \frac{j^n}{u_i} \right). \quad (2-61)$$

Likewise, we have,

$$K_4 \frac{j^*}{u_i} + K_5 \frac{j}{b_i} = rb , \quad (2-62)$$

where
$$K_4 = 1 , K_5 = -\frac{\Delta\xi}{2} , \quad (2-63)$$

and
$$rb = \sum_{m=1}^{i-1} \Delta\xi \frac{j}{b_m} . \quad (2-64)$$

The governing equation in the upper deck, equation (2-49), is also centrally differenced about the node (i, j, q) . Therefore, we can write:

$$Q_1 \frac{j^{q-1}}{\hat{e}_i} + Q_2 \frac{j^q}{\hat{e}_i} + Q_3 \frac{j^{q+1}}{\hat{e}_i} = rue^q , \quad (2-65)$$

where
$$rue^q = \frac{1}{(\Delta\xi)^2} \left[\frac{j^q}{\hat{e}_{i-1}} + \frac{j^q}{\hat{e}_{i+1}} \right] + \frac{1}{(\Delta\eta)^2} \left[\frac{j^{-1q}}{\hat{e}_i} + \frac{j^{+1q}}{\hat{e}_i} \right] . \quad (2-66)$$

Furthermore, from matching to the main deck, equation (2-51b), we have:

$$K_6 \frac{j}{b_i} + K_7 \frac{j^1}{\hat{e}_i} + K_8 \frac{j^2}{\hat{e}_i} + K_9 \frac{j^3}{\hat{e}_i} = re , \quad (2-67)$$

and
$$re = \frac{2 \Delta z_u}{(\Delta\xi)^2} \left(\frac{j}{b_{i+1}} + \frac{j}{b_{i-1}} \right) + \frac{2 \Delta z_u}{(\Delta\eta)^2} \left(\frac{j^{+1}}{b_i} + \frac{j^{-1}}{b_i} \right) , \quad (2-68)$$

where K_6, \dots, K_9 and $Q_{1,2,3}$ are the same as in the steady-state problem, given by equations (2-39a) and (2-29a). From the boundary conditions at the wall, equation (2-45a), and at the outer edge of the upper deck, equation (2-50), we know that:

$$\frac{j^1}{U_i} = \frac{j^1}{W_i} = 0 \quad \text{and} \quad \frac{j^m}{E_i} = 0 . \quad (2-69)$$

Applying the above system of equations along a line perpendicular to the wall at any node (i, j) , we can solve the system of equations given below in matrix form to obtain $\bar{u}, \bar{w}, \bar{e}, b$ and \hat{e} for all k and q along that line.

i	$j =$	1	2	3	4	5	6	7	8	9	10	11	12	13	.	.	$2n$	
1		b_3^2	b_4^2	a_7^2	
2		a_3^2	a_4^2	a_5^2	a_6^2	a_7^2	
3		b_1^3	b_2^3	b_3^3	a_4^3	a_7^3	
4		a_1^3	a_2^3	a_3^3	a_4^3	a_5^3	a_6^3	a_7^3	
5		.	.	b_1^4	b_2^4	b_3^4	b_4^4	a_7^4	
6		.	.	a_1^4	a_2^4	a_3^4	a_4^4	a_5^4	a_6^4	a_7^4	
7		b_1^4	b_2^4	b_3^4	b_4^4	a_7^4	
8		a_1^5	a_2^5	a_3^5	a_4^5	a_5^5	a_6^5	a_7^5	
9		b_1^4	b_2^4	b_3^4	b_4^4	a_7^5	
10		a_1^6	a_2^6	a_3^6	a_4^6	a_5^6	a_6^6	.	.	.	a_7^6	
11		b_1^4	b_2^4	b_3^4	b_4^4	.	.	.	a_7^6	
.		
$2(n-2)-2$		
$2(n-1)-3$		b_1^{n-1}	b_2^{n-1}	b_3^4	b_4^4	
$2(n-1)-2$		a_1^{n-1}	a_2^{n-1}	a_3^{n-1}	a_4^{n-1}	a_5^{n-1}	a_6^{n-1}	a_7^{n-1}	
$2n-3$		b_1^n	b_2^n	b_3^n	b_4^n	
$2n-2$		k_1	k_{10}	k_2	k_3	
$2n-1$		k_4	k_5	
$(2n-1)+1$		k_6	k_7	Q_1	Q_2	Q_3	.	.	.	
$(2n-1)+2$		Q_1	Q_2	Q_3	.	.	.	
$(2n-1)+3$		Q_1	Q_2	Q_3	.	.	
$(2n-1)+4$		Q_1	Q_2	Q_3	.	.	
.		
$(2n-1)+(n-4)$		Q_1	Q_2	Q_3	.	
$(2n-1)+(n-3)$		Q_1	Q_2	Q_3	
$(2n-1)+(n-2)$		Q_1	Q_2	Q_3
$(2n-1)+(n-1)$		Q_1	Q_2

Figure 4. The system of governing equations along the line at (i, j) .

The above sparse system is easily solved using standard Gaussian elimination. To find the next iterative values over the entire domain, the above system of equations is marched forward in ξ . This procedure is started at the node $i = 1$ and $j = 0$, where $i = 0$ is the upstream boundary, $\xi = \xi_{\infty}$, at which point the solution to the unsteady boundary layer is imposed. Also, $j = 0$ is the location of the line of symmetry, where the usual symmetry conditions are applied. The governing equations in both the lower and upper decks are solved simultaneously over the entire range of the normal directions, z and z_u . After the solution is found along this line, normal to the wall, the procedure is marched forward in ξ until the entire $\xi - \eta$ plane is covered. The process is then repeated at all the other η locations (i-fastest) to obtain this iteration of the solution over the entire domain.

Once the new values of \bar{u} , \bar{w} , \bar{e} , b and \hat{e} are found over the entire domain, the definition of \bar{e} is used to solve for the new values of unsteady pressure. The following Poisson's equation is solved using the Successive-Over-Relaxation technique with $\omega_{SOR} = 1.6$

$$\partial_{\xi\xi} p + \partial_{\eta\eta} p = \bar{e}(\xi, \eta), \quad (2-70)$$

subject to the boundary conditions:

$$p(\xi, \eta) \rightarrow 0 \quad \text{as} \quad \xi \rightarrow -\infty, \quad (2-71a)$$

$$\partial_{\xi} p \rightarrow i K_{\xi} p(\xi, \eta) \quad \text{as} \quad \xi \rightarrow \infty, \quad (2-71b)$$

$$\partial_{\eta} p \rightarrow i K_{\eta} p(\xi, \eta) \quad \text{as} \quad \eta \rightarrow \pm\infty. \quad (2-71c)$$

Hence, a new value for pressure at the node (i, j) is found from the following equation:

$$p_{inew}^j = P0 p_i^j + P1 \left(p_{i+1}^j + p_{i-1}^j \right) + P2 e_i^j + P3 \left(p_{i+1}^{j+1} + p_{i-1}^{j-1} \right), \quad (2-72)$$

$$\text{where } P0 = (1 - \omega_{SOR}), \quad P1 = \frac{\omega_{SOR} (\Delta\eta)^2}{2 [(\Delta\xi)^2 + (\Delta\eta)^2]}, \quad (2-73a)$$

$$\text{and } P2 = \frac{-\omega_{SOR} (\Delta\xi)^2 (\Delta\eta)^2}{2 [(\Delta\xi)^2 + (\Delta\eta)^2]}, \quad P3 = \frac{\omega_{SOR} (\Delta\xi)^2}{2 [(\Delta\xi)^2 + (\Delta\eta)^2]}. \quad (2-73b)$$

The above iterative procedure is applied to the entire $\xi - \eta$ plane (i-fastest) until convergence (maximum change in p is less than 10^{-7}) is achieved.

Having found the pressure values at this global iterative step, we march the original η -momentum equation (1-72) in ξ to calculate new values for v . The η -momentum equation is written below with the right hand side assumed known at this level,

$$\begin{aligned} U \partial_\xi v + (\partial_\eta V - i S_0) v + W \partial_z v - \partial_{zz} v \\ = -V \partial_\eta v - \partial_\eta p - \partial_z V w \\ - \partial_\xi V \left[1 + u - \exp\left(i^{\frac{3}{2}} S_0^{\frac{1}{2}} z\right) \right], \end{aligned} \quad (2-74)$$

subject to the following boundary conditions:

$$v(\xi, \eta, z) \rightarrow 0 \quad \text{as} \quad \xi \rightarrow -\infty, \quad (2-75a)$$

$$v = 0 \quad \text{at} \quad z = 0 \quad \text{and} \quad \partial_{\xi} v \rightarrow -\frac{\partial_{\eta} p(\xi, \eta)}{(z + hF)} \quad \text{as} \quad z \rightarrow \infty. \quad (2-75b)$$

Three-point central differencing is used about the node $(i - \frac{1}{2}, j \text{ and } k)$ to approximate the above equations. This results in a tri-diagonal system of equations which can easily be solved using the Thomas algorithm. The difference equations are given by:

$$c1^k v_i^{j^{k-1}} + c2^k v_i^{j^k} + c3^k v_i^{j^{k+1}} = rv^k, \quad (2-76)$$

where

$$c1^k = -\frac{1}{4(\Delta z)} W_{i-\frac{1}{2}}^{j^k} - \frac{1}{2(\Delta z)^2}, \quad (2-77a)$$

$$c2^k = \frac{K_F}{\Delta \xi} U_{i-\frac{1}{2}}^{j^k} + \frac{1}{2} \left([\partial_{\eta}^j V]_{i-\frac{1}{2}}^k - i S_0 \right) + \frac{1}{(\Delta z)^2}, \quad (2-77b)$$

$$c3^k = \frac{1}{4(\Delta z)} W_{i-\frac{1}{2}}^{j^k} - \frac{1}{2(\Delta z)^2}, \quad (2-77c)$$

and

$$rv^k = \left(\frac{K_F}{\Delta \xi} U_{i-\frac{1}{2}}^{j^k} - \frac{1}{2} [\partial_{\eta}^j V]_{i-\frac{1}{2}}^k + \frac{i}{2} S_0 \right) v_{i-1}^{j^k} - \frac{1}{4\Delta z} W_{i-\frac{1}{2}}^{j^k} \left(v_{i-1}^{j^{k+1}} - v_{i-1}^{j^{k-1}} \right) \quad (2-77d)$$

$$\begin{aligned}
& + \frac{1}{2(\Delta z)^2} \left[v_{i-1}^{j^{k+1}} - 2v_{i-1}^{j^k} + v_{i-1}^{j^{k-1}} \right] \\
& - V_{i-\frac{1}{2}}^{j^k} [\partial_\eta v]_{i-\frac{1}{2}}^k - [\partial_\eta p]_{i-\frac{1}{2}}^k - [\partial_z V]_{i-\frac{1}{2}}^k w_{i-\frac{1}{2}}^{j^k} \\
& - [\partial_\xi V]_{i-\frac{1}{2}}^k \left(1 + u_{i-\frac{1}{2}}^{j^k} - \left[\exp \left(\frac{j}{i^{\frac{3}{2}}} S_0^{\frac{1}{2}} z \right) \right]_{i-\frac{1}{2}}^k \right).
\end{aligned}$$

At this point we integrate the continuity equation (1-72a) to evaluate the new values for the w-velocity. From the continuity equation we have:

$$\bar{u} + \partial_z w = 0, \quad (2-78)$$

or

$$w(\xi, \eta, z) = \int_0^z -\bar{u}(\xi, \eta, \zeta) d\zeta. \quad (2-79)$$

By using simple trapezoidal integration the above integral can be approximated between z-steps $k-1$ & k :

$$w_i^{j^k} = w_i^{j^{k-1}} - \frac{\Delta z}{2} \left(\frac{j^k}{u_i} + \frac{j^{k-1}}{u_i} \right). \quad (2-80)$$

Finally, the u-velocity component is updated by integrating the definition of \bar{u} (See equation (2-40)). Again after using trapezoidal integration the above relationship can be approximated between ξ -steps $i-1$ & i to evaluate $u_i^{j^k}$:

$$\begin{aligned}
u_i^{j,k} = u_{i-1}^{j,k} &+ \frac{\Delta E}{2} \left(\frac{j^k}{u_i} + \frac{j^k}{u_{i-1}} \right) \\
&- \frac{1}{2 \Delta \eta} \left(\frac{j+1^k}{v_i} - \frac{j-1^k}{v_i} \right) \\
&- \frac{1}{2 \Delta \eta} \left(\frac{j+1^k}{v_{i-1}} - \frac{j-1^k}{v_{i-1}} \right) .
\end{aligned} \tag{2-81}$$

All the above steps constitute one global iteration. The solution (all the flow variables in their primitive form) obtained after one iteration is used as an initial guess for the next iterative step. This process is continued until global convergence is attained on the disturbance streamwise velocity u . That is:

$$\max \left[\frac{j^k}{u_{i_{new}}} - \frac{j^k}{u_{i_{old}}} \right] < \hat{\epsilon} \quad \text{for all } i, j, k \tag{2-82}$$

where $\hat{\epsilon}$ is a small number, usually in the order of 10^{-5} .

CHAPTER III

STEADY-STATE RESULTS

III.1 Comparison with Prior Works

As mentioned in Chapter 2, two different numerical schemes are utilized to solve the steady-state problem. This is due to the fact that at first we used the modified Keller-Box scheme described in Section 2.1.1a. However, when we tried to check our code, we could not reproduce the results reported by Bodonyi and Duck [24]. Although the trends are similar, their figures under predict the results in the wake of the hump. Now we are convinced that our code is correct and know the cause of this discrepancy. Nevertheless, this was not clear at first. Therefore, after exhaustive review of our code, not finding any mistakes, it was decided to alter the code and use the same central-difference scheme, described in Section 2.1.1b, as is used in reference [24]. To our surprise, the new scheme reproduced the same results as our first method.

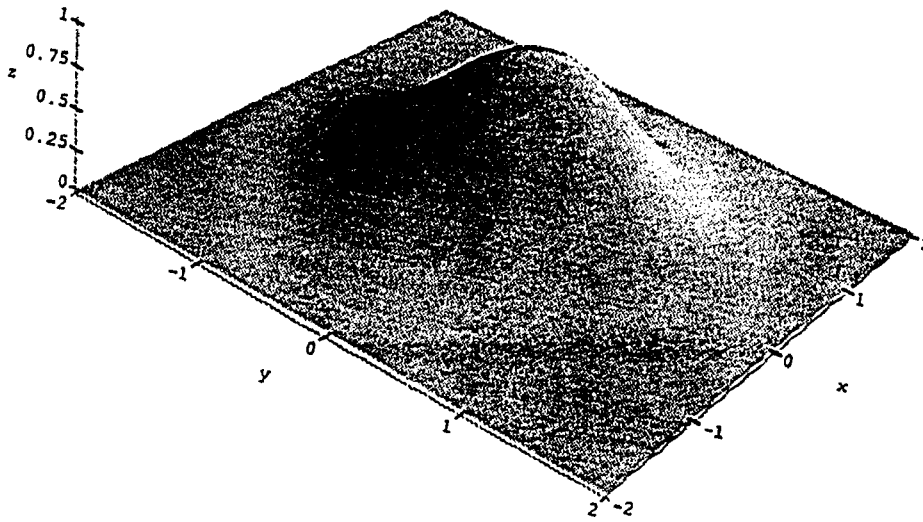


Figure 5. Hump shape given by $F(x, y) = \exp[-x^2 - y^2]$.

To compare our code with Bodonyi and Duck [24], we use the same hump shape, $h F(x, y)$ with h as a scaled height parameter , as reported in their work (see figure 5):

where:
$$F(x, y) = \exp[-x^2 - y^2] \quad \text{for all } x \text{ and } y . \quad (3-1)$$

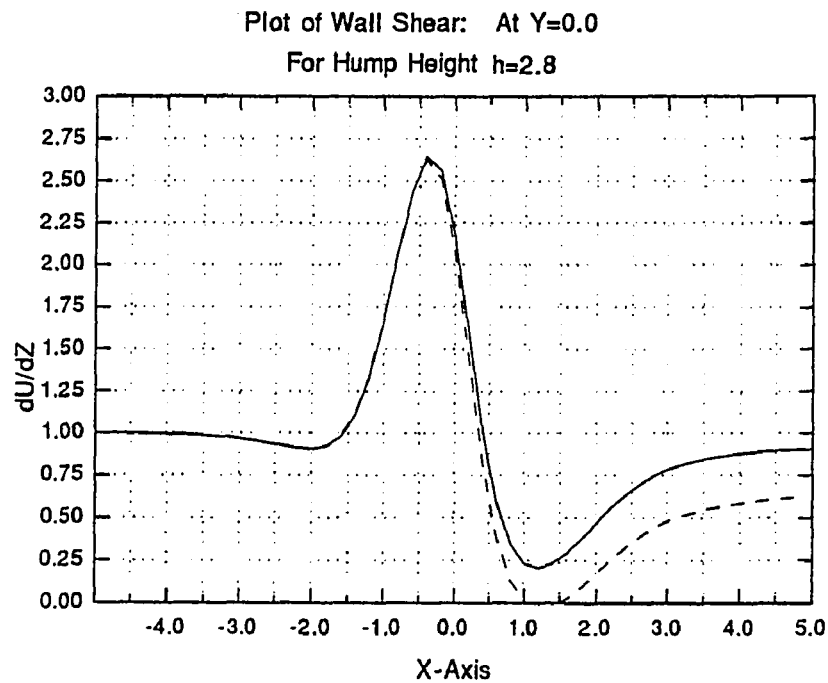


Figure 6. Comparison of streamwise wall shear on the centerline, $Y=0$, with reference [24] (the dashed line).

Here, for convenience, we have replaced ξ , η , and z_i by X , Y , and Z respectively. Furthermore, we use the same grid spacings as taken by Bodonyi and Duck [24]. In the streamwise direction $\Delta X = 0.20$, $-5.0 < X < 5.0$; along the lateral direction we have $\Delta Y = 0.25$, $0 < Y < 3.75$, and in the normal direction within the lower deck region $\Delta Z = 0.30$ and $0 < Z < 6.0$. These values correspond to using 51, 16, and 21

points in the X, Y, and Z directions respectively. In the upper deck region the same values were used for ΔX and ΔY while $\Delta Z_u = 0.125$ and $0 < Z_u < 2.5$, corresponding to the same number of grid points as in the lower-deck problem.

Figure 6. shows a comparison of streamwise wall shear, dU/dZ , between the three codes. The top solid line is generated by both schemes utilized in this work, and the bottom dashed line is given by Bodonyi and Duck [24] in their figure 1a. As stated previously, their results differ from ours, and they under predict the wall shear.

After further review of all the codes, it was found that the difference lies in the way Bodonyi and Duck averaged some of the terms in the z-direction. In Section 2.1.1b, all the derivatives and flow parameters in the momentum equation (2-3) are written about the node at $(i - \frac{1}{2}, j \text{ and } k)$. In particular, the term $\partial_z U \bar{W}$ in equation (2-3) is represented as:

$$[\partial_z^j U]_{i-\frac{1}{2}}^k = \frac{1}{2} \left(\frac{j^k}{W_i} + \frac{j^k}{W_{i-1}} \right) \quad (3-2)$$

However, Bodonyi and Duck use the following representation:

$$[\partial_z^j U]_{i-\frac{1}{2}}^k = \frac{1}{4} \left(\frac{j^{k+1}}{W_i} + \frac{j^{k+1}}{W_{i-1}} + \frac{j^{k-1}}{W_i} + \frac{j^{k-1}}{W_{i-1}} \right) \quad (3-3)$$

This variance in differencing such terms would not matter in a much finer mesh. Nonetheless, in a region of rapid change in the Z direction, as in the immediate wake of the hump, with $\Delta Z = 0.30$ the difference is noticeable (see figure 6.). This is consistent with their figure 1d which shows an upward movement of the wall shear curve in the

wake of the hump as ΔZ is reduced. They had also correctly noted their scheme's sensitivity to the choice of ΔZ . Using a finer mesh does not change the results produced by our codes; however, that would improve their results. The spectral results of Duck and Burggraf [28], given in Bodonyi and Duck's figure 1a, are very close to the values given in our figure 6. Furthermore, the code in reference [24] produces the same results as in our figure 6 when a finer mesh is used in the Z direction.

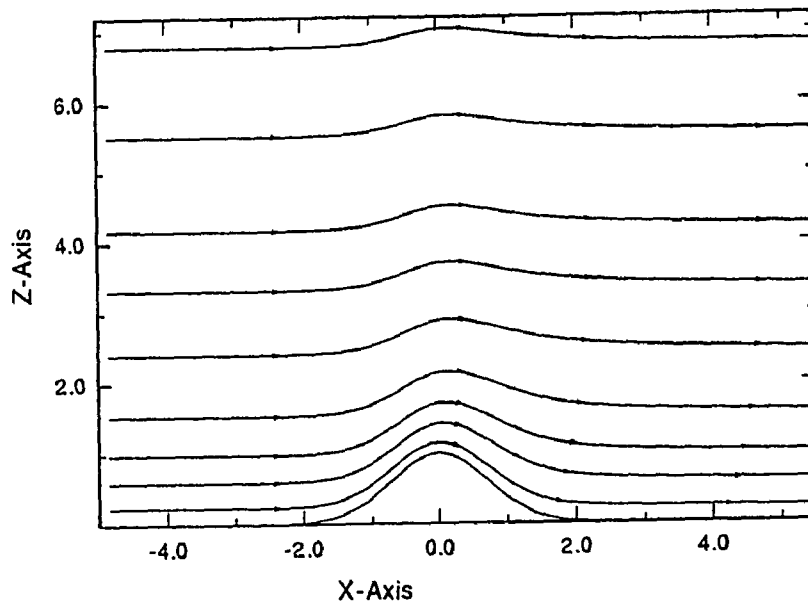
III.2 Flow Structure Over the Hump

Since we are interested in a general study of the problem, the choice of the hump shape is not crucial. To be consistent with prior works, we use the same hump shape as given by equation (3-1). In order to get a better understanding of the steady-state flow, we study three different hump sizes, $h=1.0, 2.8$ and 4.5 , in detail. In these steady-flow computations the following values were used for the parameters except where noted. In the streamwise direction $\Delta X = 0.10$, $-5.0 < X < 10.0$; along the lateral direction we have $\Delta Y = 0.10$, $0 < Y < 5.0$, and in the normal direction within the lower-deck region $\Delta Z = 0.10$ and $0 < Z < 9.0$. These values correspond to using 151, 50, and 90 points in the X, Y, and Z directions, respectively. In the upper-deck region the same values were used for ΔX and ΔY while $\Delta Z_u = 0.10$ and $0 < Z_u < 6.0$, corresponding to the same number of grid points in X and Y directions as in the lower-deck problem with 60 points used in the Z direction.

For the first two hump heights, $h=1.0$ and $h=2.8$, the boundary layer is displaced over the hump without separation. However, for $h > 4$, a small separation region is formed behind the hump. This is clearly evident in the flow streamlines at the plane of symmetry, $Y=0$, presented in figures 7a, 7b, and 7c.

Another way of looking at the three-dimensional separation is by analyzing the surface streamlines (see Lighthill [29]). Surface streamlines or skin friction lines are the lines on the surface of the body, everywhere tangent to the skin friction vector, $(dU/dZ, dV/dZ)$. Surface streamlines cannot cross each other, except at certain points, such as stagnation points, where the length of the skin friction vector vanishes and its direction is, therefore, indeterminate. There are basically two types of singular points: a **nodal point**, through which infinitely many skin friction lines either pass with the same slope or may spiral in case of a vortical node; a **saddle point**, where only two distinct skin friction lines pass through it. These skin friction patterns can be visualized experimentally by using oil streak lines on the surface.

Figures 8a and 8b show the surface streamlines for the humps with height $h=1.0$ and $h=2.8$, respectively. The skin friction lines never cross. Therefore, the flow is always attached. But for the hump with $h=4.5$, two singular points are present (see figures 8c and 8d). A nodal point of separation at $X=0.7$ and a saddle point of attachment at $X=2.25$ can be observed in figure 8d. The flow seems to separate from the wall along the line of converging surface streamlines in the vicinity of the nodal point. However, all the



a) Flow streamlines at the plane of symmetry for $h=1.0$.

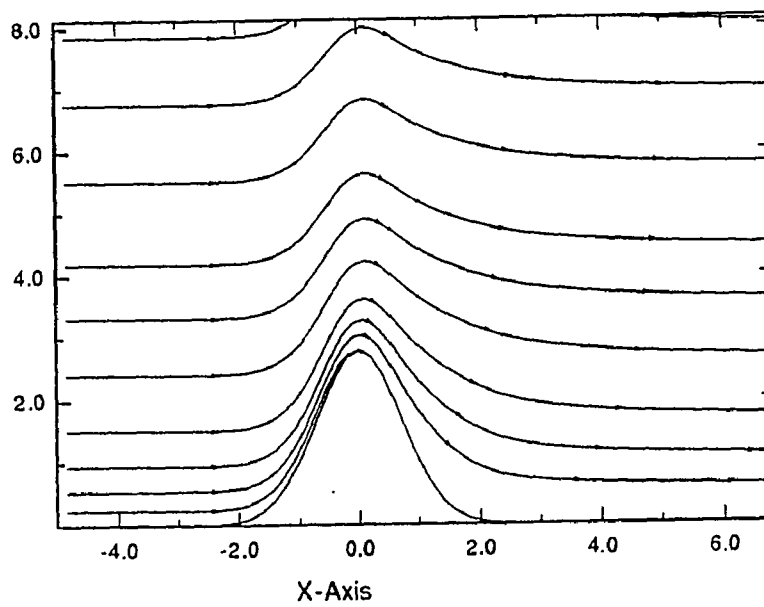
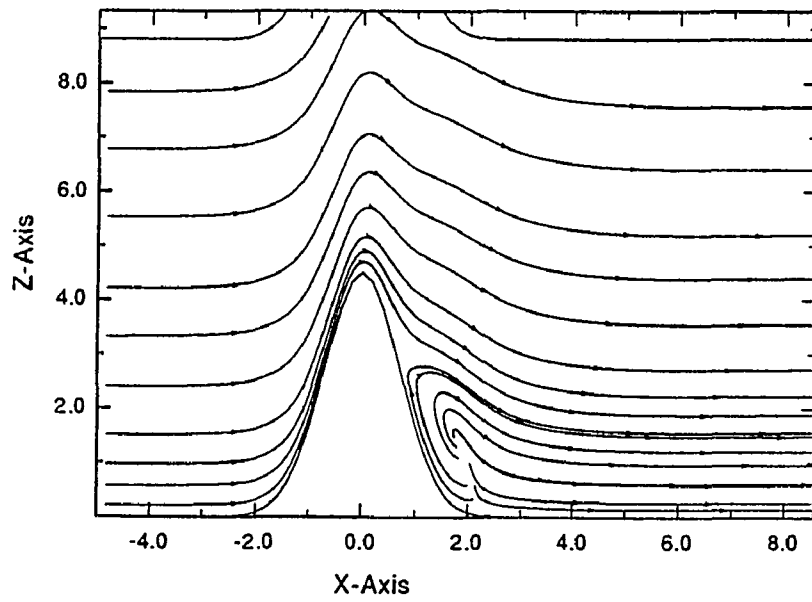


Figure 7. b) Flow streamlines at the plane of symmetry for $h=2.8$.



c) Flow streamlines at the plane of symmetry for $h=4.5$.

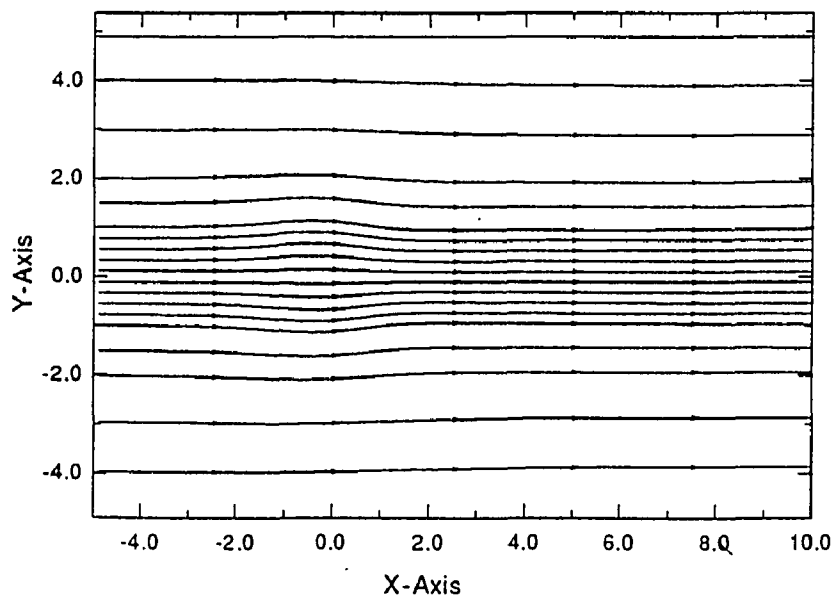


Figure 8. a) Surface streamlines for the hump with $h=1.0$.

Figure 8. continued

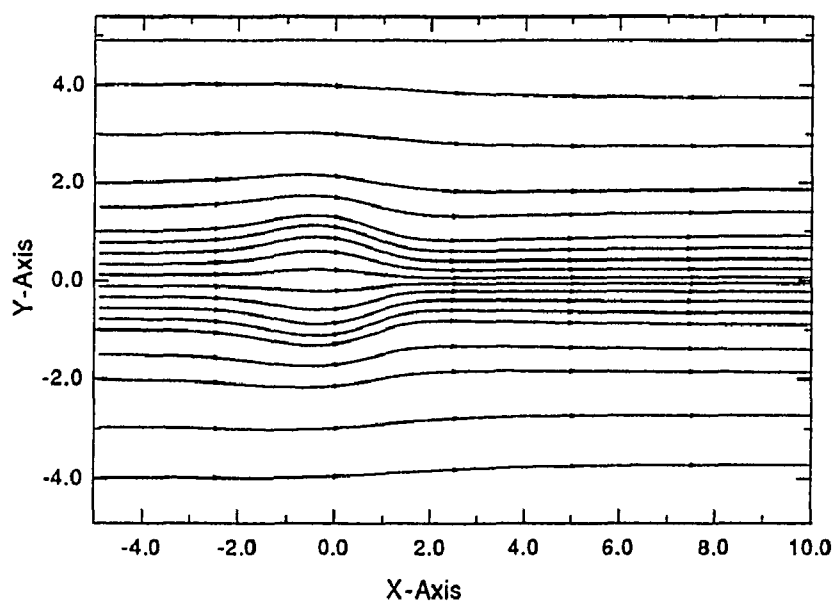
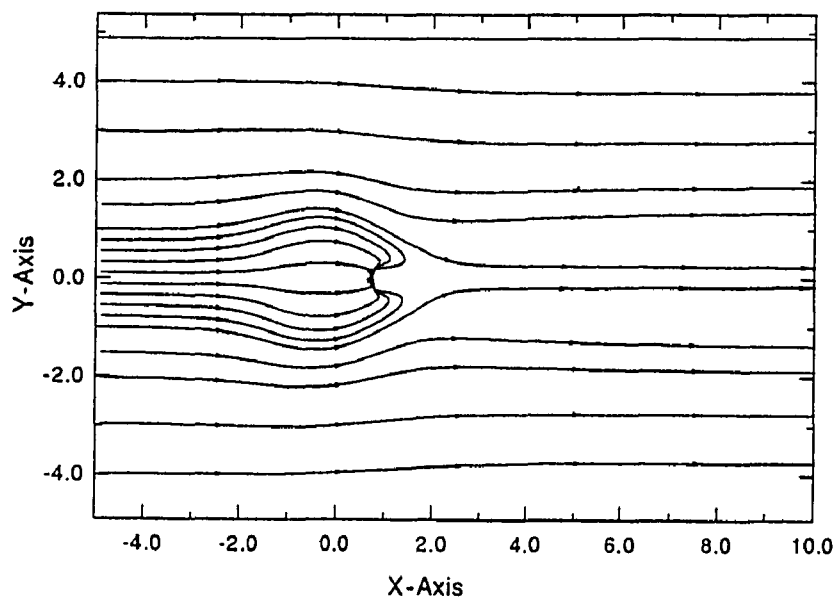
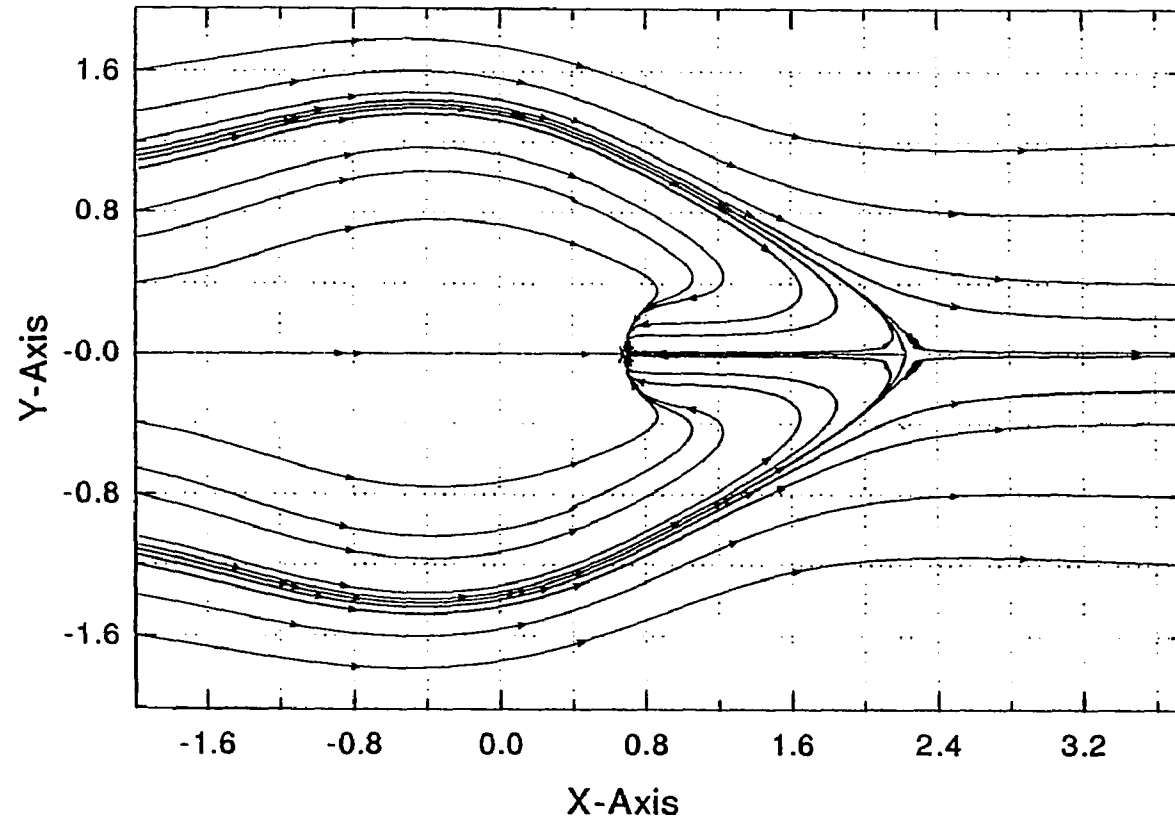
b) Surface streamlines for the hump with $h=2.8$.c) Surface streamlines for the hump with $h=4.5$.

Figure 8. continued



d) Surface streamlines for the hump with $h=4.5$ (enlarged) .

surface points are accessible by surface flow from upstream. This skin friction line pattern for the hump is similar to the one reported by Duck and Burggraf [28].

Figures 9a, 9b, and 9c present the boundary-layer pressure contours for all three humps. As it can be seen from these figures, the flow is first slowed ahead of the hump giving rise to the pressure peak there, afterward the flow is accelerated over the hump to reach a minimum pressure point at the tip of the hump. Subsequently, the flow is rapidly decelerated behind the hump. If this second deceleration is rapid enough, as in the case of $h=4.5$ (figure 9c), the flow would separate due to this unfavorable pressure gradient. It should be noted that for a higher value of the hump height, the first deceleration of the flow should bring about another separation region ahead of the hump. But this could not be pursued due to a numerical breakdown of our code.

Contour plots of the streamwise shear at the surface, $dU/dZ (X,Y,Z=0)$, are presented in figures 10a, 10b, and 10c. The flow decelerations and accelerations mentioned previously are apparent in these figures. However, in figure 10c the "corridor effect" in the wake of the hump as reported by Sykes [26] is evident. This is caused by a pair of counter-rotating vortices generated behind the hump. $A(X,Y)$, negative of the displacement thickness, is a measure of the slope of the flow over the hump. Contour plots of $A(X,Y)$ are presented in figures 11a, 11b, and 11c, respectively. They also indicate of the formation of the above vortex pair. The generation of these vortices can be associated with the wrapping of the flow field as it tries to go over and turn around the hump. This flow wrapping can be followed downstream by looking at contour plots of V - and

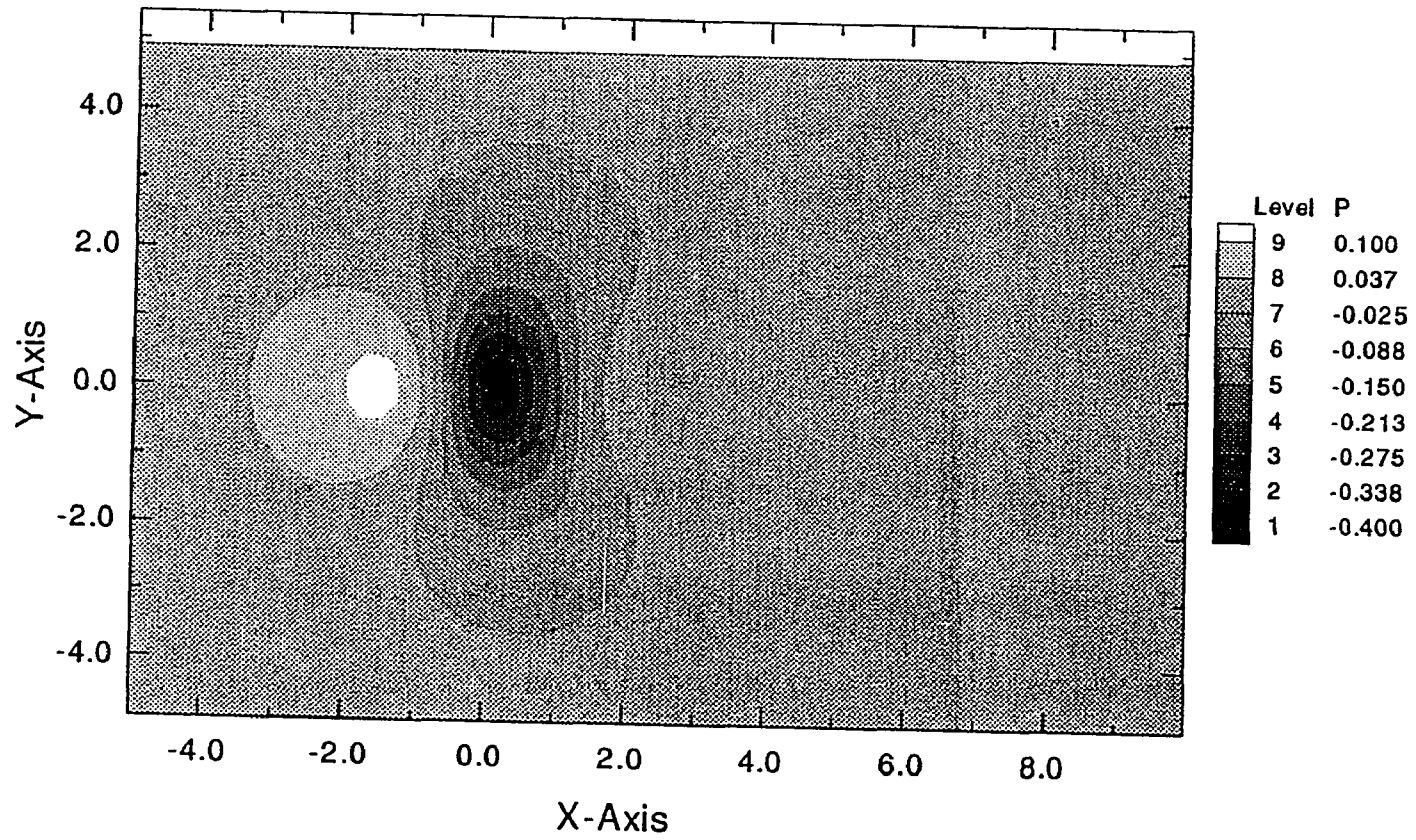
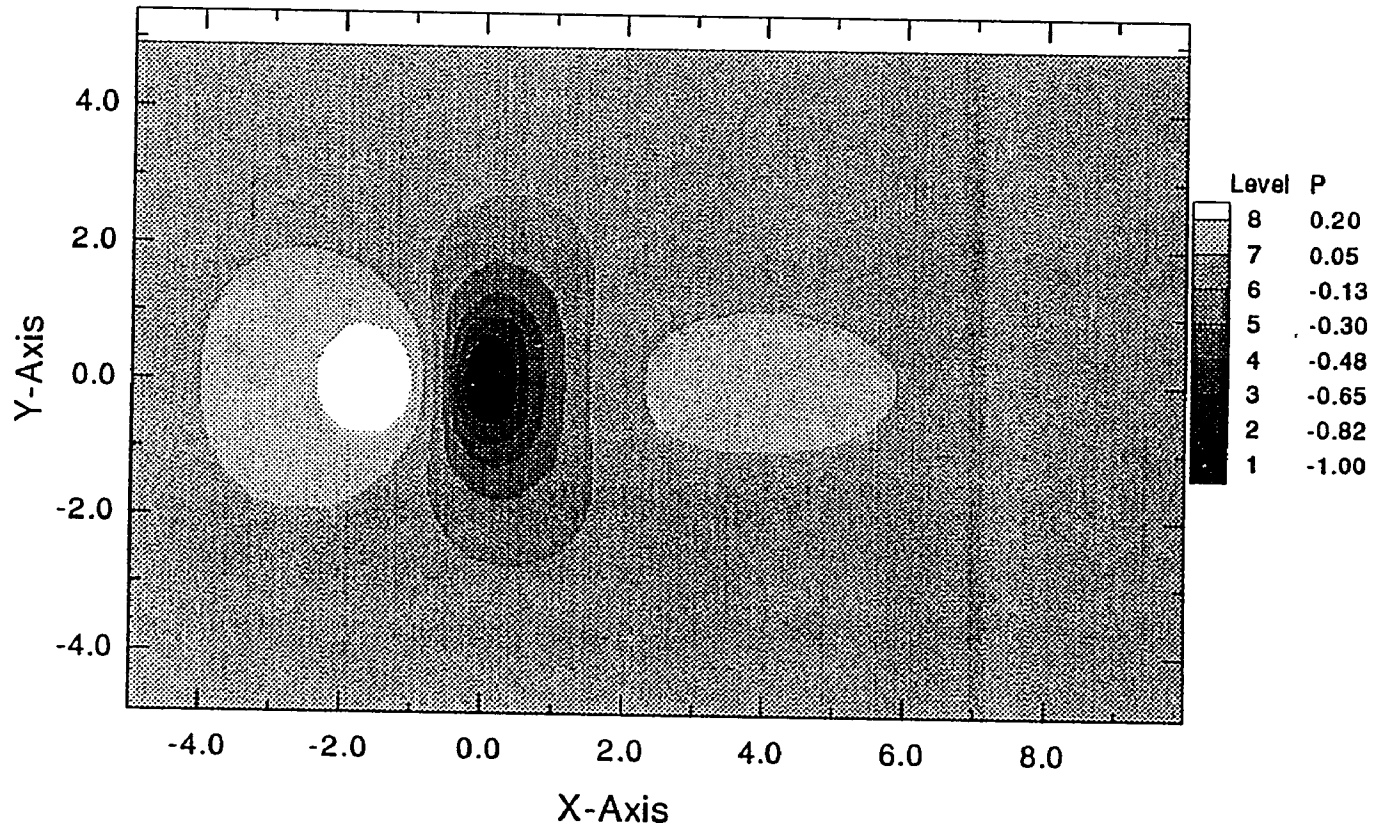


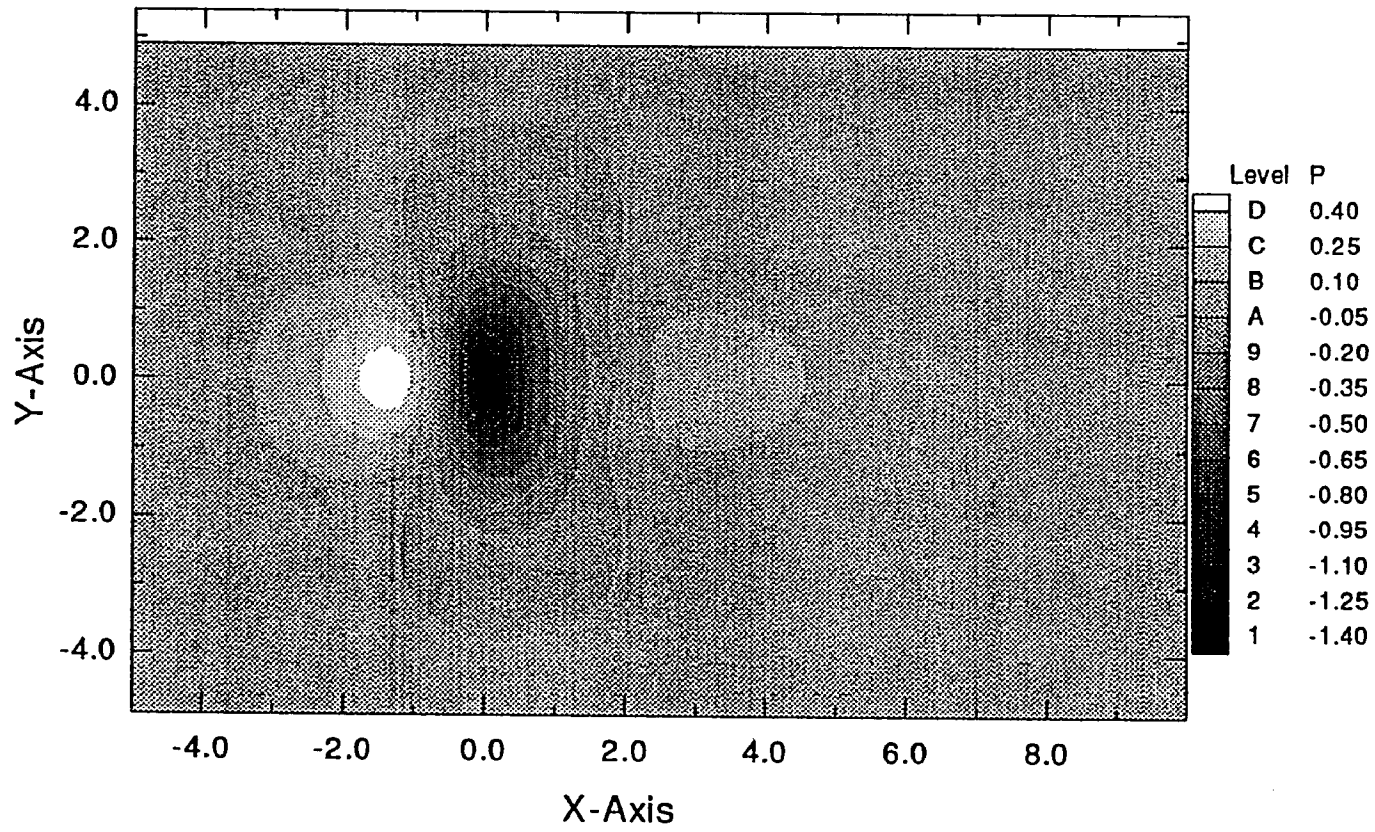
Figure 9. a) Contour plot of steady pressure for the hump with $h=1.0$.

Figure 9. continued



b) Contour plot of steady pressure for the hump with $h=2.8$.

Figure 9. continued



c) Contour plot of steady pressure for the hump with $h=4.5$.

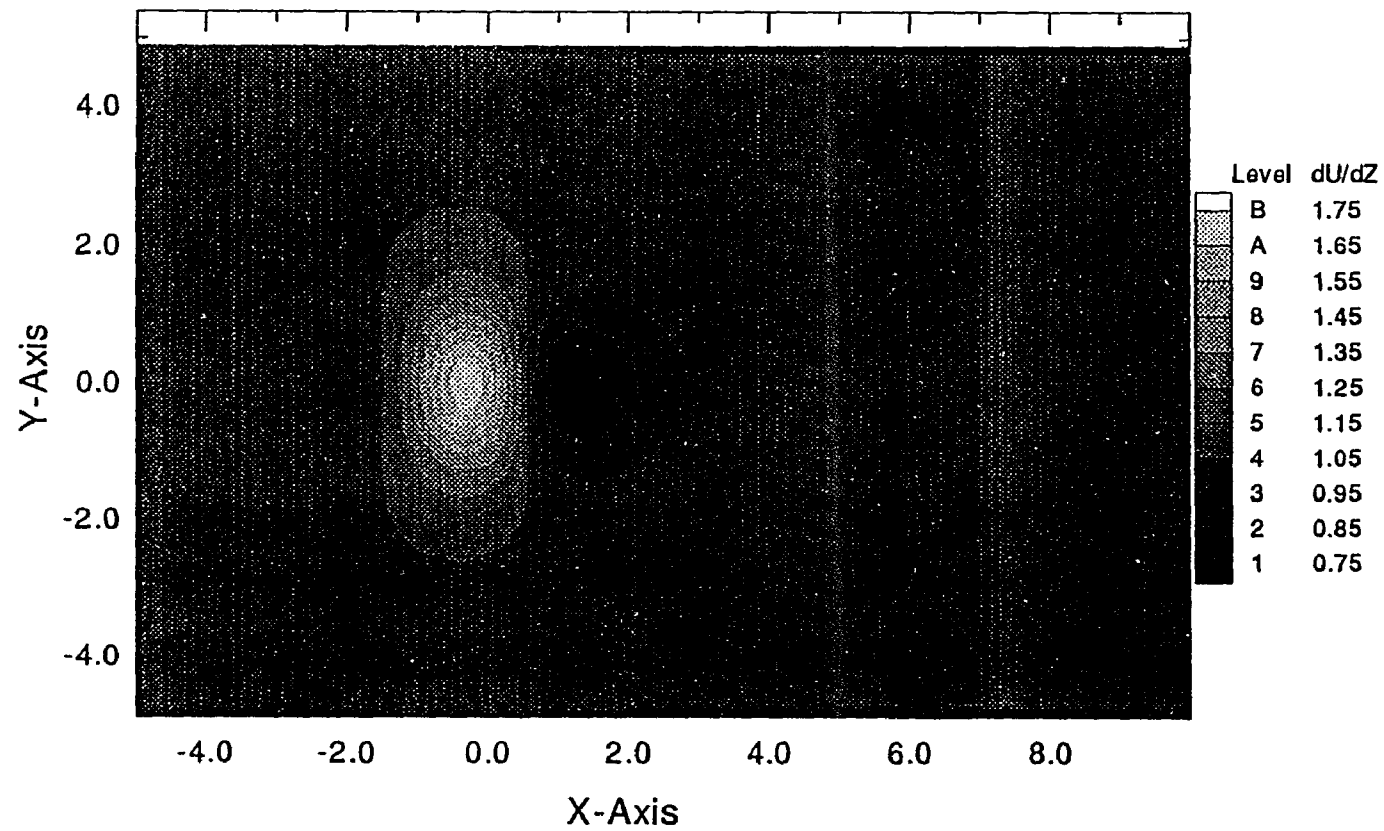
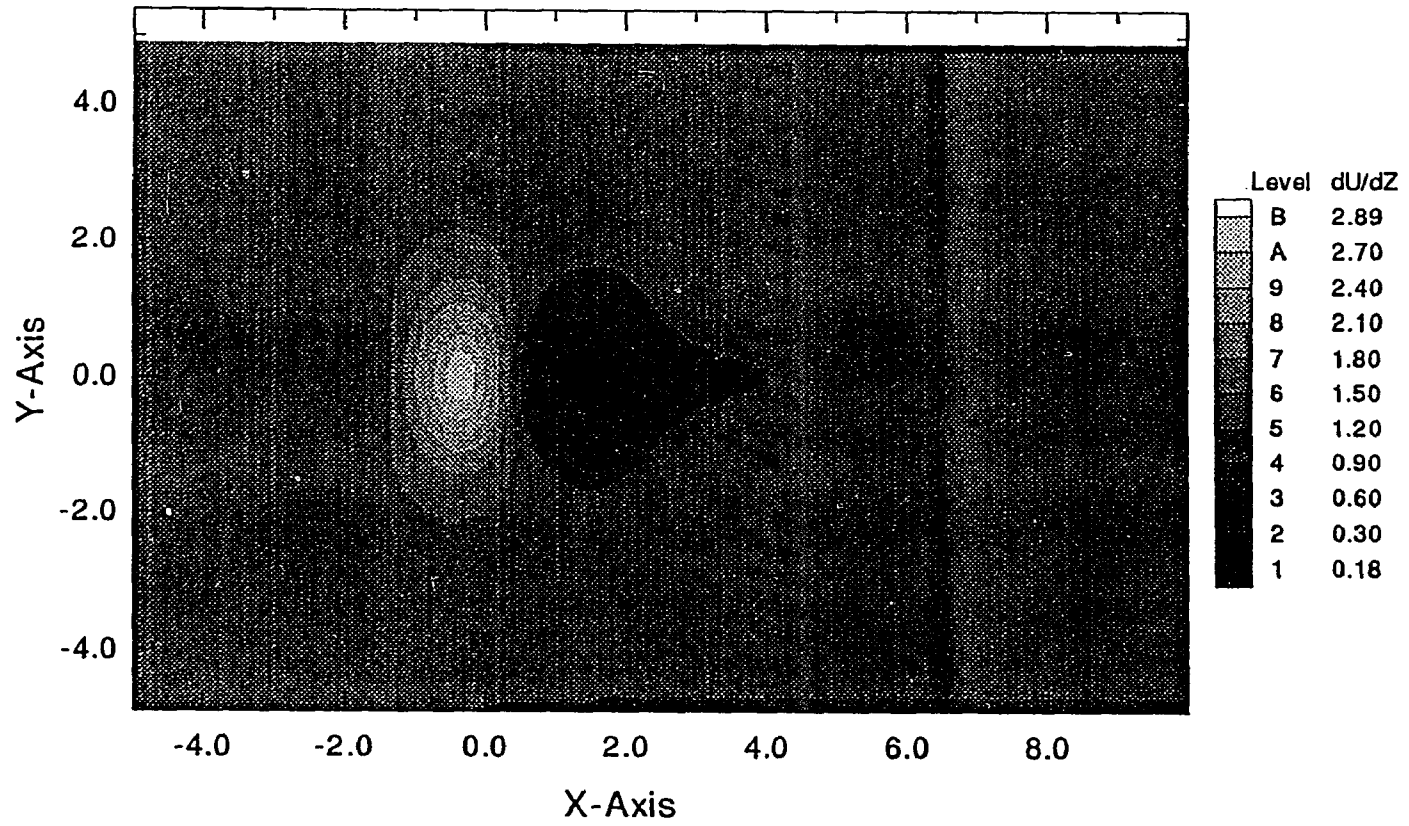


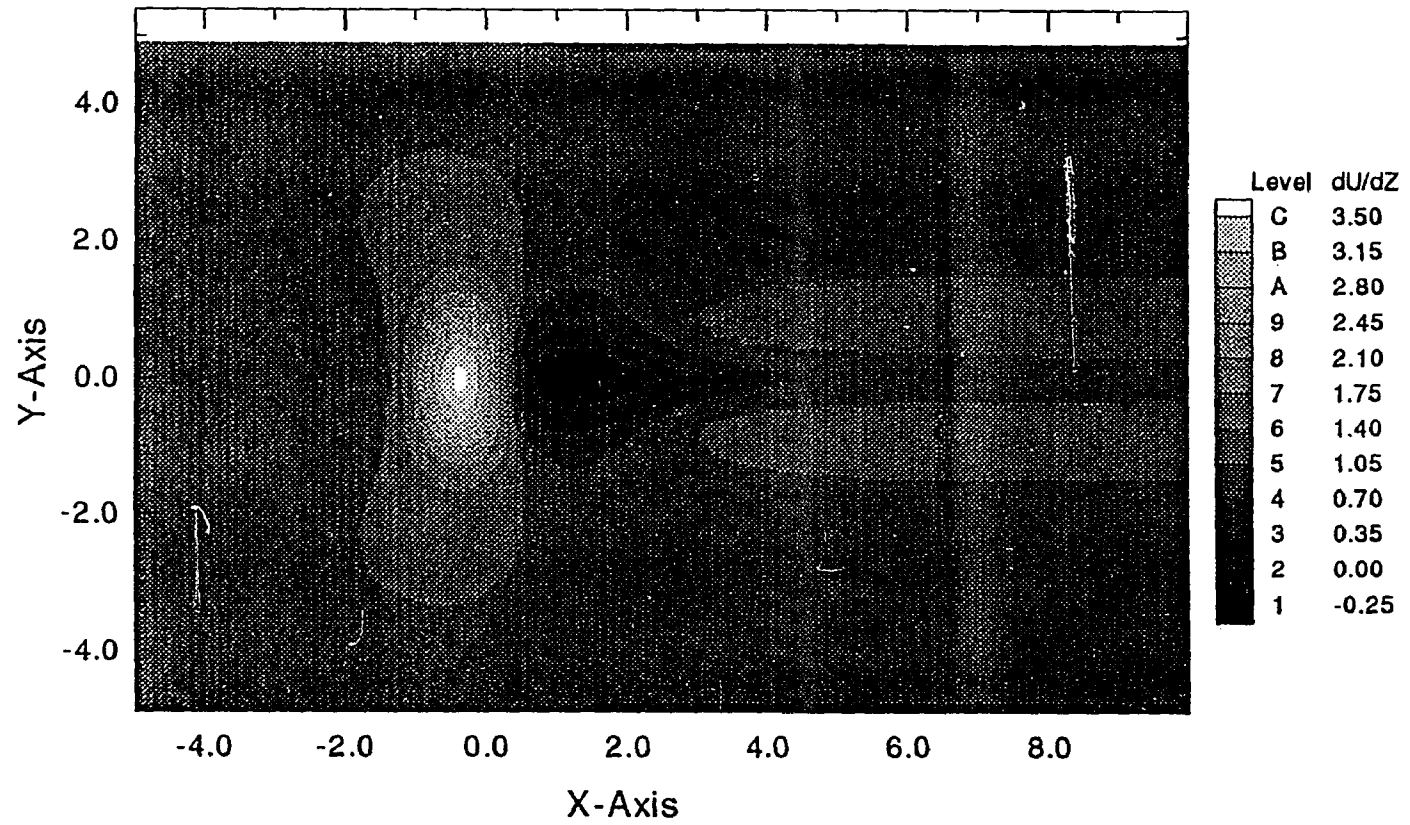
Figure 10 a) Contour plot of streamwise wall shear for the hump with $h=1.0$.

Figure 10. continued



b) Contour plot of streamwise wall shear for the hump with $h=2.8$.

Figure 10. continued



c) Contour plot of streamwise wall shear for the hump with $h=4.5$.

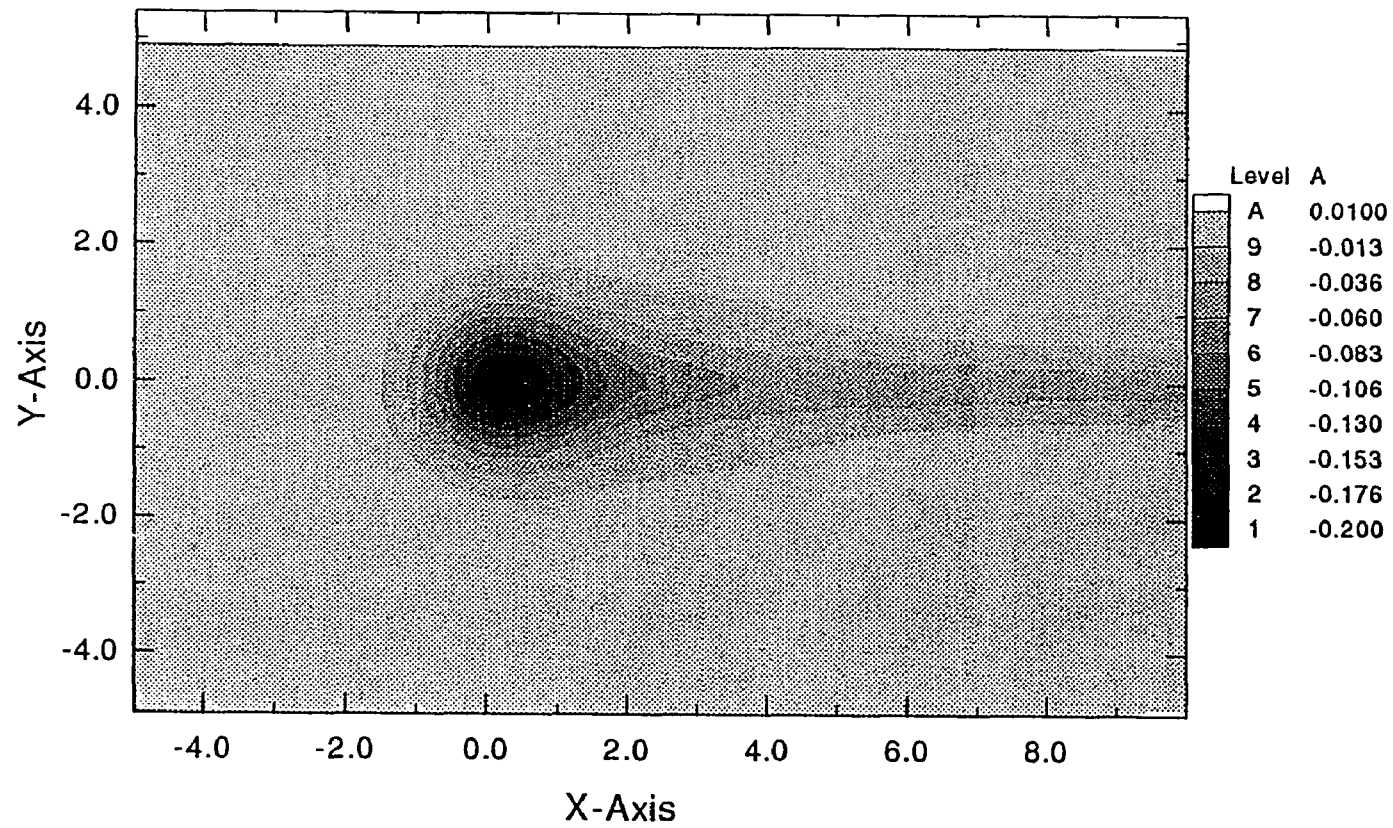
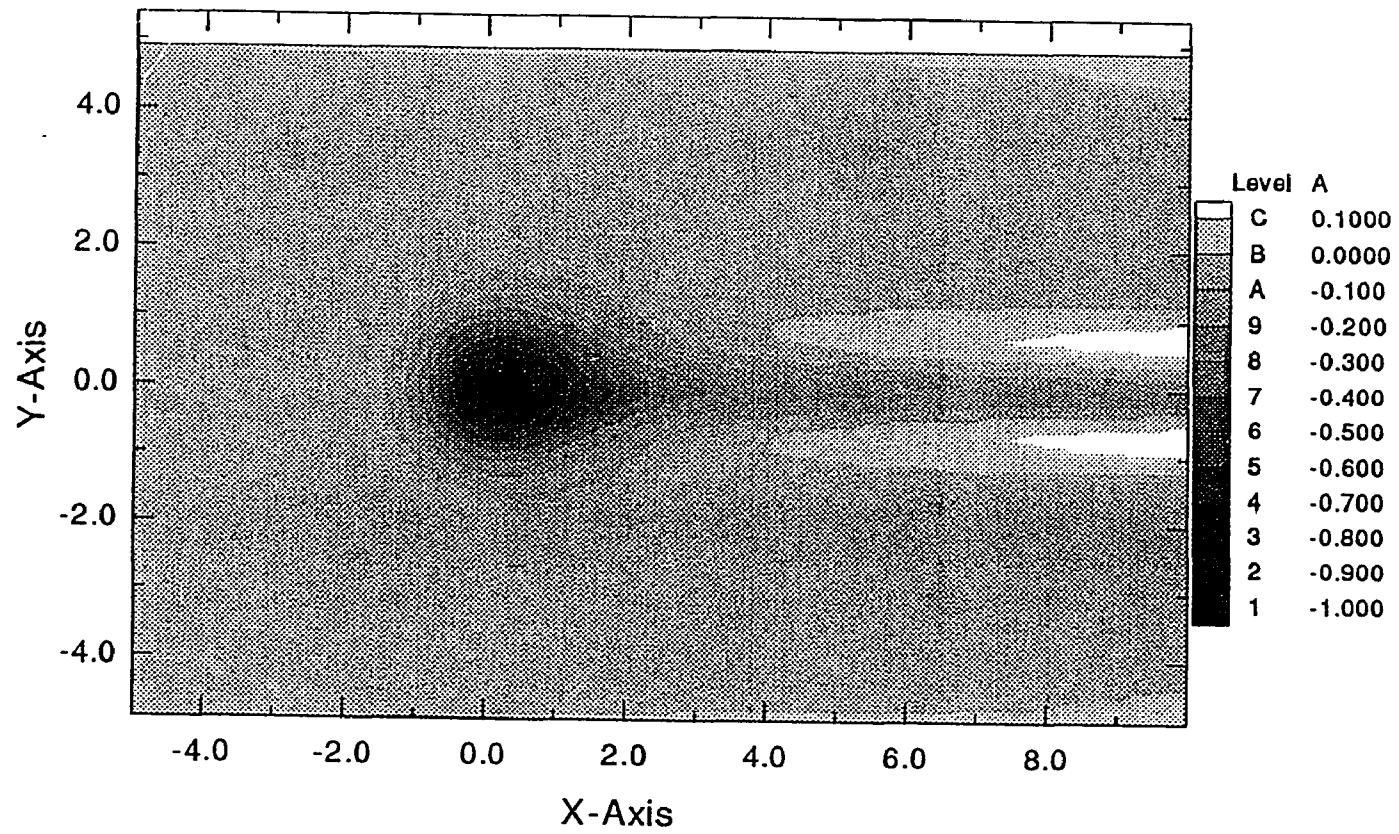


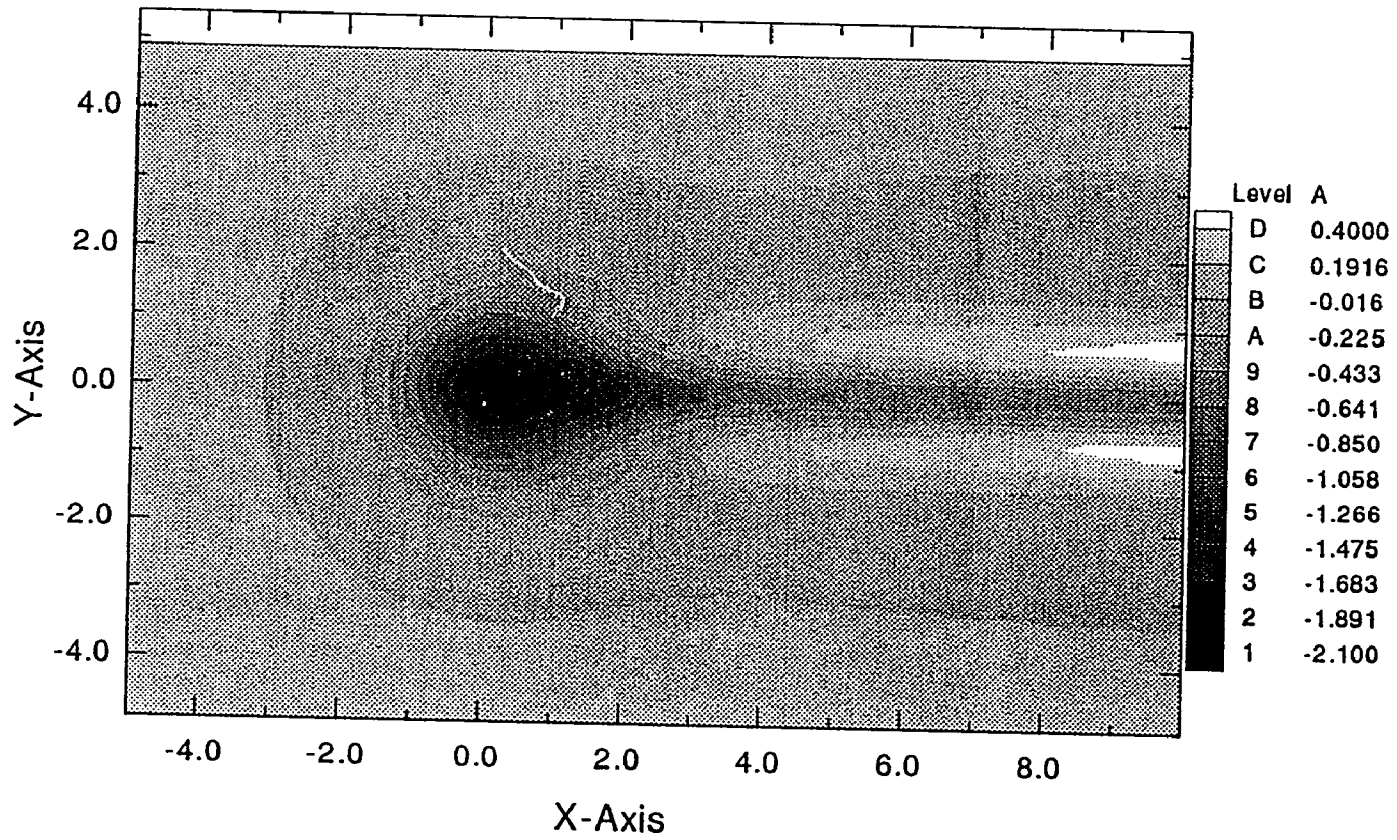
Figure 11 a) Contour plot of $A(X, Y)$ for the hump with $h=1.0$.

Figure 11. continued



b) Contour plot of $A(X, Y)$ for the hump with $h=2.8$.

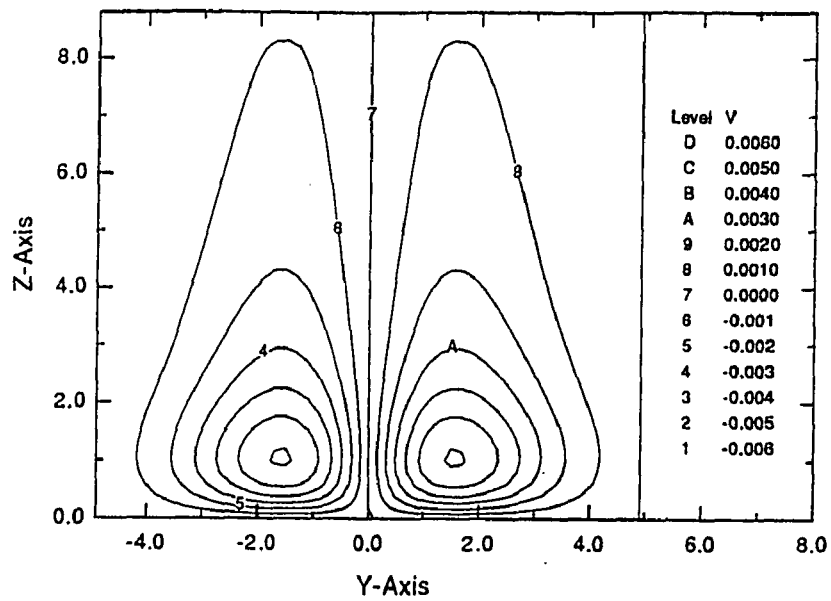
Figure 11. continued



c) Contour plot of $A(X, Y)$ for the hump with $h=4.5$.

W-velocities, in Y-Z plane cuts, at several X locations along the flow.

Here we will present V-velocity and/or W-velocity contour plots for the hump with $h=4.5$ unless otherwise stated. The smaller humps produce the same effects on the flow, however on a weaker scale. Figures 12a and 12b show the V- and W-velocity contours at $X=-4.0$. Upstream of the hump, the flow senses the hump's presence due to the pressure field induced by the hump and starts moving upwards while turning away from the hump. Figures 13a and 13b present the same results at $X=-0.5$. Here the flow has climbed the hump and is being pushed away to the side. Recalling the pressure field set up by the hump, figure 9c, near the hump surface about the $X=0$ location, there is no mechanism to counteract this pressure gradient in the Y direction. Hence near the surface fluid climbs toward the pressure minimum at the peak of the hump. Thus this mechanism sets up a fluid motion toward the hump beneath the general movement, away from the hump, swept down from upstream. This phenomenon is seen in the V- and W-velocity contours presented in figures 14a and 14b. V-velocity contours are also given for the humps with $h=1.0$ and $h=2.8$ in figures 15 and 16, respectively. Due to the slower basic flow motion in the X-direction for the smaller humps, this sublayer motion can diffuse further into the main flow away from the wall around $X=0$. This mechanism is responsible for pushing away the upstream V- and W-velocity structure, and sets up the new V- and W-velocity framework for wrapping the flow around the hump. Figures 17a and 17b present the velocity contours just downstream from the hump's peak at $X=0.5$. The new flow structure has pushed the now weakened old structure away from the hump, and fluid is being



a) V-velocity contours at $X=-4.0$ for the hump with $h=4.5$.

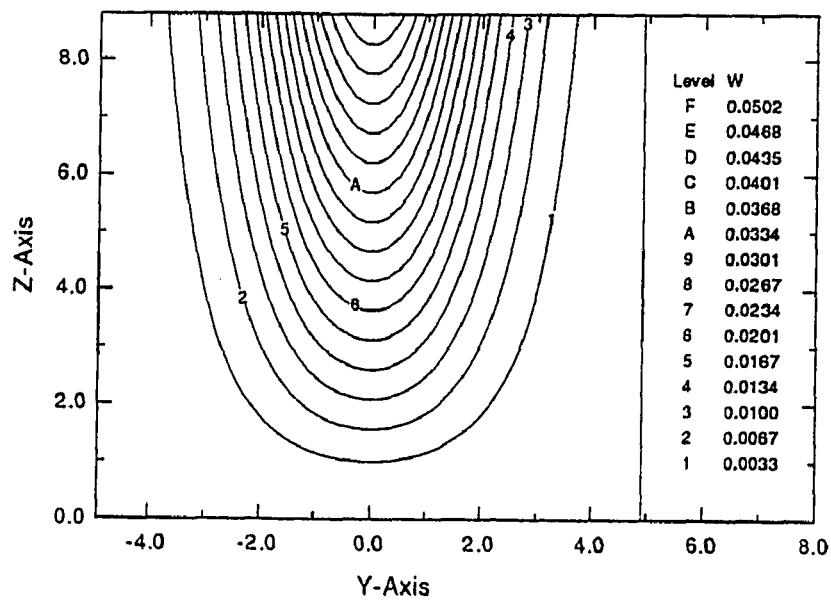
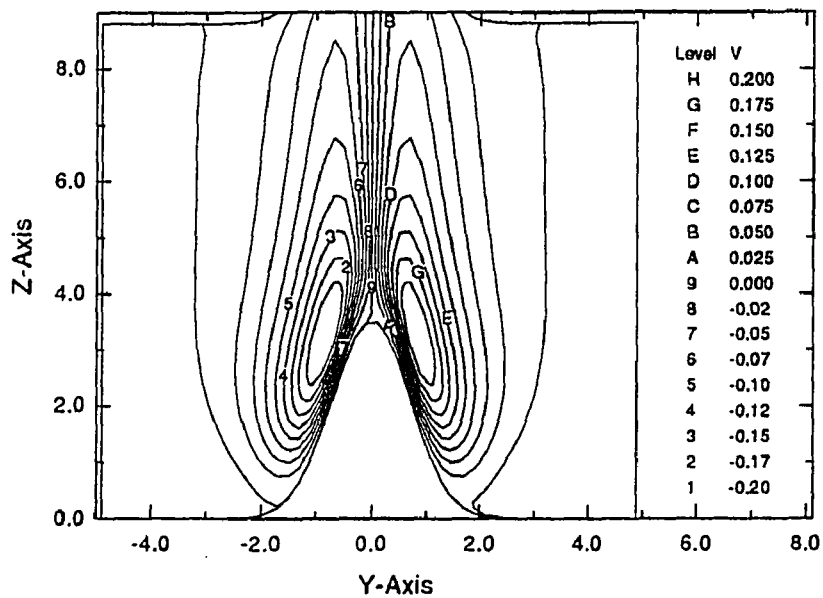


Figure 12. b) W-velocity contours at $X=-4.0$ for the hump with $h=4.5$.



a) V-velocity contours at $X=-0.5$ for the hump with $h=4.5$.

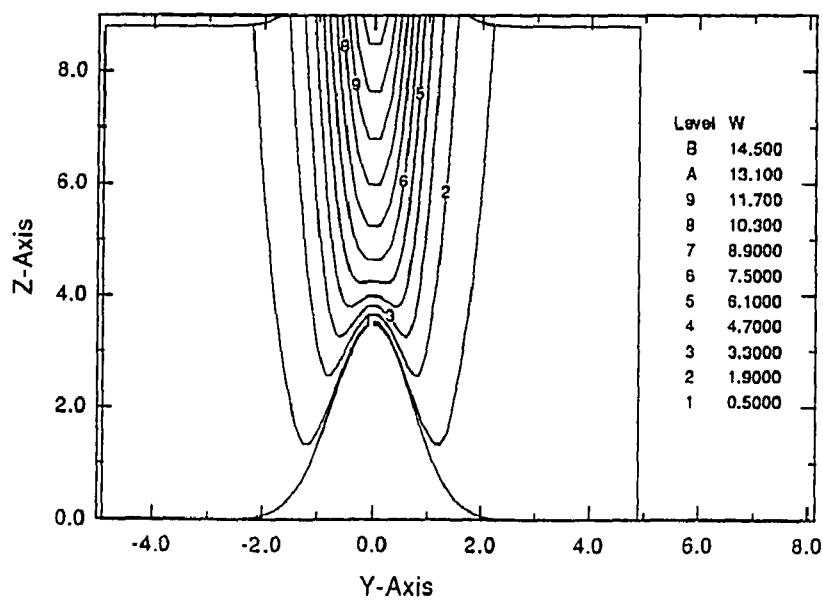
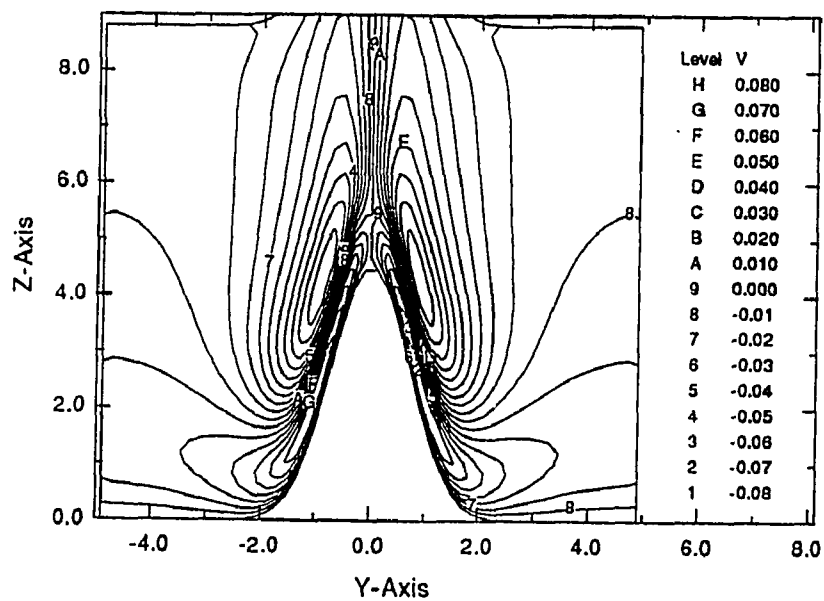


Figure 13. b) W-velocity contours at $X=-0.5$ for the hump with $h=4.5$.



a) V-velocity contours at $X=0$ for the hump with $h=4.5$.

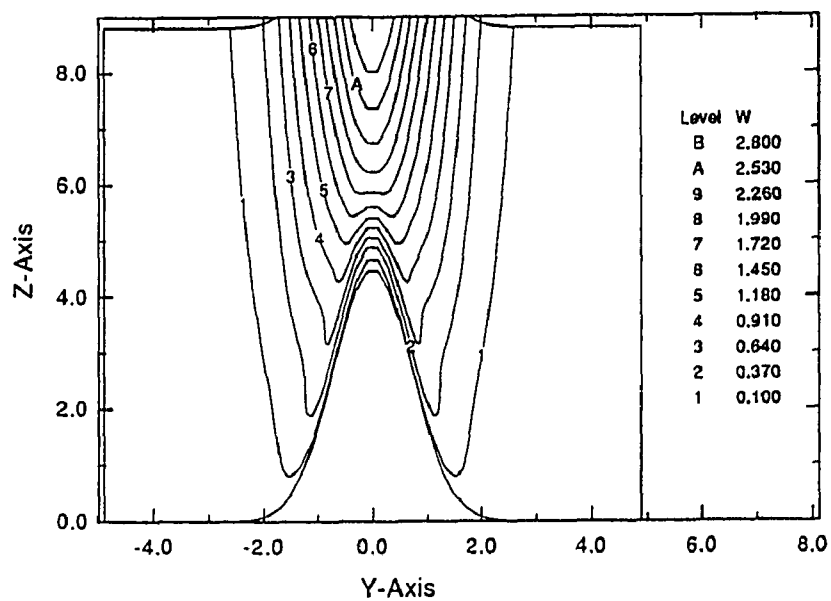


Figure 14. b) W-velocity contours at $X=0$ for the hump with $h=4.5$.

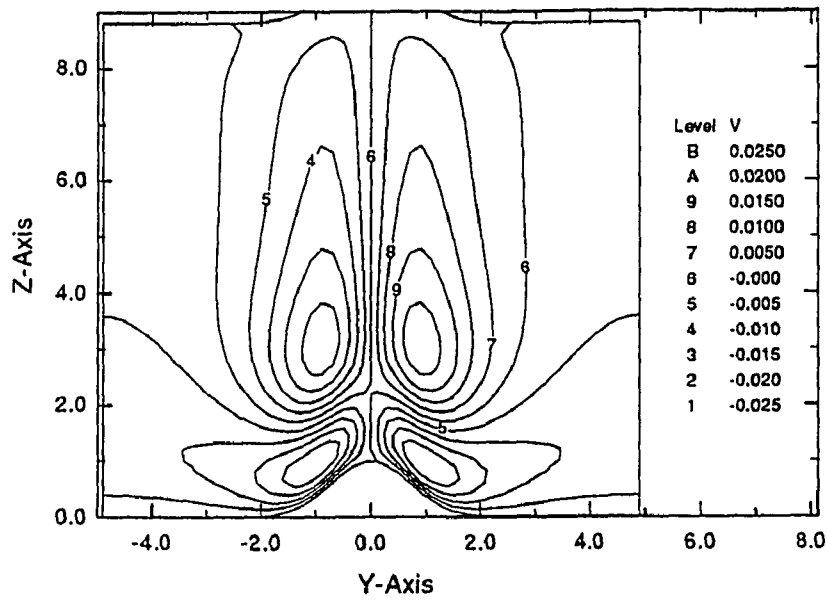


Figure 15. V-velocity contours at $X=0$ for the hump with $h=1.0$.

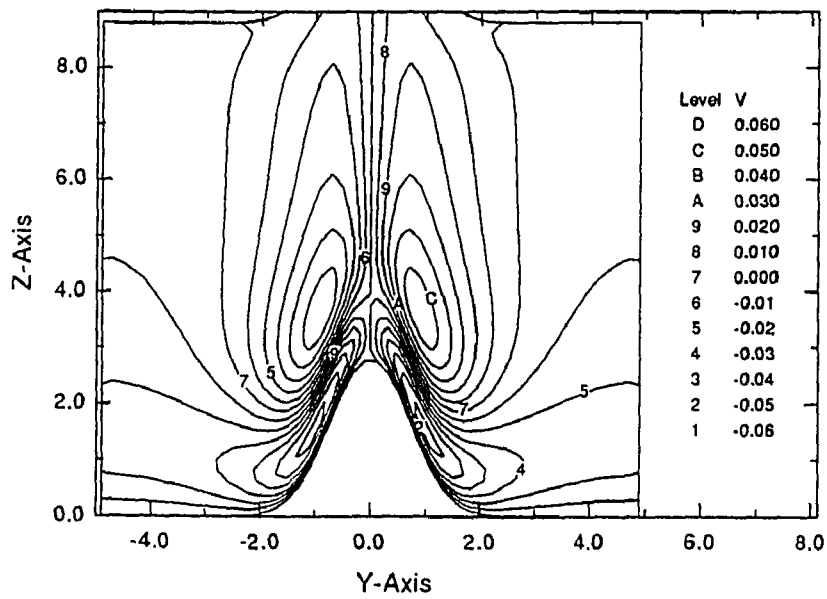
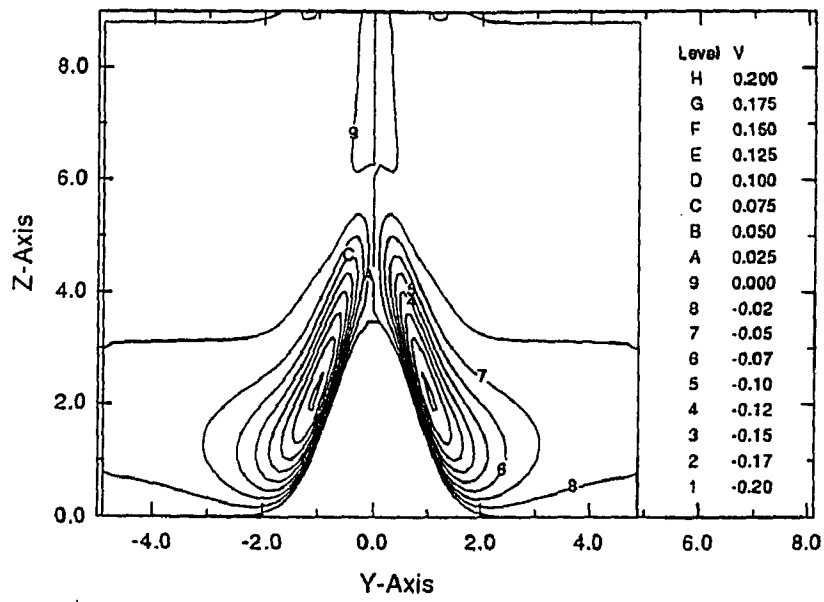


Figure 16. V-velocity contours at $X=0$ for the hump with $h=2.8$.



a) V-velocity contours at $X=0.5$ for the hump with $h=4.5$.

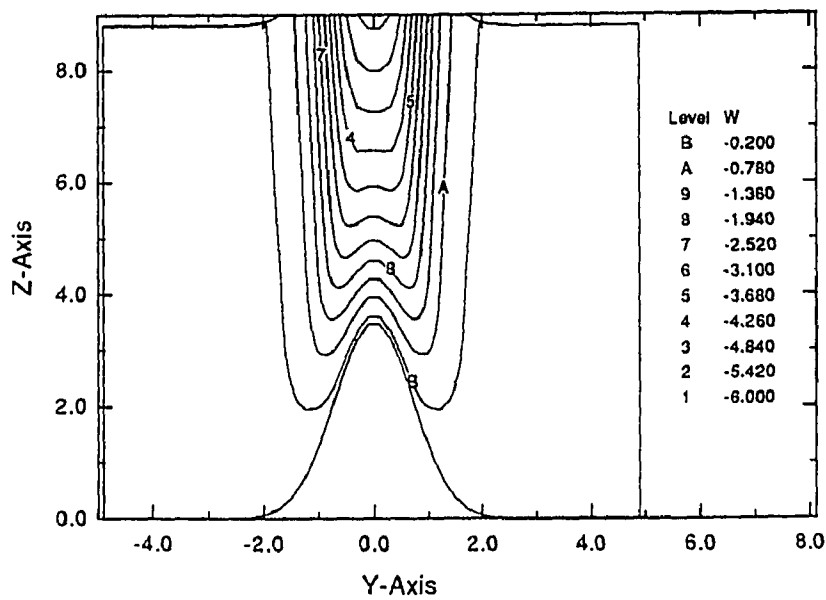
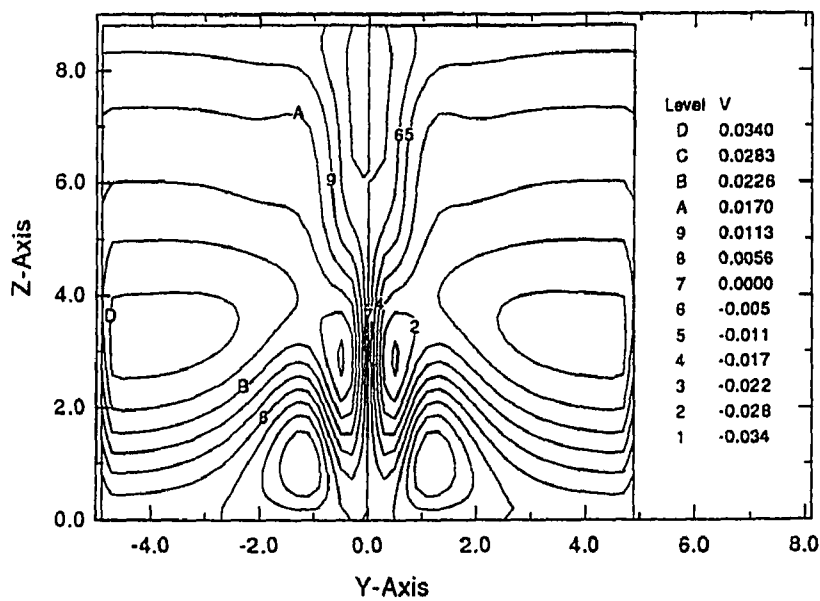


Figure 17 b) W-velocity contours at $X=0.5$ for the hump with $h=4.5$.

rushed down and towards the hump. Further downstream, the downward flow existing near the line of symmetry will also weaken, and its interaction with the weak upward motion away from the center, $Y=0$, sets up a pair of counter-rotating vortices. Existence of this vortex structure is evident in figures 18a and 18b, giving V- and W-velocity contours at $X=5.0$. The same mechanism exists for smaller humps. However, it is much weaker and the vortical structure may diffuse before it can become obvious. Figures 19 and 20 present the V-velocity contours for the hump with $h=1.0$ and $h=2.8$ at $X=5.0$ respectively. These figures also show the possible existence of a very weak vortical structure.

III.3 Steady Flow Conclusions

Results of this chapter may be summarized in one graph. Figure 21 represents the streamwise wall shear along the line of symmetry for all three humps considered. As the hump's height is increased, a tendency for flow separation in the regions of adverse pressure gradient, both ahead of and behind the hump, becomes stronger, and it will lead to separation for sufficiently large h . The nodal point of separation at $X=0.7$ and a saddle point of attachment at $X=2.25$, as observed in figure 8d, correspond to the points where the wall shear crosses the zero axis in figure 21. A pair of counter-rotating vortices in the wake of the hump is set up by the hump's presence. The mechanism to set up this vortex pair is general, however, it would become dominant for larger humps only.



a) V-velocity contours at $X=5.0$ for the hump with $h=4.5$.

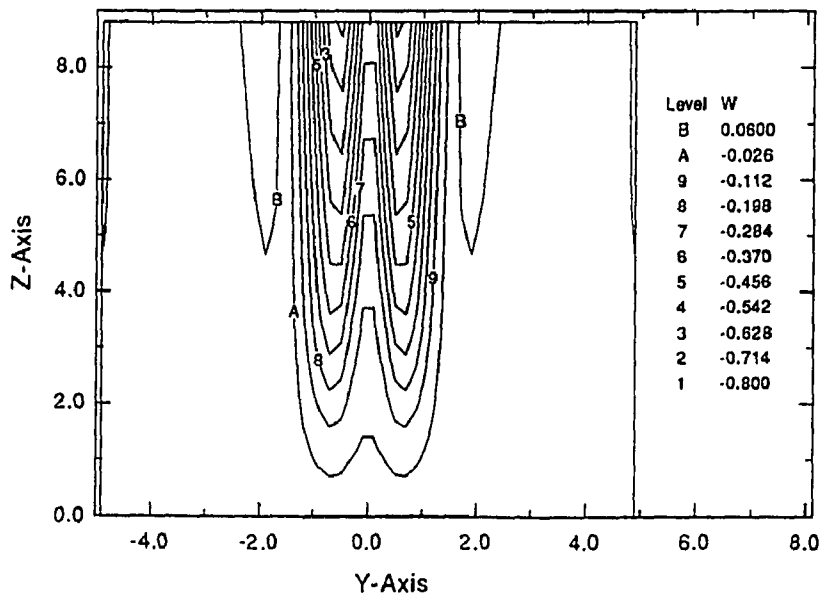


Figure 18. b) W-velocity contours at $X=5.0$ for the hump with $h=4.5$.

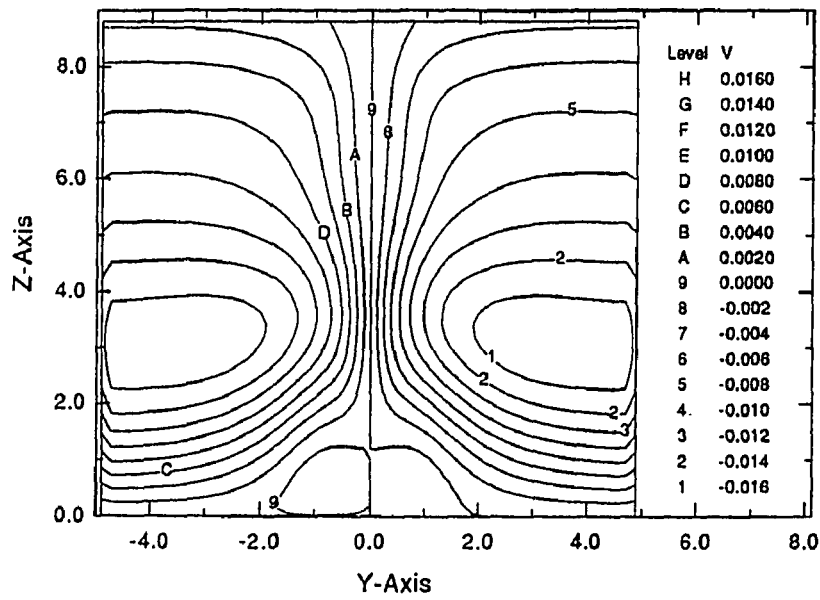


Figure 19. V-velocity contours at $X=5.0$ for the hump with $h=1.0$.

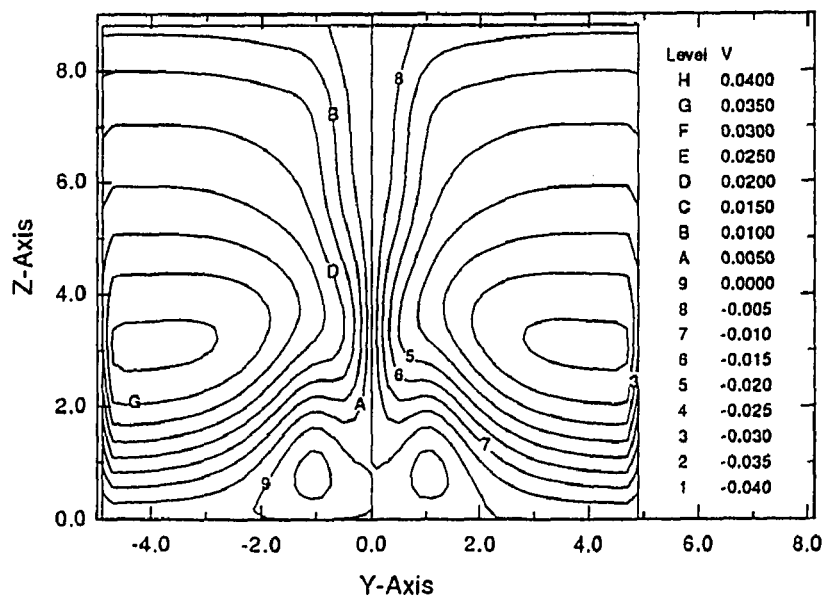


Figure 20. V-velocity contours at $X=5.0$ for the hump with $h=2.8$.

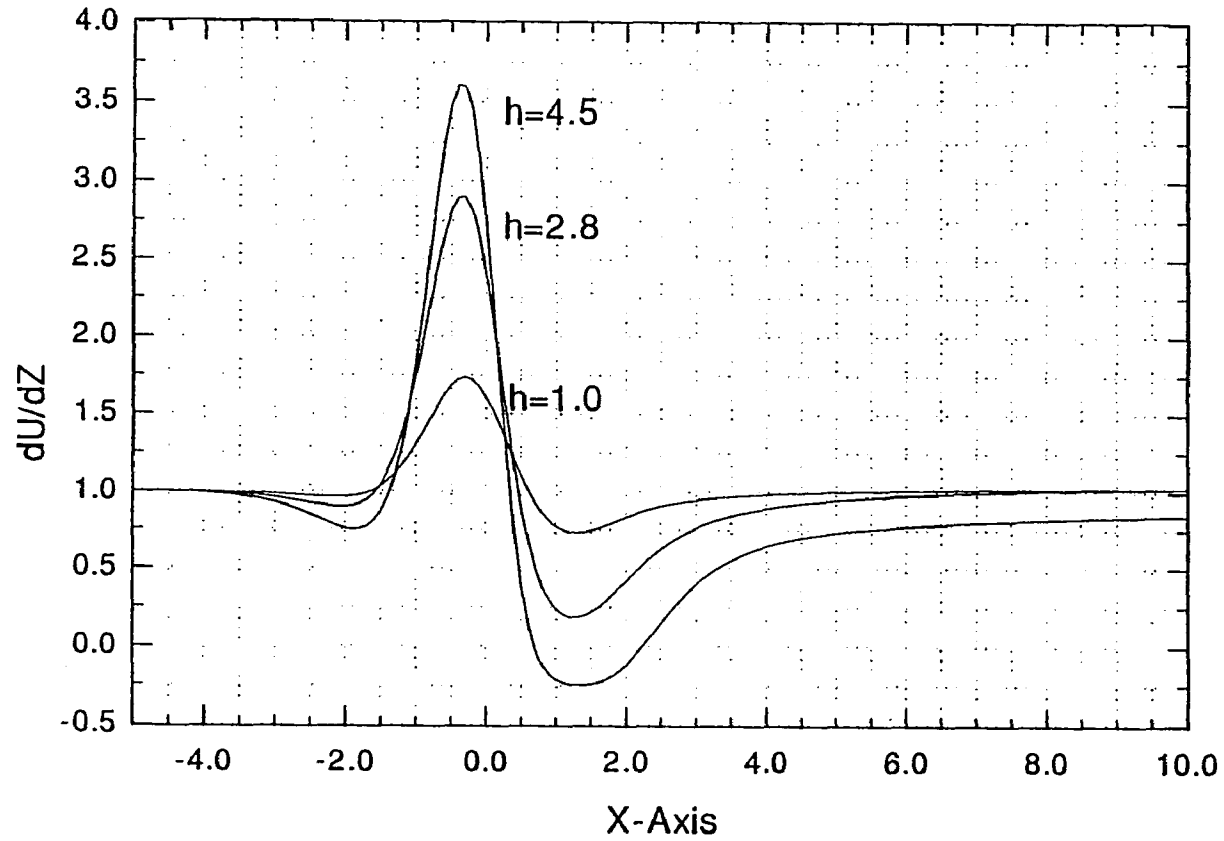


Figure 21. Streamwise wall shear along the line of symmetry, $Y=0$, for the steady flow over the humps with $h=1.0, 2.8$, & 4.5 .

Evolution of this vortical structure can be seen by following patterns of cross-flow streamlines downstream in the wake of the hump. Figures 22a thru 22g represent these patterns at $X=2.5$, 3.0, 3.5, 4.0, 5.0, and 10.0 respectively. At $X=2.5$ (figure 22a) cross-flow streamlines are pushed towards the wall and swept downstream. About $X=3.0$ a pair of counter-rotating vortices forms near the wall. As it moves downstream it lifts up away from the wall and slightly moves towards the center. The relative importance of this vortex pair in the cross flow increases significantly as the downward motion of fluid near the center decays. Downstream of the hump, the vortex system sets up a vortical motion by bringing fluid towards the wall in the center and moving it away from the wall along a line on the side of the hump. The above vortex pair has the same rotational direction as the "horseshoe vortex" observed experimentally (see figure 22h). It is also useful to compare the experimental flow-patterns of figure 22h with the displacement thickness contours shown in figure 11c .

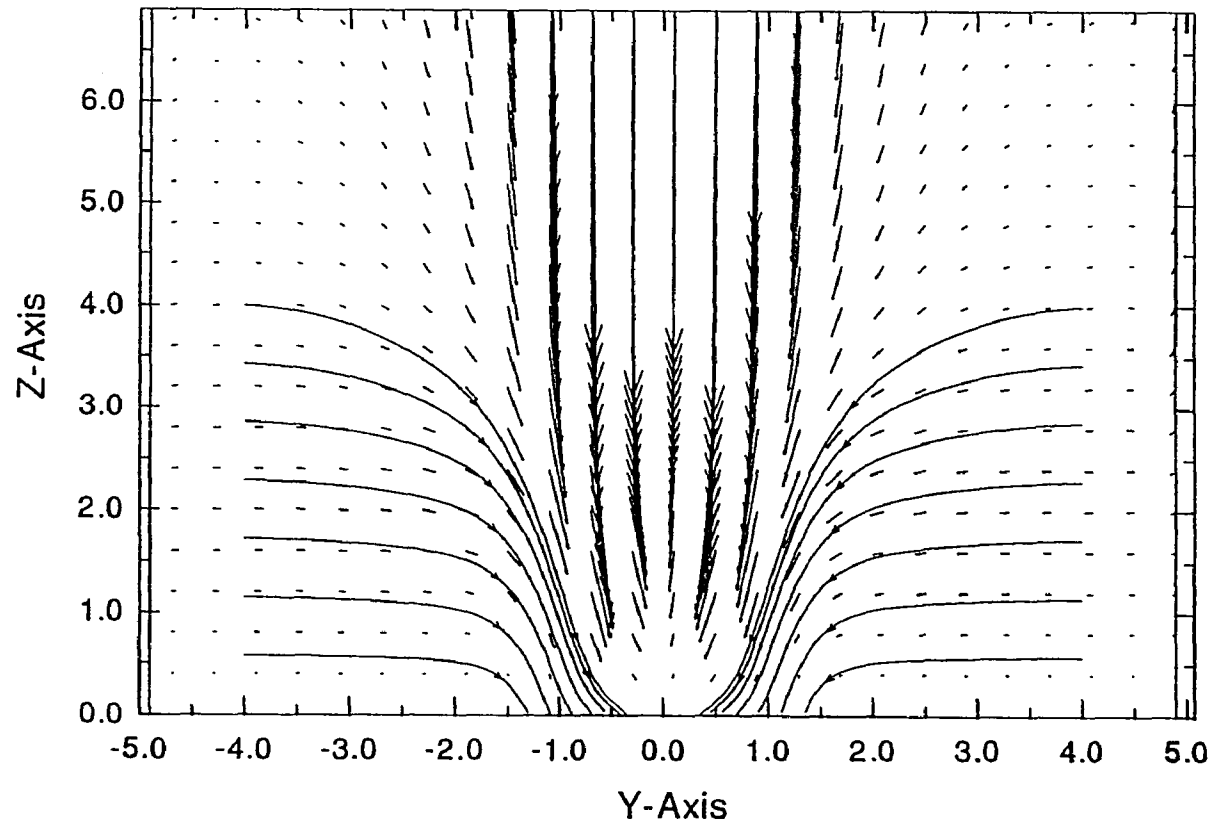
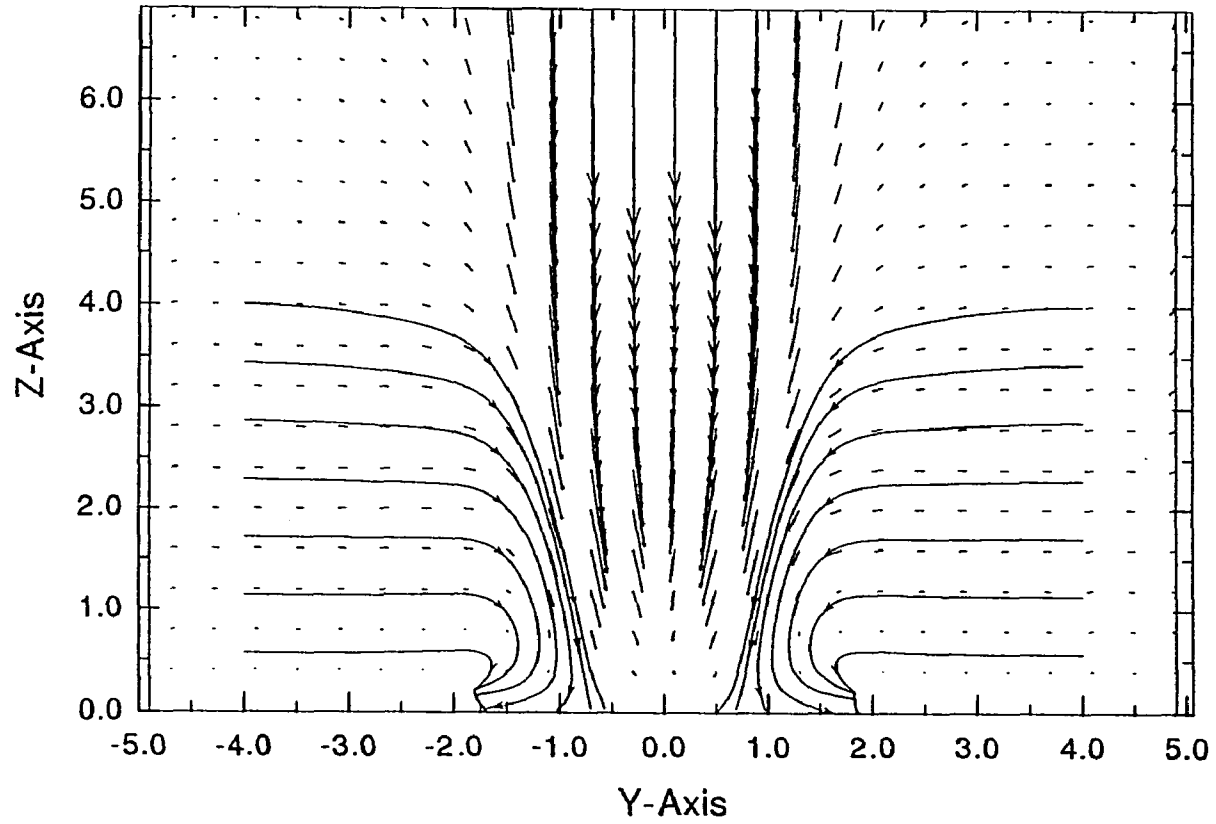


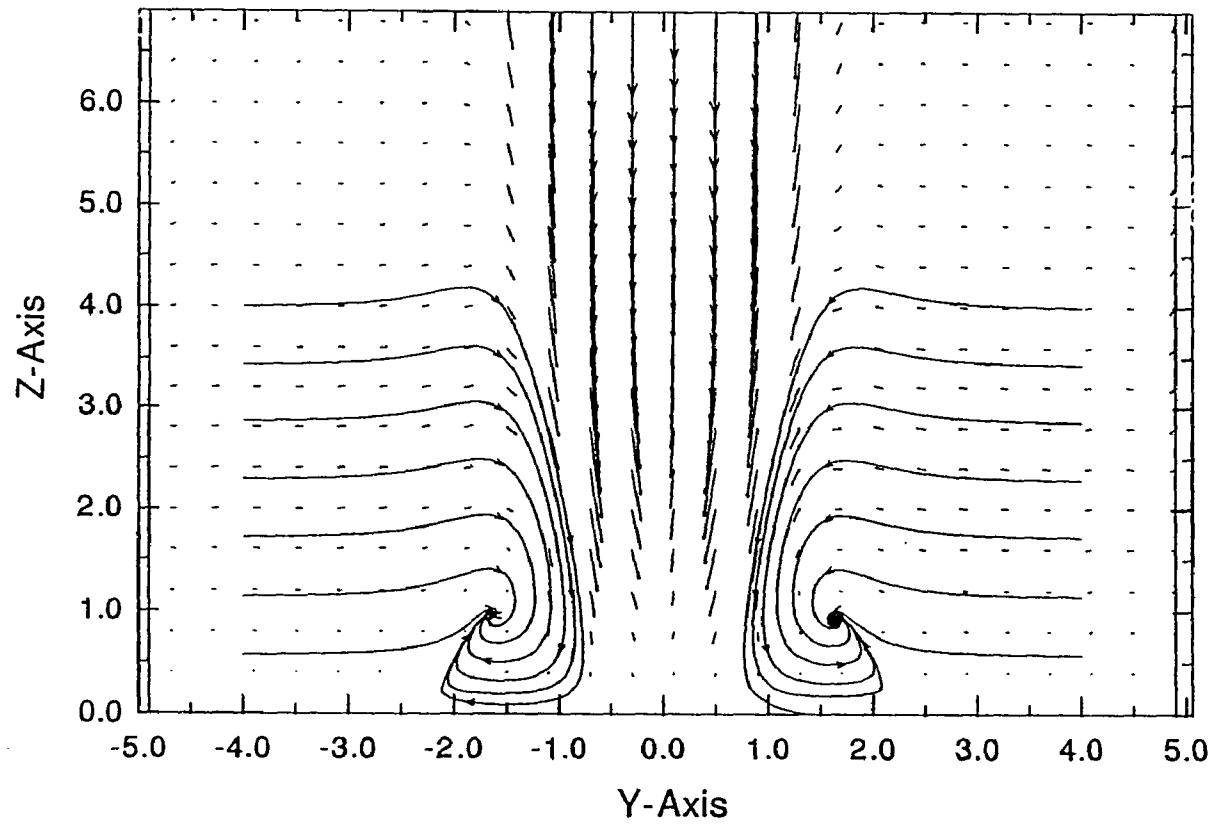
Figure 22. a) Cross-flow streamlines pattern at $X=2.5$ ($h=4.5$).

Figure 22. continued



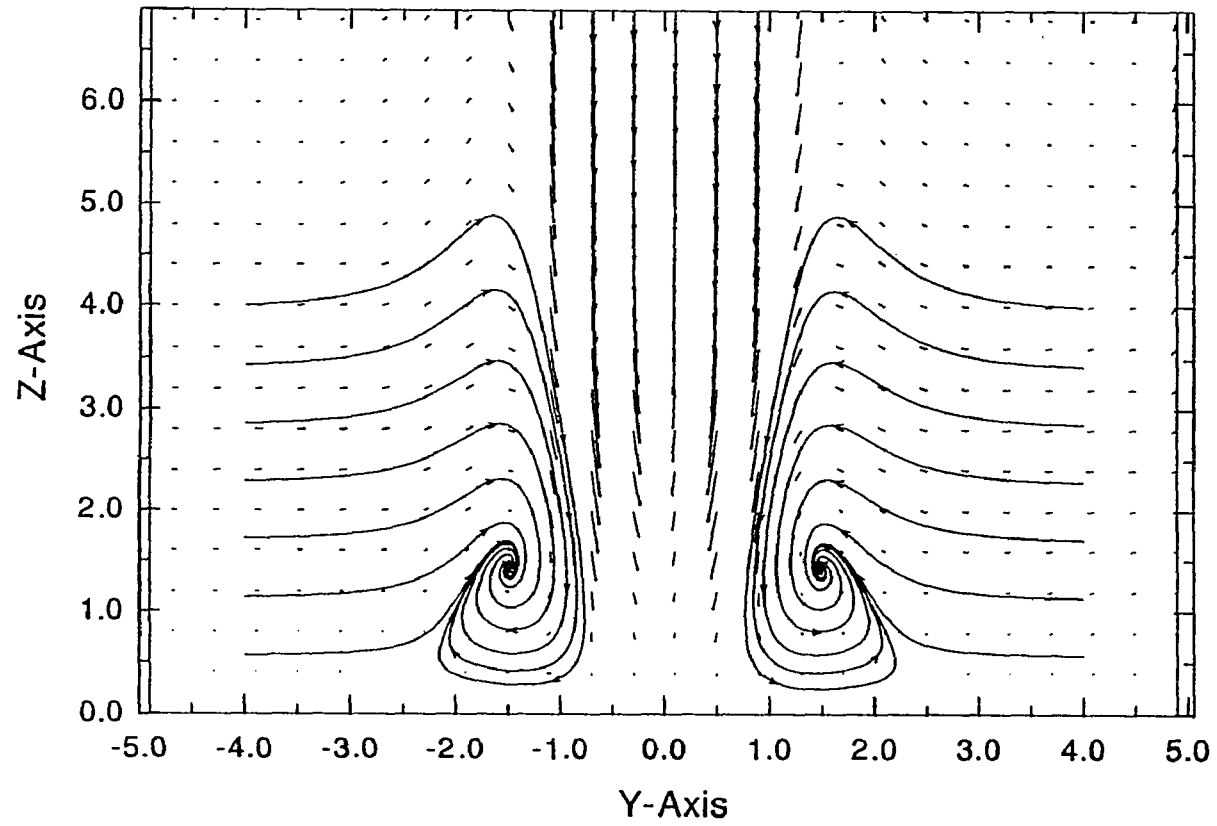
b) Cross-flow streamlines pattern at $X=3.0$ ($h=4.5$) .

Figure 22. continued



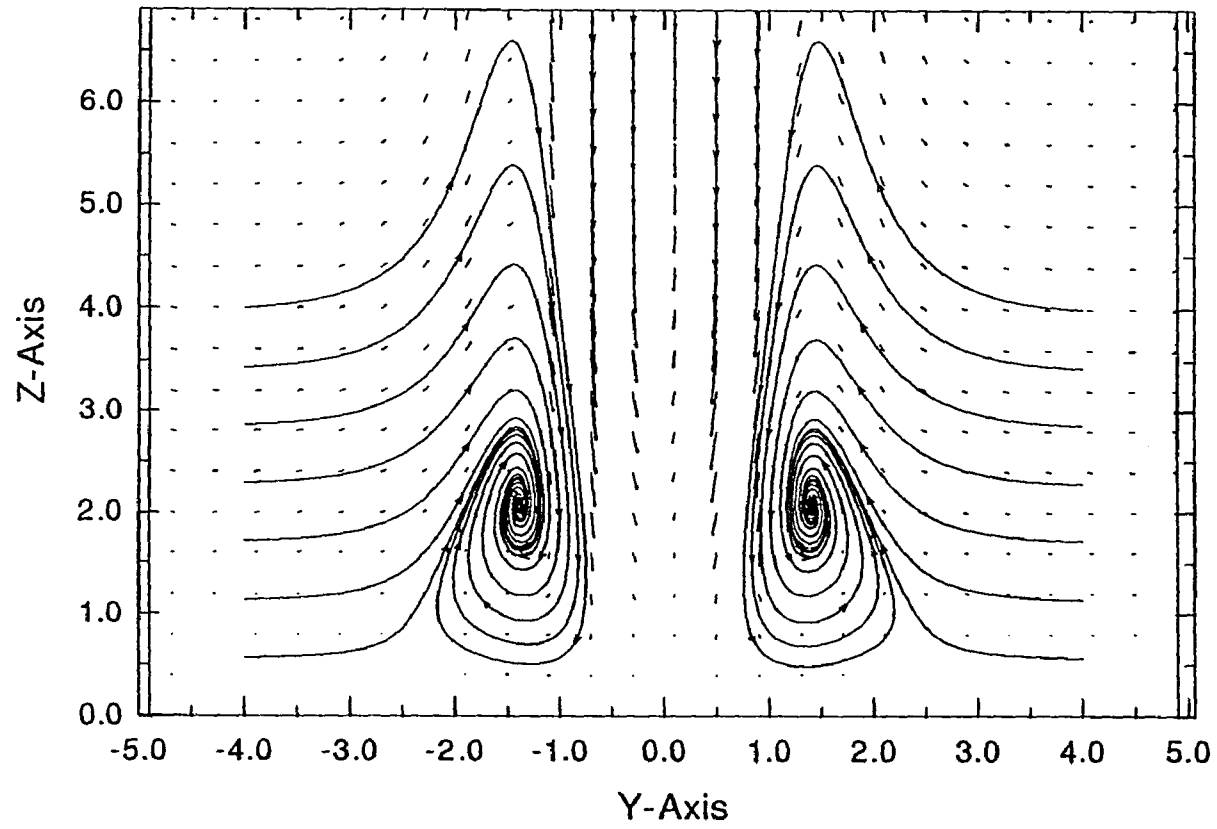
c) Cross-flow streamlines pattern at $X=3.5$ ($h=4.5$) .

Figure 22. continued



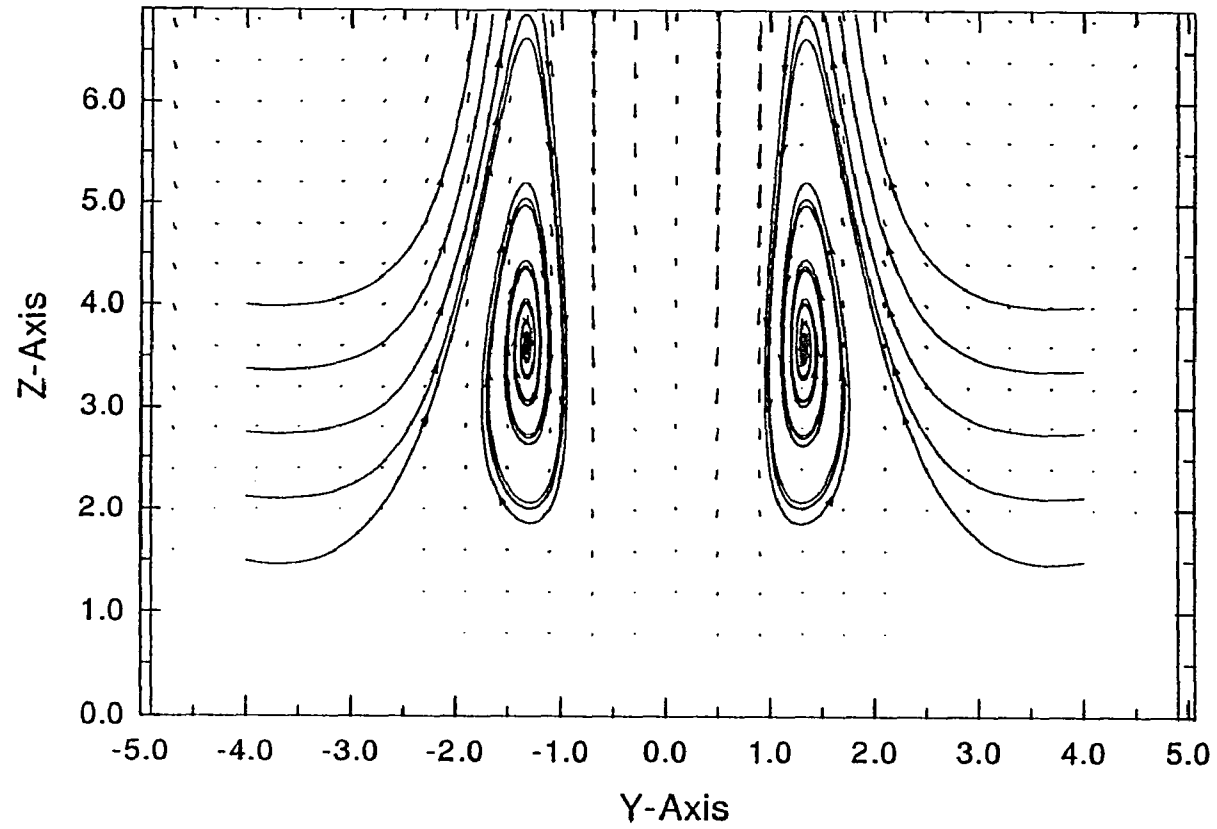
d) Cross-flow streamlines pattern at $X=4.0$ ($h=4.5$) .

Figure 22. continued



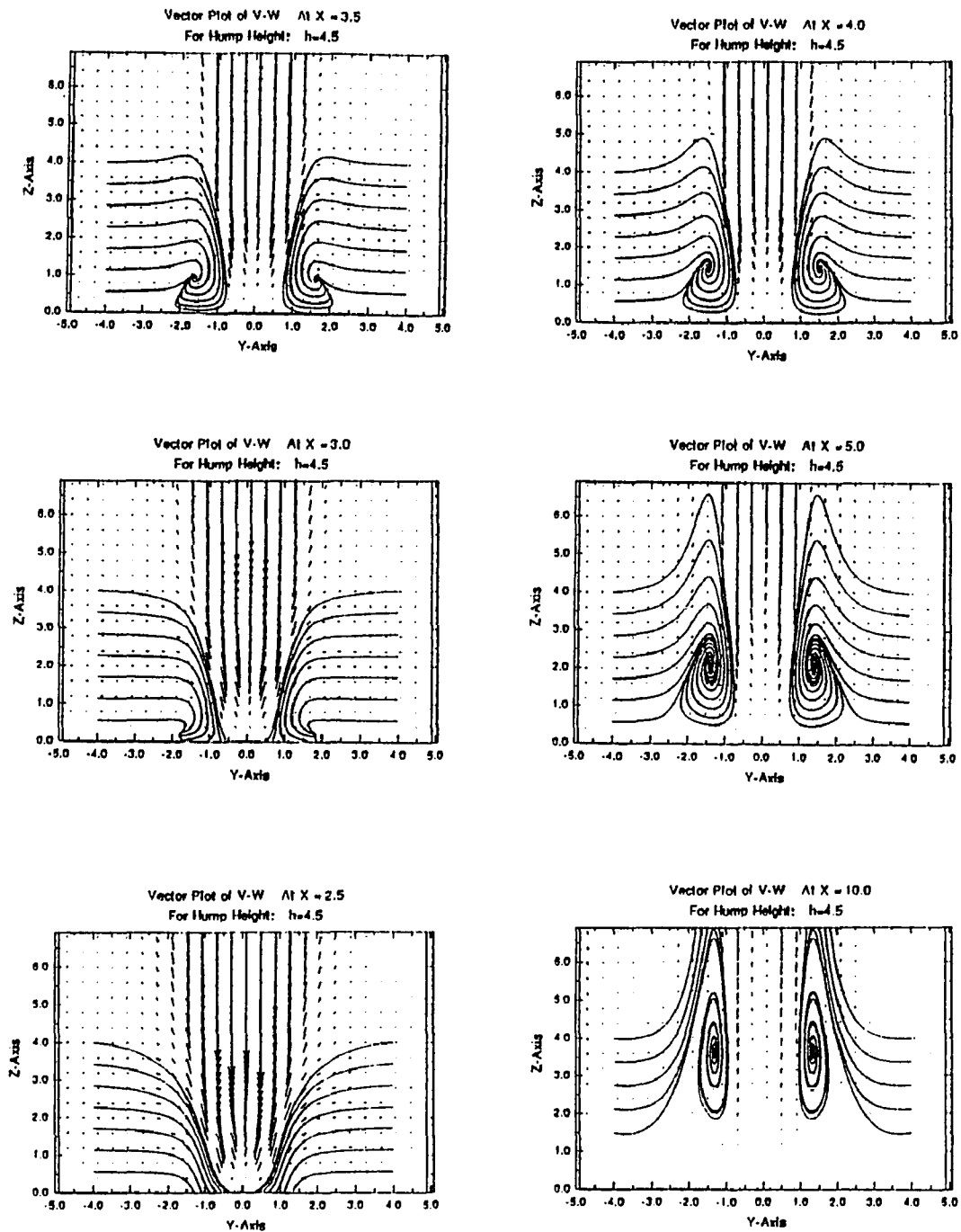
e) Cross-flow streamlines pattern at $X=5.0$ ($h=4.5$).

Figure 22. continued

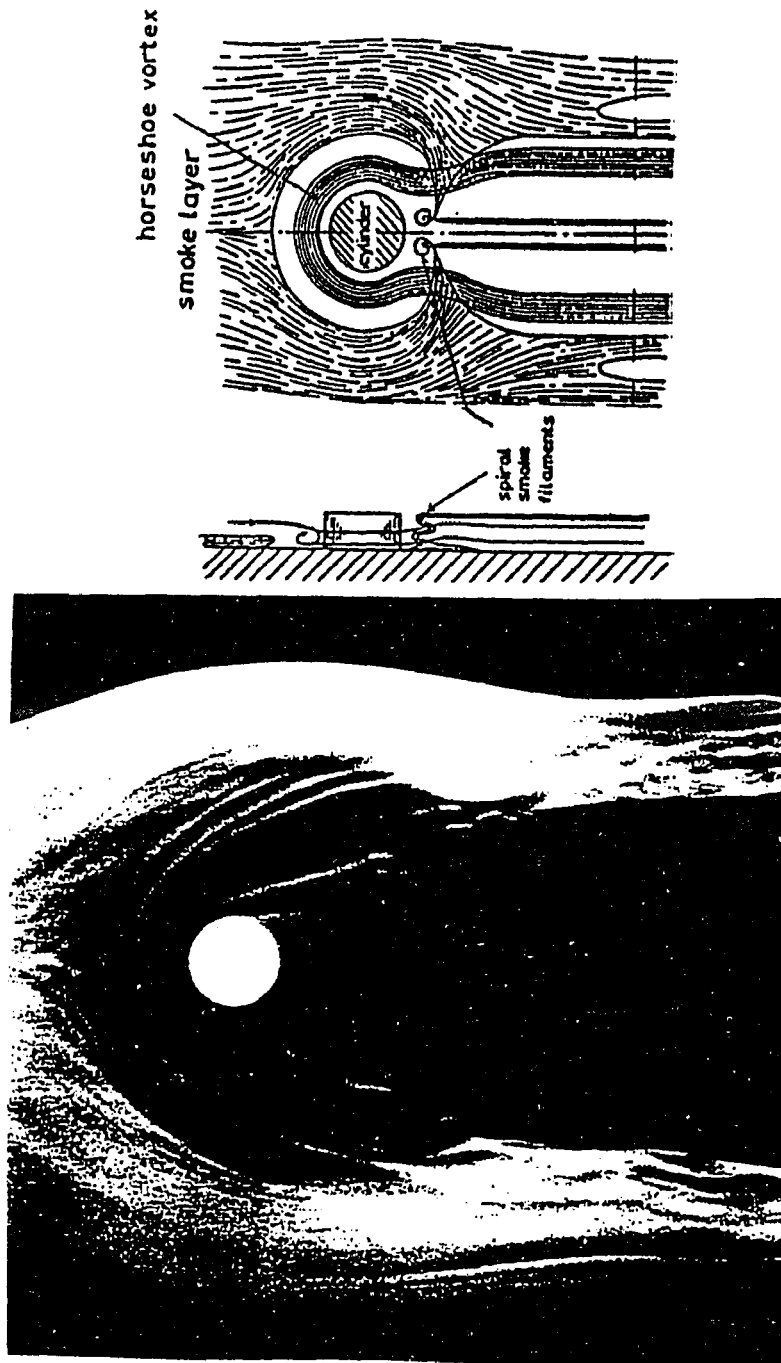


f) Cross-flow streamlines pattern at $X=10.0$ ($h=4.5$) .

Figure 22. continued



g) Evolution of the cross-flow vortex pair as it moves downstream by looking at figures 22a - 22f (reduced into one page, start from the figure in the lower left) .



h) (Top) Representation of flow past a cylindrical roughness element on a flat plate (taken from AGARD-R-709 Fig. 47, Chap. I). (Bottom) Horseshoe vortices made visible by a sheet of smoke (taken from Van Dyke, M. "An Album of Fluid Motion", Fig. 93)

CHAPTER IV

DISTURBANCE FLOW RESULTS

IV.1 Receptivity of the Laminar Flow

The main goal of this study is to investigate the receptivity of a laminar boundary layer to the local interaction of free-stream disturbances with a small three-dimensional roughness element. Guided by the two-dimensional studies of Bodonyi, Welch, Duck, and Tadjfar [16], we expect the crucial parameter to be the scaled Strouhal number, S_0 . Here we restrict ourselves to the hump shape given by equation (3-1). Results of Chapter 3 indicate that two types of basic steady flow exist. For humps with height, $h < 4$, the basic flow is attached, but at higher h values a small region of flow separation is formed behind the hump. To investigate the receptivity of both types of steady flow, numerical solutions are found for different values of the Strouhal number at hump heights $h=1.0$ and $h=4.5$.

First, we present the results for the hump with height of $h=1.0$. In our disturbance-flow computer program, all the flow variables are complex valued and all the steady-flow variables are needed to evaluate the coefficients. Therefore, due to computer time limitations, a coarser mesh than the one used to evaluate the steady-state flow field is necessary. However, this is not crucial for the smaller hump height. As in Chapter 3, for convenience, we have replaced ξ , η , and z_i by X , Y , and Z respectively. Furthermore, the following values were used for the parameters except where noted. In the streamwise direction $\Delta X = 0.30$, $-3.6 < X < 11.4$; along the lateral direction we have $\Delta Y = 0.20$, $0 < Y < 6.0$, and in the normal direction within the lower-deck region $\Delta Z = 0.30$ and $0 < Z < 6.3$. These values correspond to using 50, 30, and 21 points in the X , Y , and Z directions, respectively. In the upper-deck region the same values were used for ΔX and ΔY while $\Delta Z_u = 0.20$ and $0 < Z_u < 3.2$, corresponding to the same number of grid points in X and Y directions as in the lower-deck problem with 16 points used in the Z_u direction.

The effect of using this mesh on these computations is examined by computing the results for $h=1$ and $S_0 = 1.0$ with different mesh sizes. In separate numerical calculations the number of points in one direction is doubled with all the other parameters unchanged. This is repeated for all three directions in the lower deck and the normal direction in the upper deck. The range of the mesh is also extended in all the directions in separate computations. No noticeable changes, less than one percent, in the results are observed. Hence, it is concluded that the above mesh is sufficient for studying the

disturbance-flow field over the smaller hump. For all these computations the steady flow field is calculated on a finer mesh with twice as many points being used in all directions compared to the above mesh. For the steady-flow computations, the upstream influence of the hump's presence required that the upstream boundary conditions be applied at $X=-5.0$. However, in the disturbance-flow computations, the upstream propagation of the disturbance decays more rapidly. Therefore, making it possible to apply the upstream boundary conditions at $X=-3.6$ (to lower the computational costs).

From our numerical calculations, the following flow variables, $\vec{v}_c(X,Y,Z)$, $p_c(X,Y)$,and $a_c(X,Y)$ are obtained as complex-valued functions. However, the physical disturbance-flow properties are real and harmonic in time (see equation (1-25)). Hence, we can write:

$$\vec{v}(X,Y,Z,t) = \text{Real} \{ e^{-it} \vec{v}_c(X,Y,Z) \} , \quad (4-1a)$$

$$p(X,Y,t) = \text{Real} \{ e^{-it} p_c(X,Y) \} , \quad (4-1b)$$

$$a(X,Y,t) = \text{Real} \{ e^{-it} a_c(X,Y) \} . \quad (4-1c)$$

Breaking the numerical results into their real and imaginary parts, provides:

$$\vec{v}(X,Y,Z,t) = \vec{v}_r(X,Y,Z) \cos(t) + \vec{v}_i(X,Y,Z) \sin(t) , \quad (4-2a)$$

$$p(X,Y,t) = p_r(X,Y) \cos(t) + p_i(X,Y) \sin(t) , \quad (4-2b)$$

$$a(X,Y,t) = a_r(X,Y) \cos(t) + a_i(X,Y) \sin(t) . \quad (4-2c)$$

This implies that the real part of the solution represents the disturbance flow at times $t = n\pi$ where $n = 0, 2, 4, \dots$ and its negative describes the flow at times where $n = 1, 3, 5, \dots$. Similarly the imaginary parts represent the flow at times where $n = \frac{1}{2}, \frac{5}{2}, \frac{9}{2}, \dots$ and so on.

Without the hump, the free-stream disturbances, to the first order, produce the classical Stokes flow near the wall in the lower deck (see Appendix A). In equations (1-71), we subtracted this uniform Stokes flow out of our solution. Hence, in the hump's absence the disturbance flow is zero everywhere. For all order-one scaled Strouhal numbers, the interaction of the hump and the free-stream disturbances introduces a spectrum of all spatial disturbances in the boundary layer around the hump. For $S_0 = 1.0$, this initial kink decays rapidly as it moves downstream. This can be seen in the contour plots of the disturbance pressure, p , at $t = 0, \frac{\pi}{4},$ and $\frac{\pi}{2}$ presented in figures 23a, 23b, and 23c, respectively. The time-averaged amplitude of the pressure for this spatial wave is given by the modulus of the complex pressure, $|p|$. Contour map of the disturbance-pressure amplitude for this Strouhal number is given in figure 23d. Rapid spatial decay of the disturbance's pressure-field is clearly evident.

$a(X, Y)$ can be interpreted as the limiting value of the streamwise disturbance velocity, u , at the outer edge of the lower deck by equation (1-75a). Figure 24a is the contour plot of $a(X, Y)$ at time $t = 0$. The contour map of $|a|$ is also given in figure 24b. The spatial decay can also be seen in these figures. However, it seems to indicate that the vorticity field is decaying at a slower rate than the pressure field.

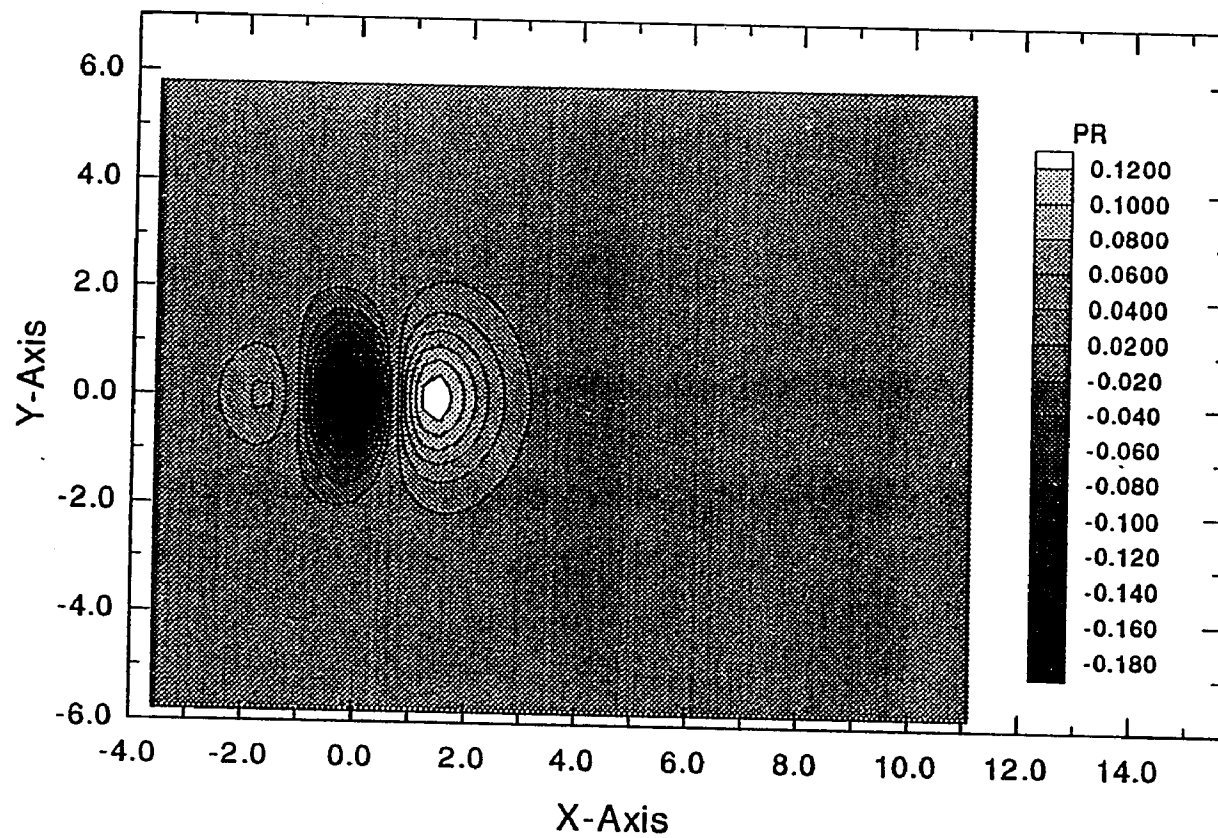
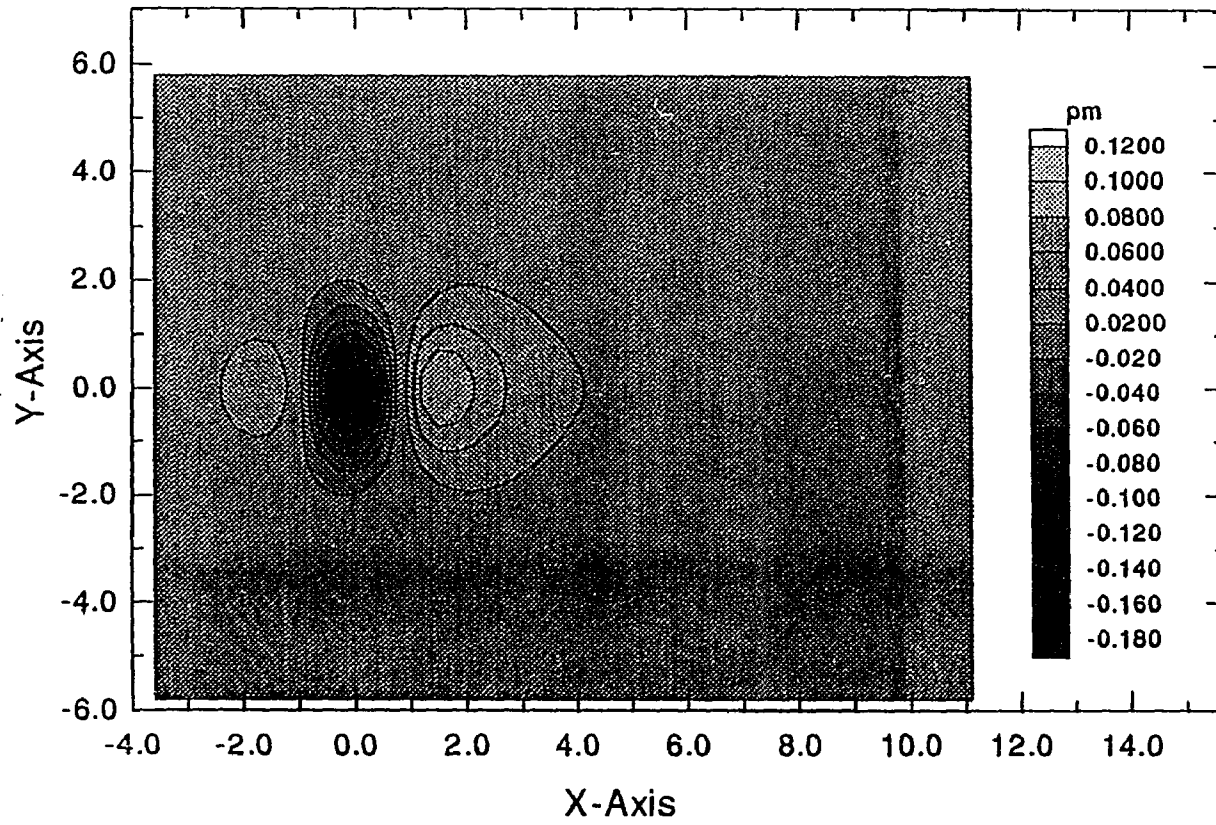


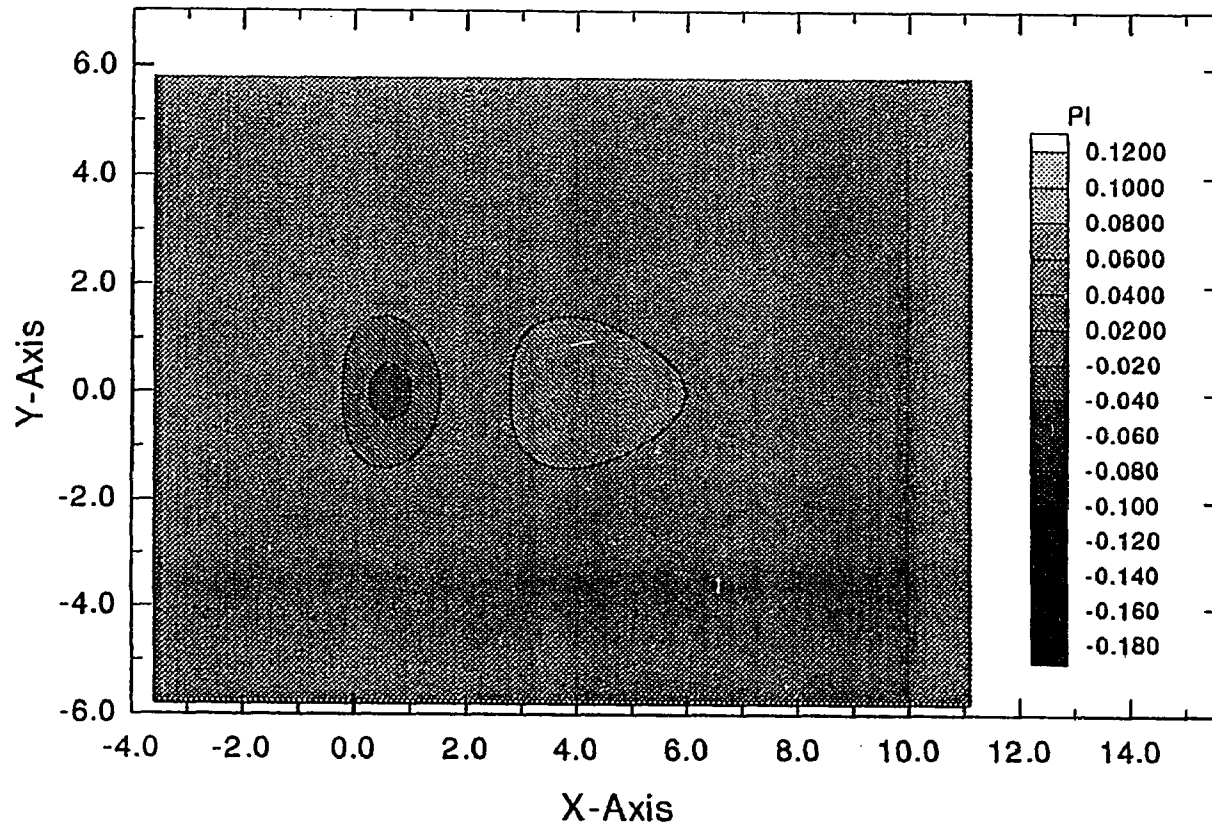
Figure 23. a) Contour plot of disturbance pressure for $h=1.0$, $S_0 = 1.0$, and $t = 0$.

Figure 23. continued



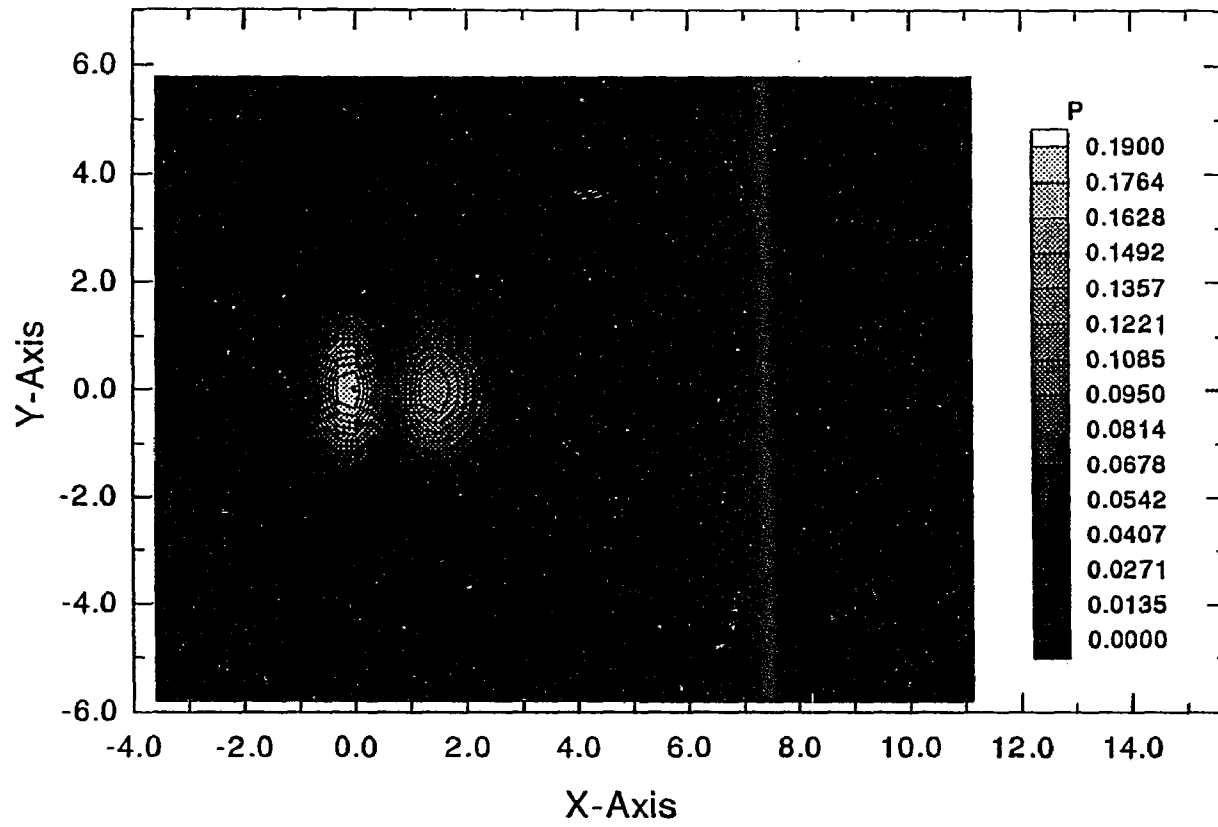
b) Contour plot of disturbance pressure for $h=1.0$, $S_0=1.0$, and $t = \frac{\pi}{4}$.

Figure 23. continued



c) Contour plot of disturbance pressure for $h=1.0$, $S_0 = 1.0$, and $t = \frac{\pi}{2}$.

Figure 23. continued



d) Contour map of disturbance-pressure amplitude, $|p|$, for $h=1.0$ and $S_0 = 1.0$.

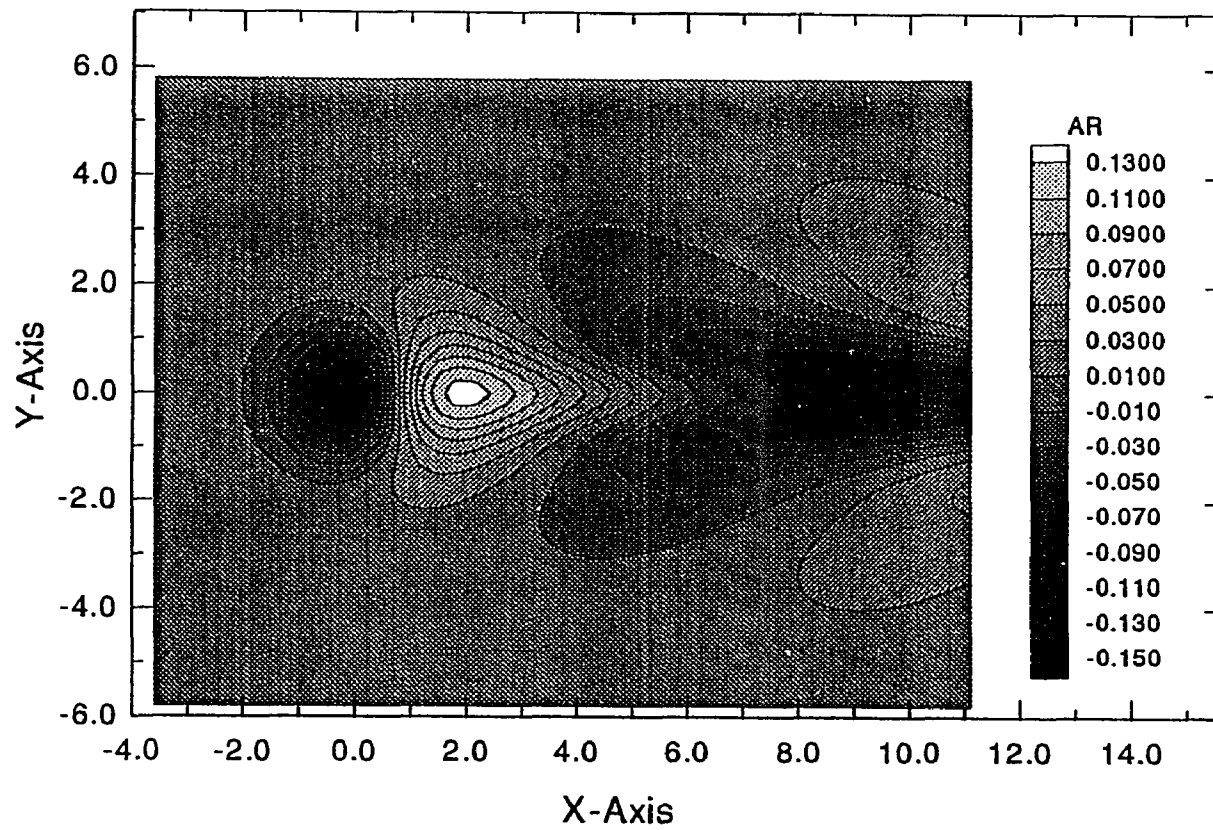
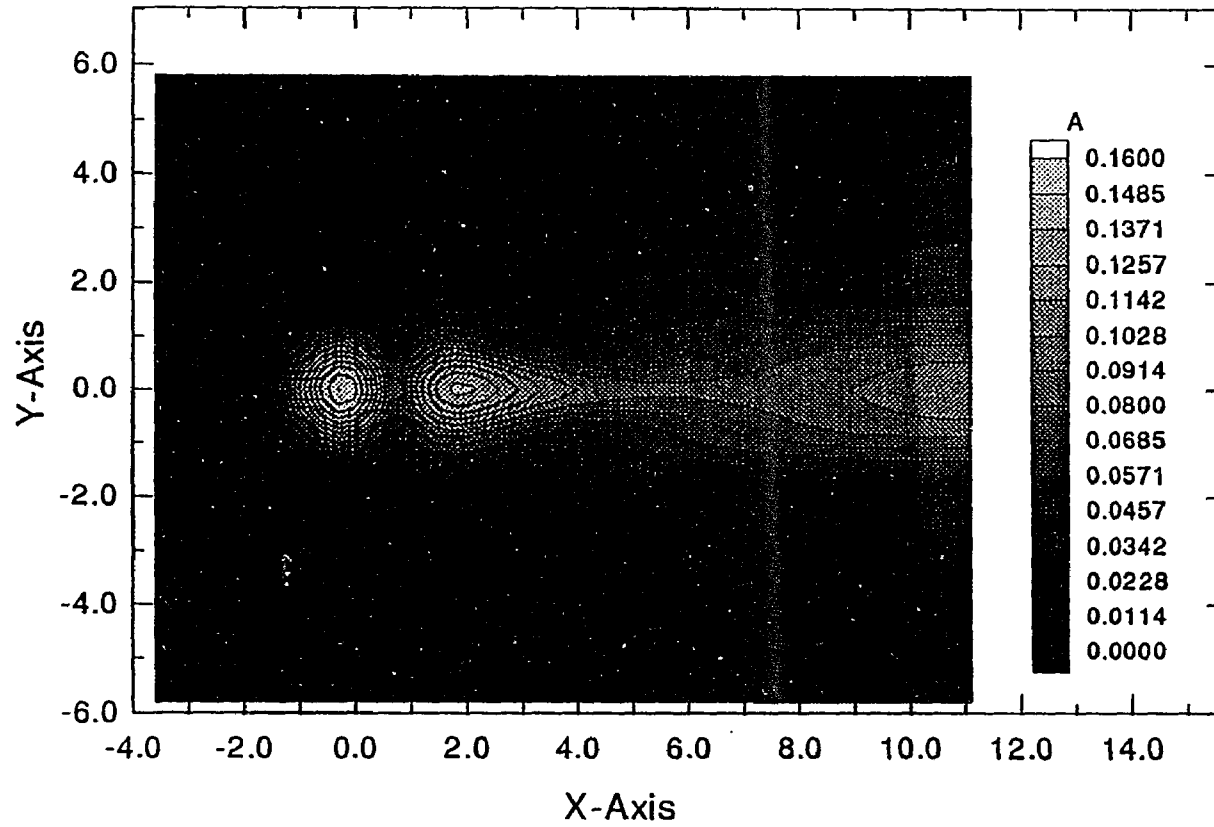


Figure 24. a) Contour plot of $a(X, Y)$ for $h=1.0$, $S_0=1.0$, and $t=0$.

Figure 24. continued



b) Contour map of $|a(X,Y)|$ for $h=1.0$ and $S_0=1.0$.

Contour plots of the disturbance velocities, u and w , in the X - Z plane along the line of symmetry, $Y = 0$, at $t = 0$ and $\frac{\pi}{2}$ are shown in figures 25 and 26, respectively. Along the line of symmetry $v = 0$ identically. Again, from these velocity contours, we can see that the hump is scattering a spatially-decaying wave downstream of the hump.

Next, we present the results for $S_0 = 2.0$. In figures 27a, 27b, and 27c, contour plots of disturbance pressure at $t = 0$ and $\frac{\pi}{2}$, and the pressure amplitude, $|p|$, are given, respectively. The scattered wave introduced by the hump is still decaying as it travels downstream for this value of the Strouhal number. This is also apparent in the contour plot of function $a(X, Y)$ at time $t = 0$ and its time-averaged amplitude, $|a|$, given in figures 28a and 28b, respectively. The effect of increased Strouhal number, nondimensionalized frequency, is to lower the rate of spatial attenuation and also to decrease the streamwise wavelength of the wave. This wavelength shortening can alternatively be viewed by looking at the contour plots of the streamwise velocity, u , in the X - Z plane at $Y = 0$. These contour plots at $t = 0$ and $\frac{\pi}{2}$ and contours of constant $|u|$ are presented in figure 29.

Further increases in the Strouhal number of the free-stream disturbances slows the spatial decay of the wave. In fact, for Strouhal numbers of $S_0 > 2.3$, the disturbance introduced by the hump amplifies as it moves downstream. The rate of this amplification increases as the Strouhal number is increased. This wave amplification decreases the rate of numerical convergence of our code significantly. The number of global iterations

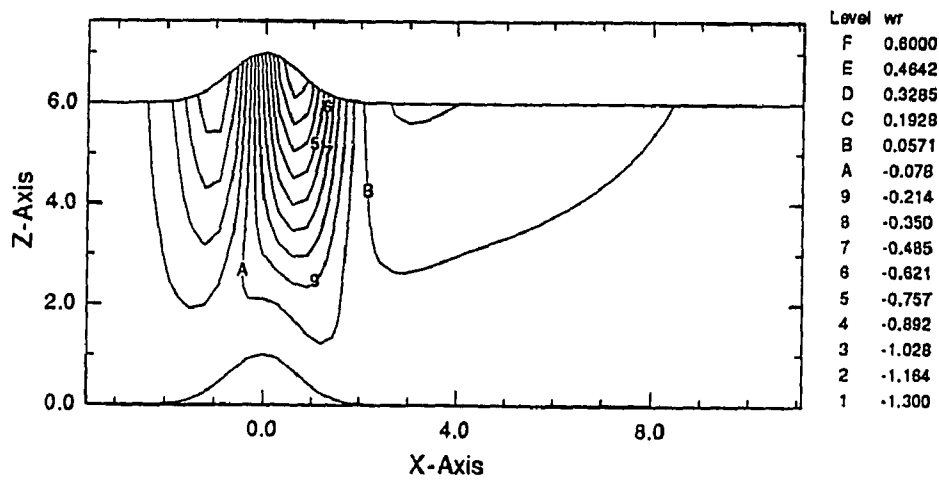
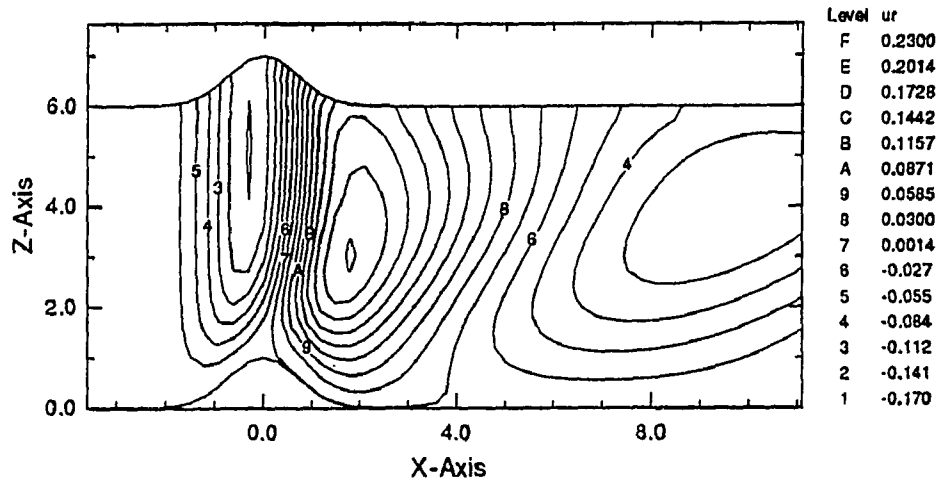


Figure 25. Contour plots of disturbance velocities, u and w , for $h=1.0$, $Y=0$, $S_0 = 1.0$ and $t = 0$.

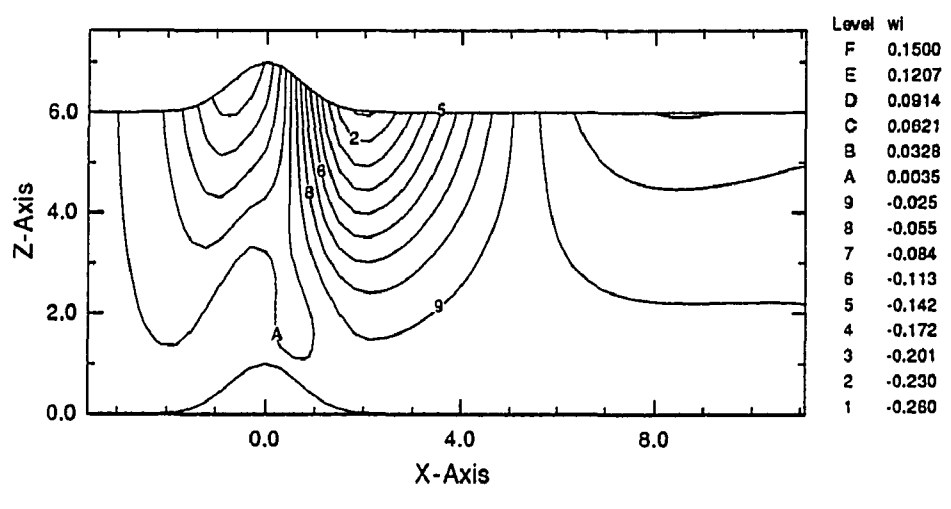
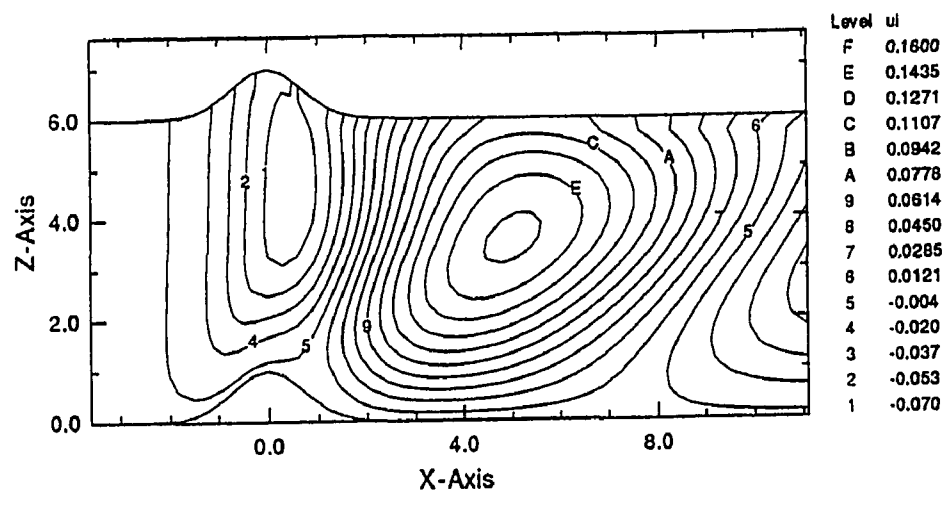


Figure 26. Contour plots of disturbance velocities, u and w , for $h=1.0$, $Y=0$, $S_0 = 1.0$,
and $t = \frac{\pi}{2}$.

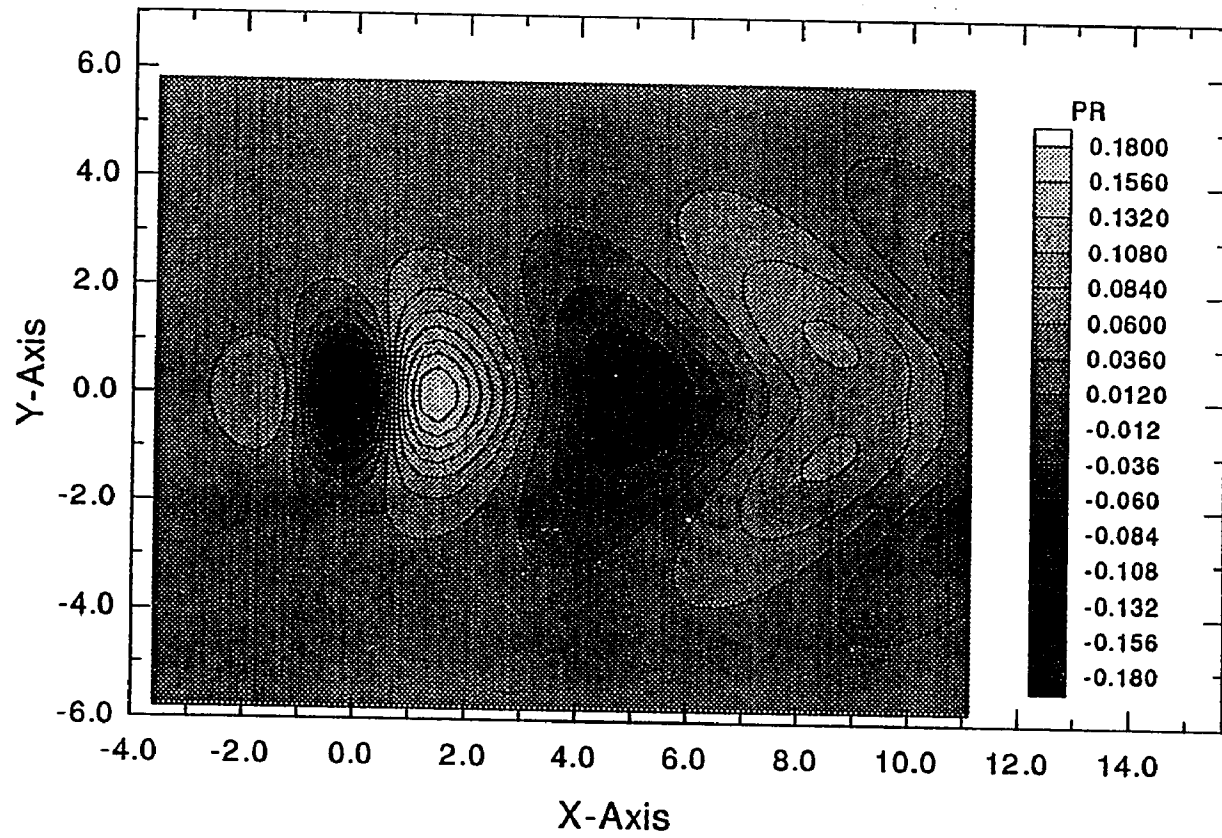
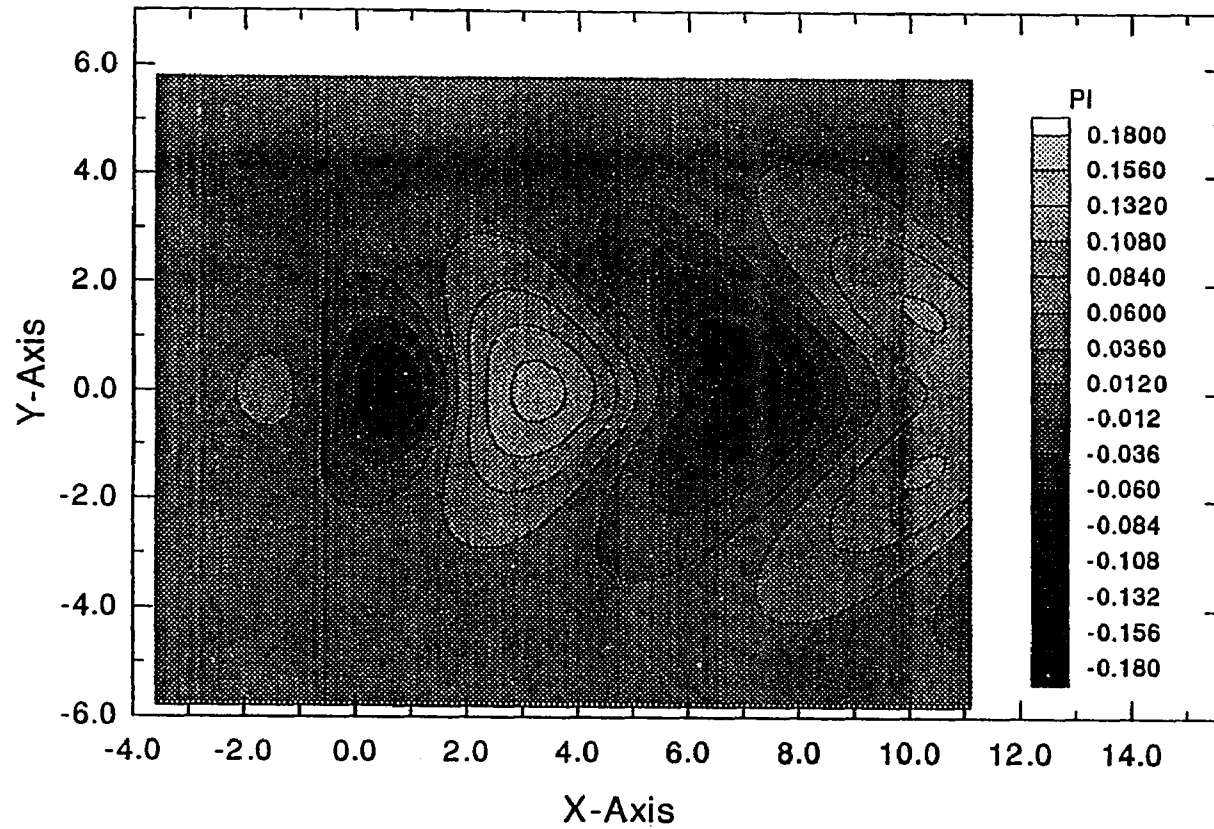


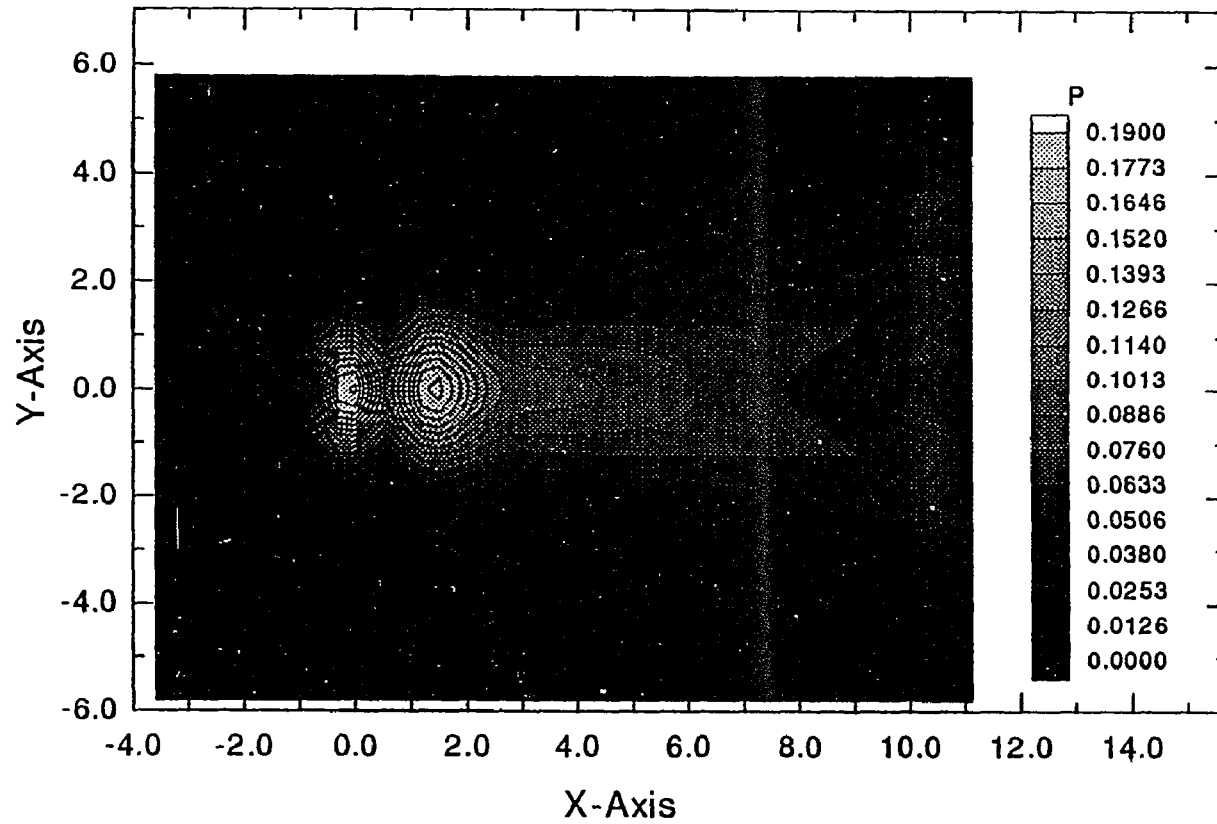
Figure 27. a) Contour plot of disturbance pressure for $h=1.0$, $S_0 = 2.0$, and $t = 0$.

Figure 27. continued



b) Contour plot of disturbance pressure for $h=1.0$, $S_0=2.0$, and $t=\frac{\pi}{2}$.

Figure 27. continued



c) Contour map of disturbance-pressure amplitude, $|p|$, for $h=1.0$ and $S_0=2.0$.

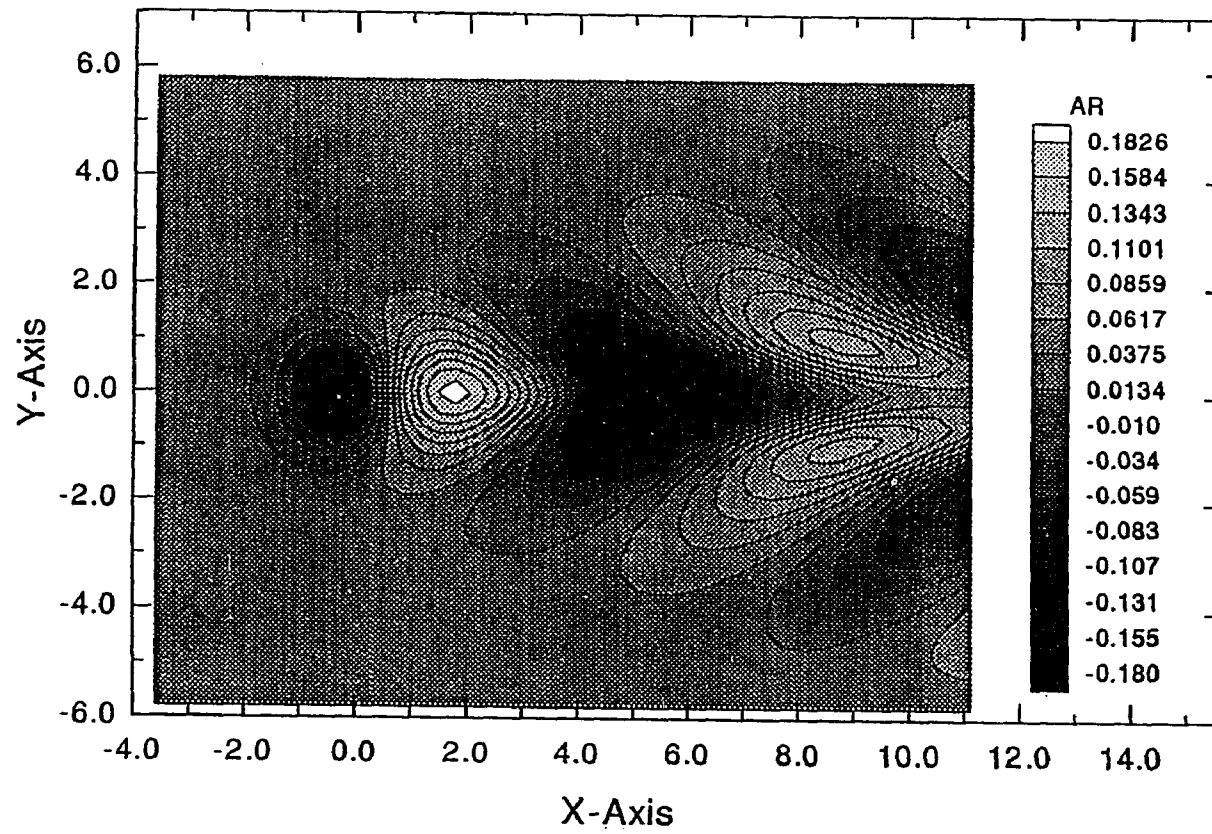
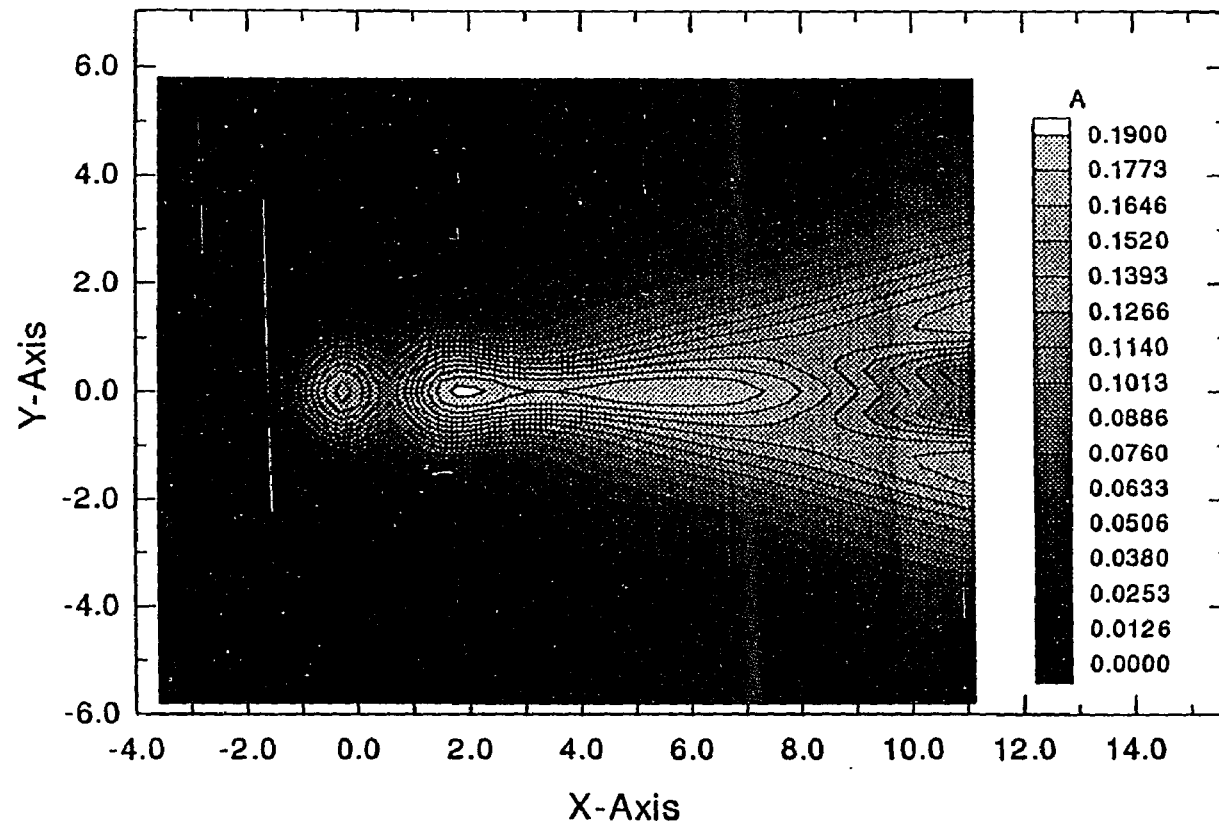


Figure 28. a) Contour plot of $a(X, Y)$ for $h=1.0$, $S_0=2.0$, and $t=0$.

Figure 28. continued



b) Contour map of $|a(X,Y)|$ for $h=1.0$ and $S_0=2.0$.

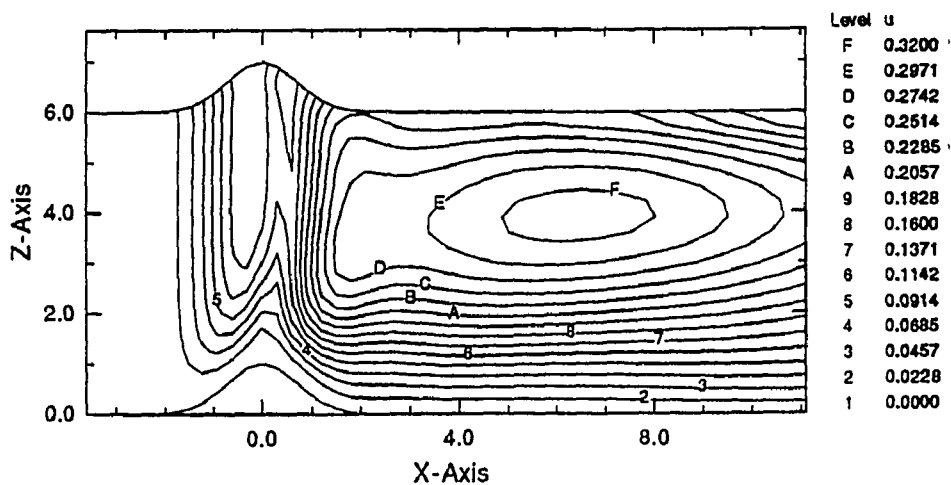
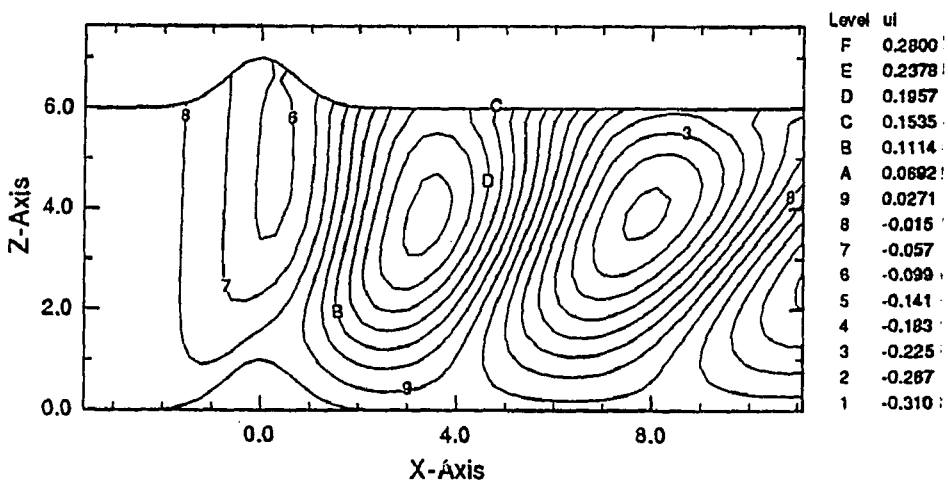
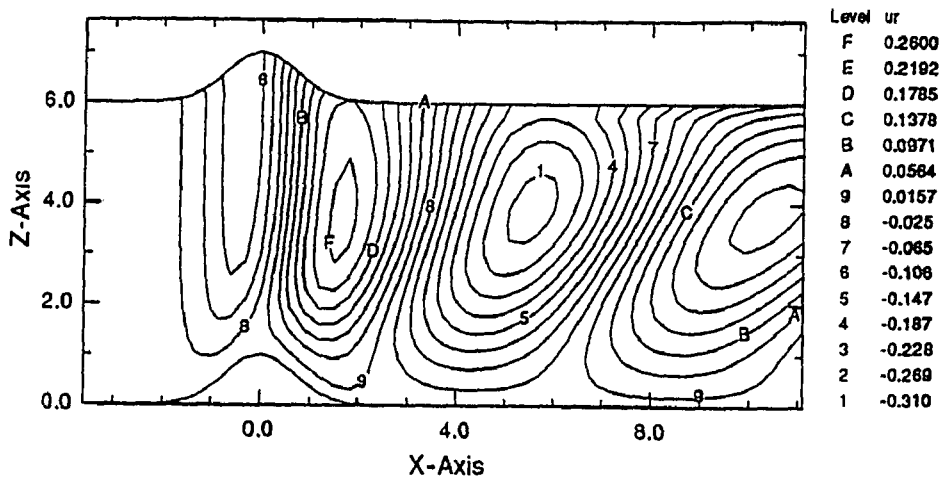


Figure 29. Contour plots of disturbance u-velocity at $t = 0$, $t = \frac{\pi}{2}$ and its modulus for $h=1.0$, $Y=0$, and $S_0 = 2.0$.

required to achieve numerical convergence increases rapidly as S_0 is increased. Therefore, smaller increments of increase in S_0 are required between converged solutions. The computational cost of calculations beyond $S_0 = 3.0$ for the given mesh is prohibitive. To obtain solutions for higher values of Strouhal number, the number of points in the streamwise direction, X , was reduced to 35 with all other parameters kept unchanged. This implies a reduction in the downstream side of the computational mesh to $-3.6 < X < 6.9$. Even with this reduced mesh, numerical solutions are only feasible up to $S_0 = 4.5$. The actual production CPU time on a CRAY Y-MP supercomputer for the $h=1.0$ case was about 25 hours, with most of the time spent on the higher Strouhal number solutions.

Here, we present the results for a spatially growing wave at $S_0 = 3.0$. Contour plots of the disturbance u-velocity at the outer edge of the lower deck at $t = 0$ and $\frac{\pi}{2}$, and its modulus, $|a|$, are given in figures 30a, 30b, and 30c, respectively. In these figures, the wave is amplified inside a wedge-shaped region behind the hump as it moves downstream. In particular, the second trough of the wave has moved from $X=7.0$ to $X=8.0$, and its peaks (off the axis of symmetry) have become more pronounced. In figure 30c, contours of velocity amplitude, $|a|$, are at a seemingly constant oblique angle, 18° to 23° , from the streamwise direction. The same trend can be seen in figure 31, showing contours of constant pressure at $t = 0$ and $\frac{\pi}{2}$. Contour plots of the X- and Y-components of wall shear (du/dZ and dv/dZ at $Z=0$) at times $t = 0$ and $\frac{\pi}{2}$ are given in figures 32 and 33, respectively. In the above figures, contour patterns for p and a are

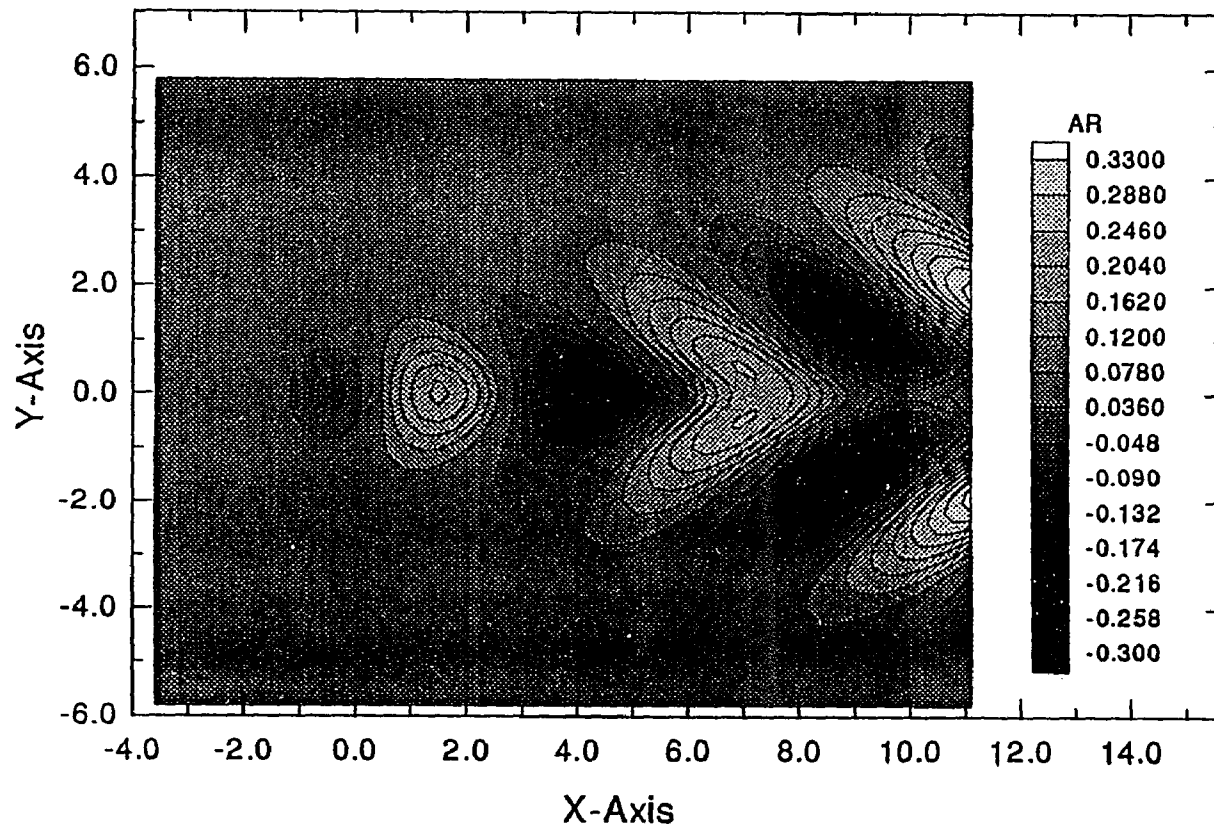
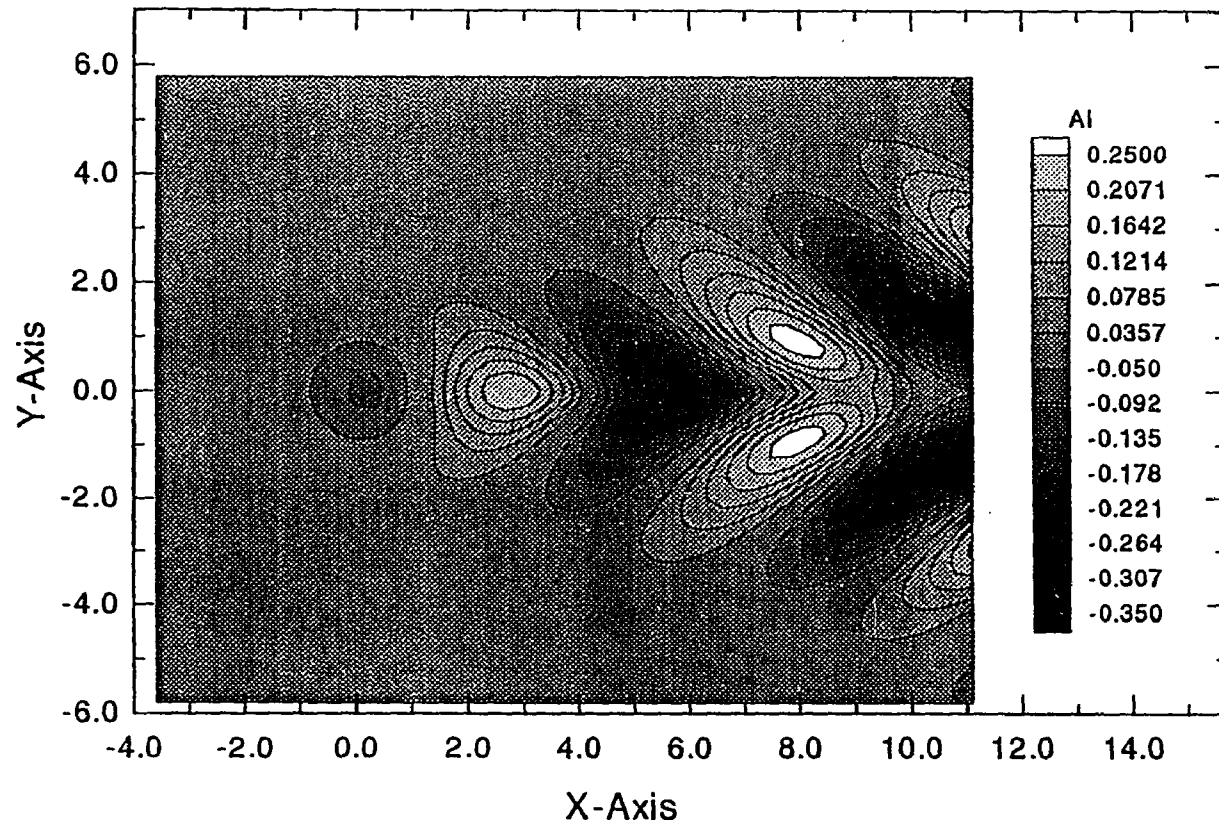


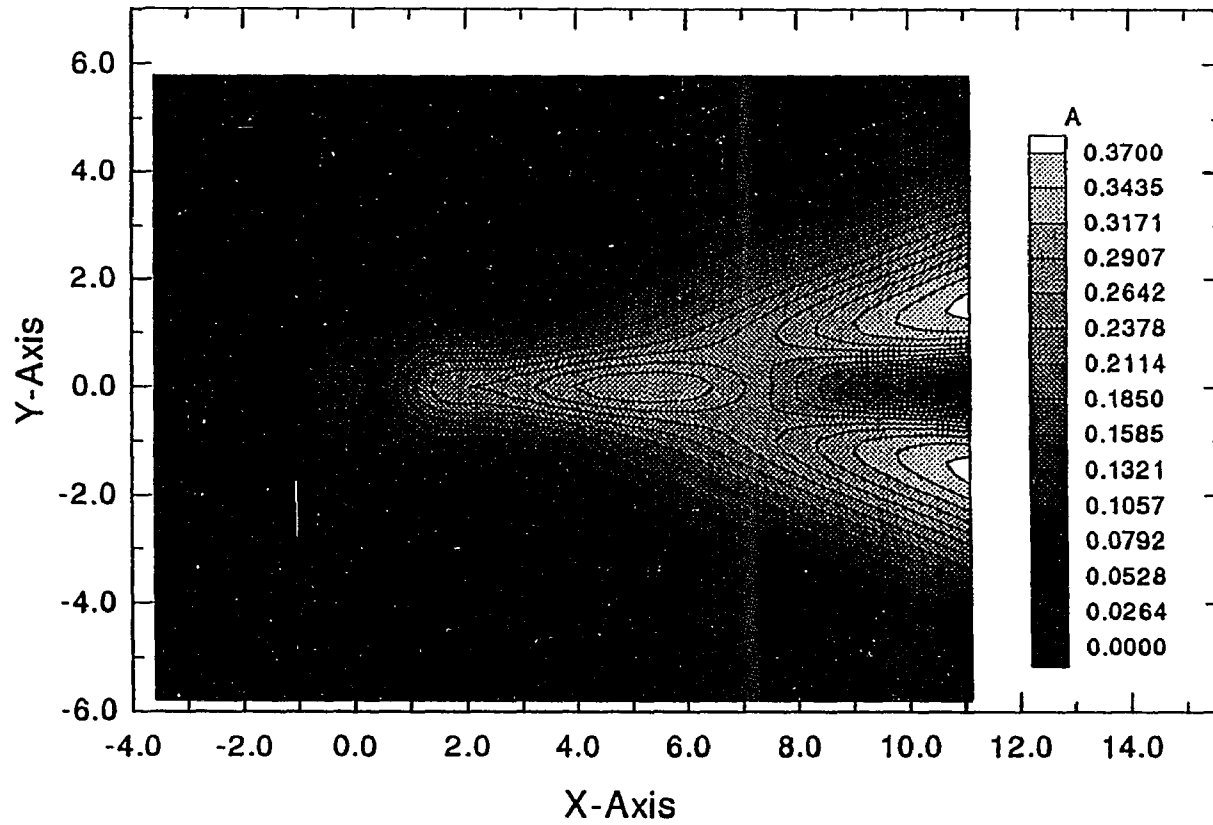
Figure 30. a) Contour plot of $a(X, Y)$ for $h=1.0$, $S_0=3.0$, and $t=0$.

Figure 30. continued



b) Contour plot of $a(X, Y)$ for $h=1.0$, $S_0=3.0$, and $t = \frac{\pi}{2}$.

Figure 30. continued



c) Contour map of $a(X,Y)$ amplitude, $|a|$, for $h=1.0$ and $S_0=3.0$.

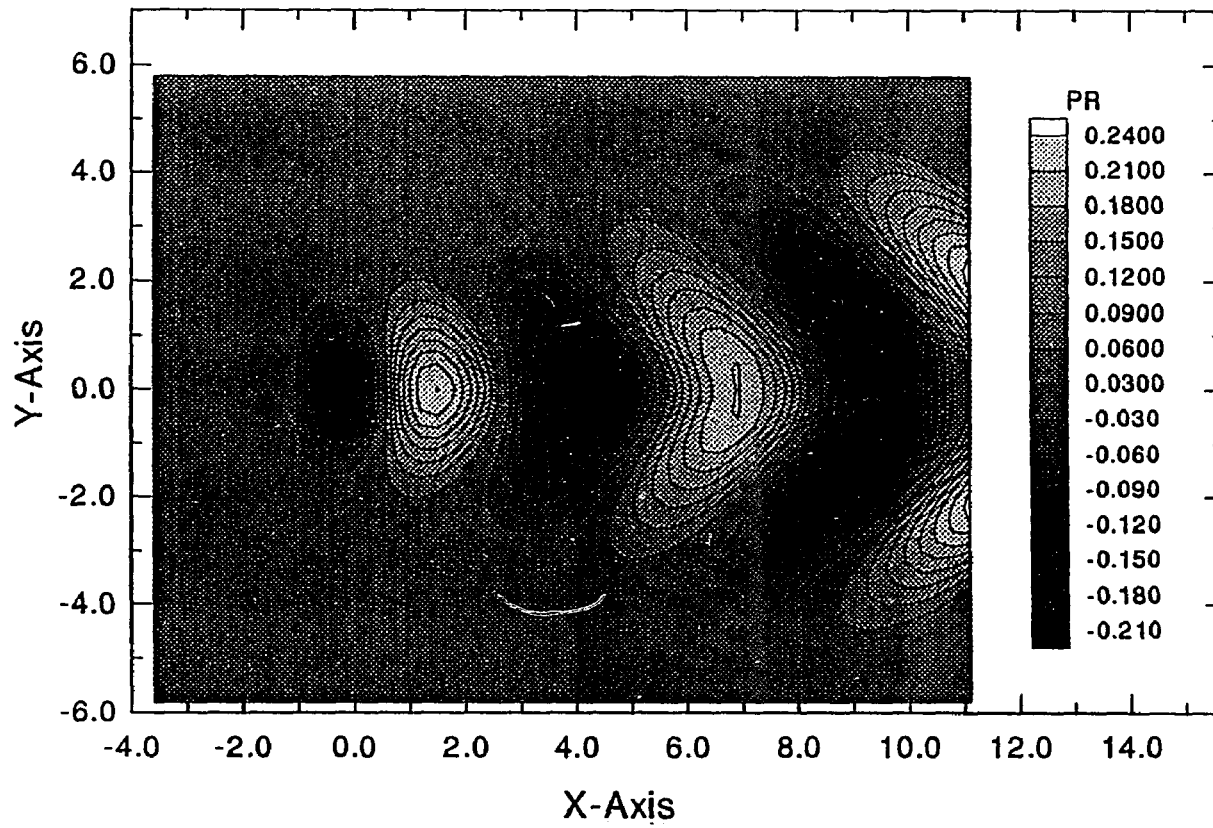
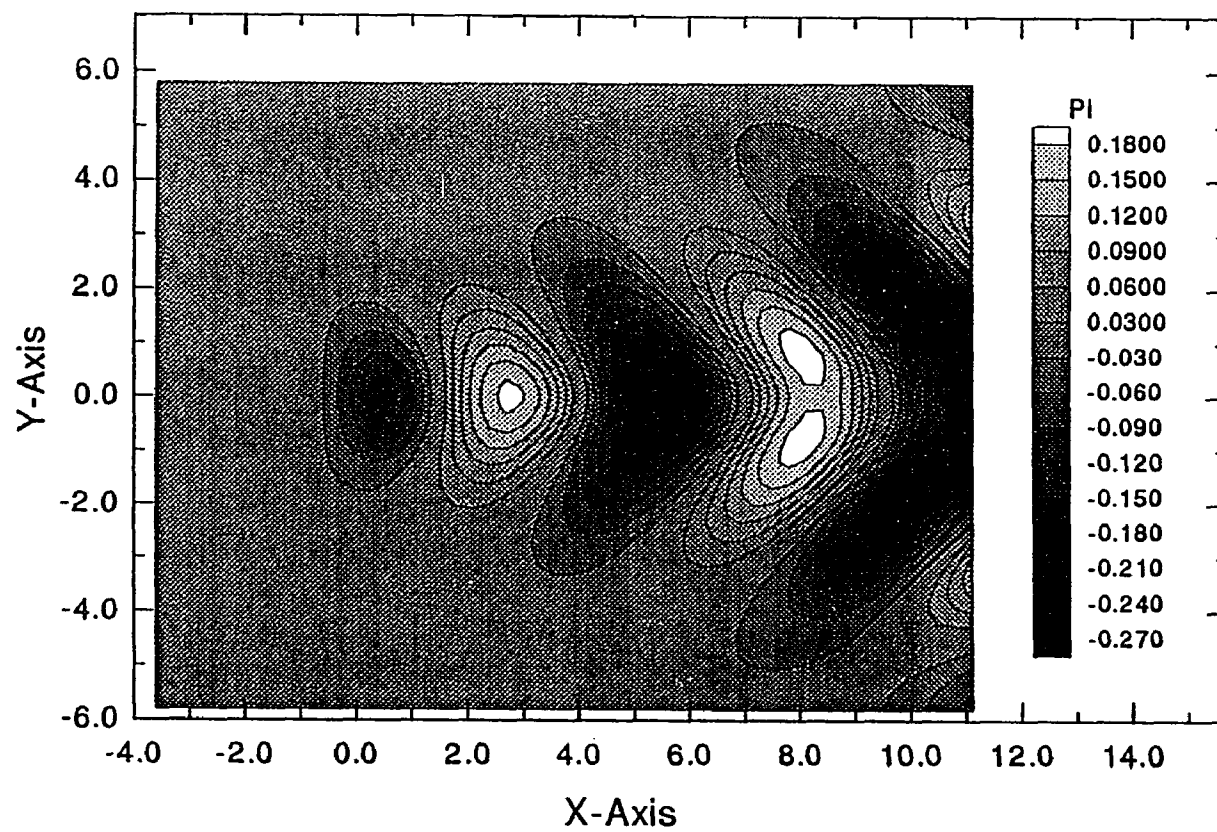


Figure 31. a) Contour plot of disturbance pressure for $h=1.0$, $S_0 = 3.0$, and $t=0$.

Figure 31. continued



b) Contour plot of disturbance pressure for $h=1.0$, $S_0 = 3.0$, and $t = \frac{\pi}{2}$.

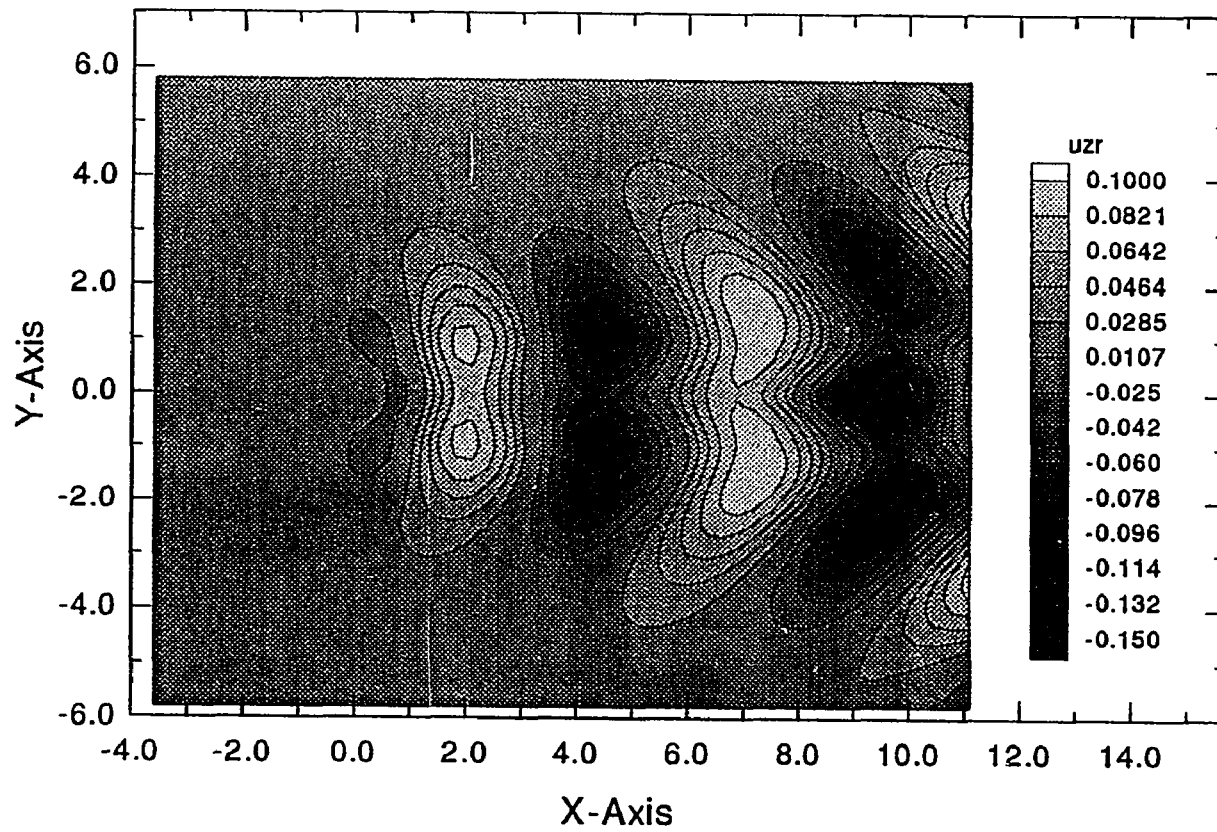
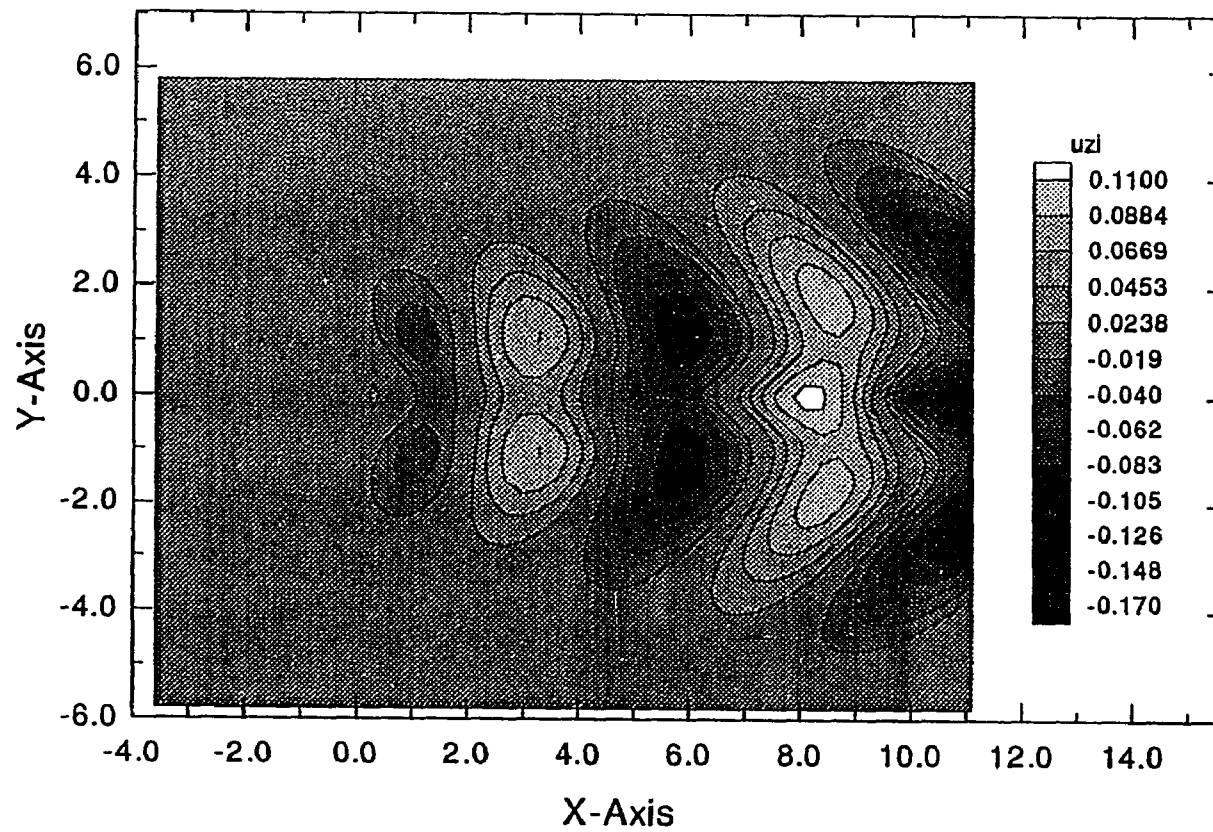


Figure 32. a) Contour plot of du/dZ for $h=1.0$, $S_0=3.0$, and $t=0$.

Figure 32. continued



b) Contour plot of du/dZ for $h=1.0$, $S_0 = 3.0$, and $t = \frac{\pi}{2}$.

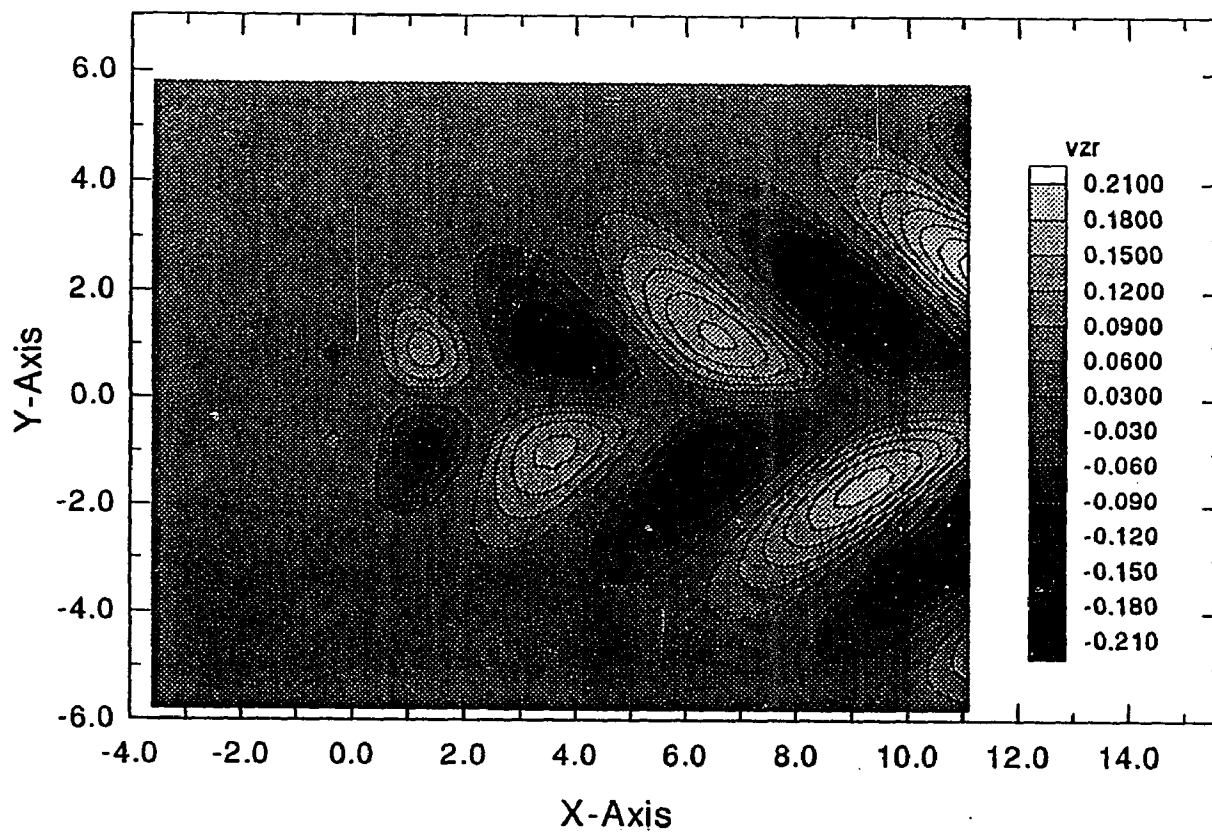
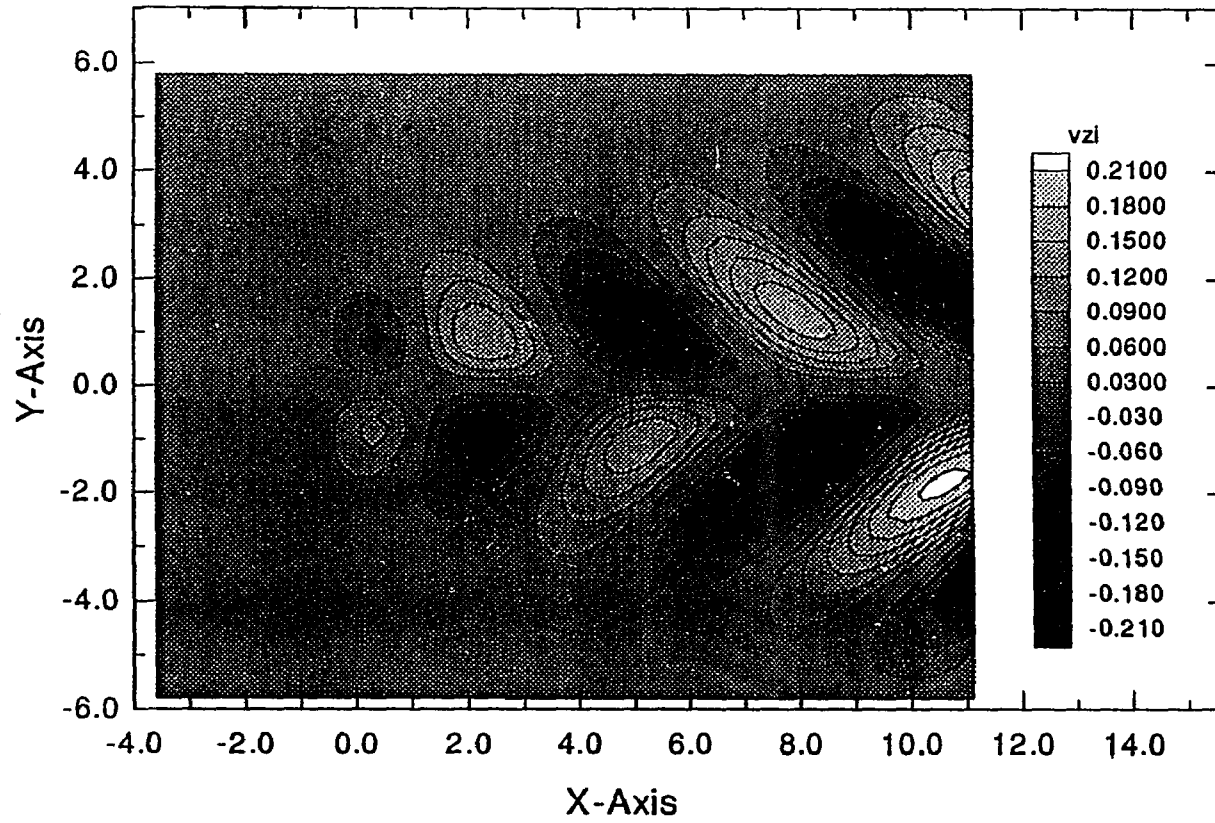


Figure 33. a) Contour plot of dv/dZ for $h=1.0$, $S_0=3.0$, and $t=0$.

Figure 33. continued



b) Contour plot of dv/dZ for $h=1.0$, $S_0=3.0$, and $t=\frac{\pi}{2}$.

similar and are in phase with each other. But the patterns for du/dZ , representative of u-velocity near the wall, are more elaborate than those of p and a , indicating a more complex flow structure near the wall. There is also a phase lag in the patterns for the X-component of the wall shear compared to the u-velocity contours at the outer edge of the lower deck. However, contour patterns for dv/dZ , representative of v-velocity near the wall are in phase with the patterns for p and a . In the next section we study the time harmonic flow structure of this complicated three-dimensional and spatially growing wave.

IV.2 Detailed Flow Structure of an Amplifying Wave

Here, the disturbance flow field generated by the hump for $h=1.0$ and $S_0 = 3.0$ is explored in detail. It is believed that this structure is representative of the scattered patches of T-S waves observed intermittently in natural transition. Figures 34a - 34c present the u-velocity contours in the X-Z plane at $Y=0$ and $t = 0, \frac{\pi}{4}, \frac{\pi}{2}, \frac{3\pi}{4}, \pi, \frac{5\pi}{4}, \frac{3\pi}{2}, \frac{7\pi}{4}$, and 2π , respectively. The wave amplification is clearly evident as it moves downstream. The positive peak, $u = 0.27$, at $X=1.5$ and $t = 0$ has amplified to $u = 0.57$ at $t = 2\pi$ as it propagated downstream to $X= 7.2$. In fact, looking at the u-velocity contour plot at $t = 0$, the first crest located at $X=4.2$ can be viewed as the negative of the first trough at $X=1.5$, having moved downstream, at $t = \pi$. Similarly, the second trough at $X=7.2$ is the evolution of the first trough at time $t = 2\pi$. Contour plots of w-velocity at

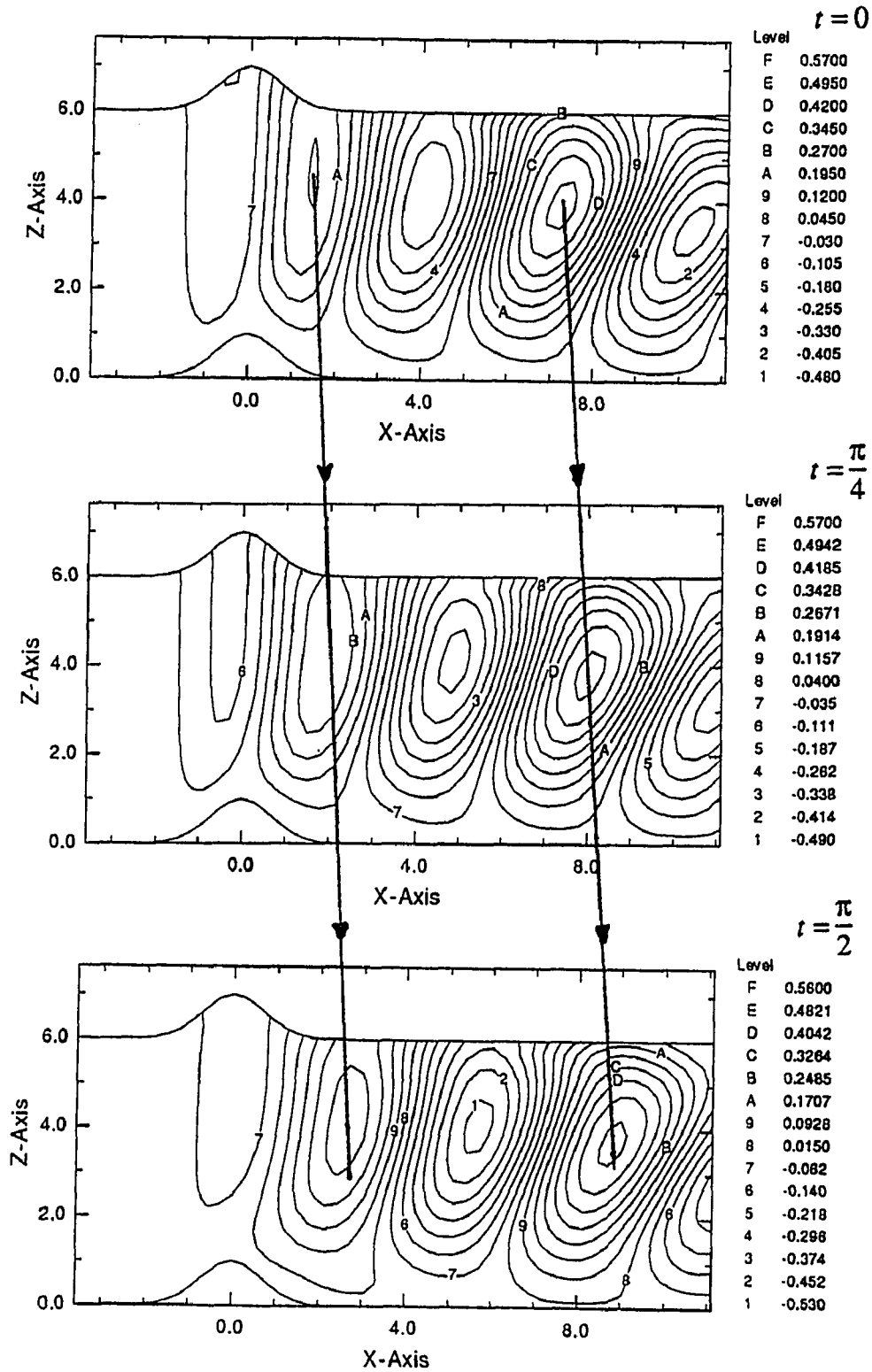
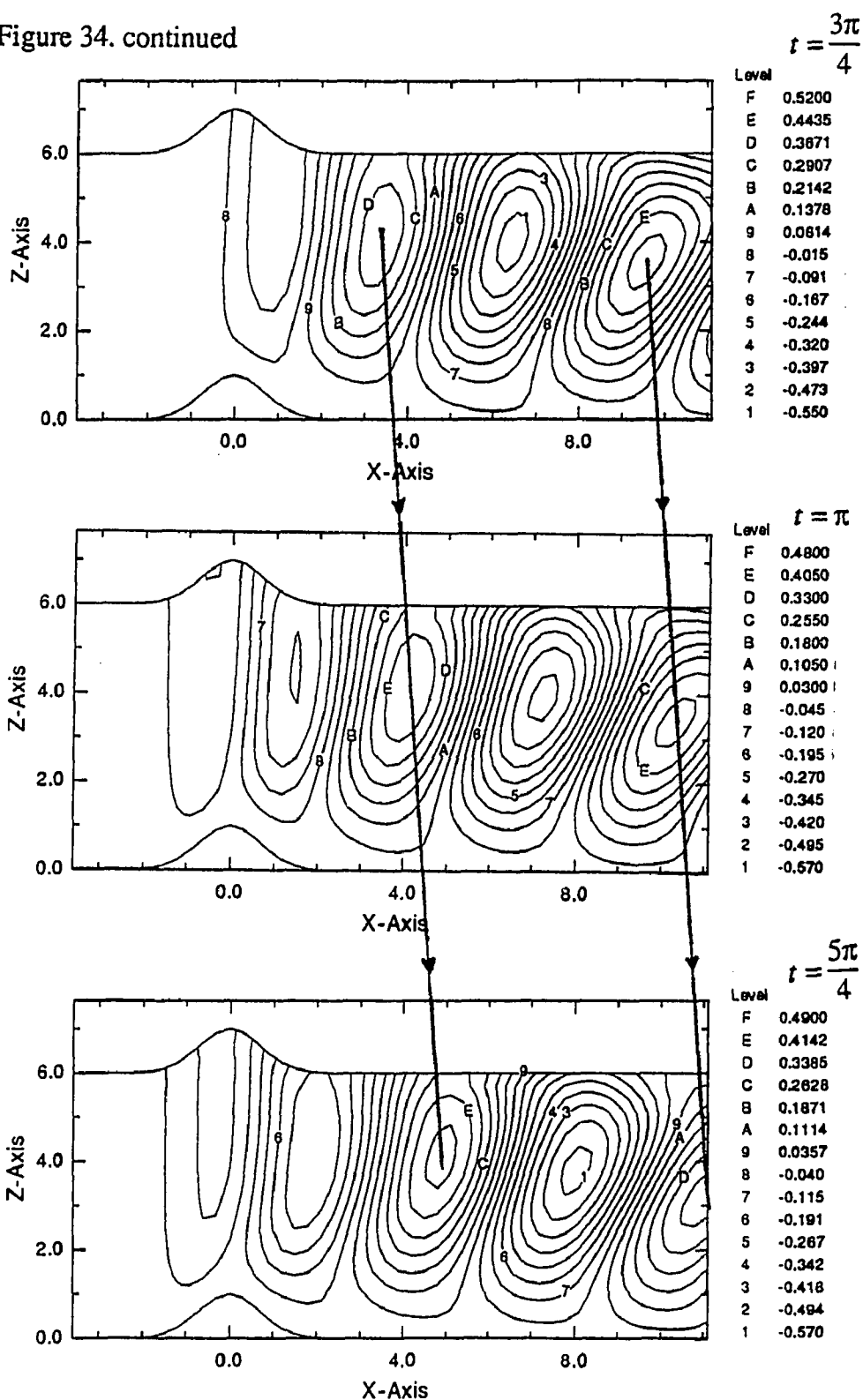


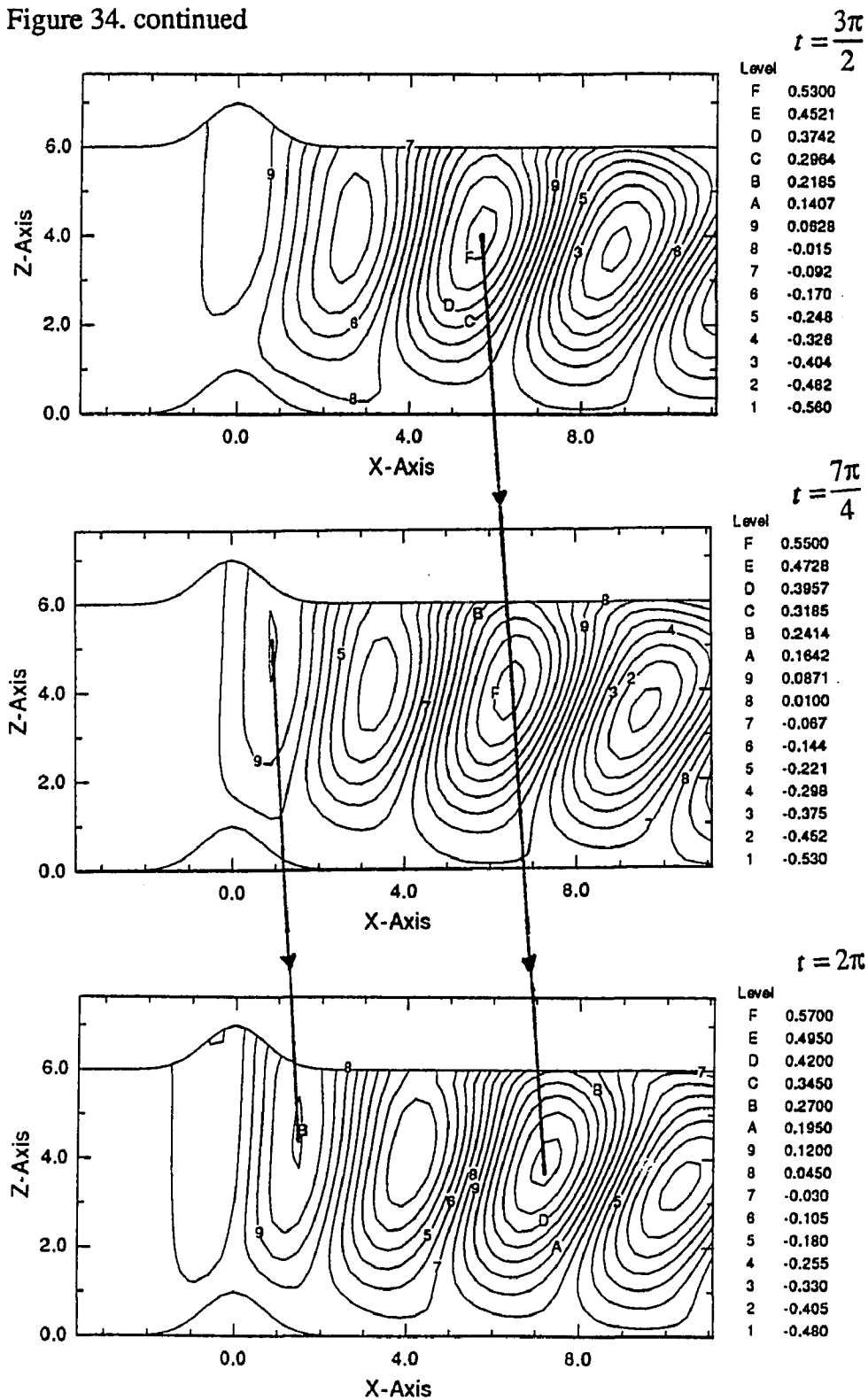
Figure 34. a) Contour plots of disturbance u-velocity at $t = 0, \frac{\pi}{4},$ and $\frac{\pi}{2}$ for $h=1.0, Y=0,$ and $S_0 = 3.0$.

Figure 34. continued



b) Contour plots of disturbance u-velocity at $t = \frac{3\pi}{4}$, π , and $\frac{5\pi}{4}$ for $h=1.0$, $Y=0$, and $S_0 = 3.0$.

Figure 34. continued



c) Contour plots of disturbance u -velocity at $t = \frac{3\pi}{2}$, $\frac{7\pi}{4}$, and 2π for $h=1.0$, $Y=0$, and $S_0 = 3.0$.

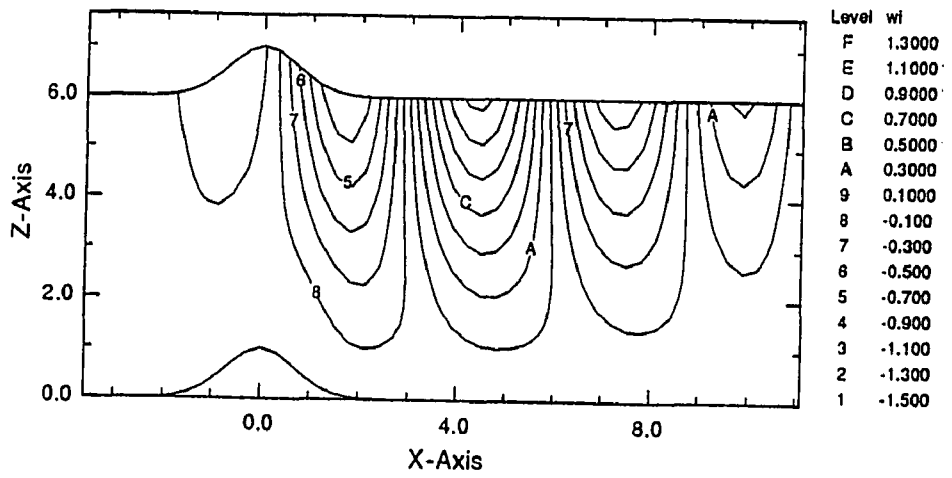
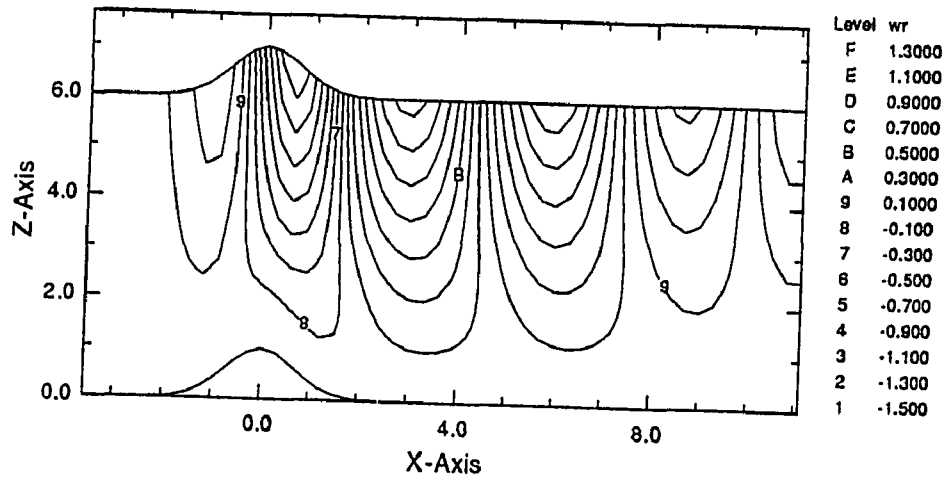


Figure 35. Contour plots of disturbance w -velocity at $t = 0$ and $t = \frac{\pi}{2}$ for $h=1.0$, $Y=0$, and $S_0 = 3.0$.

$t = 0$, and $\frac{\pi}{2}$ are given in figure 35 for your consideration. As the wave moves downstream, it also spreads off the axis of symmetry. To follow this movement, contour plots of disturbance velocity in the X-Z plane at $Y=2.0$ and $Y=4.0$ are given in figures 36 and 37, respectively.

From this point on, we are only looking at a frozen picture of fluid motion at time $t = 0$ and all the figures are given at this time unless otherwise stated. The phase lag, between the bottom and top of the lower deck, mentioned in the last section, can be seen in the forward twist of the u- and v-velocity contour patterns. All across the lower deck, except in the region adjacent to the wall, u- and v-velocity contours are in phase with each other. However, both lag behind the w-velocity contours. This can be explained by the fact that the direction and magnitude of the disturbance motion is related to whether the slower fluid is being pushed away from the wall or faster fluid is being brought near the wall. In all these figures, the positive u contours are slightly lagged behind negative w contours, correspondingly, positive w-contours are followed by negative u-velocity contours. Disturbance-flow streamlines along the axis of symmetry, $Y = 0$, are shown in figure 38 . Similarly, we have plotted the projection of streamlines into the X-Z planes at $Y=2.0$ and $Y=4.0$, and these plots are given in figures 39 and 40, respectively.

These streamline plots are presented for flow visualization purpose only and no information about mass flow is implied by them. Hence, they should be viewed in conjunction with the actual velocity contours, given in figures 34 through 37 , to maintain the

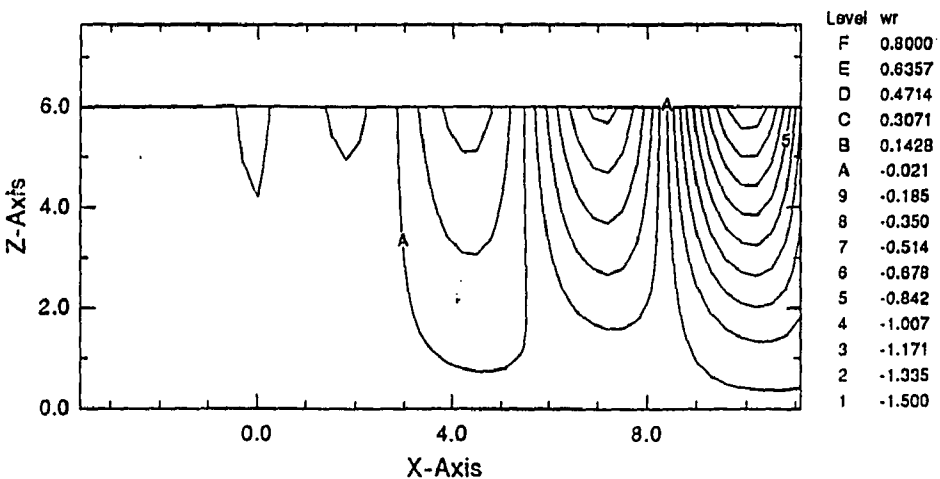
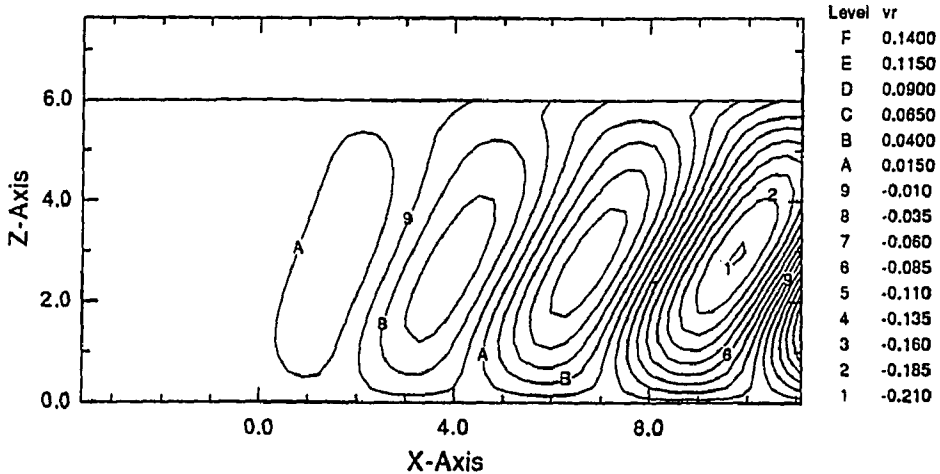
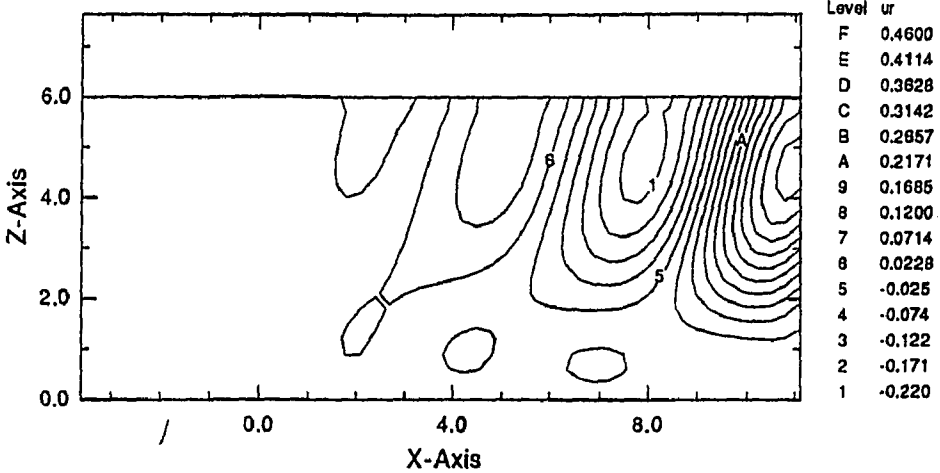


Figure 36. Contour plots of disturbance velocities, u, v, and w at $t = 0$ for $h=1.0$, $Y=2.0$, and $S_0 = 3.0$.

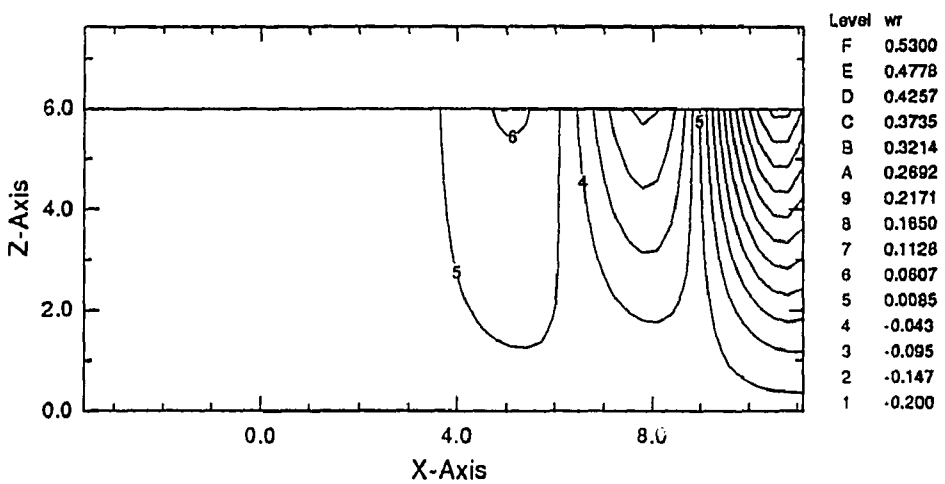
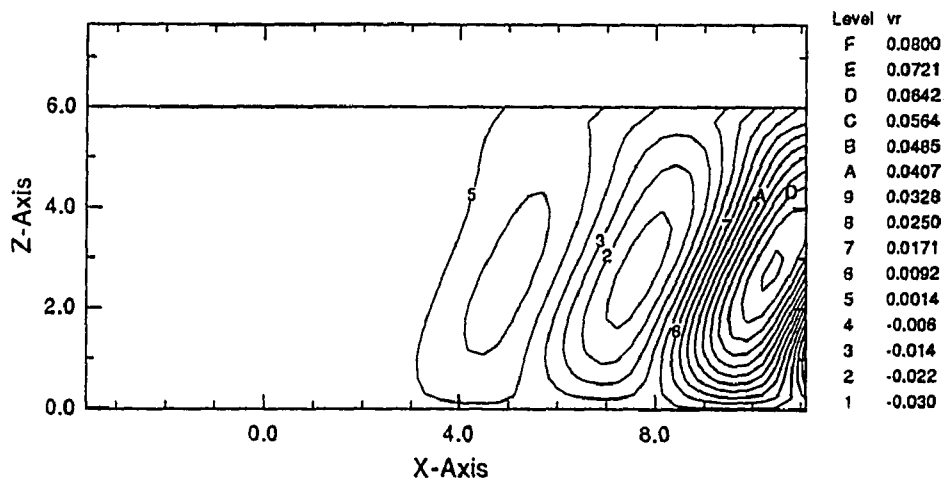
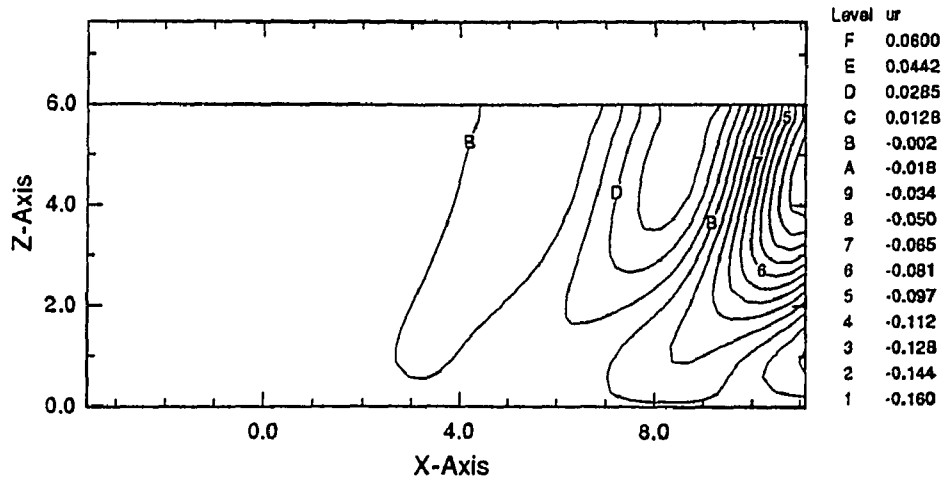


Figure 37. Contour plots of disturbance velocities, u , v , and w at $t = 0$ for $h=1.0$, $Y=4.0$, and $S_0 = 3.0$.

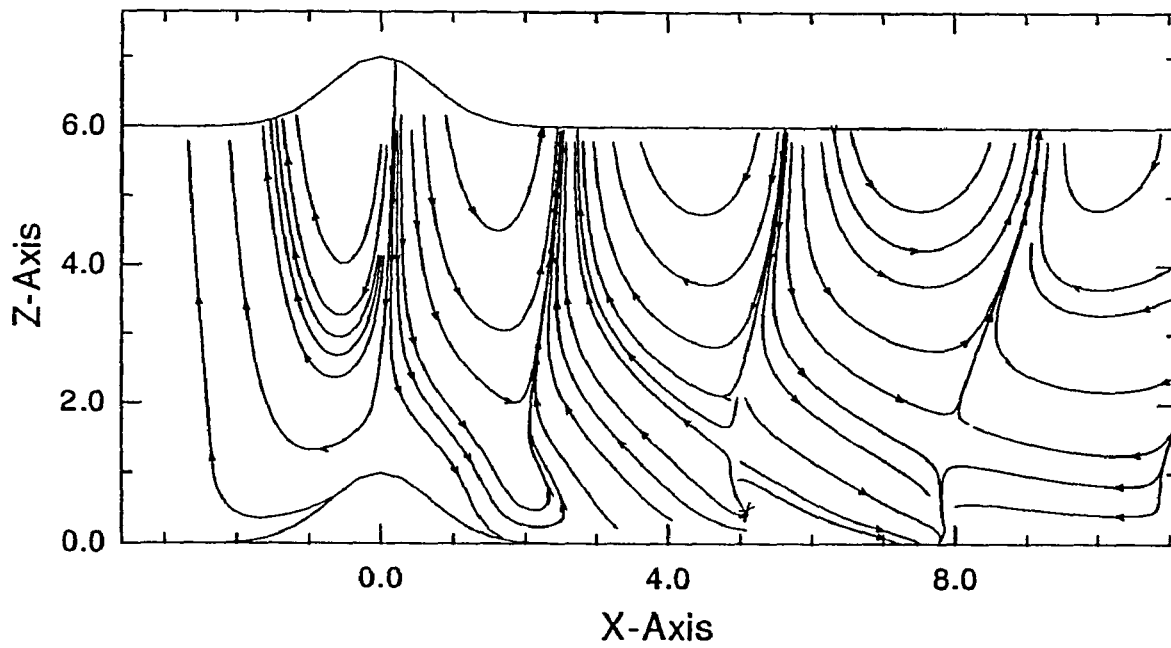


Figure 38. Disturbance-flow streamlines in the X-Z plane at $Y=0$ for $h=1.0$, $t=0$ and $S_0=3.0$.

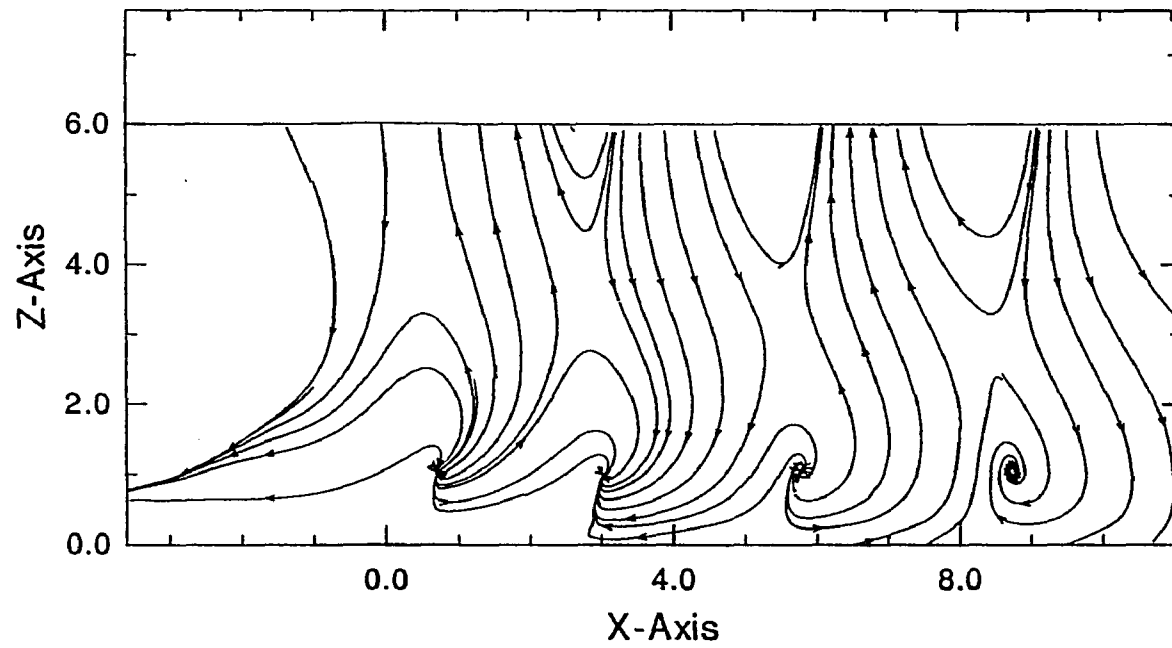


Figure 39. Projection of disturbance-flow streamlines onto the X-Z plane at $Y=2.0$ for $h=1.0$, $t=0$ and $S_0=3.0$.

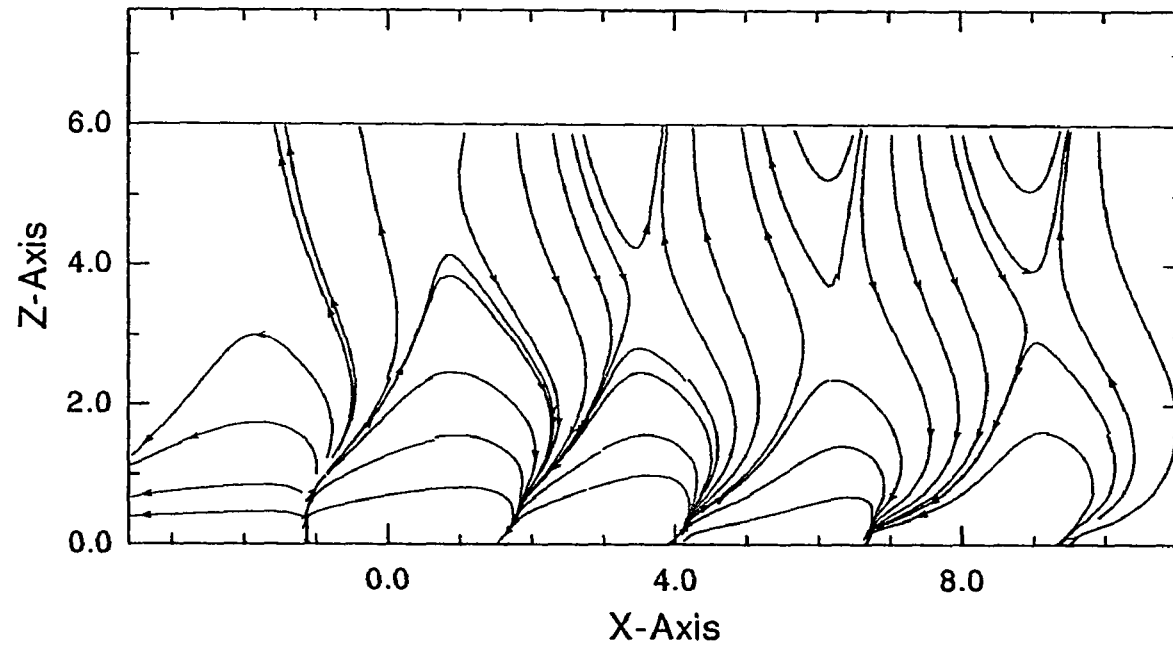


Figure 40. Projection of disturbance-flow streamlines onto the X-Z plane at $Y=4.0$ for $h=1.0$, $t=0$ and $S_0=3.0$.

strength of the flow in perspective. Evidently, the wave produces a surge of fluid away from the wall at its crests and a surge of fluid towards the wall at its troughs. Initially, the core of this fluid surge is behind the hump, on the line of symmetry, having a circular cross section (possibly due to the hump's circular cross section). As the wave moves downstream, the core divides in half and gradually shifts away from the center on both sides. This can be seen in contours of w -velocity in the X - Y plane, at $Z=3.9$, shown in figure 41. On each side of the wave crests and troughs a pair of counter-rotating vortices is formed. It should be kept in mind that we are talking about "vortices" in the disturbance flow and not the total flow, where the contribution of the steady-state flow is much larger than the small time-dependant perturbations. These vortices exist in between the regions of opposite motion in the X - Y plane. In general, the fluid motion is away from the core of the troughs, bringing fluid towards the wall, while at the same time fluid is being sucked into the core of the crests to be pushed away from the wall. These vortices are evident in the projection of streamlines into the X - Y plane at $Z=3.9$, shown in figure 42. Projections of the velocity vector into the same plane are also presented in figure 43 for completeness.

The wave motion has to satisfy the parallel flow requirement, $w \& dw/dZ = 0$ (see equation (1-73), very close to the wall. Hence, the jet-like fluid motion has to turn just above the wall. Therefore, these fluid jets close into each other near the wall and form a chain of connected U-shaped jets, bringing fluid down one end of the U and ejecting fluid from the other end. A chain of connected U-shaped jets exists on each side of the X -axis,

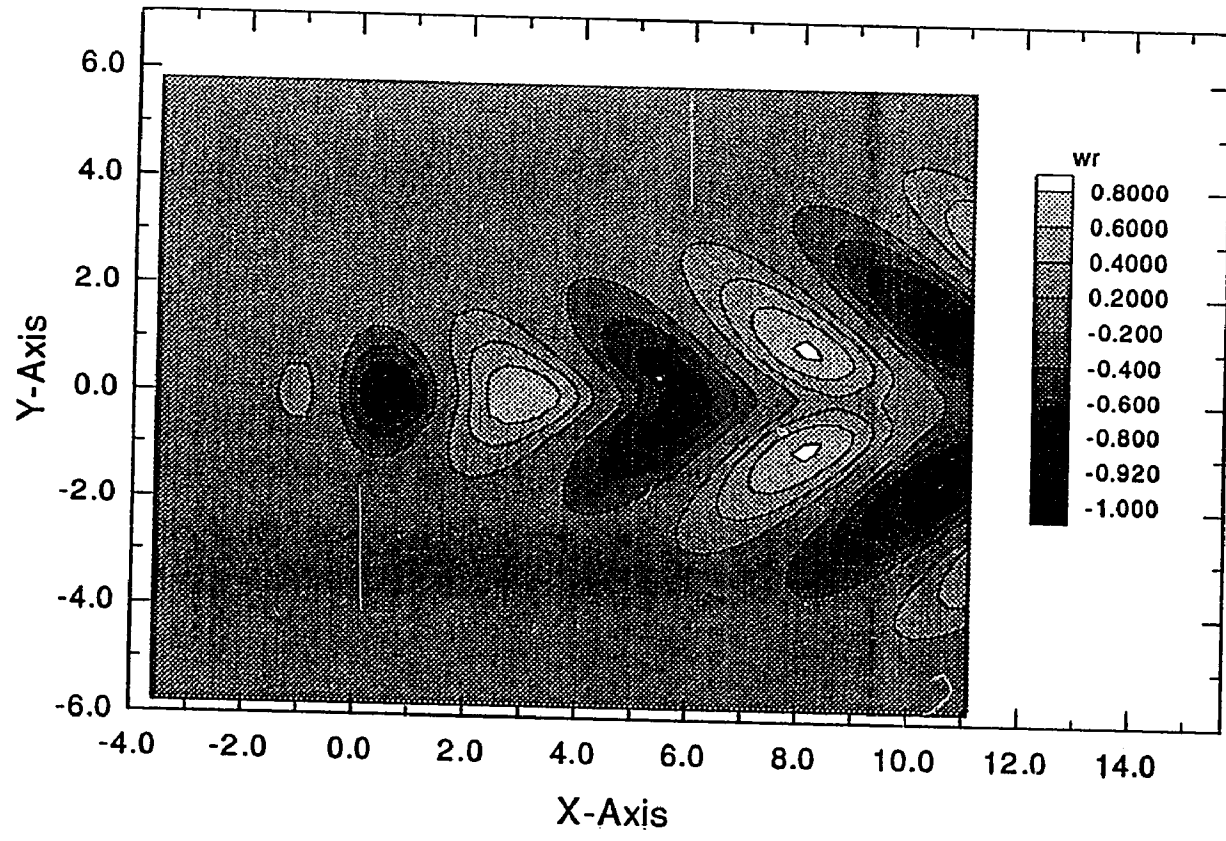


Figure 41. Contour plot of w-velocity in the X-Y plane at $Z=3.9$ for $h=1.0$, $t=0$ and $S_0=3.0$.

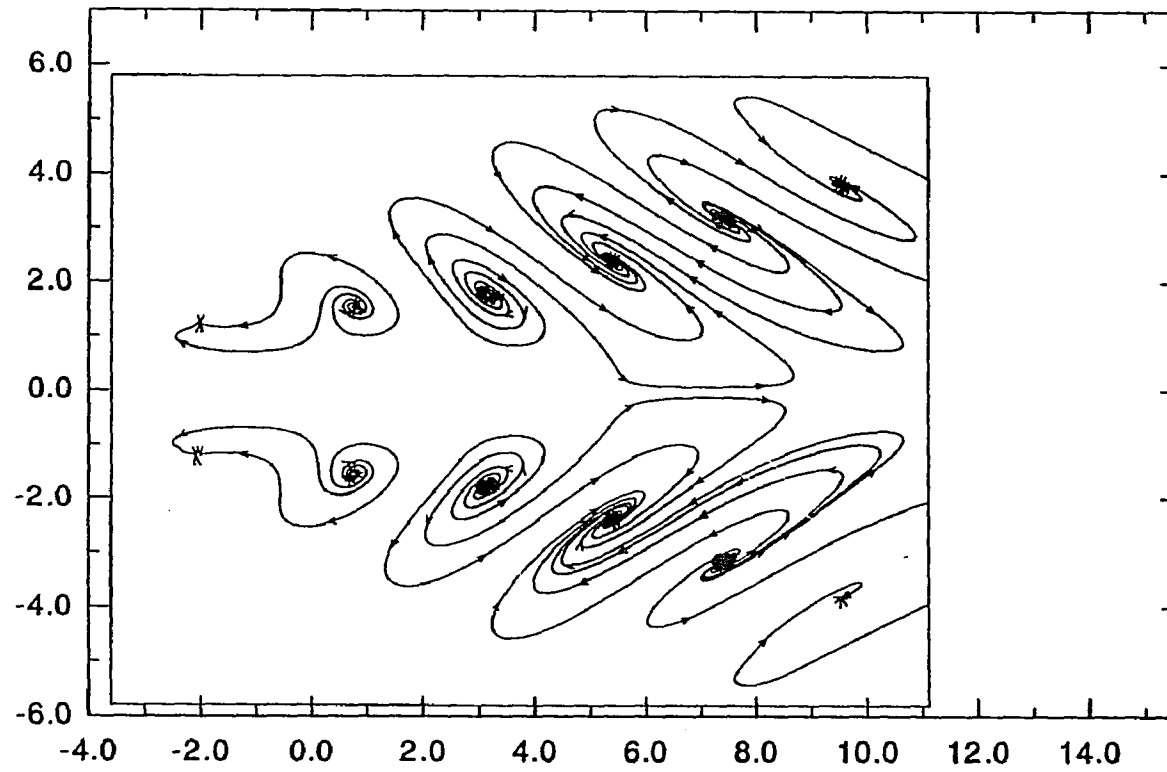


Figure 42. Projection of disturbance-flow streamlines onto the X-Y plane at $Z=3.9$ for $h=1.0$, $t=0$ and $S_0=3.0$.

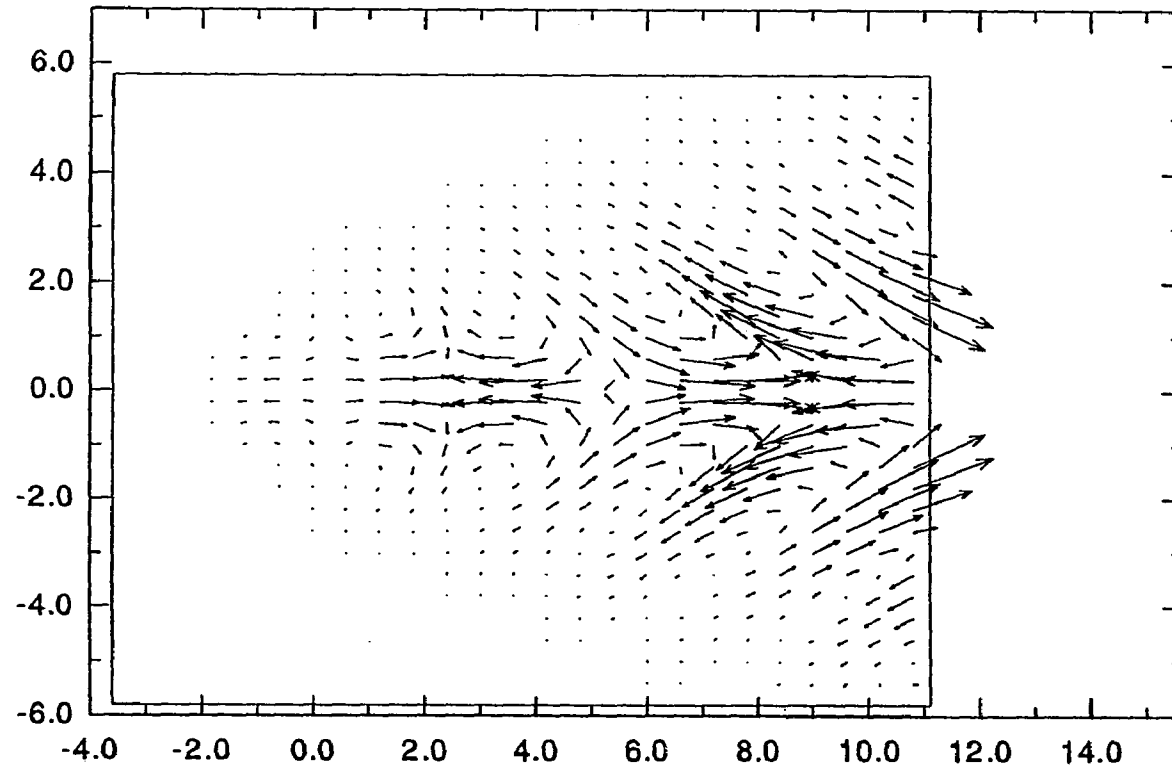


Figure 43. Projection of disturbance-flow velocity vector onto the X-Y plane at $Z=3.9$ for $h=1.0$, $t=0$ and $S_0=3.0$.

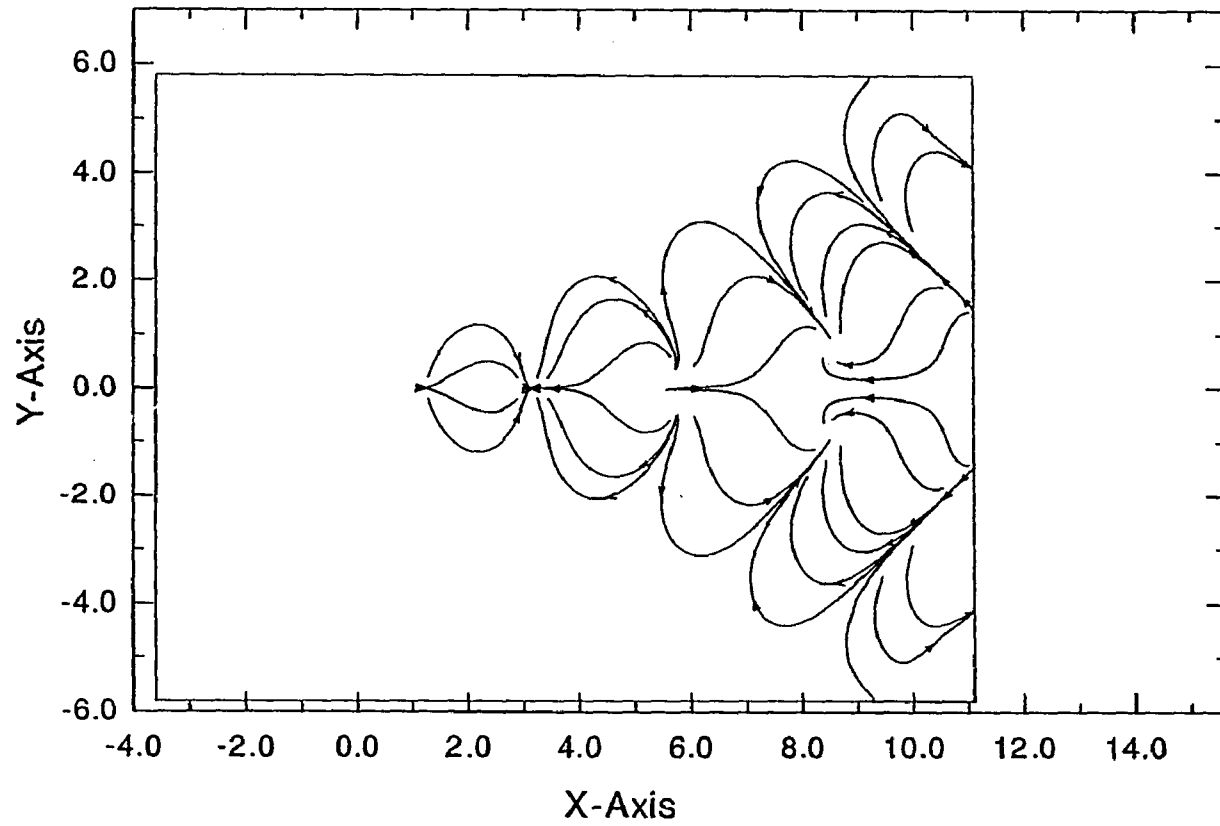


Figure 44. Disturbance surface-streamlines for $h=1.0$, $t=0$ and $S_0=3.0$.

with both chains joined right behind the hump. Both chains extend downstream at an oblique angle to the X-axis (see figures 38 through 40). To satisfy the no-slip condition and the law of conservation of mass, near the wall an accommodating flow pattern is established by the flow. This flow pattern can be viewed by looking at the disturbance surface-streamlines (skin-friction lines) shown in figure 44.

Here, we survey the disturbance flow by looking at cross sections of it projected onto the Y-Z plane at several X locations. Upstream of the hump, at $X=-1.5$, there exists a decaying motion up and away from the hump (or towards the hump at $t = \frac{\pi}{2}$). This can be seen in the velocity contours given at this location in figure 45 . Hence, the three-dimensional hump scatters the disturbance in all directions. However, it is only amplified in a wedge-shaped region extending downstream of the hump. A full wavelength of the wave can be studied by looking at the motion between the first crest at $X=3.0$ and the second crest at $X=8.7$. Contour plots of the disturbance velocity in the Y-Z plane at $X=3.0$ are given in figures 46a and 46b . Projection of the streamlines into the Y-Z plane at the same location are also shown in figure 46c . At this location, the bulk of the fluid is coming from upstream and being pushed away from the wall. The incoming flow is a portion of the fluid being pushed towards the wall at $X=6.0$. The remaining fluid is moving downstream to be pushed upwards by the second crest at $X=8.7$. The inner vortices, seen in figure 46c, are the same side vortices observed in figure 42 . These vortices also turn near the wall and form closed loops. The outer vortices in figure 46c are much weaker (see v contours in figure 46a) and are formed in response to the former by the

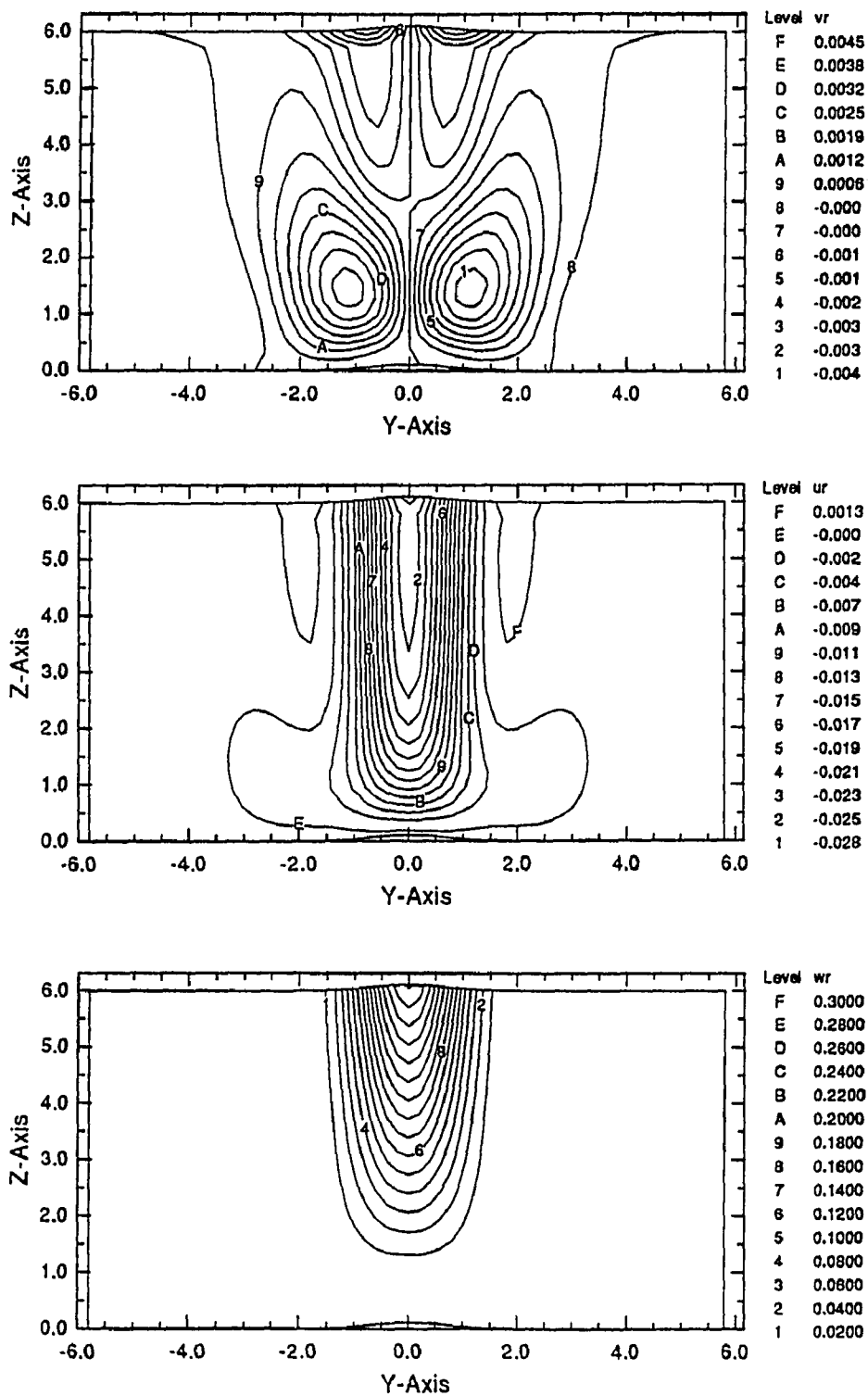


Figure 45. Contour plots of u-, v-, and w-velocity in the Y-Z plane at $X=-1.5$ for $h=1.0$, $t=0$ and $S_0=3.0$.

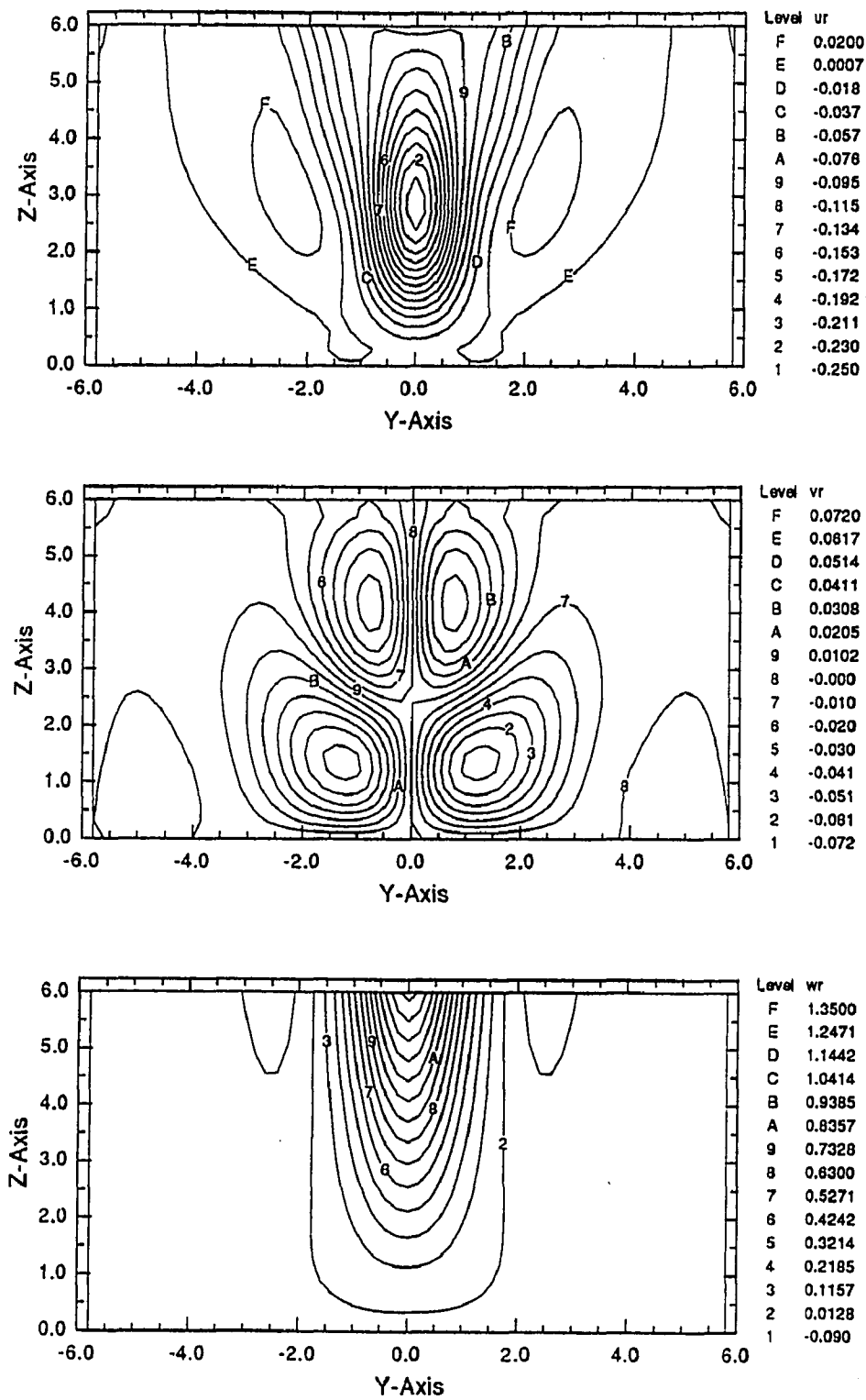
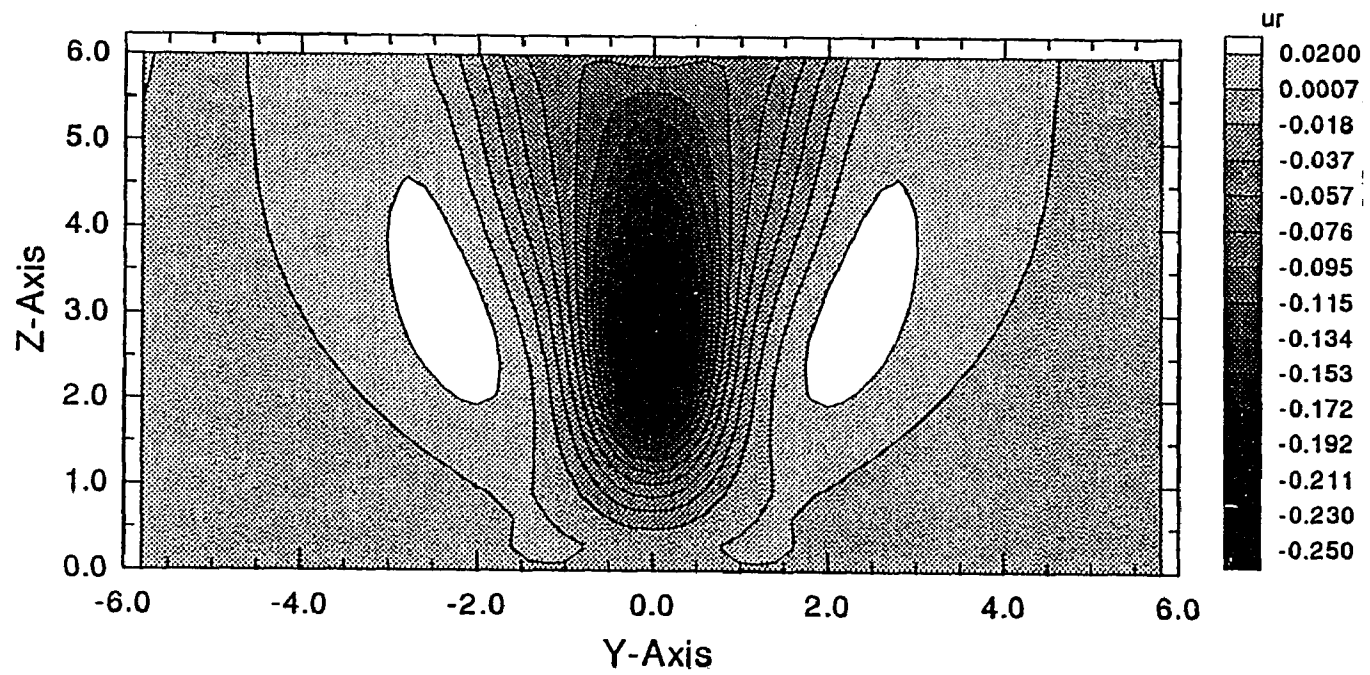


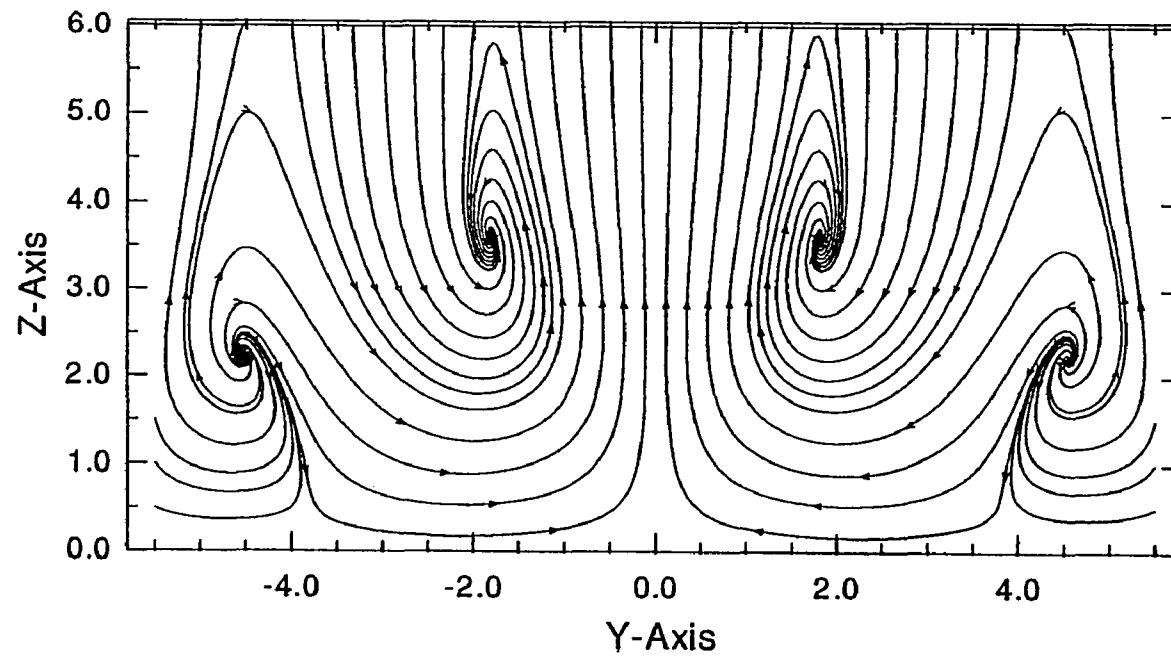
Figure 46. a) Contour plots of u-, v-, and w-velocity in the Y-Z plane at X=3.0 for h=1.0, t = 0 and S₀ = 3.0 .

Figure 46. continued



b) Contour plot of u-velocity in the Y-Z plane at $X=3.0$ for $h=1.0$, $t=0$ and $S_0=3.0$.

Figure 46. continued



c) Projection of disturbance-flow streamlines onto the Y-Z plane at $X=3.0$ for $h=1.0$,
 $t=0$ and $S_0=3.0$.

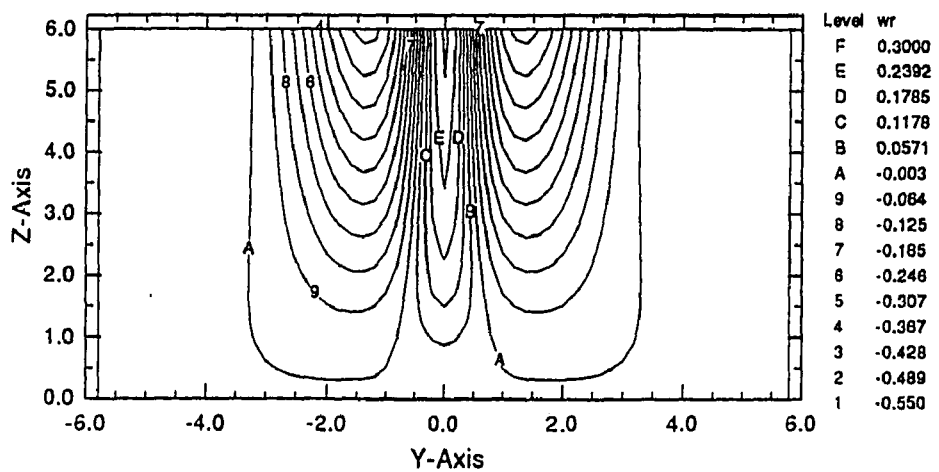
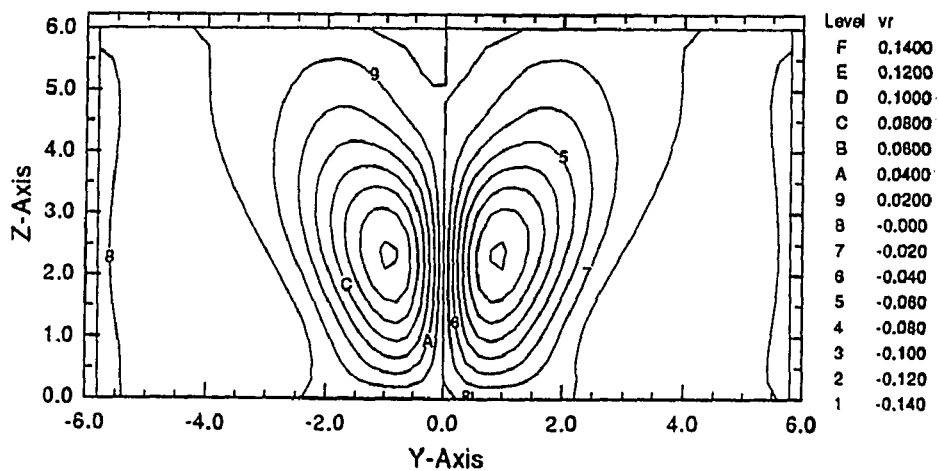
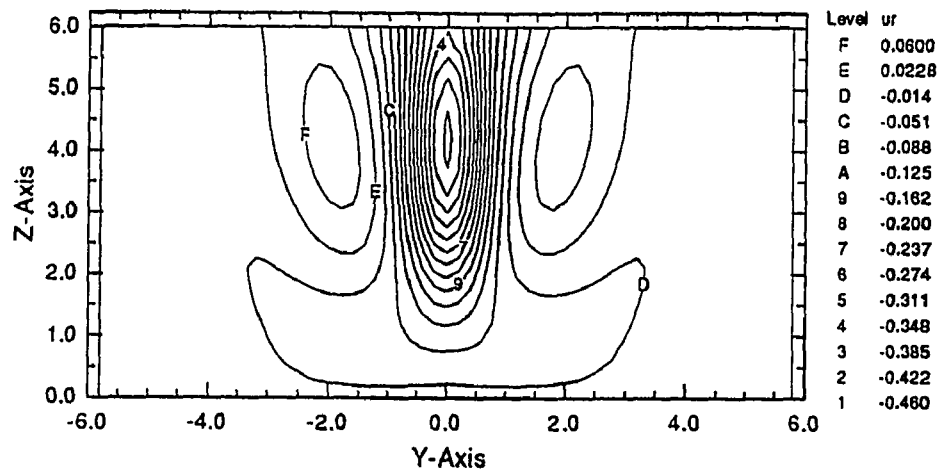
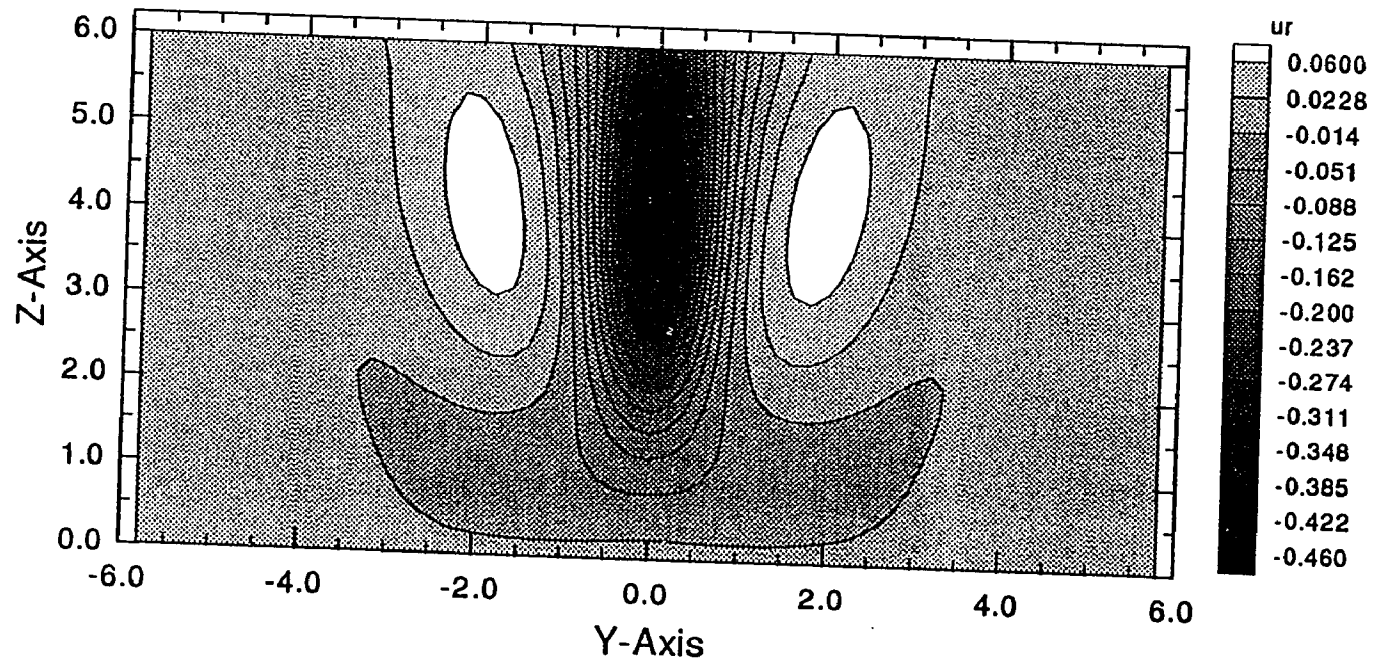


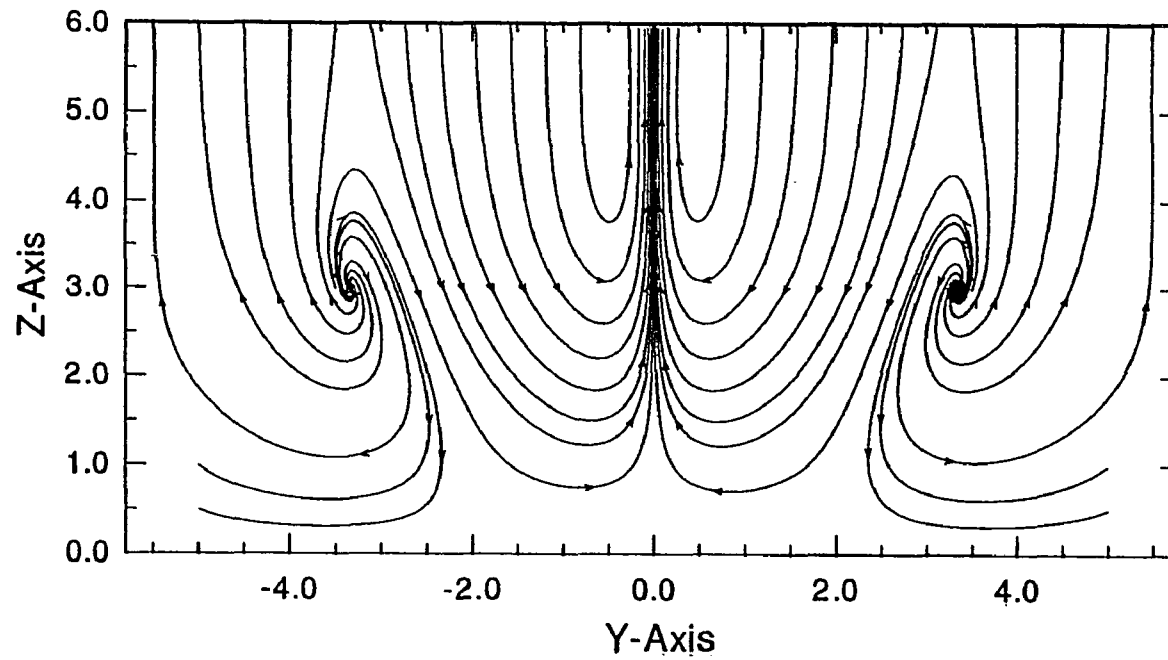
Figure 47. a) Contour plots of u-, v-, and w-velocity in the Y-Z plane at X=4.2 for h=1.0, t = 0 and S₀ = 3.0 .

Figure 47. continued



b) Contour plot of u-velocity in the Y-Z plane at $X=4.2$ for $h=1.0$, $t=0$ and $S_0=3.0$.

Figure 47. continued



c) Projection of disturbance-flow streamlines onto the Y-Z plane at $X=4.2$ for $h=1.0$,
 $t = 0$ and $S_0 = 3.0$.

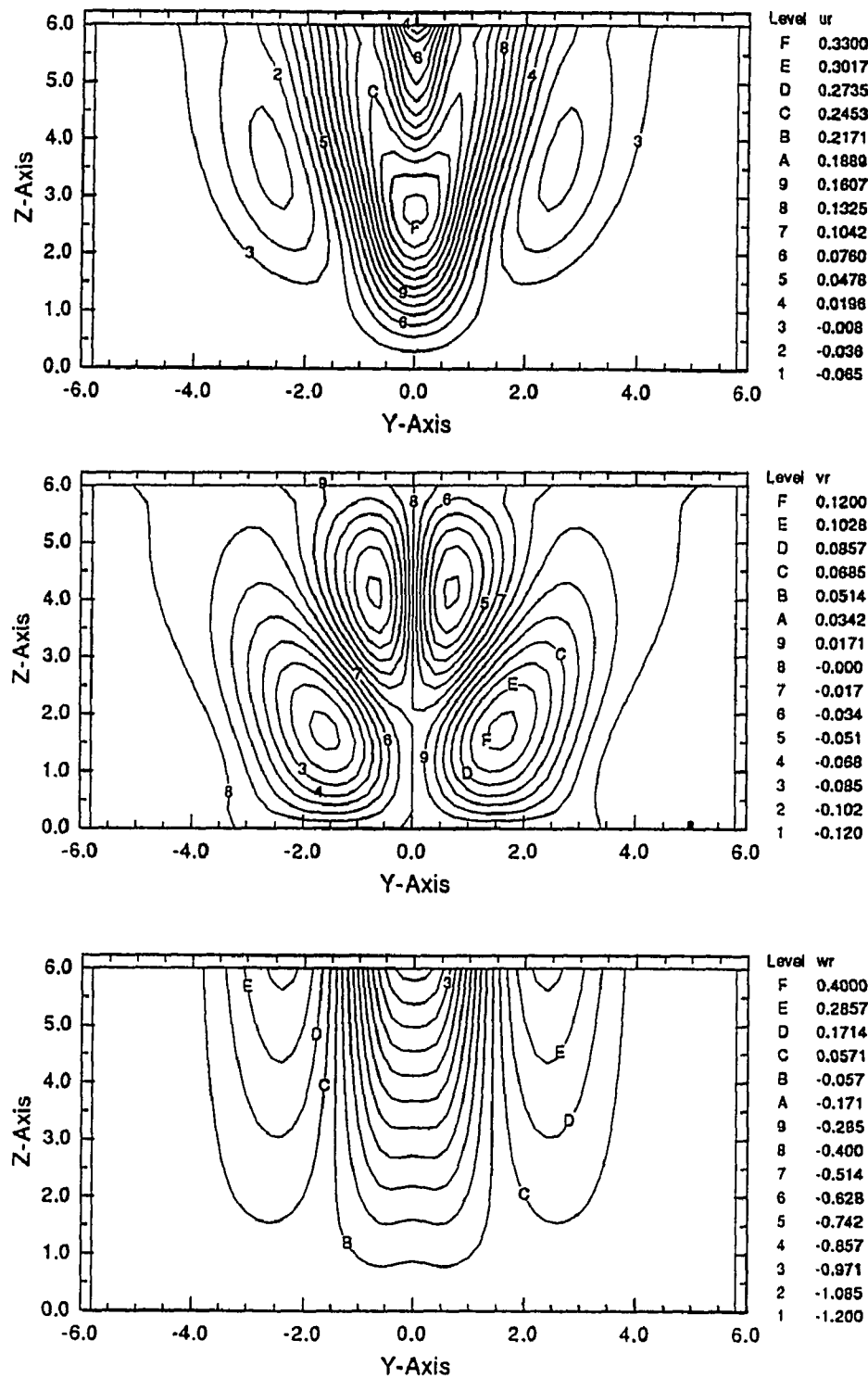
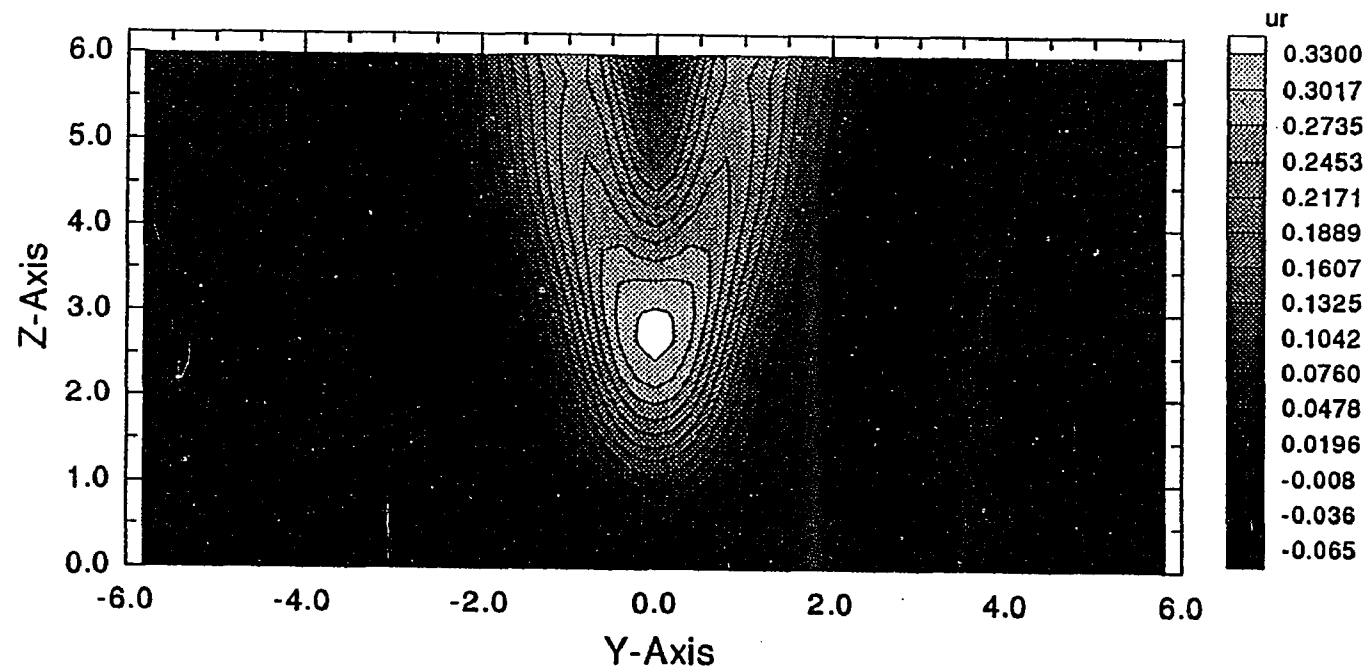


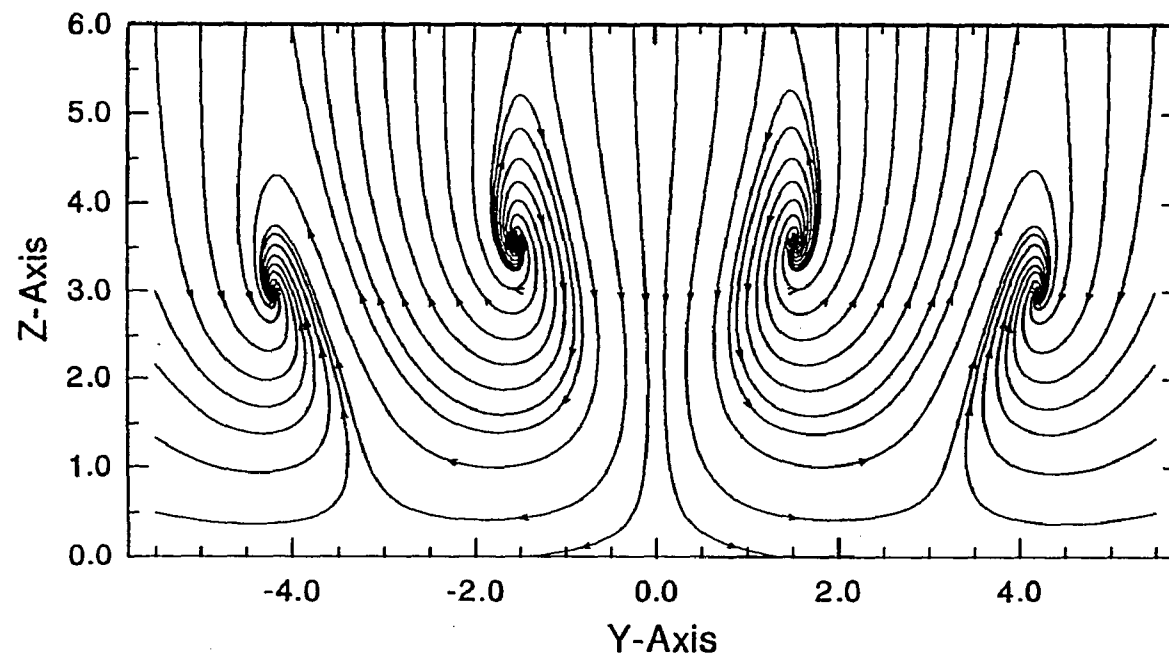
Figure 48. a) Contour plots of u -, v -, and w -velocity in the Y-Z plane at $X=6.0$ for $h=1.0$, $t=0$ and $S_0=3.0$.

Figure 48. continued



b) Contour plot of u-velocity in the Y-Z plane at X=6.0 for h=1.0, $t = 0$ and $S_0 = 3.0$.

Figure 48. continued



c) Projection of disturbance-flow streamlines onto the Y-Z plane at $X=6.0$ for $h=1.0$,
 $t=0$ and $S_0=3.0$.

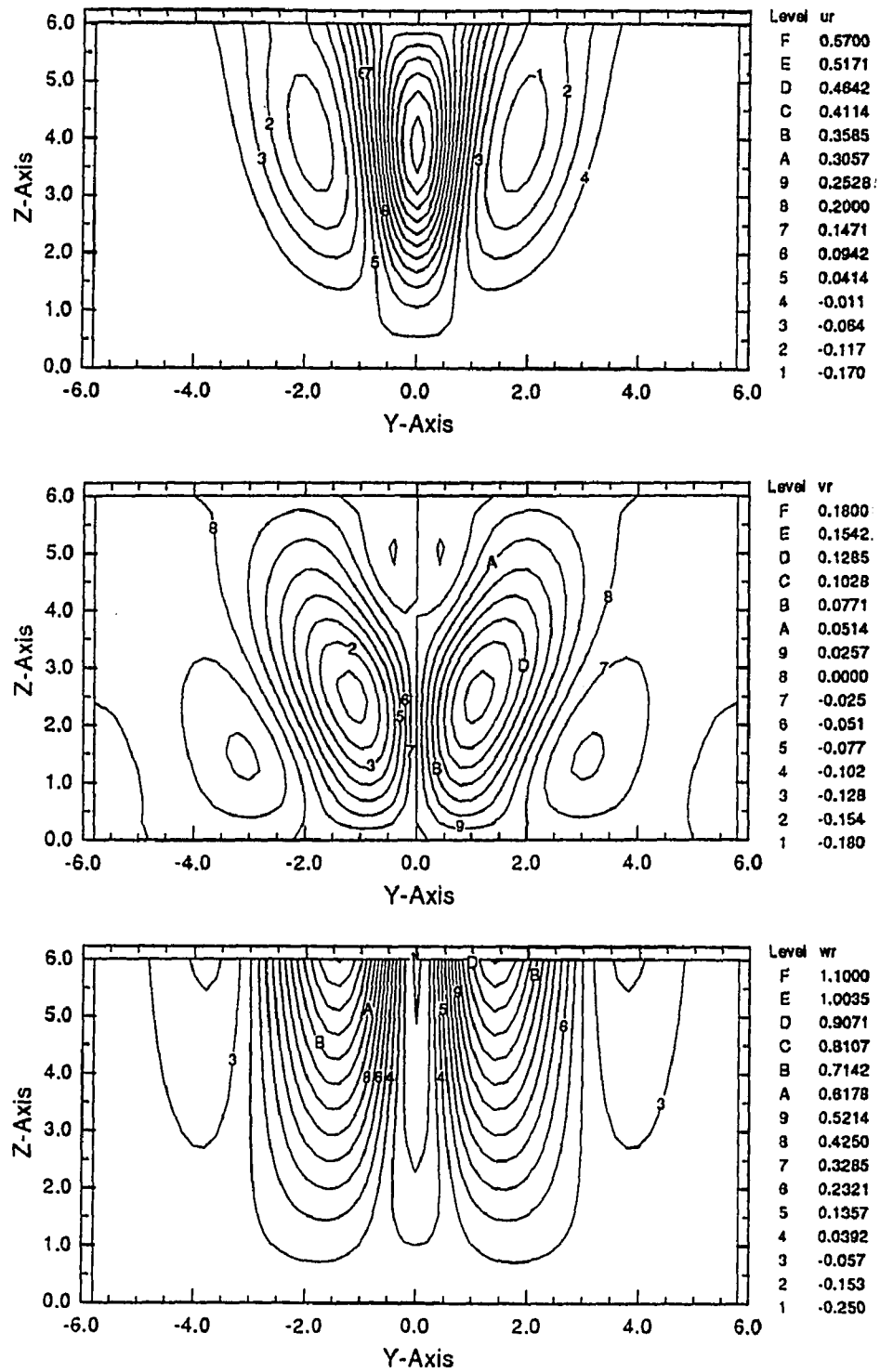
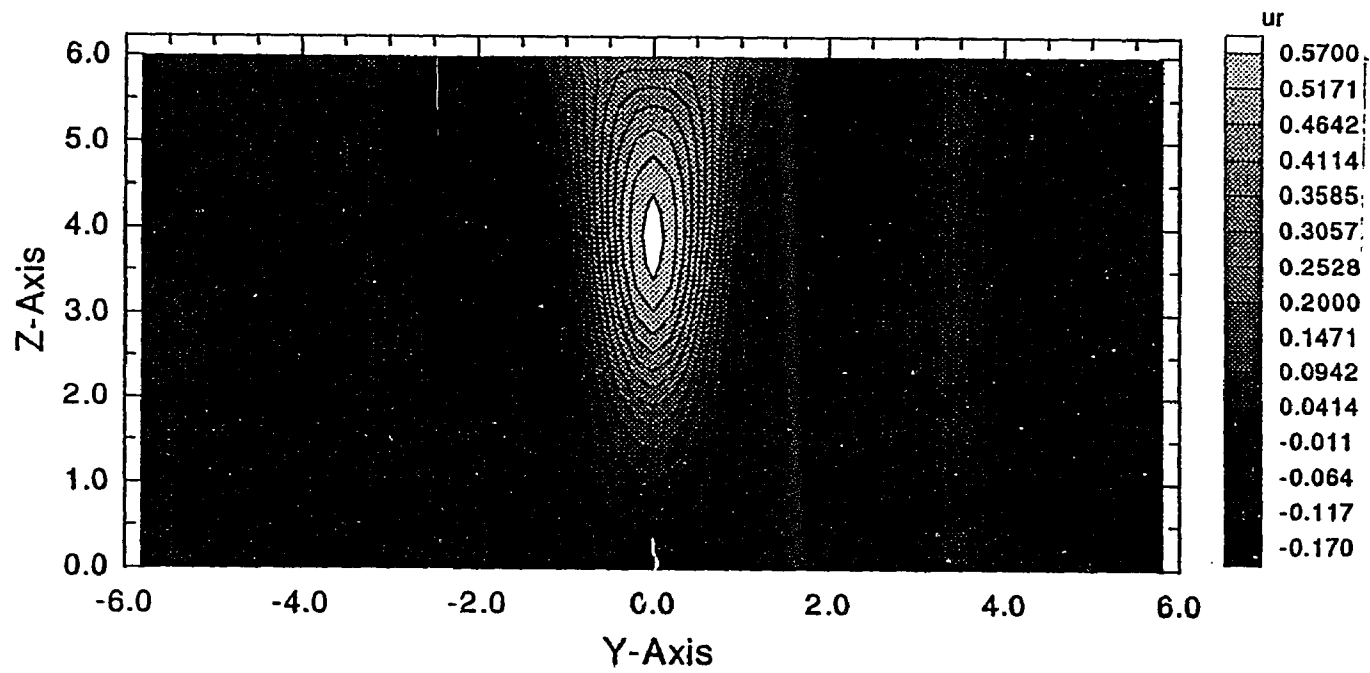


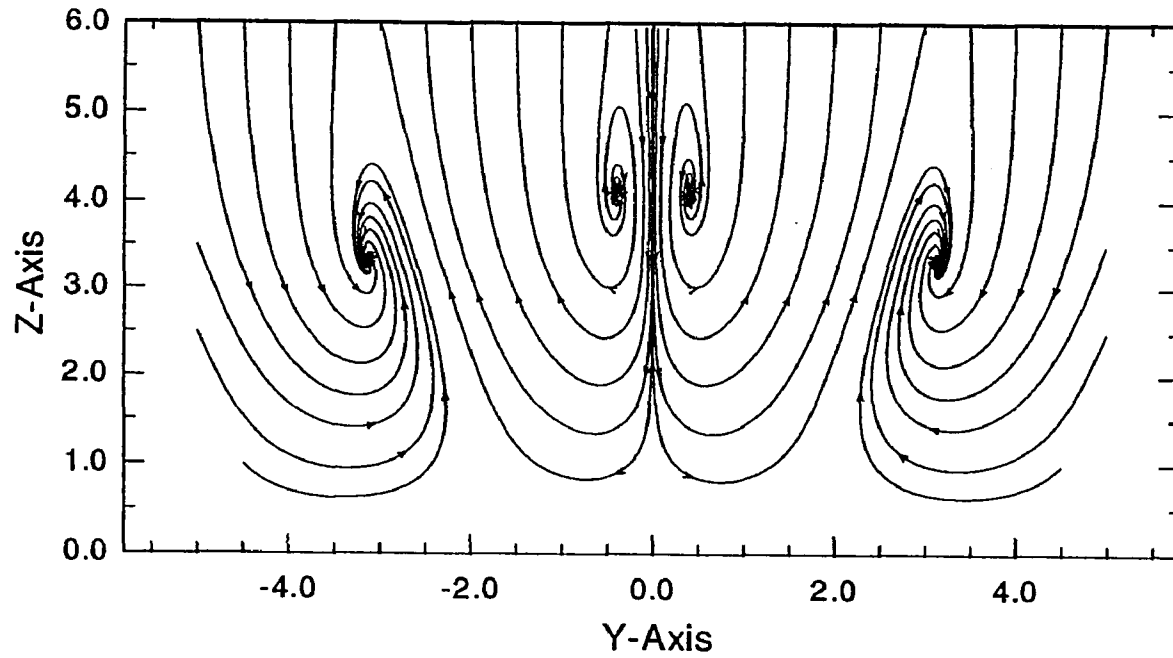
Figure 49. a) Contour plots of u -, v -, and w -velocity in the Y - Z plane at $X=7.2$ for $h=1.0$, $t=0$ and $S_0=3.0$.

Figure 49. continued



b) Contour plot of u-velocity in the Y-Z plane at X=7.2 for h=1.0, $t = 0$ and $S_0 = 3.0$.

Figure 49. continued



c) Projection of disturbance-flow streamlines onto the Y-Z plane at $X=7.2$ for $h=1.0$,
 $t=0$ and $S_0=3.0$.

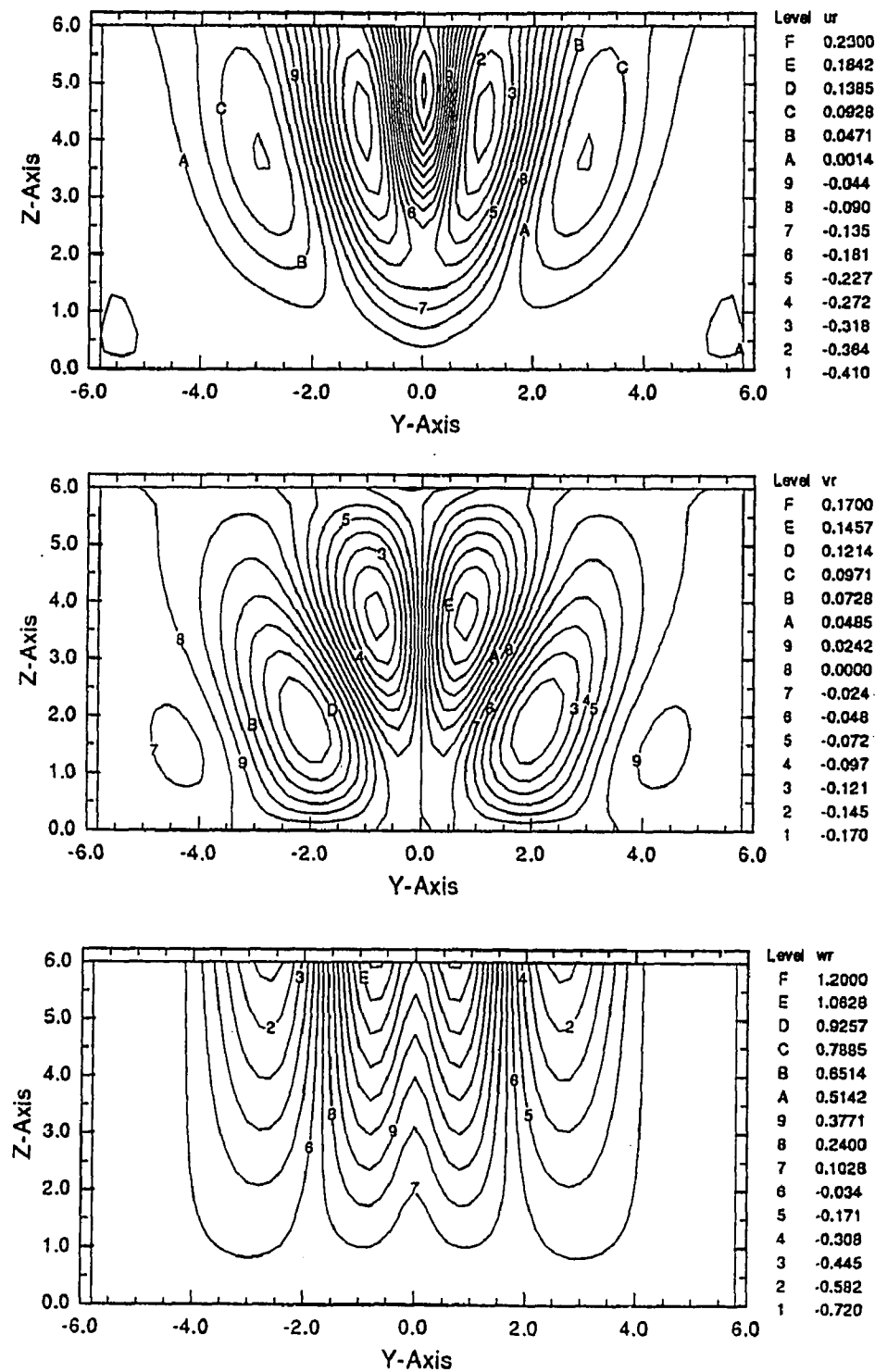
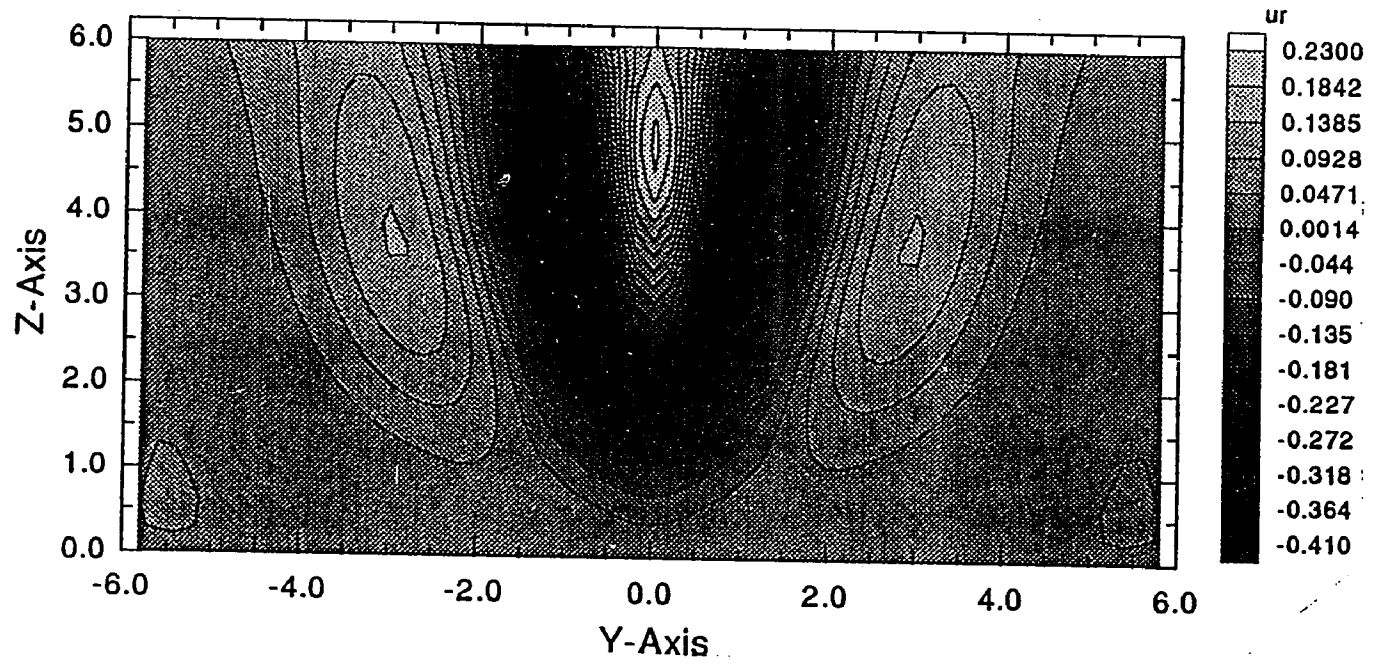


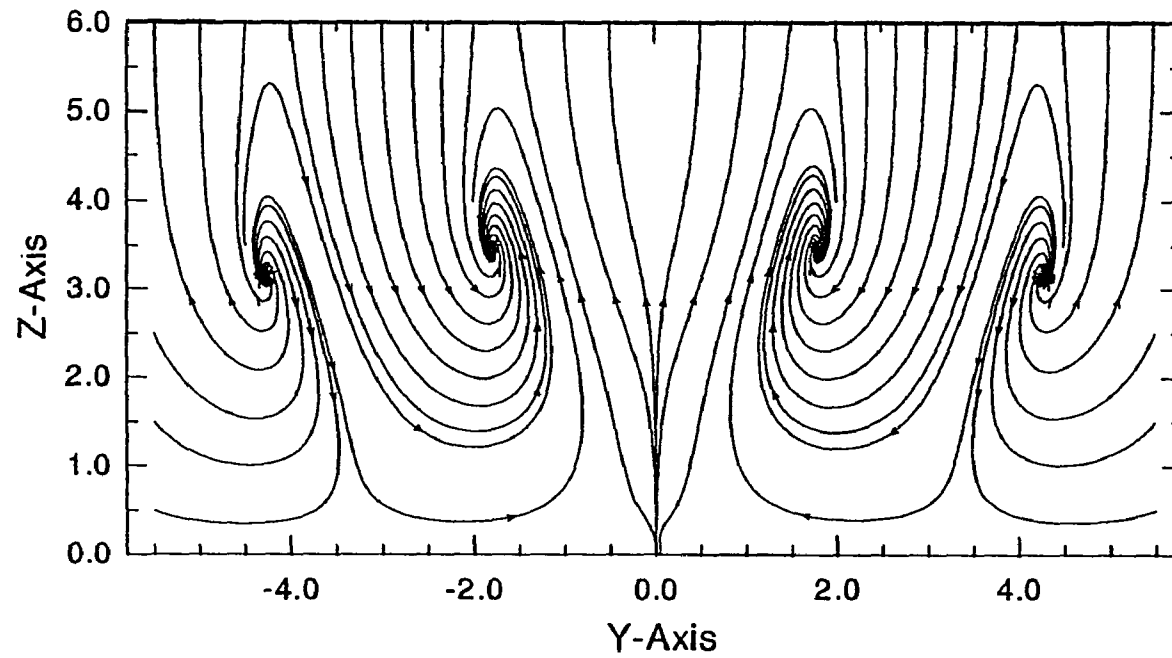
Figure 50. a) Contour plots of u -, v -, and w -velocity in the Y-Z plane at $X=8.7$ for $h=1.0$, $t=0$ and $S_0=3.0$.

Figure 50. continued



b) Contour plot of u-velocity in the Y-Z plane at $X=8.7$ for $h=1.0$, $t=0$ and $S_0=3.0$.

Figure 50. continued



c) Projection of disturbance-flow streamlines onto the Y-Z plane at $X=8.7$ for $h=1.0$,
 $t=0$ and $S_0=3.0$.

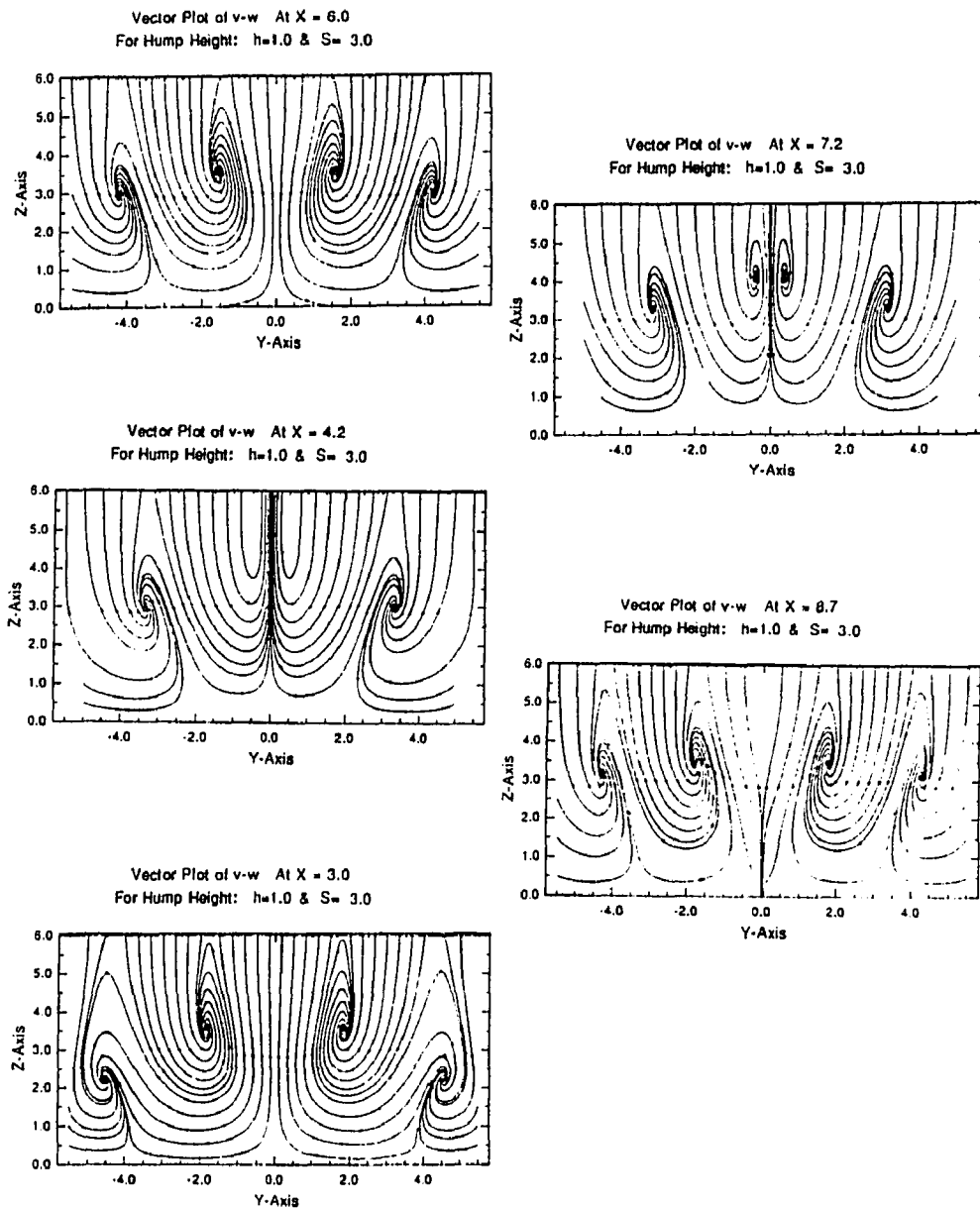


Figure 51. Projection of disturbance-flow streamlines onto the Y-Z plane at $X=3.0, 4.2, 6.0, 7.2,$ and 8.7 for $h=1.0, \tau = 0$ and $S_0 = 3.0$ (start with lower left figure).

flow pattern near the wall. The same cross flow plots at $X=4.2$, $X=6.0$, $X=7.2$, and $X=8.7$ are also presented, in figures 47 through 50 respectively. The cross-flow streamlines of the previous figures are summarized in figure 51. In figure 50b, the u -velocity contours are very similar to the ones at the first crest in figure 46b, except for the movement of the velocity peaks away from the center.

IV.3 Disturbance Flow Due to a Hump with Local Separation

To study the receptivity for the basic flow with a small separation region behind the hump, we compute the disturbance flow for the hump with $h=4.5$. Here, we need to increase the range of our mesh to accommodate for the larger hump being studied. Keeping the same grid spacing, we use the following mesh. In the streamwise direction $-5 < X < 13$; along the lateral direction we have $0 < Y < 6.0$, and in the normal direction within the lower-deck region $0 < Z < 8.7$. These values correspond to using 60, 30, and 30 points in the X , Y , and Z directions respectively. In the upper-deck region $0 < Z_u < 5.8$, corresponding to 30 points used in the Z_u direction.

However, this mesh proved to be insufficient. Numerically "converged" solutions contained numerical oscillations. This can be seen in figure 52, showing the disturbance pressure along $Y=0$ at $S_0 = 1.0$. The actual solutions are obtained by resorting to a finer mesh.

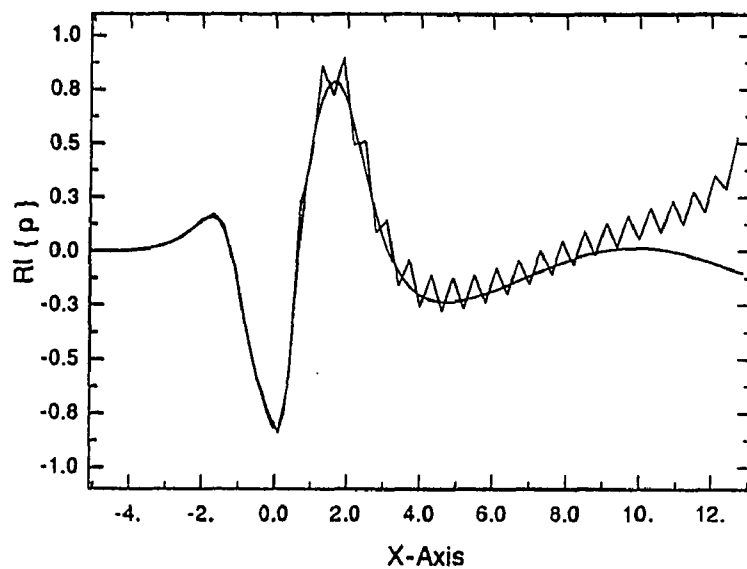



Figure 52. Plot of disturbance pressure at $Y=0$ for $h=4.5$, $S_0 = 1.0$, and $t = 0$.

(fine mesh — coarse mesh ).

In the new mesh the same range is used with twice as many points taken in the X - and Z -direction. This corresponds to $\Delta X = 0.15$ and $\Delta Z = 0.15$, using 120 and 60 points in the X and Z directions, respectively. However, numerical solutions much beyond

$S_0 = 1.0$ are not feasible due to the amount of computations required. This is explained below. Using the converged solution at $S_0 = 1.0$ as an initial guess and increasing the Strouhal number in increments of $\Delta S_0 = 0.1$, to obtain the solution for $S_0 = 1.1$ required several thousands of global iterations. Each global iteration uses 2 seconds of CPU time on CRAY Y-MP supercomputer. We expect that as the Strouhal number increases, the number of global iterations required would also increase. Hence, obtaining solutions for higher Strouhal numbers is beyond the resources available for this study. The two-dimensional studies of Bodonyi et al. [16] encountered similar difficulties beyond $S_0 = 1.2$ for steady profiles with a small separation region.

Contour plots of the disturbance pressure at times $t = 0$ and $t = \frac{\pi}{2}$ are given in figures 53a and 53b, respectively. The disturbance-pressure field clearly decays as it moves downstream. The initial kink generated by the hump is 5 to 7 times stronger than the one for $h=1.0$ shown in figure 23. In figures 54a - 54d, contour plots of disturbance velocity at times $t = 0, \frac{\pi}{4}, \frac{\pi}{2},$ and $\frac{3\pi}{4}$ are given, respectively. The disturbance-velocity contour patterns are similar to the ones for $h=1.0$ in shape. However, in the half wavelength available by our computations, the velocity profiles amplify significantly as they move downstream. Furthermore, the peaks in u-velocity contours are 12 to 34 times larger than the ones found for $h=1.0$ (see figures 25 and 26). This is probably caused by the much higher velocity gradients present behind the larger hump (see figure 7).

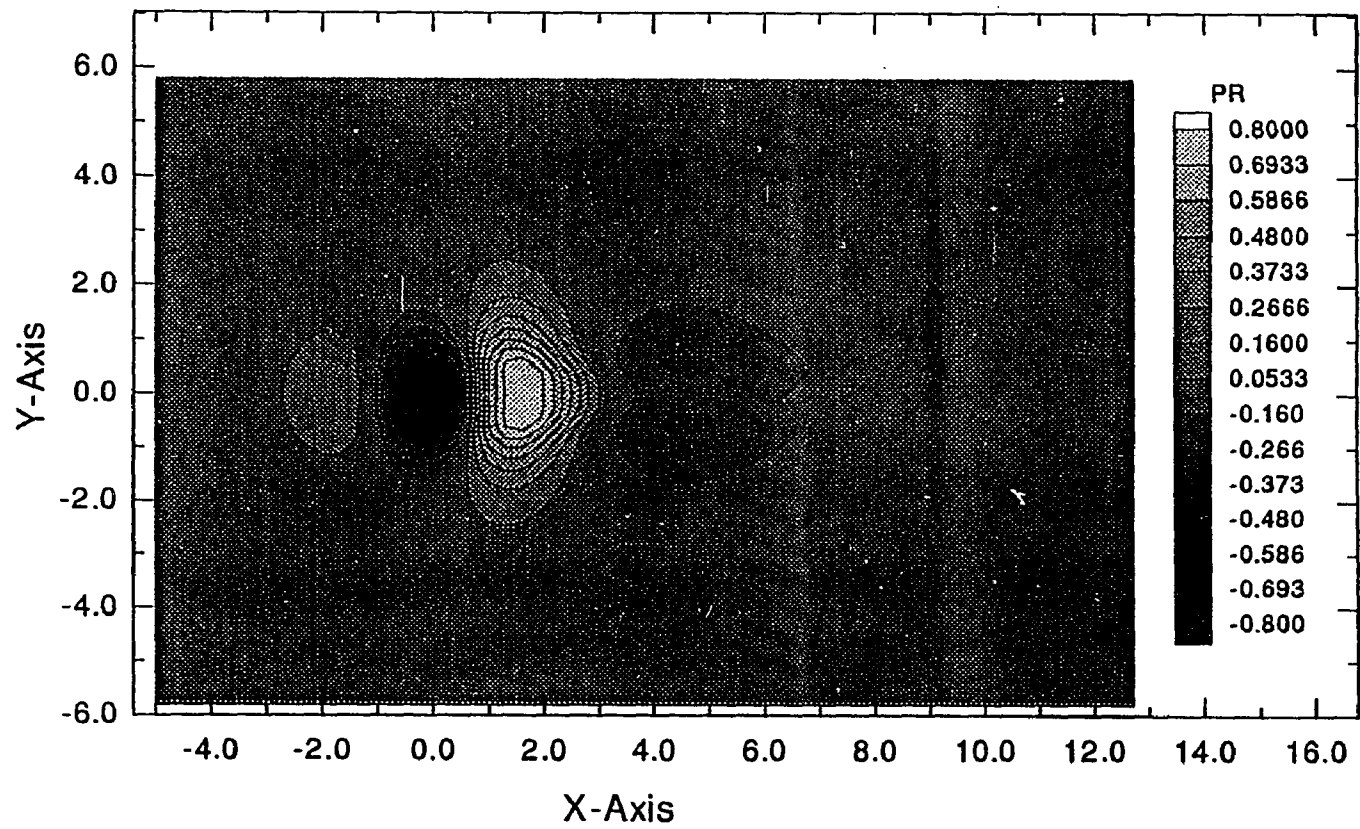
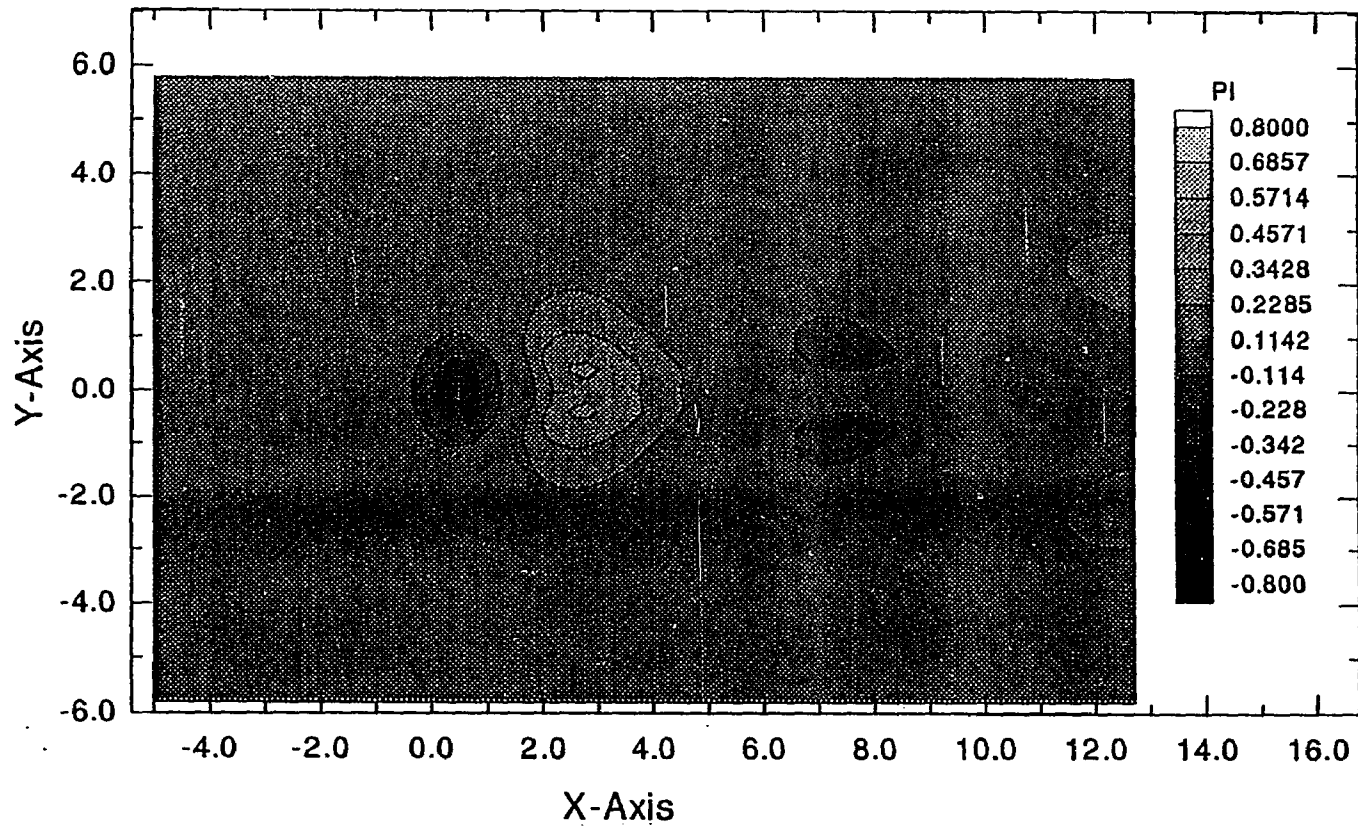


Figure 53. a) Contour plot of disturbance pressure for $h=4.5$, $t = 0$ and $S_0 = 1.0$.

Figure 53. continued



b) Contour plot of disturbance pressure for $h=4.5$, $t = \frac{\pi}{2}$ and $S_0 = 1.0$.

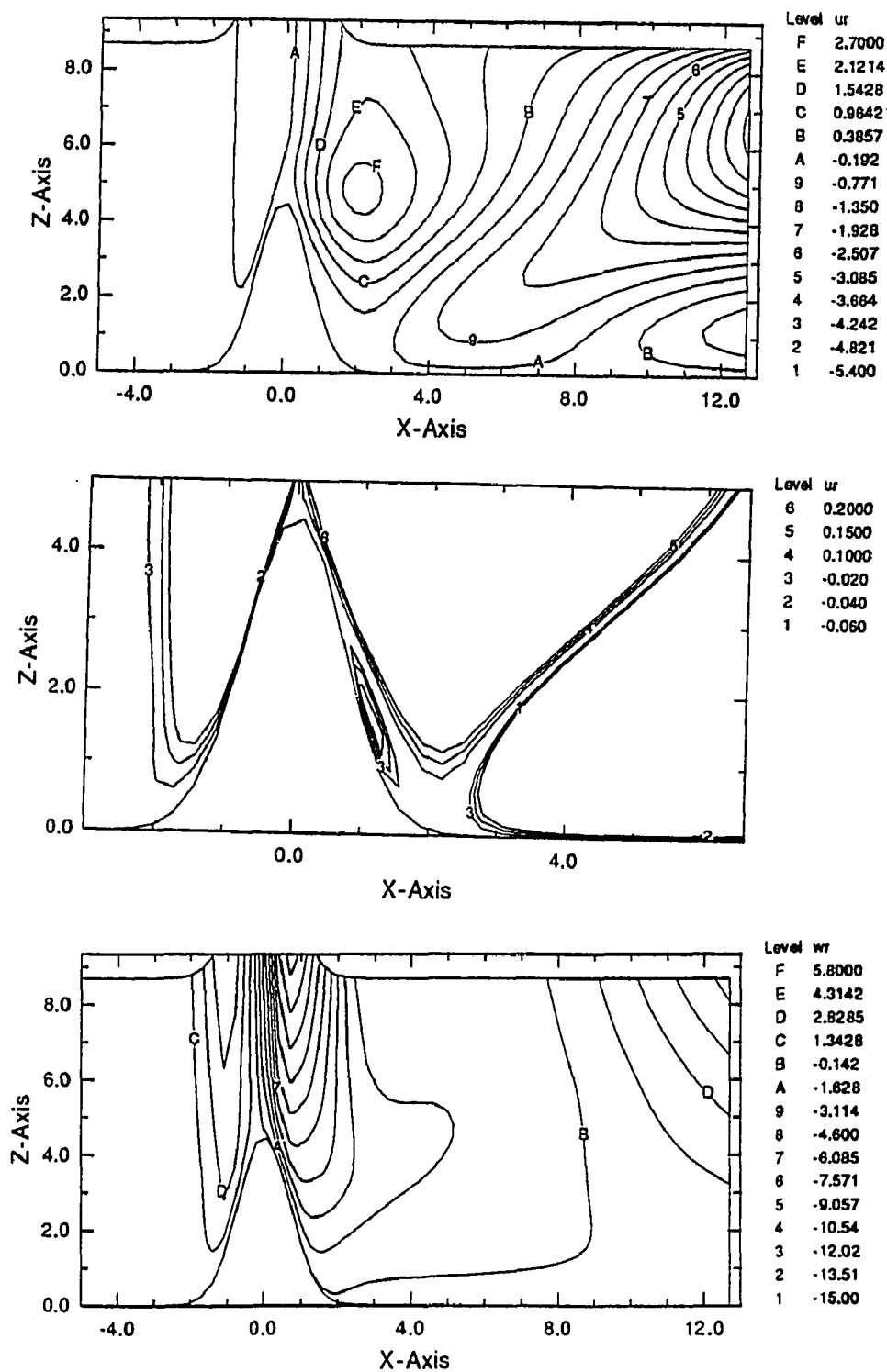
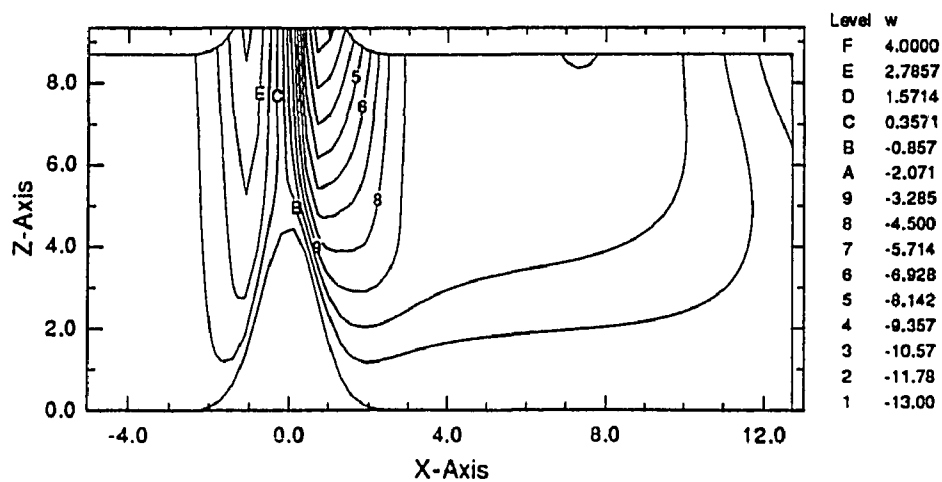
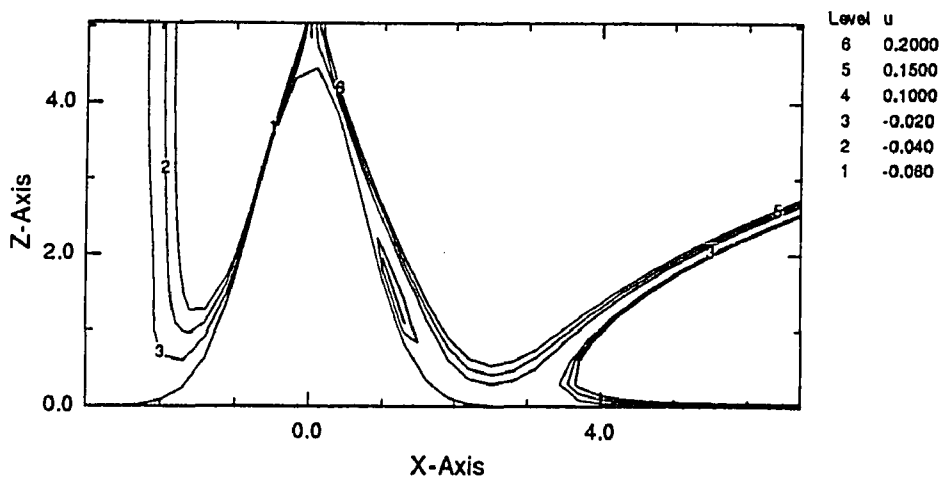
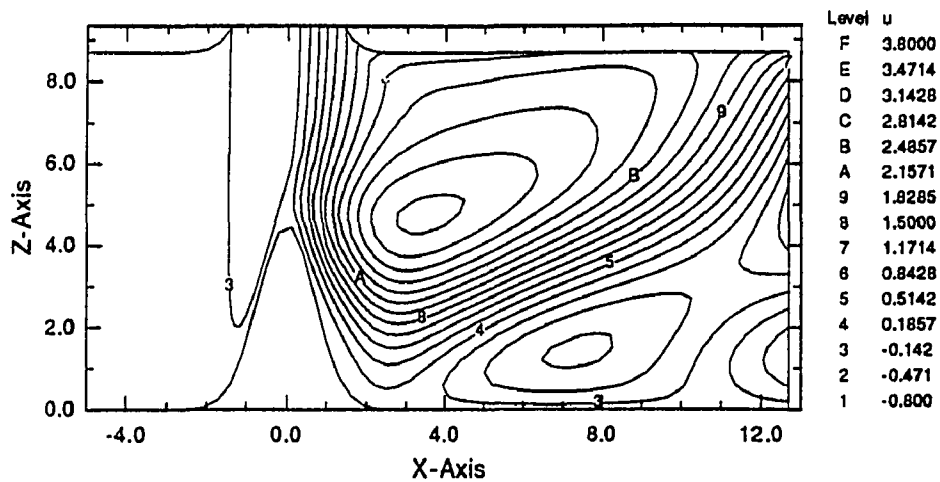


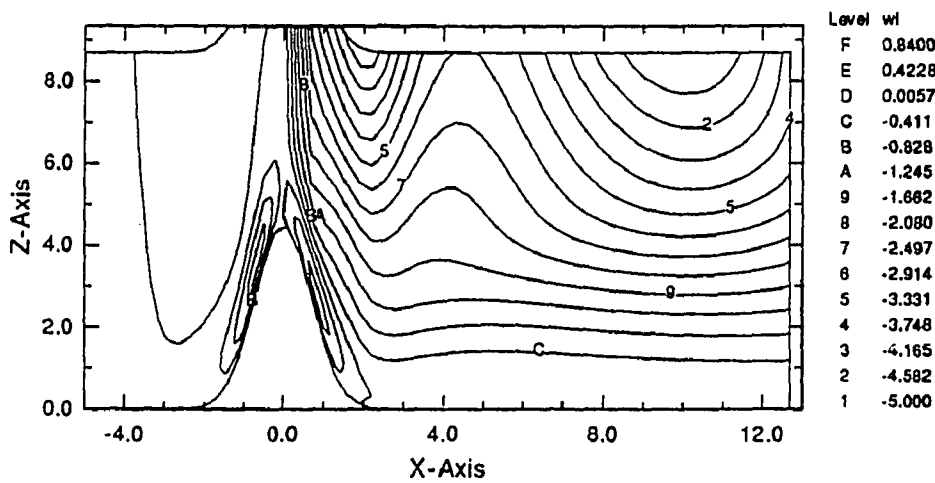
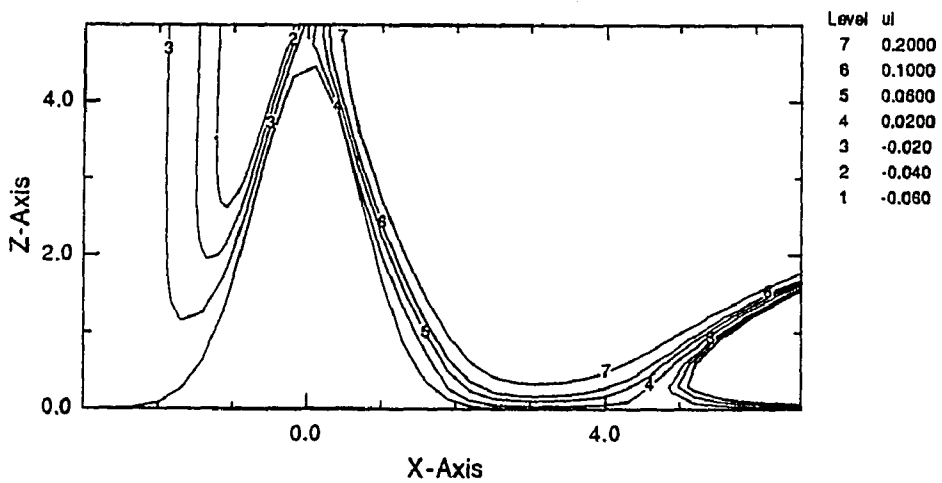
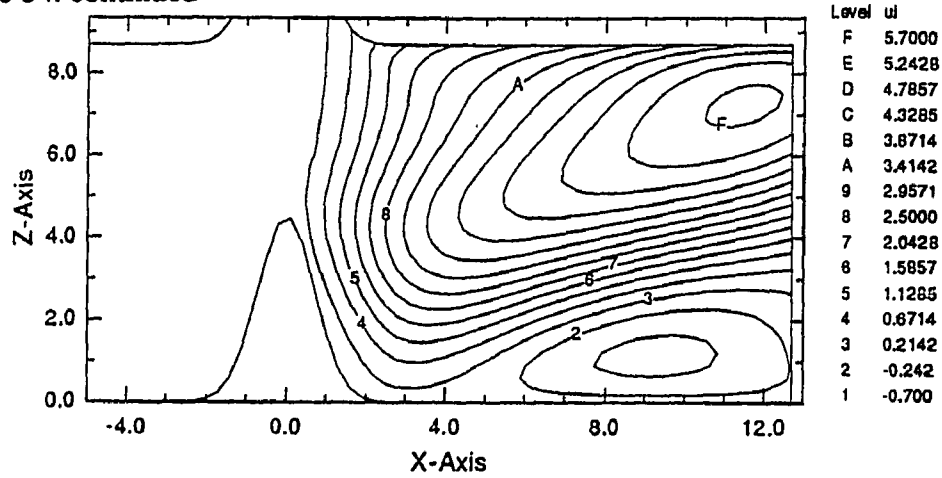
Figure 54. a) Contour plots of u - and w -velocity in the X-Z plane at $Y=0$ for $h=4.5$, $t=0$ and $S_0=1.0$ (the middle figure is a magnification of the u contours near the hump).

Figure 54. continued



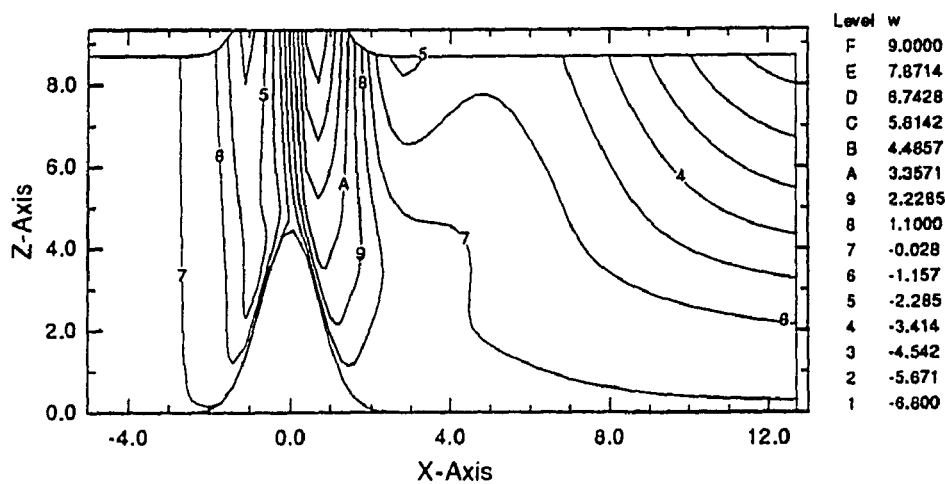
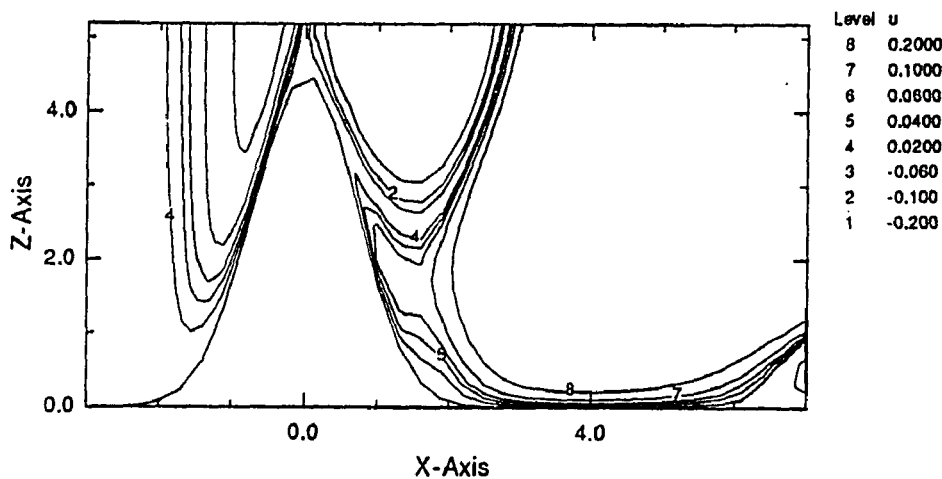
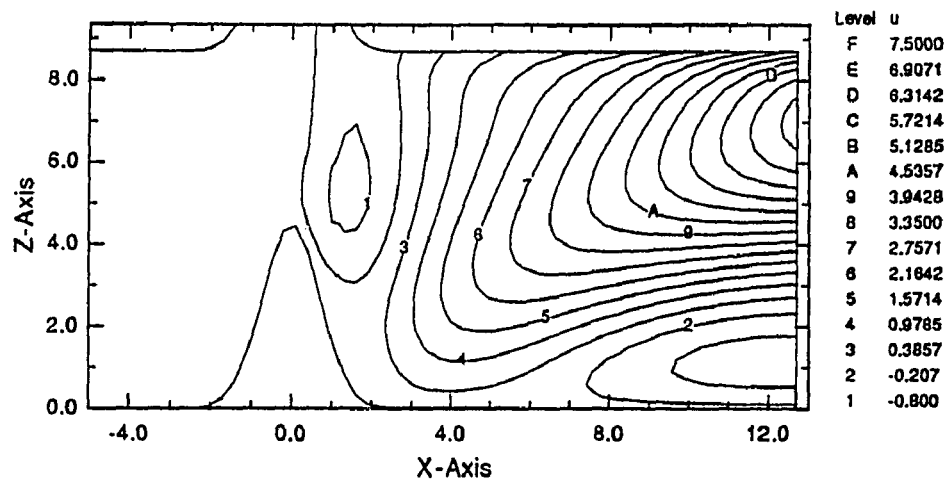
b) Contour plots of u - and w -velocity in the X - Z plane at $Y=0$ for $h=4.5$, $t = \frac{\pi}{4}$ and $S_0 = 1.0$ (the middle figure is a magnification of the u contours near the hump).

Figure 54. continued



c) Contour plots of u- and w-velocity in the X-Z plane at Y=0 for $h=4.5$, $t = \frac{\pi}{2}$ and $S_0 = 1.0$
 (the middle figure is a magnification of the u contours near the hump).

Figure 54. continued



- d) Contour plots of u - and w -velocity in the X - Z plane at $Y=0$ for $h=4.5$, $t = \frac{3\pi}{4}$ and $S_0 = 1.0$
 (the middle figure is a magnification of the u contours near the hump).

Since the pressure field decays as it moves downstream, we expect that the wave is spatially decaying at $S_0 = 1.0$. Nevertheless, we expect a nonlinear increase in the receptivity to be caused by the larger hump. The u-velocity contour plots are magnified to examine the separated mean-flow region in figures 53 and 54. The disturbance seems to have been damped inside the small separated region behind the hump from time $t = 0$ to $t = \frac{\pi}{2}$.

IV.4 Discussion and Conclusions

In the absence of any roughness element, the free-stream disturbances, to the first order, produce the classical Stokes flow, in the thin Stokes layer near the wall (on the order of our lower deck). However, with the introduction of a small (also stubby in our case) three-dimensional roughness element, the interaction between the hump and the Stokes flow introduces a spectrum of all spatial disturbances inside the boundary layer. For values of $S_0 < 2.29\dots$, this initial kink decays rapidly with the slowest attenuation rates occurring downstream of the hump. The Strouhal number, $S_0 = 2.29\dots$ corresponds to the asymptotic behavior of the lower branch of the neutral stability curve at high Reynolds numbers. For higher values of the scaled Strouhal number, $S_0 > 2.29\dots$, the three-dimensional hump scatters the disturbance in all directions. However, it is only amplified in a wedge-shaped region extending downstream of the hump (see figures 30 through 33). The amplification rate is increased as the Strouhal number is increased and

there is also a visible shortening in the wavelength of the disturbances associated with this increase. These effects can be seen in figures 55 through 57 presenting the disturbance pressure along the axis of symmetry, for the hump with $h=1.0$, at $S_0 = 1.0, 2.5$, and 4.0 respectively.

The disturbances generated by the hump are the classical Tollmien-Schlichting waves. In fact, the critical Strouhal number in our study, $S_0 = 2.29\dots$, describes the lower branch of the neutral-stability curve for the Blasius profile. The wavelength of these waves is of the order $O(\epsilon^3)$ (of the same scale as X and Y). The free stream is traveling at the velocity U_∞^* and the imposed infinitesimal oscillations have the frequency $\omega = 2\pi f$. Therefore, the free-stream disturbances have the wavelength $\frac{U_\infty^*}{f}$. When nondimensionalized by L^* the wavelength becomes $2\pi S^{-1}$. Hence, the interaction of much longer oscillations, order $2\pi O(\epsilon^2)$, in the free stream with a small three-dimensional roughness element have generated much shorter T-S waves, order $O(\epsilon^3)$, inside the laminar boundary layer.

Our results could qualitatively be compared with the wave-packet experiments of Gaster [4,6]. In his experiments a wave packet was injected into the boundary layer from a small hole in the wall. In figure 7 of reference [4], given here as figure 58, contours of signal amplitude and their evolution in time, as they move downstream, are shown. The smooth, elliptically shaped, initial patterns with their peak at the center are gradually distorted into kidney-shaped contours as the wave travels downstream. Two amplitude peaks are also formed on either side of the axis of symmetry as the wave moves

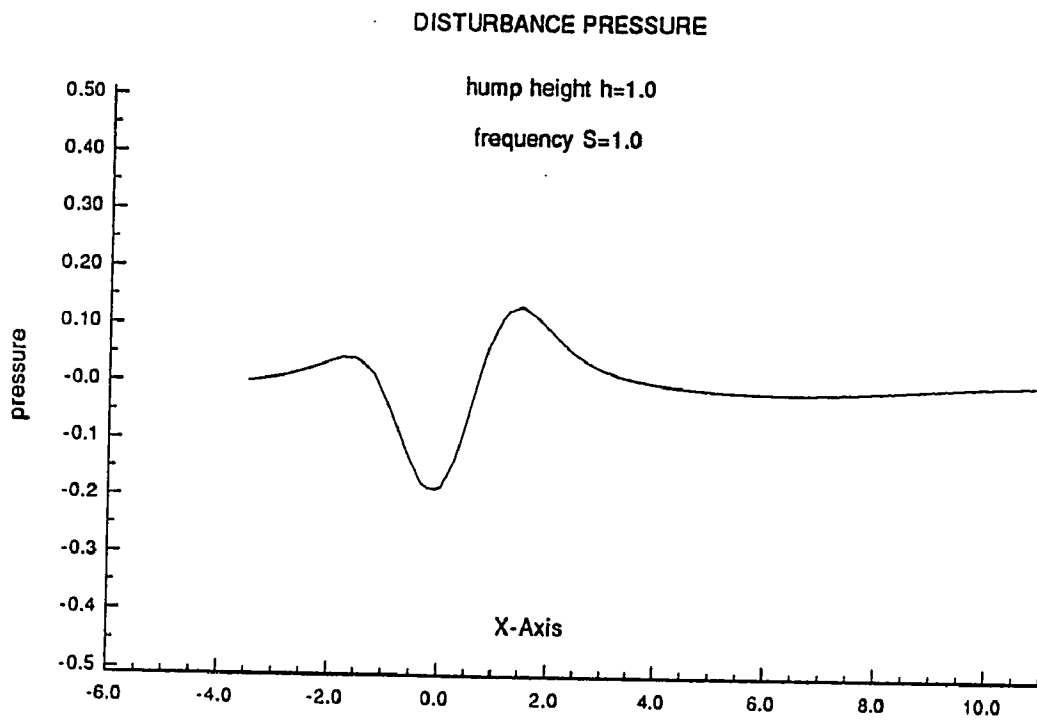


Figure 55. Plot of disturbance pressure for $h=1.0$, at $Y=0$, $t=0$ and $S_0=1.0$.

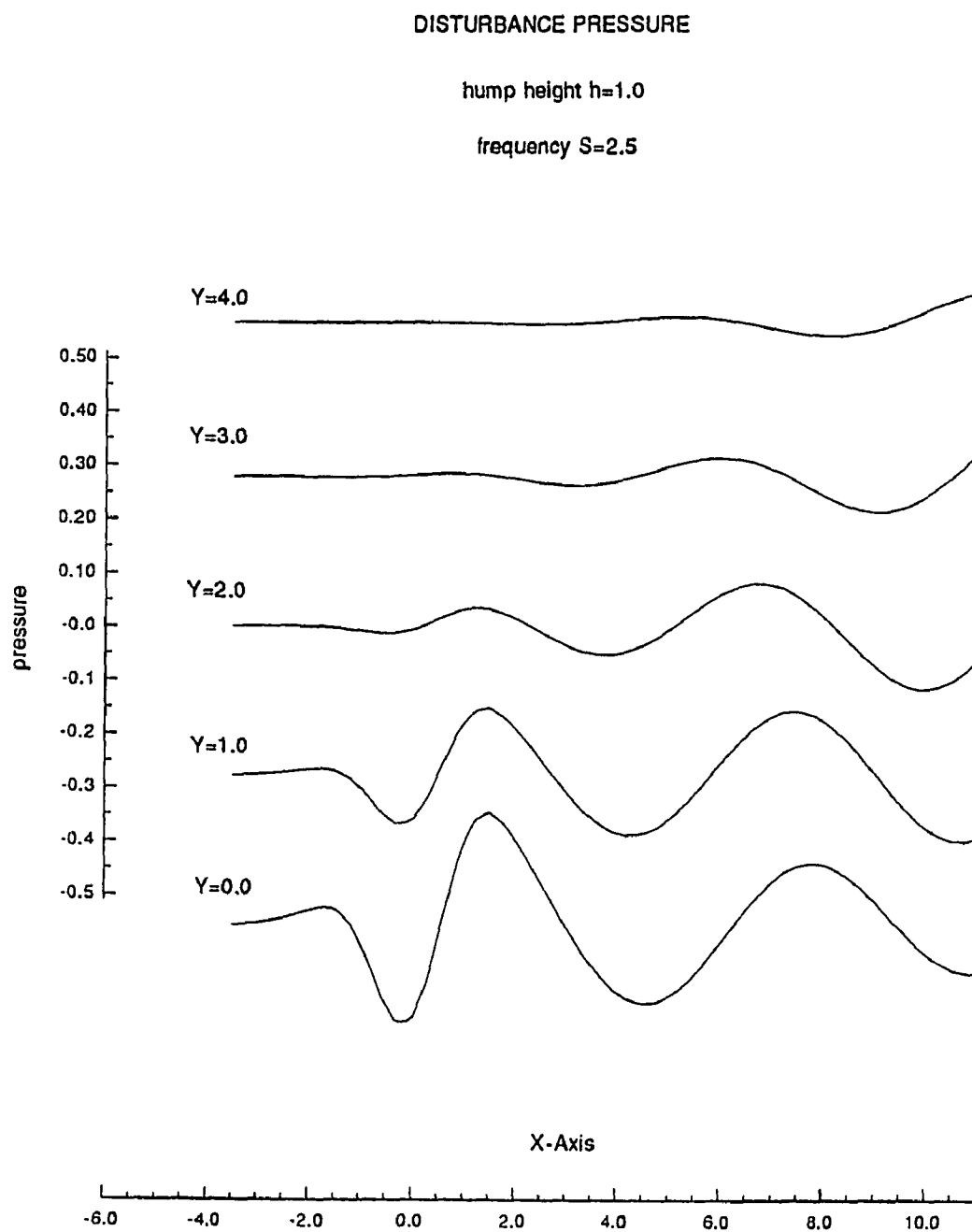


Figure 56. Plot of disturbance pressure for $h=1.0$, $t = 0$ and $S_0 = 2.5$.

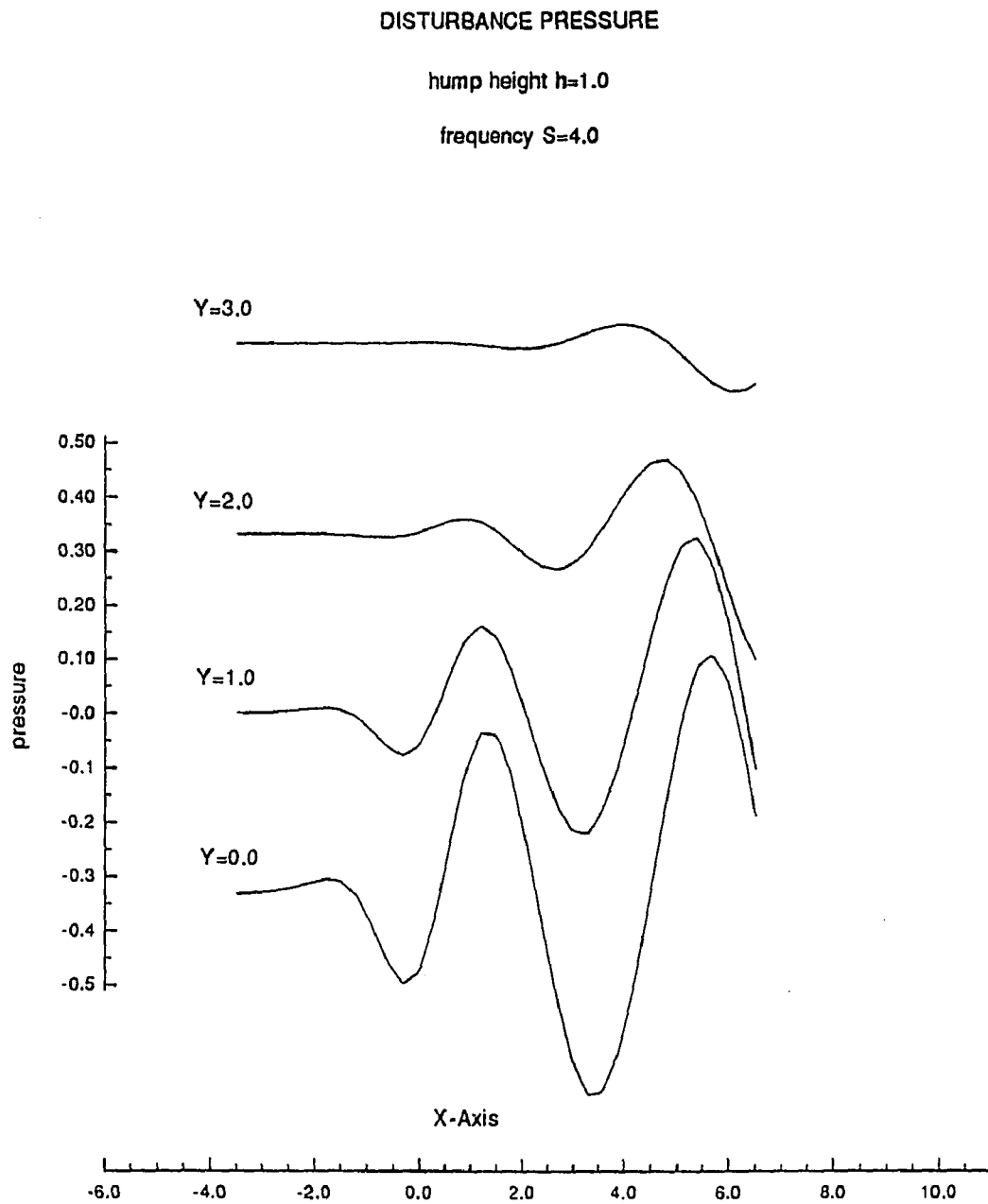


Figure 57. Plot of disturbance pressure for $h=1.0$, $t=0$ and $S_0=4.0$.

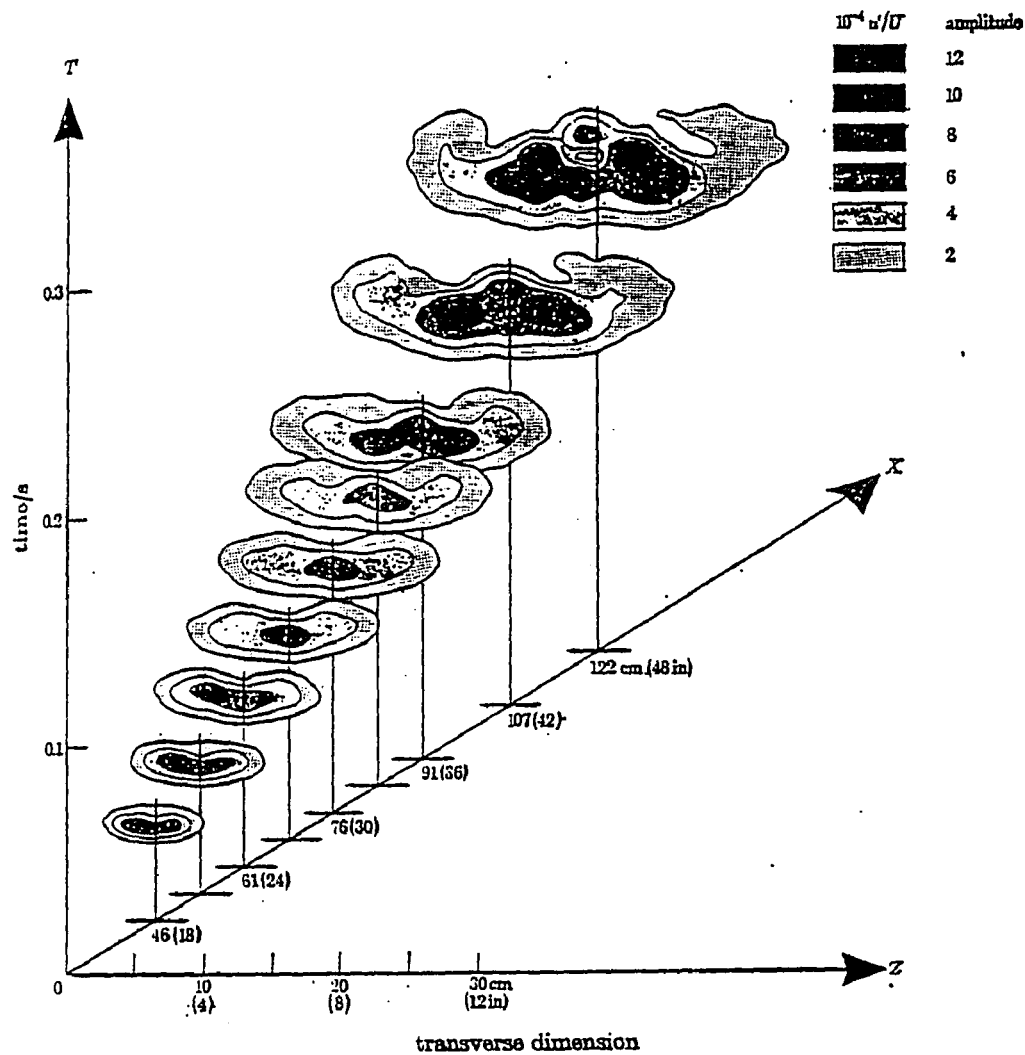


FIGURE 7. Contours of the signal envelope amplitude at various distances from the source.

Figure 58. Contours of signal amplitude and their evolution in time for a wave packet observed experimentally (taken from reference [4]).

downstream. This is qualitatively similar to the evolution of our wave as it moves downstream. The experiments of Gilev et al [7] , Kachanov [8] , and Kendall [9] with the wave patterns formed behind a time harmonic source point observed a growing wave inside a wedge-shaped region downstream of the source point. They also observed that further downstream the peaks of disturbance intensity move off the center in an oblique angle. In all the above experiments, the most significant result is the fact that the most amplified disturbances are at an oblique direction to that of the basic flow. These basic tendencies are also in agreement with the linearized analyses, $\lim_{h \rightarrow 0}$, of Kerschen [30].

We have examined the disturbance flow field generated by an amplifying wave behind the roughness element. It is believed that this structure is representative of the scattered patches of T-S waves observed intermittently in natural transition. The wave motion consists of two series, one on each side of the basic flow direction behind the roughness element, of ascending and descending jets. Near the wall, the wave motion has to satisfy the parallel flow requirement. Hence, the jet-like fluid motion has to turn just above the wall. Therefore, these fluid jets, on each side of the X-axis, close into each other near the wall and form two chains of connected U-shaped jets, bringing fluid down one end of the U and ejecting fluid from the other end. Both chains, joined near the hump, extend downstream at an oblique angle, 18° to 23° , to the X-axis (see figures 38 through 44). On each side of the jets a pair of counter-rotating vortices are formed. These vortices exist to the side and in between the jets. Near the wall an accommodating

flow pattern is set up to satisfy the continuity equation. This wall-flow pattern is evident in the disturbance surface-streamlines given in figure 44.

For the larger hump, $h=4.5$, at $S_0 = 1.0$ the pressure field decays as the wave moves downstream. The disturbance-velocity contour patterns are also similar to those for $h=1.0$ in shape. However, in the half wavelength available by our computations, the velocity profiles amplify significantly as they move downstream. Since the pressure field decays as it moves downstream, we expect the wave is spatially decaying at $S_0 = 1.0$. Additionally, the peaks of u-velocity contours are 12 to 34 times larger than the ones found for $h=1.0$, even though the hump height is only 4.5 times bigger. Hence, we expect a nonlinear increase in the receptivity of the laminar-boundary layer as the hump's height is increased.

Finally, profiles of the disturbance intensity along the lower deck at several locations downstream of the hump are given for a particular Reynolds number, $Re = 1000000$ and a particular choice of the amplitude of the free-stream fluctuations, $\delta = .01$. These profiles are shown in Appendix D and are generated by using the relationships in Appendix C.

IV.4.1 Further Research

This was a general study of the interaction between a small three-dimensional roughness element and free-stream disturbances. The only parameters investigated are the scaled Strouhal number, S_0 , and an order one scale of the roughness height, h . Any other parameter study, for example; the effect of roughness shape, spacing between two neighboring roughness elements, or the effect of an array of distributed roughness on receptivity, etc. can be studied using the existing code. To study the receptivity of slot injection or suction through a hole in the wall can be achieved by a simple modification of our code.

This code can also be modified to study the effect of much larger roughness elements on the receptivity of the laminar boundary layer at finite Reynolds numbers. This can be achieved by altering this code to solve the interactive-boundary layer equations.

APPENDIX A

Upstream Boundary Conditions

Our roughness element and the associated triple-deck structure is a local phenomenon placed at a distance L^* from the leading edge. Upstream boundary conditions for this flow structure are given by the conditions generated at $x^* = L^*$, due to a boundary layer flow with free-stream disturbances on a flat wall without the roughness element. Asymptotic solutions have been obtained for the unsteady incompressible boundary layer on a semi-infinite flat plate with small periodic fluctuations in the free-stream velocity by Ackerberg and Phillips [31]. Their solution had to be modified due to a sign change, which causes a sign change in the highest derivatives of the system of ODE's generated in the analysis. This modified solution is presented here and is used as the upstream boundary condition in our problem formulation and in our numerical scheme.

Let us consider an incompressible unsteady boundary-layer flow on a semi-infinite flat plate with small time-harmonic fluctuations in the free-stream velocity given by:

$$U^* = U_{\infty}^* + u_{\infty}^* \exp(-i\omega t^*) , \quad (A-1)$$

and

$$\delta \equiv \frac{u_{\infty}^*}{U_{\infty}^*} . \quad (A-2)$$

The magnitude of δ is assumed small but large enough to insure that the predominant perturbation to the Blasius flow is the free-stream fluctuation and not a higher-order correction to boundary-layer theory.:

$$\frac{\omega v}{U_{\infty}^{*2}} \ll |\delta| \ll 1 , \quad (A-3)$$

where $\frac{u_{\infty}^{*2}}{\omega v}$ plays the role of a conventional Reynolds number.¹

Introducing nondimensional variables in the following manner:

$$t = \omega t^* , \quad \bar{x} = \frac{\omega x^*}{U_{\infty}^*} , \quad \bar{z} = \left(\frac{\omega}{v}\right)^{\frac{1}{2}} z^* , \quad \psi^*(x^*, z^*, t^*) = \left(\frac{\omega}{v U_{\infty}^{*2}}\right)^{\frac{1}{2}} \tilde{\psi}(\bar{x}, \bar{z}, t) ,$$

$$\bar{u} = \frac{u^*}{U_{\infty}^*} = \tilde{\psi}_{\bar{x}} , \quad \bar{w} = (\omega v)^{\frac{1}{2}} w^* = -\tilde{\psi}_{\bar{z}} , \quad (A-4)$$

¹ In our notation,

$$\frac{\omega v}{U_{\infty}^{*2}} = \frac{\omega L^*}{U_{\infty}^*} \frac{v}{U_{\infty}^* L^*} = \frac{S}{Re}$$

we seek a similarity solution plus a small time-harmonic perturbation. Therefore, using the Blasius coordinate, η , we define transformed flow variables as:

$$\xi = \bar{x}, \quad \eta = \frac{\bar{z}}{(2\bar{x})^{\frac{1}{2}}}, \quad t, \quad (A-5)$$

$$\tilde{\psi}(\bar{x}, \bar{z}, t) = (2\xi)^{\frac{1}{2}} \Phi(\xi, \eta, t), \quad (A-6a)$$

$$\text{with } \bar{u} = \Phi_{\eta} \text{ and } \bar{w} = (2\xi)^{\frac{1}{2}} \{ \eta \Phi_{\eta} - 2\xi \Phi_{\xi} - \Phi \}. \quad (A-6b)$$

Substituting the above definition for the stream function into the Navier-Stokes equations, and using the usual boundary-layer assumptions, the x-momentum equation in terms of Φ can be written as:

$$\Phi_{\eta\eta\eta} + \Phi \Phi_{\eta\eta} - 2\xi \{ \Phi_{\eta t} + \Phi_{\eta} \Phi_{\eta\xi} - \Phi_{\eta\eta} \Phi_{\xi} + \delta i \exp(-it) \} = 0. \quad (A-7)$$

Since the resulting equations for the perturbations will be linear, we can assume, without loss of generality,

$$\Phi(\xi, \eta, t) = F(\eta) + \delta \exp(-it) G(\xi, \eta). \quad (A-8)$$

Substituting the above form into equation (A-7) and taking the limit as $\delta \rightarrow 0$, gives the Blasius equation:

$$F''' + FF'' = 0, \quad (A-9)$$

$$\text{subject to } F(0) = 0 = F'(0), \quad (A-10a)$$

$$\text{and } F'(\eta) \rightarrow 1 \text{ as } \eta \rightarrow \infty. \quad (A-10b)$$

The first-order equation in δ is found to be (dropping e^{-i})

$$G_{\eta\eta\eta} + FG_{\eta\eta} + F'G - 2\xi(-iG_{\eta} + F'G_{\eta\xi} - F''G_{\xi} + i) = 0, \quad (A-11)$$

$$\text{subject to} \quad G(\xi, 0) = 0 = G_{\eta}(\xi, 0), \quad (A-12a)$$

$$\text{and} \quad G_{\eta}(\xi, \eta) \rightarrow 1 \text{ as } \eta \rightarrow \infty, \quad (A-12b)$$

$$\text{also} \quad G(0, \eta) = \frac{1}{2}(\eta F' + F) \quad (\text{see Ackerberg}). \quad (A-12c)$$

A-1 Asymptotic Solutions

Ackerberg et al. [31] found an asymptotic solution far downstream of the leading edge, at large \bar{x} , for the flow over a flat plate. This expansion is obtained by introducing a new independent variable,

$$\alpha = \xi^{\frac{1}{2}}. \quad (A-13)$$

It should be remembered that we are looking for boundary conditions upstream of our triple-deck structure. Hence, we are looking for solution at a distance L^* from the leading edge. The above mentioned asymptotic solution is valid for any $L^* \gg \epsilon^2$. This can be shown by defining the order one nondimensionalized variables,

$$(X, Z) = \frac{(x^*, z^*)}{L^*}. \quad (A-14)$$

Therefore, we can relate nondimensional variables defined by equations (A-4) , (A-14) and those defined in Chapter 1 :

$$\begin{aligned} \xi &= \bar{x} = \frac{\omega x^*}{U_*} = \frac{\omega L^* x^*}{U_* L^*} \\ &= S X = S_0 \epsilon^{-2} X . \end{aligned} \quad (A-15)$$

At $x^* = L^*$ (or $X = 1$) the condition $\bar{x} = S_0 \epsilon^{-2} \gg 1$ is satisfied, so we can use this asymptotic solution as the upstream boundary condition of our triple-deck structure.

Additionally, we can see below that the classical Stokes wall layer, $\bar{z} \sim O(1)$, matches to the lower deck. :

$$\begin{aligned} \bar{z} &= \left(\frac{\omega}{\nu} \right)^{\frac{1}{2}} z^* = \left(\frac{\omega L^{*2}}{\nu} \right)^{\frac{1}{2}} \frac{z^*}{L^*} \\ &= \left(\frac{\omega L^*}{U_*} \right)^{\frac{1}{2}} \left(\frac{L^* U_*}{\nu} \right)^{\frac{1}{2}} Z = S^{\frac{1}{2}} Re^{\frac{1}{2}} Z \\ &= S_0^{\frac{1}{2}} \epsilon^{-5} Z = S_0^{\frac{1}{2}} z_l . \end{aligned} \quad (A-16)$$

Similarly η and α can be written as:

$$\begin{aligned}\eta &= \frac{\bar{z}}{(2\bar{x})^{\frac{1}{2}}} = \frac{S_0^{\frac{1}{2}} \varepsilon^{-5} Z}{(2S_0 \varepsilon^{-2} X)^{\frac{1}{2}}} \\ &= 2^{\frac{1}{2}} \varepsilon^{-4} \frac{Z}{X^{\frac{1}{2}}},\end{aligned}\quad (\text{A-17})$$

$$\alpha = \xi^{\frac{1}{2}} = \varepsilon (S_0 X)^{\frac{1}{2}}. \quad (\text{A-18})$$

Hence, at $X = 1$ the incoming boundary layer matches the main deck and α becomes of the order ε :

$$\eta = 2^{\frac{1}{2}} \varepsilon^{-4} Z = 2^{\frac{1}{2}} z_m, \quad (\text{A-19})$$

and
$$\alpha = \varepsilon S_0^{\frac{1}{2}}. \quad (\text{A-20})$$

Rewriting the x-momentum equation (A-11) in terms of α gives:

$$2i (G_\eta - 1) + \alpha^2 (G_{\eta\eta\eta} + F G_{\eta\eta} + F'' G) - \alpha^3 (F'' G_\alpha - F' G_{\eta\alpha}) = 0, \quad (\text{A-21})$$

where
$$\partial_\xi () = \frac{-\alpha^3}{2} \partial_\alpha (). \quad (\text{A-22})$$

A-1.1 Outer Expansion

The appearance of algebraic powers of α in equation (A-21) suggests an expansion of the form

$$G(\alpha, \eta) = \sum_{n=0} \alpha^n G_n(\eta) \quad \text{for } \alpha \rightarrow 0, \text{ \& } \eta = O(1) . \quad (A-23)$$

Substituting the expansion into equation (A-21), we obtain:

$$G'_0 = 1 , \quad (A-24a)$$

$$G'_1 = 0 , \quad (A-24b)$$

$$G'_2 = -\frac{1}{2i} F'' G_0 , \quad (A-24c)$$

etc.

which must satisfy the boundary condition as $\eta \rightarrow \infty$, therefore, requiring

$$G'_0 \rightarrow 1 \text{ and } G'_n \rightarrow 0 \text{ for } n > 0 . \quad (A-25)$$

Thus the solutions are given by

$$G_0 = \eta + C_0 , \quad (A-26a)$$

$$G_1 = C_1 , \quad (A-26b)$$

$$G_2 = -\frac{1}{2i} ((\eta + C_0) F' - F) + C_2 , \quad (A-26c)$$

etc.

where the unknown constants must be determined through matching with the inner solution near the wall.

A-1.2 Inner Expansion

Near the wall, we will reintroduce a stretched normal coordinate,

$$\sigma = (2\xi)^{\frac{1}{2}}\eta = \bar{z} \quad \text{and} \quad g(\alpha, \sigma) = (2\xi)^{\frac{1}{2}}G(\xi, \eta) . \quad (\text{A-27})$$

Rewriting the momentum equation (A-21) in terms of inner-region variables, gives:

$$4g_{\sigma\sigma\sigma} + 2^{\frac{3}{2}}\alpha F g_{\sigma\sigma} + 4i g_{\sigma} - 2\alpha^2 F'(\sigma g_{\sigma\sigma} - \alpha g_{\sigma\omega}) + 2^{\frac{1}{2}}\alpha^3 F''(\sigma g_{\sigma} - \alpha g_{\omega}) - 4i = 0 . \quad (\text{A-28})$$

Near the wall as $\eta \rightarrow 0$, the Blasius profile is linear and is given by:

$$F(\eta) = C\eta^2 + O(\eta^5) \quad \text{where:} \quad C = \frac{F''(0)}{2} = .2348\dots . \quad (\text{A-29})$$

Substituting the linear velocity profile, rewritten in the inner-region variables, into equation (A-28) gives:

$$4g_{\sigma\sigma\sigma} + 2^{\frac{1}{2}}C\sigma^2\alpha^3 g_{\sigma\sigma} + 4i g_{\sigma} + 2^{\frac{3}{2}}C \{ \sigma\alpha^3(\alpha g_{\sigma\omega} - \sigma g_{\sigma\sigma}) + \alpha^3(\sigma g_{\sigma} - \alpha g_{\omega}) \} - 4i + O(\alpha^6) = 0 . \quad (\text{A-30})$$

We now assume the expansion,

$$g(\alpha, \sigma) = \sum_{n=0} \alpha^n g_n(\sigma) \quad \text{for} \quad \alpha \rightarrow 0, \quad \& \quad \sigma = O(1) , \quad (\text{A-31})$$

and substitute in equation (A-30), yielding:

$$g_0''' + i g_0' = i , \quad (A - 32a)$$

$$g_1''' + i g_1' = 0 , \quad (A - 32b)$$

$$g_2''' + i g_2' = 0 , \quad (A - 32c)$$

etc.

which must satisfy the no slip conditions near the wall,

$$g_n(0) = 0 = g_n'(0) \quad \text{where : } n = 0, 1, 2, \dots \quad (A - 33)$$

Thus the solutions are given by

$$g_0 = \frac{1}{s} (1 - \exp(s\sigma)) + \sigma \quad \text{where } s = i^{\frac{3}{2}} , \quad (A - 34a)$$

$$g_1 = 0 \quad (A - 34b) ,$$

$$g_2 = 0 \quad (A - 34c) .$$

As is to be expected, g_0 is the classical Stokes solution for an infinite flat plate in an oscillating free stream with zero mean flow.

A-1.3 Results

To evaluate the constants in the outer solution, equation (A-26), we match that to the inner solution, equation (A-34), in their common region of validity using the Van Dyke[32] matching principle;

inner expansion:

$$G^i(\alpha, \sigma) = 2^{\frac{1}{2}}\alpha \left\{ \sigma + \frac{1}{s} (1 - \exp(s\sigma)) + O(\alpha^3) \right\}, \quad (A-35)$$

rewritten in the outer variables,

$$G^i(\alpha, \eta) = 2^{\frac{1}{2}}\alpha \left\{ 2^{\frac{1}{2}}\alpha^{-1}\eta + \frac{1}{s} \left(1 - \exp\left(s 2^{\frac{1}{2}}\alpha^{-1}\eta\right) \right) + O(\alpha^3) \right\}, \quad (A-36)$$

expand as $\alpha \rightarrow 0$,

$$G^i(\alpha \rightarrow 0, \eta) = \eta + \alpha \frac{2^{\frac{1}{2}}}{s} + O(\alpha^2). \quad (A-37)$$

outer expansion:

$$G^o(\alpha, \eta) = (\eta + C_0) + \alpha C_1 + \alpha^2 \left\{ \frac{-1}{2i} ((\eta + C_0)F' - F) + C_2 \right\} + O(\alpha^3). \quad (A-38)$$

for $\eta \rightarrow 0$,

$$G^o(\alpha, \eta \rightarrow 0) = (\eta + C_0) + \alpha C_1 + \alpha^2 \left\{ \frac{-1}{2i} ((\eta + C_0)2C\eta - C\eta^2) + C_2 \right\}, \quad (A-39)$$

matching up to the $O(\alpha^2)$ would require :

$$C_0 = 0 \quad \text{and} \quad C_1 = \frac{2^{\frac{1}{2}}}{s}. \quad (A-40)$$

Furthermore, the inner and outer expansions of the stream function are:

$$G^i(\alpha, \sigma) = 2^{\frac{1}{2}}\alpha \left\{ \sigma + \frac{1}{s}(1 - \exp(s\sigma)) \right\} + O(\alpha^4), \quad (A-41)$$

$$G^o(\alpha, \eta) = \eta + \alpha \frac{2^{\frac{1}{2}}}{s} + O(\alpha^2). \quad (A-42)$$

Using definitions (A-6b) and (A-8) the streamwise component of velocity is given by:

$$\bar{u} = \frac{u^*}{U_{\infty}^*} = \Phi_{\eta} = F'(\eta) + \delta \exp(-it) G_{\eta}(\alpha, \eta). \quad (A-43)$$

In addition, in the inner region we have,

$$\partial_{\eta}(\) = 2^{\frac{1}{2}}\alpha^{-1}\partial_{\sigma}(\) \quad \text{and} \quad F' = 2C\eta \quad (A-44)$$

Hence, substituting equation (A-41) into the relation (A-43) for the streamwise component of the velocity in the inner region we have:

$$\bar{u} = \alpha\lambda\sigma + \delta \exp(-it) \left\{ (1 - \exp(s\sigma)) + O(\alpha^3) \right\}, \quad (A-45)$$

$$\text{where} \quad \lambda = 2^{\frac{1}{2}}F''(0) = .33206\dots$$

Similarly by substituting using (A-41b) in the outer region we have,

$$\bar{u} = F'(\eta) + \delta \exp(-it) \left\{ 1 + O(\alpha^2) \right\}. \quad (A-46)$$

Also, using definition (A-6b) the component of velocity normal to the wall is given by:

$$w = \frac{w^*}{U_{\infty}^*} = \left(\frac{v}{2U_{\infty}^*x^*} \right)^{\frac{1}{2}} \left\{ \eta\Phi_{\eta} - 2\xi\Phi_{\xi} - \Phi \right\}, \quad (A-47)$$

or by using the relation (A-8) it can be written as:

$$w = (2Re_x)^{-\frac{1}{2}} \{ (\eta F' - F) + \delta \exp(-it) (\eta G_\eta - 2\xi G_\xi - G) \} . \quad (A-48)$$

Additionally, in the inner region we have,

$$G(\xi, \eta) = 2^{-\frac{1}{2}} \alpha g(\alpha, \sigma) ; \quad \alpha = \xi^{\frac{1}{2}} ; \quad \sigma = (2\xi)^{\frac{1}{2}} \eta ,$$

$$\partial_\xi () = -\frac{1}{2} \alpha^3 \partial_\alpha () + \frac{1}{2} \alpha^2 \sigma \partial_\sigma () ,$$

$$\eta \partial_\eta () = \sigma \partial_\sigma () . \quad (A-49)$$

Hence, by using the expansion (41-a), in the inner region we have,

$$w = (2Re_x)^{-\frac{1}{2}} \left\{ (\sigma F'(\sigma) - F) + \delta \exp(-it) \left(2^{-\frac{1}{2}} \alpha^2 \partial_\alpha g(\alpha, \sigma) \right) \right\} , \quad (A-50)$$

which can be simplified,

$$w = (2Re_x)^{-\frac{1}{2}} \{ (\sigma F'(\sigma) - F) + \delta \exp(-it) (0 + O(\alpha^3)) \} . \quad (A-51)$$

Similarly, by using (A-41b) in the outer region we have,

$$w = (2Re_x)^{-\frac{1}{2}} \{ (\eta F' - F) + \delta \exp(-it) (\eta G_\eta^\circ - \alpha G_\alpha^\circ - G^\circ) \} , \quad (A-52)$$

or after simplification we have,

$$w = (2Re_x)^{\frac{1}{2}} \{ (\eta F' - F) + \delta \exp(-it) (0 + O(\alpha^2)) \} . \quad (A-53)$$

To obtain the boundary condition on pressure upstream of our triple-deck structure, we evaluate the x-momentum equation (1-11) outside the boundary layer. There, the pressure gradient is related to time derivative of the free-stream velocity field by the following relationship,

$$S \partial_t u = -\partial_x P . \quad (A-54)$$

Hence, upon integrating equation (A-54) the boundary-layer pressure is given by;

$$P = i S \delta \exp(-it) X \{ 1 + O(\epsilon^2) \} . \quad (A-55)$$

Summarizing the results of this appendix:

Boundary conditions upstream of the lower deck are;

$$u = \epsilon \lambda z_t + \delta \exp(-it) \left\{ \left(1 - \exp\left(i^{\frac{3}{2}} S_0^{\frac{1}{2}} z_t\right) \right) + O(\epsilon^3) \right\} , \quad (A-56a)$$

$$w = 2^{\frac{1}{2}} \epsilon^4 \{ (\eta F' - F) + \delta \exp(-it) (0 + O(\epsilon^3)) \} , \quad (A-56b)$$

$$\text{where } \lambda = 2^{\frac{1}{2}} F'(0) = .33206... .$$

Also, in the main deck the upstream boundary conditions are given by:

$$u = F'(\eta) + \delta \exp(-i\tau) \{ 1 + O(\epsilon^2) \} , \quad (A-57a)$$

$$w = 2^{\frac{1}{2}} \epsilon^4 \{ (\eta F' - F) + \delta \exp(-i\tau) (0 + O(\epsilon^2)) \} , \quad (A-57b)$$

$$\text{where } \eta = 2^{\frac{1}{2}} z_m .$$

Finally the incoming boundary layer is two dimensional, therefore, the cross stream velocity is:

$$v = 0 . \quad (A-58)$$

APPENDIX B

λ Scalings

In this appendix we derive the required scaling of all flow variables, both independent and dependent, such that λ can be scaled out of the problem formulation. Here $\lambda \equiv U'_B(0)$ is the slope of the incoming velocity profile at the wall. First we consider the governing equations in the steady flow, repeated below for convenience, :

in the lower deck:

$$\partial_x U_1 + \partial_y V_1 + \partial_{z_1} W_1 = 0 , \quad (B-1)$$

$$U_1 \partial_x U_1 + V_1 \partial_y U_1 + W_1 \partial_{z_1} U_1 = -\partial_x P_1 + \partial_{z_1 z_1} U_1 , \quad (B-2)$$

$$U_1 \partial_x V_1 + V_1 \partial_y V_1 + W_1 \partial_{z_1} V_1 = -\partial_y P_1 + \partial_{z_1 z_1} V_1 . \quad (B-3)$$

in the upper deck:

$$\partial_{xx} \hat{P}_1 + \partial_{yy} \hat{P}_1 + \partial_{z_1 z_1} \hat{P}_1 = 0 , \quad (B-4)$$

subject to the boundary conditions:

$$U_1 = V_1 = W_1 = 0 \quad \text{on} \quad Z_1 = hF(x, y) , \quad (B-5)$$

$$U_1 \rightarrow \lambda z_1 , \quad V_1, W_1, P_1 \rightarrow 0 \quad \text{as} \quad x \rightarrow -\infty \text{ and/or } y \rightarrow \pm\infty , \quad (B-6)$$

$$U_1 \rightarrow \lambda (z_1 + A(x, y)) \quad \text{as} \quad z_1 \rightarrow \infty , \quad (B-7)$$

$$\partial_x V_1 \rightarrow -\frac{\partial_y P_1(x, y)}{\lambda z_1} \quad \text{as} \quad z_1 \rightarrow \infty , \quad (B-8)$$

where $F(x, y)$ is an order one hump shape with h as a scaling parameter. $A(x, y)$ is the negative of the boundary-layer displacement thickness, and it is defined by asymptotic matching of all the three decks. The above equations in the lower and upper decks are coupled together by the matching conditions :

$$\hat{P}_1(x, y, z_u \rightarrow 0) = P_1(x, y) , \quad (B-9)$$

and

$$\partial_{z_u} \hat{P}_1(x, y, z_u \rightarrow 0) = \partial_{xx} A(x, y) . \quad (B-10)$$

We define the new variables scaled by powers of λ as given below,

$$x = \lambda^\alpha x^p \quad \Rightarrow \quad \partial_x = \lambda^{-\alpha} \partial_{x^p} , \quad (B-11a)$$

$$y = \lambda^\beta y^p \quad \Rightarrow \quad \partial_y = \lambda^{-\beta} \partial_{y^p} , \quad (B-11b)$$

$$z_1 = \lambda^\gamma z_1^p \quad \Rightarrow \quad \partial_{z_1} = \lambda^{-\gamma} \partial_{z_1^p} , \quad (B-11c)$$

$$z_u = \lambda^\delta z_u^p \quad \Rightarrow \quad \partial_{z_u} = \lambda^{-\delta} \partial_{z_u^p} , \quad (B-11d)$$

$$U_1 = \lambda^a U^p \quad , \quad P_1 = \lambda^d P^p \quad , \quad (B-12a)$$

$$V_1 = \lambda^b V^p \quad , \quad A = \lambda^e A^p \quad , \quad (B-12b)$$

$$W_1 = \lambda^c W^p \quad , \quad F = \lambda^f F^p \quad , \quad (B-12c)$$

$$\text{and } \hat{P}_1 = \lambda^g \hat{P}^p \quad . \quad (B-12d)$$

Substituting the new variables into the governing equations yields:

$$\text{from (9):} \quad g = d \quad , \quad (B-13)$$

$$\text{from (5):} \quad f = \gamma \quad , \quad (B-14)$$

$$\text{from (7):} \quad e = \gamma \quad , \quad (B-15)$$

$$\text{from (6):} \quad \lambda^a U^p \propto \lambda^{\gamma+1} z_i^p \Rightarrow a = \gamma + 1 \quad , \quad (B-16)$$

$$\begin{aligned} \text{from (4):} \quad \lambda^{-2\alpha} \partial_{x^p x^p} \hat{P}^p + \lambda^{-2\beta} \partial_{y^p y^p} \hat{P}^p + \lambda^{-2\delta} \partial_{z_i^p z_i^p} \hat{P}^p &= 0 \quad , \\ \alpha = \beta = \delta \quad , \end{aligned} \quad (B-17)$$

$$\begin{aligned} \text{from (1):} \quad \lambda^{a-\alpha} \partial_{x^p} U^p + \lambda^{b-\beta} \partial_{y^p} V^p + \lambda^{c-\gamma} \partial_{z_i^p} W^p &= 0 \quad , \\ a - \alpha = b - \beta = c - \gamma \Rightarrow a = b \quad , \end{aligned} \quad (B-18)$$

$$\text{from (8):} \quad \lambda^{b-\alpha} \propto \lambda^{d-\beta-(\gamma+1)} \Rightarrow d = 2(\gamma+1) \quad , \quad (B-19)$$

$$\begin{aligned} \text{from (2):} \quad \lambda^{c+a-\gamma} W^p \partial_{z_i^p} U^p &\propto \lambda^{a-2\gamma} \partial_{z_i^p} U^p \quad , \\ c + a - \gamma = a - 2\gamma \Rightarrow c = -\gamma \quad , \end{aligned} \quad (B-20)$$

$$\text{and from} \quad a - \alpha = c - \gamma \Rightarrow \alpha = 3\gamma + 1 \quad , \quad (B-21)$$

and finally,

from (10): $\lambda^{g-\delta} \propto \lambda^{e-2\alpha} \Rightarrow \gamma = -\frac{3}{4}$. (B-22)

Therefore, all the powers can be evaluated:

$$a = b = \frac{1}{4}, \quad c = \frac{3}{4}, \quad d = g = \frac{1}{2}, \quad e = f = -\frac{3}{4},$$

$$\alpha = \beta = \delta = -\frac{5}{4} \quad \text{and} \quad \gamma = -\frac{3}{4}. \quad \text{(B-23)}$$

Now the governing equations for the receptivity problem are repeated below. In the lower deck we have:

$$\partial_x \bar{u}_0 + \partial_y \bar{v}_0 + \partial_{z_1} \bar{w}_0 = 0, \quad \text{(B-24)}$$

$$\begin{aligned} -i S_0 \bar{u}_0 + \partial_x U_0 \bar{u}_0 + \partial_y U_0 \bar{v}_0 + \partial_{z_1} U_0 \bar{w}_0 \\ + U_0 \partial_x \bar{u}_0 + V_0 \partial_y \bar{u}_0 + W_0 \partial_{z_1} \bar{u}_0 \\ = -\partial_x \bar{p}_0 + \partial_{z_1 z_1} \bar{u}_0, \end{aligned} \quad \text{(B-25)}$$

$$\begin{aligned} -i S_0 \bar{v}_0 + \partial_x V_0 \bar{u}_0 + \partial_y V_0 \bar{v}_0 + \partial_{z_1} V_0 \bar{w}_0 \\ + U_0 \partial_x \bar{v}_0 + V_0 \partial_y \bar{v}_0 + W_0 \partial_{z_1} \bar{v}_0 \\ = -\partial_y \bar{p}_0 + \partial_{z_1 z_1} \bar{v}_0, \end{aligned} \quad \text{(B-26)}$$

and in the upper deck for the pressure we have,

$$\partial_{xx} \hat{p}_1 + \partial_{yy} \hat{p}_1 + \partial_{z_1 z_1} \hat{p}_1 = 0. \quad \text{(B-27)}$$

The above equations are subject to the following boundary conditions:

$$\bar{u}_0 = \bar{v}_0 = \bar{w}_0 = 0 \quad \text{on} \quad z_l = h F(x, y) . \quad (B - 28)$$

Also, as $x \rightarrow -\infty$ we have (see Appendix A) :

$$\bar{u}_0 \rightarrow 1 - e^{i^3 \lambda S_0^{1/2} z_l} , \quad (B - 29)$$

$$\bar{v}_0, \bar{w}_0 \rightarrow 0 , \quad (B - 30)$$

$$\bar{p}_0 \rightarrow i S_0 x . \quad (B - 31)$$

From matching to the main deck, as $z_l \rightarrow \infty$,

$$\bar{u}_0 \rightarrow 1 + \lambda a(x, y) , \quad (B - 32)$$

$$\bar{w}_0 \rightarrow -\lambda z_l \partial_x a(x, y) , \quad (B - 33)$$

$$\partial_x \bar{v}_0 \rightarrow -\frac{\partial_y \bar{p}_0(x, y)}{\lambda z_l} . \quad (B - 34)$$

Furthermore, from matching the unsteady pressure between the upper and lower decks, we can write:

$$\hat{p}_1(x, y, z_u \rightarrow 0) = p_0(x, y) , \quad (B - 35a)$$

$$\partial_{z_u} \hat{p}_1(x, y, z_u \rightarrow 0) = \partial_{xx} a(x, y) . \quad (B - 35b)$$

Now we define the new variables scaled by powers of λ for the unsteady flow parameters,

$$\begin{aligned}
\bar{u}_0 &= \lambda^h u^p & , & & \bar{p}_0 &= \lambda^k p^p & , \\
\bar{v}_0 &= \lambda^i v^p & , & & a &= \lambda^m a^p & , \\
\bar{w}_0 &= \lambda^j w^p & , & & \hat{p}_1 &= \lambda^n \hat{p}^p & , \\
&& & & \text{and } S_0 &= \lambda^q S_0^p & .
\end{aligned} \tag{B-36}$$

After substitution into the above equations, we have:

$$\begin{aligned}
\text{from (29):} \quad & \lambda^h \propto \lambda^0 \propto \lambda^{\frac{q}{2}+\gamma} & , \\
& \Rightarrow h=0 \text{ and } q=-2\gamma=\frac{3}{2} & ,
\end{aligned} \tag{B-37}$$

$$\text{from (31):} \quad \lambda^k \propto \lambda^{q+\alpha} \Rightarrow k=\gamma+1=\frac{1}{4} & , \tag{B-38}$$

$$\text{from (32):} \quad \lambda^{m+1} \propto \lambda^0 \Rightarrow m=-1 & , \tag{B-39}$$

$$\text{from (33):} \quad \lambda^j \propto \lambda^{1+\gamma+m-\alpha} \Rightarrow j=\frac{1}{2} & , \tag{B-40}$$

$$\text{from (35):} \quad \Rightarrow n=k=\frac{1}{4} & , \tag{B-41}$$

$$\text{from (34):} \quad \lambda^{i-\alpha} \propto \lambda^{k-\beta-1-\gamma} \Rightarrow i=0 & . \tag{B-42}$$

Using the given scalings, summarized below, we can rewrite the governing equations with the appropriate boundary and matching conditions in the new variables. The effect of this transformation is the same as replacing all the flow parameters with the new rescaled variables and setting $\lambda = 1$ in those equations. The rescaled variables are:

the coordinates:

$$x = \lambda^{\frac{3}{4}} x^p, \quad y = \lambda^{\frac{5}{4}} y^p, \quad (B-43a)$$

$$z_l = \lambda^{\frac{3}{4}} z_l^p, \quad z_u = \lambda^{\frac{5}{4}} z_u^p, \quad (B-43b)$$

the steady flow variables:

$$U_1 = \lambda^{\frac{1}{4}} U^p, \quad P_1 = \lambda^{\frac{1}{2}} P^p, \quad (B-44a)$$

$$V_1 = \lambda^{\frac{1}{4}} V^p, \quad A = \lambda^{\frac{3}{4}} A^p, \quad (B-44b)$$

$$W_1 = \lambda^{\frac{3}{4}} W^p, \quad F = \lambda^{\frac{3}{4}} F^p, \quad (B-44c)$$

$$\text{and } \hat{P}_1 = \lambda^{\frac{1}{2}} \hat{P}^p, \quad (B-44d)$$

the unsteady flow variables:

$$\bar{u}_0 = u^p, \quad \bar{p}_0 = \lambda^{\frac{1}{4}} p^p, \quad (B-45a)$$

$$\bar{v}_0 = v^p, \quad a = \lambda^{-1} a^p, \quad (B-45b)$$

$$\bar{w}_0 = \lambda^{\frac{1}{2}} w^p, \quad \hat{p}_1 = \lambda^{\frac{1}{4}} \hat{p}^p, \quad (B-45c)$$

$$\text{and } S_0 = \lambda^{\frac{3}{2}} S_0^p. \quad (B-45d)$$

APPENDIX C

Flow Variables and Properties

In this appendix, we summarize the relationship between numerical results, i.e. those obtained in our computer program by solving equations (1-72) - (1-79), and physical flow properties and variables. These relationships are presented below.

The flow coordinates and time are:

$$X = \xi = Re^{\frac{3}{8}} \lambda^{\frac{5}{4}} \frac{x^* - L^*}{L^*}, \quad (C-1)$$

$$Y = \eta = Re^{\frac{3}{8}} \lambda^{\frac{5}{4}} \frac{y^*}{L^*}, \quad (C-2)$$

$$Z = z + hF(\xi, \eta) = Re^{\frac{5}{8}} \lambda^{\frac{3}{4}} \frac{z^*}{L^*}, \quad (C-3)$$

$$Z_u = z_u = Re^{\frac{3}{8}} \lambda^{\frac{5}{4}} \frac{z^*}{L^*}, \quad (C-4)$$

$$t = \omega t^*, \quad (C-5)$$

The steady-flow variables are:

$$U = Re^{\frac{1}{3}} \lambda^{\frac{1}{4}} \frac{U^*}{U_{\infty}^*}, \quad (C-6)$$

$$V = Re^{\frac{1}{3}} \lambda^{\frac{1}{4}} \frac{V^*}{U_{\infty}^*}, \quad (C-7)$$

$$W^T = Re^{\frac{3}{8}} \lambda^{\frac{3}{4}} \left[\frac{W^*}{U_{\infty}^*} - h \partial_x F^* \frac{U^*}{U_{\infty}^*} - h \partial_y F^* \frac{V^*}{U_{\infty}^*} \right]; \quad (C-8)$$

however, to regain the physical meaning of the W-velocity; in the steady-flow results presented in Chapter 3, we have inverted the Prandtl transposition, equation (1-66b), to obtain;

$$\begin{aligned} W &= W^T + h \partial_x F U + h \partial_y F V \\ &= Re^{\frac{3}{8}} \lambda^{\frac{3}{4}} \frac{W^*}{U_{\infty}^*}, \end{aligned} \quad (C-8)$$

and,

$$P = Re^{\frac{2}{3}} \lambda^{\frac{1}{2}} \frac{P^* - P_{\infty}^*}{\rho U_{\infty}^{*2}}, \quad (C-9)$$

$$A = Re^{\frac{5}{3}} \lambda^{\frac{3}{4}} \frac{A^*}{L^*}, \quad (C-10)$$

$$F = Re^{\frac{5}{3}} \lambda^{\frac{3}{4}} \frac{F^*}{L^*}, \quad (C-11)$$

$$\hat{P} = Re^{\frac{2}{3}} \lambda^{\frac{1}{2}} \frac{\hat{P}^* - P_{\infty}^*}{\rho U_{\infty}^{*2}}. \quad (C-12)$$

In the disturbance-flow results presented in Chapter 4, we have subtracted out the Stokes flow (see equations (1-71) and (1-76)). So we can only consider the T-S waves generated by the receptivity problem.

The disturbance-flow variables are:

$$\begin{aligned}
 u &= \text{Real} \{ e^{-it} u_c \} \\
 &= \delta^{-1} \left[\frac{u^*}{U_\infty^*} - \delta \text{Real} \left\{ e^{-i\omega t} \left[1 - \exp \left(i^{3/2} Re^{1/2} S^{1/2} \frac{(z^* - hF^*)}{L^*} \right) \right] \right\} \right], \quad (C-13)
 \end{aligned}$$

$$v = \text{Real} \{ e^{-it} v_c \} = \delta^{-1} \frac{v^*}{U_\infty^*}, \quad (C-14)$$

$$\begin{aligned}
 w^T &= \text{Real} \{ e^{-it} w_c \} \\
 &= \delta^{-1} Re^{\frac{2}{3}} \lambda^{\frac{1}{2}} \left[\frac{w^*}{U_\infty^*} - h \partial_x F^* \frac{u^*}{U_\infty^*} - h \partial_y F^* \frac{v^*}{U_\infty^*} \right]; \quad (C-15)
 \end{aligned}$$

again, to regain the physical meaning of the w-velocity; we have inverted the Prandtl transposition, equation (1-66a), to obtain;

$$\begin{aligned}
 w &= \text{Real} \{ e^{-it} [w_c + h \partial_x F (u_c + 1 - \exp(i^{3/2} S_0^{1/2} z)) + h \partial_y F v_c] \}, \\
 &= \delta^{-1} Re^{\frac{2}{3}} \lambda^{\frac{1}{2}} \frac{w^*}{U_\infty^*}, \quad (C-15)
 \end{aligned}$$

$$\begin{aligned}
p &= \text{Real} \{ e^{-it} p_c \} \\
&= \delta^{-1} Re^{\frac{1}{8}} \lambda^{\frac{1}{4}} \left[\frac{p^*}{\rho U_-^2} - \delta \text{Real} \left\{ e^{-i\alpha x^*} i S \frac{(x^* - L^*)}{L^*} \right\} \right],
\end{aligned} \tag{C-16}$$

$$a = \text{Real} \{ e^{-it} a_c \} = \delta^{-1} Re^{\frac{4}{8}} \lambda \frac{a^*}{L^*}, \tag{C-17}$$

$$\begin{aligned}
\hat{p} &= \text{Real} \{ e^{-it} \hat{p}_c \} \\
&= \delta^{-1} Re^{\frac{1}{8}} \lambda^{\frac{1}{4}} \left[\frac{\hat{p}^*}{\rho U_-^2} - \delta \text{Real} \left\{ e^{-i\alpha x^*} i S \frac{(x^* - L^*)}{L^*} \right\} \right],
\end{aligned} \tag{C-18}$$

$$S_0 = Re^{\frac{2}{8}} \lambda^{\frac{3}{2}} S; \tag{C-19}$$

$$\text{where} \quad S = \frac{\omega L^*}{U_-^*}, \tag{C-20}$$

and, λ is the slope of the incoming boundary-layer velocity profile at the wall (i.e. $\lambda \equiv U'_B(0)$).

APPENDIX D

T-S Wave Profiles in The Lower Deck

In this appendix, we present representative T-S wave profiles at several locations downstream of the hump for the case of an amplifying wave ($S_0 = 3.0$). These profiles are for a particular Reynolds number, $Re = 1000000$, with the amplitude of the free-stream fluctuations taken to be $\delta = .01$ and, λ is the slope of the incoming Blasius velocity-profile at the wall ($\lambda \equiv U'_B(0)$). Here we give profiles of u_{rms} (defined below) as an estimate of the T-S wave intensity along the direction normal to the wall.

Where u_{rms} is nondimensionalized by the free-stream velocity U_∞^* :

$$u_{rms} = \left[\left(\frac{u_{TS}^*}{U_\infty^*} \right)^2 + \left(\frac{v_{TS}^*}{U_\infty^*} \right)^2 + \left(\frac{w_{TS}^*}{U_\infty^*} \right)^2 \right]^{\frac{1}{2}}, \quad (D-1)$$

where the subscript "TS" indicates T-S wave, implying that the Stokes flow is subtracted out (see equation (1-71a)). Profiles of u_{rms} in the lower deck are shown below for two different Y-locations, Y=0 and Y=1.0, in figure 88 at the following X-locations downstream of the hump: X = 1.5, 3.0, 4.2, 6.0, 7.2, 8.7, and 10.2 .

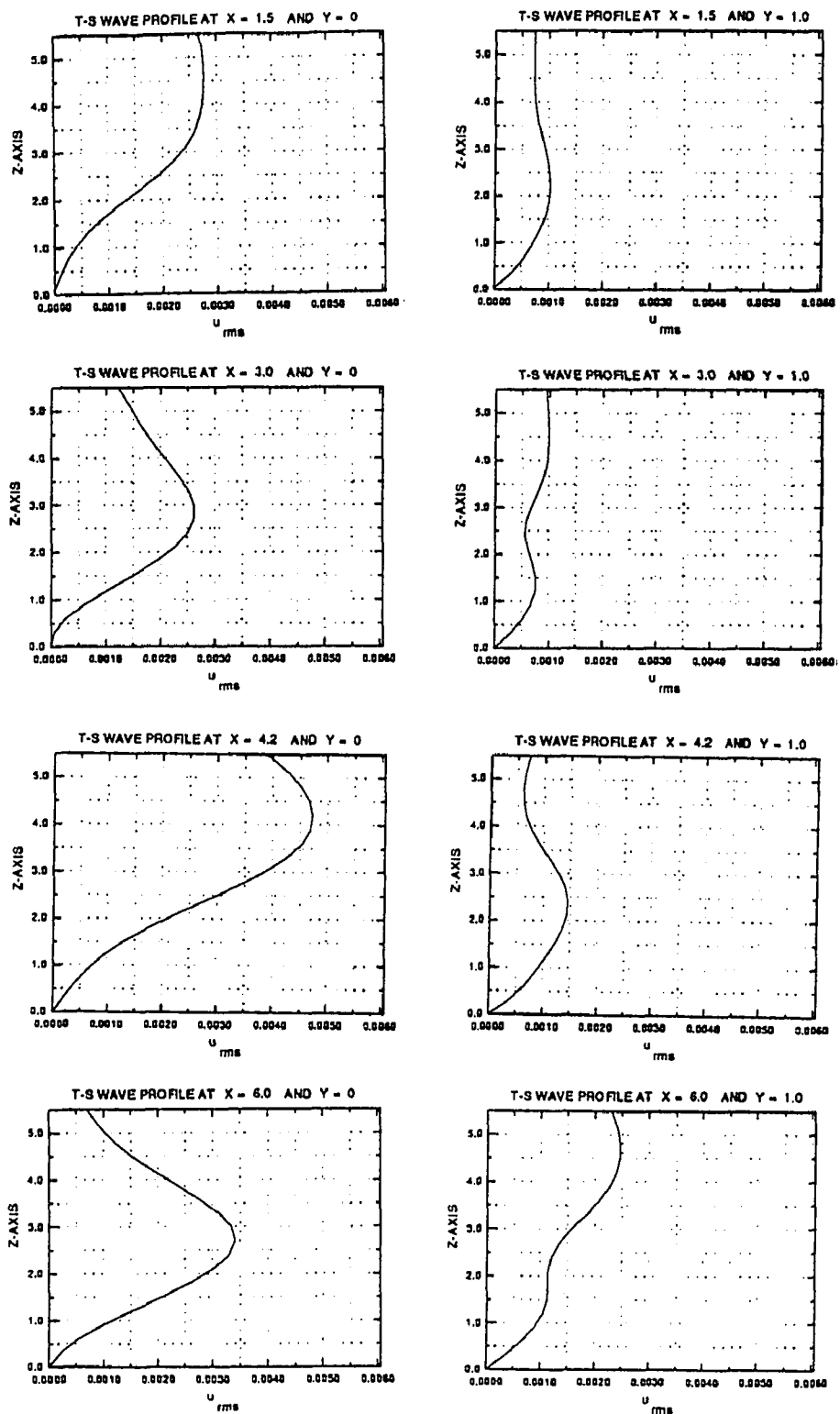
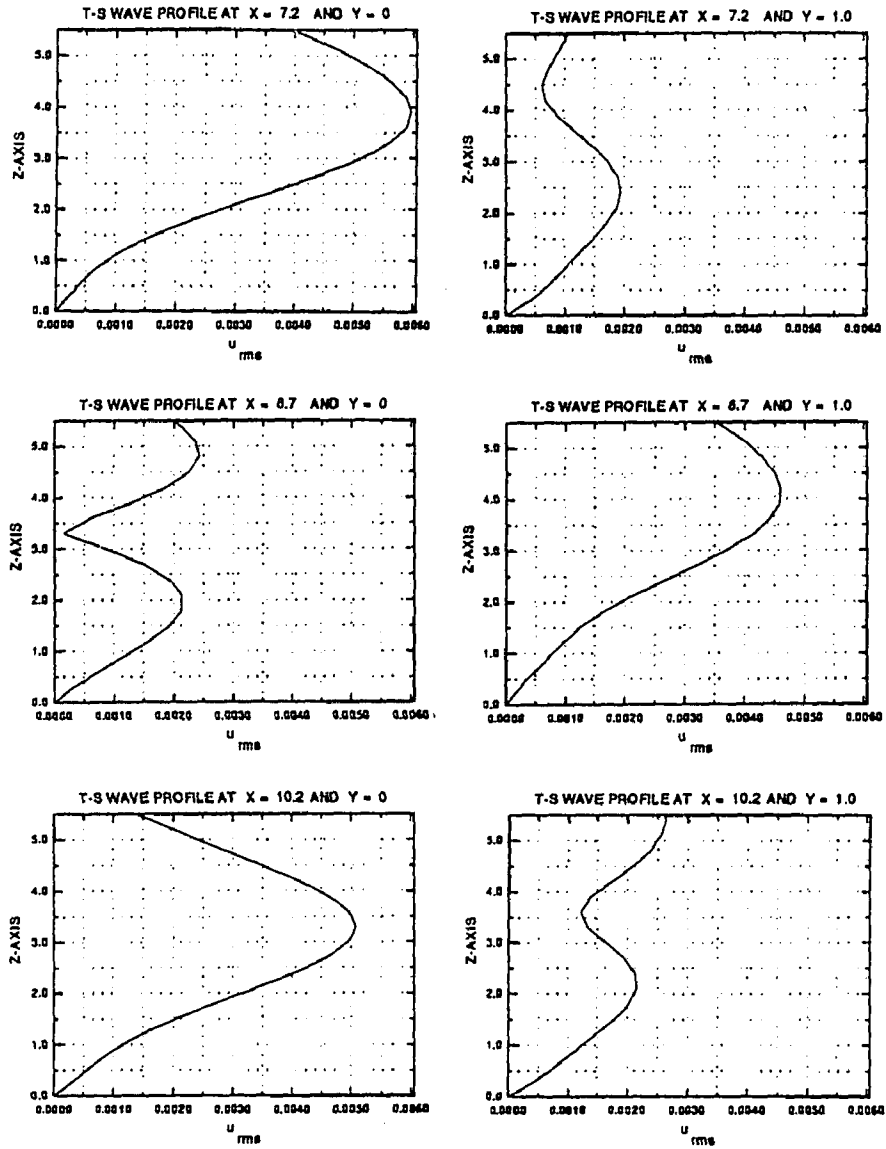


Figure 59. Profiles of u_{rms} (defined by equation (D-1)) in the lower deck for an amplifying wave, $S_0 = 3.0$, $Re = 1000000$, and $\delta = .01$, for two different Y-locations, $Y=0$ and $Y=1.0$, downstream of the hump, $h=1$, at: $X = 1.5, 3.0, 4.2, 6.0, 7.2, 8.7, \text{ and } 10.2$.

Figure 59. continued



LIST OF REFERENCES

1. Reshotko, E. "Boundary-Layer Stability and Transition," *Ann. Rev. Fluid Mech.*, Vol. 8, pp. 311-349 1976 .
2. Mack, L. "Boundary-Layer Linear Stability Theory," AGARD special course on stability and transition, March 1984 .
3. Herbert, Th. and Bodonyi, R. "Studies of Transition in Boundary Layers" AIAA meeting, Reno , AIAA-89-0034 Jan. 1989 .
4. Gaster, M. and Grant, I. "An Experimental Investigation of the Formation and Development of Wavepacket in a Laminar Boundary Layer," *Proc. Roy. Soc. A.347*, p. 253 1975 .
5. Gaster, M. "A Theoretical model of a Wavepacket in the Boundary Layer on a Flat Plate," *Proc. Roy. Soc. A.347*, p. 271 1975 .
6. Gaster, M. "On Wave Packets in Laminar Boundary Layers" IUTAM Symposium, Novosibirsk, USSR, Laminar-Turbulent Transition, editor V. V. Kozlov, Springer-Verlag, 1985 .
7. Gilev, V.M., Kachanov, Y.S., and Kozlov, V.V. , "Development of a Spatial wave packet in a Boundary Layer" Preprint No. 34-81, Inst. of Theoretical and Appl. Math., USSR Acad. Sci., Novosibirsk 1981 .
8. Kachanov, Y.S. "Development of Spatial Wave Packets in Boundary Layer" IUTAM Symposium, Novosibirsk, USSR, Laminar-Turbulent Transition, editor V. V. Kozlov, Springer-Verlag, 1985 .
9. Mack L.M. and Kendall J.M. "Wave Pattern Produced by a Localized Harmonic Source in a Blasius Boundary Layer" AIAA meeting, Reno, AIAA-83-0046 Jan. 1983 .

10. Reshotko, E. "Environment and Receptivity", AGARD Report 709, NATO, Paris 1984 .
11. Goldstein, M. " The Evolution of Tollmien-Schlichting Waves Near a Leading Edge" *J. Fluid Mech.*, Vol. 127, pp. 59-81 1983 .
12. Goldstein, M. "Scattering of acoustic waves into Tollmien-Schlichting Waves by a Small Streamwise Variations in Surface Geometry" *J. Fluid Mech.* , Vol. 154, pp. 509-529 1985 .
13. Goldstein, M. and Hultgren L.S. "A Note on the Generation of Tollmien-Schlichting Waves by Sudden Surface Curvature Change" *J. Fluid Mech.* , Vol. 181, pp. 519-525 1987 .
14. Goldstein, M. and Hultgren L.S. "Boundary Layer Receptivity To Long-Wave Free-Stream Disturbances" *Ann. Rev. Fluid Mech.*, Vol. 21, pp. 137-166 1989 .
15. Stewartson, K. "Multistructured boundary layers on flat plates and related bodies" *Adv. in Appl. Mech.*, Vol 14, pp. 145-239 1974 .
16. Bodonyi, R., Welch, P., Duck, P., and Tadjfar, M. "A numerical study of the interaction between unsteady free-stream disturbances and localized variations in surface geometry", *J. Fluid Mech.* , Vol. 209, pp. 285-308 1989 .
17. Stewartson, K. and Williams, P.G. "Self-Induced Separation" *Proc. Roy. Soc. London A.312*, pp. 181-206 1969 .
18. Messiter, A.F. "Boundary Layer Flow Near the Trailing Edge of a Flat Plate" *SIAM J. Appl. Math.* , Vol. 18, pp. 241-257 1970 .
19. Neiland, V.Y. "Towards a Theory of Separation of the Laminar Boundary Layer in a Supersonic Stream" *Izv. Akad. Nauk SSSR, Mekh. Zhidk. Gaza.* , pp. 53-57. Translated in *Fluid. Dyn.* Vol. 4, pp. 33-35 1969 .
20. Smith F.T., "On the High Reynolds Number Theory of Laminar Flows" *IMA J. Of Appl. Math* , Vol. 28, pp. 207-281 1982 .

21. Smith F.T. "Steady and Unsteady Boundary-Layer Separation " *Ann. Rev. Fluid Mech.*, Vol. 18, pp. 197-220 1986 .
22. Lin C.C. "The Theory of Hydrodynamic Stability" Cambridge University Press 1955 .
23. Smith F.T. "Properties, and a Finite-Difference Approach, for Interactive Three-Dimensional Boundary Layers" UTRC-83-46 1983 .
24. Bodonyi, R. and Duck, P. "A Numerical Method for Treating Strongly Interactive Three-Dimensional Viscous-inviscid Flows", *Computers & Fluids*, Vol. 16, No. 3, pp. 279-290 1988 .
25. Anderson, Tannehill and Pletcher "Computational Fluid Mechanics and Heat Transfer" hpc. pp. 349-354 1984 .
26. Sykes R.I. "On Three-Dimensional Boundary Layer Flow Over Surface Irregularities" *Proc. Roy. Soc. London A.*373, pp. 311-320 1980 .
27. Reyhner T.A., Flugge-Lotz, I. *Int. J. Nonlinear Mech.*, vol. 3, p.173 1968 .
28. Duck P. and Burggraf O. "Spectral Solutions for Three-dimensional Triple-Deck Flow Over Surface Topography" *J. Fluid Mech.* , Vol. 162, pp. 1-22 1986 .
29. Lighthill, M.J. "Laminar Boundary Layers" edited by L. Rosenhead, Dover, Sections 2.6-2.9 1988 .
30. Kerschen, E. J. "Boundary Layer Receptivity Theory" *Appl Mech Rev* vol 43, no 5, Part 2, May 1990 .
31. Ackerberg, R. C. and Phillips, J. H. " The unsteady laminar boundary layer on a semi-infinite flat plate due to small fluctuations in the magnitude of the free-stream velocity " *J. Fluid Mech.* , vol. 51, pp. 137-157 1972 .
32. Van Dyke, M. "Perturbation Methods In Fluid Mechanics" Parabolic Press 1975 .

33. Williams, P.G., Proc. 4th. Int. Conf. on Num. Methods in Fluid Dynamics 1974